

## ABSTRACT

NADERI, GOLSA. Understanding Processing, Microstructure and Transport Relationships of  $\text{Bi}_2\text{Sr}_2\text{CaCu}_2\text{O}_x/\text{Ag}$  Round Wires. (Under the direction of Prof. Justin Schwartz).

Superconducting magnets generating magnetic fields above 25 T are needed for many scientific applications. Due to fundamental limitations to NbTi and  $\text{Nb}_3\text{Sn}$ , such high-field superconducting magnets require alternative high-field conductors. One candidate conductor is round wire composites of  $\text{Bi}_2\text{Sr}_2\text{CaCu}_2\text{O}_x$  sheathed in an Ag-alloy matrix (Bi2212/Ag). The performance of such wires is sensitive to the heat treatment, so improvements in the critical current density ( $J_c$ ) require a thorough understanding of the processing-structure-properties relationships. Due to the complex microstructure-transport relationships, their performance is far from optimized, and the potential for further increase in  $J_c$  remains.

In this research a new heat treatment approach, saw-tooth processing (STP) is introduced based upon previous results showing that Bi2212 nucleation is site-saturation limited. STP increases  $J_c$  by 120% and 70% relative to partial-melt processing at 5 T and self-field respectively. The effects of STP heat treatment parameters on the microstructure and transport properties are discussed. It is shown that wires with the highest transport critical current densities primarily have filaments with two types of microstructures, one comprised primarily highly textured Bi2212 grains, and another with a noticeable amount of  $\text{Bi}_2\text{Sr}_2\text{CuO}_x$  with the Bi2212.

After processing, multifilamentary Bi2212 round wires have complex microstructures. In melt processed Bi2212/Ag wires the primary impurity is  $\text{Bi}_2\text{Sr}_2\text{CuO}_x$

(Bi2201), which forms as mesoscopic grains and nanoscopic intergrowths. Microstructure-properties relationship studies are performed based on the hypothesis that Bi2201 plays critical roles in transport depending on the micron-size length scale. Mesoscopic microstructures are analyzed quantitatively using a statistical approach in which filaments are categorized based on the predominant phases observed by scanning electron microscope (SEM). A Matlab program is created to analyze the SEM micrographs and categorize over 100 filaments within each image. The majority of filaments (78% of all filaments classified) are either predominantly Bi2212 or containing-large-Bi2201 grains.  $J_c$  is directly proportional to the percentage of “predominantly-Bi2212” filaments. Although typically 70-90% of the containing-large-Bi2201 filament cross-sections is actually Bi2212 phase,  $J_c$  is inversely proportional to the percentage of this type of filament.

To study the impact of nanoscale Bi2201 intergrowths on the superconducting properties, Bi2212 grains are extracted from filaments with and without significant Bi2201 grains present. By relating scanning transmission electron microscopy results to the Bi2212 coherence length, anisotropic magnetization behavior and magnetic-field dependent transport the effects of Bi2201 intergrowths on c-axis transport and magnetic flux pinning is studied. Wide Bi2201 (15-25 nm), intergrowths are barrier to c-axis transport within Bi2212 grains, whereas narrow half (1.3 nm wide),- and full-cell (2.5 nm wide) Bi2201 intergrowths are not detrimental to c-axis transport and are likely magnetic flux pinning centers. Microstructural, magnetization and transport studies designate effective contribution of c-axis transport in Bi2212/Ag multifilamentary wires; because the continuous favorable a–b plane current path is obstructed randomly.

In addition to conventionally-processed wires, 100 atm over pressured partial melt processed wires (OP-PMP) are studied on different length scales. OP causes grain growth in the pre-annealing, increases the peritectic melting temperature in the partial melt, improves oxygen uptake during solidification, and enhances the grain connectivity in sintering. The increase in transport of OP-PMP wire is related to increase in filament density. Yet OP-PMP wire shows higher area fraction of filaments with large Bi2201 grains. To even further improve the transport, optimization of OP-PMP is essential. This study confirms that after porosity, Bi2201 grains has the greatest negative impact on Bi2212 wires and further enhancements in Bi2212 wire performance requires either avoiding the formation of Bi2201 grains, or ensuring complete conversion of Bi2201 to Bi2212 grains.

© Copyright 2014 Golsa Naderi

All Rights Reserved

Understanding Processing, Microstructure and Transport Relationships of  $\text{Bi}_2\text{Sr}_2\text{CaCu}_2\text{O}_x/\text{Ag}$   
Round Wires

by  
Golsa Naderi

A dissertation submitted to the Graduate Faculty of  
North Carolina State University  
in partial fulfillment of the  
requirements for the degree of  
Doctor of Philosophy

Materials Science and Engineering

Raleigh, North Carolina

2014

APPROVED BY:

---

Prof. Justin Schwartz  
Committee Chair

---

Prof. Carl Koch

---

Prof. Elizabeth Dickey

---

Prof. Frank Hunte

---

Prof. Korukonda Murty

## **DEDICATION**

This thesis is dedicated to

my parents, maman Pari and baba Habib,

my love , Ali,

for their endless support and encouragement.

## **BIOGRAPHY**

Golsa Naderi was born in Arak, Iran on July 6th, 1981. After finishing her high school in NODET (National Organization for Development of Exceptional talents), she was admitted to the Materials science and engineering (Ceramics), Dept. of Material Science and Engineering, Iran University of Science and Technology in 1999 as her first choice. In 2004, she was admitted to the Master of Science Materials Engineering Graduate Degree Program, Dept. of Mechanical Engineering, K.N. Toosi University of Technology, Tehran, Iran. During and after the Master's degree, Golsa was an inspector and Technical expert in Cany Mes Company (Engineering and Technical Services Company In Mines and Industries). She came to the US in Aug., 2009 and joined Prof. Schwartz group at North Carolina State University in 2010 and took her PhD in Materials Science and engineering in July 2014.

## **ACKNOWLEDGMENTS**

It is a pleasure to thank all who made this thesis possible. I wish to express my sincere gratitude to my supervisor Professor Schwartz for his guidance, encouragement and support throughout the course of my research. I would like to acknowledge the valuable feedback provided by my research advisory committee members: Professors. Koch, Hunte, Dickey and Murty. I would also like to thank Edna Deas and every single member of Schwartz research group who gave me numerous help since my admission until graduation.

## TABLE OF CONTENTS

LIST OF TABLES .....	vi
LIST OF FIGURES .....	vii
<b>Chapter 1: Introduction and overview .....</b>	<b>1</b>
<b>REFERENCES .....</b>	<b>47</b>
<b>Chapter 2: Understanding processing - microstructure – properties relationships in</b> <b>Bi<sub>2</sub>Sr<sub>2</sub>CaCu<sub>2</sub>O<sub>x</sub>/Ag round wires and enhanced transport through saw-tooth processing</b> .....	<b>65</b>
<b>REFERENCES .....</b>	<b>101</b>
<b>Chapter 3: Statistical analysis of the relationship between electrical transport and</b> <b>filament microstructure in multifilamentary Bi<sub>2</sub>Sr<sub>2</sub>CaCu<sub>2</sub>O<sub>x</sub>/Ag/Ag-Mg round wire..</b>	<b>109</b>
<b>REFERENCES .....</b>	<b>127</b>
<b>APENDICES .....</b>	<b>132</b>
<b>Chapter 4: On the roles of Bi<sub>2</sub>Sr<sub>2</sub>CuO<sub>x</sub> intergrowths in Bi<sub>2</sub>Sr<sub>2</sub>CaCu<sub>2</sub>O<sub>x</sub>/Ag round</b> <b>wires: c-axis transport and magnetic flux pinning .....</b>	<b>143</b>
<b>REFERENCES .....</b>	<b>156</b>
<b>APENDICES .....</b>	<b>161</b>
<b>Chapter 5: Multiscale studies of processing-microstructure-transport relationships in</b> <b>over- pressure processed Bi<sub>2</sub>Sr<sub>2</sub>CaCu<sub>2</sub>O<sub>x</sub>/Ag multifilamentary round wire.....</b>	<b>166</b>
<b>REFERENCES .....</b>	<b>186</b>
<b>APENDICES .....</b>	<b>193</b>

<b>Chapter 6: Conclusions and Future Suggested works</b> .....	194
<b>REFERENCES</b> .....	198

## LIST OF TABLES

Table 4.1. Characteristics of representative wires 1 and 2 used for magnetization and transport studies. $H_p$ is the magnetic field with maximum magnetic field penetration. The anisotropy parameter $\alpha$ is obtained from magnetization hysteresis measurements at 4.2 K at fields of $H_p$ and 2 T using equation 2 .....	151
Table 5-1 $I_c$ and $J_c$ at 4.2 K, 5 T, for the PMP and OP-PMP Bi2212/Ag wires.....	174
Table 5-2 Semi-quantitative EDS results of the corresponding four samples (shown in Figure 5-6).....	184
Table 5-3 Semi-quantitative EDS-STEM results of the Bi2212 colony shown in Figure 5-8. ....	183

## LIST OF FIGURES

Figure 1-1. Attractive force between electron pairs through the medium [6] .....	2
Figure 1-2. Magnetization behavior of type II superconductors in an external magnetic field [6].....	4
Figure 1-3. Structure of a flux line, at the presence of $H_e$ where the order parameter is locally lost in $\xi$ the radius area and the condensation energy increases there. The magnetic field penetrates in the radius and the magnetic energy is decreased. The normal conducting core is surrounded by the magnetic field with the radius of $\lambda$ [6].....	5
Figure 1-4. (a) Crystal structure of $\text{Bi}_2\text{Sr}_2\text{CuO}_8$ (Bi2201, Raveau Phase), $\text{Bi}_2\text{Sr}_2\text{CaCuO}_8$ (Bi2212) and $\text{Bi}_2\text{Sr}_2\text{Ca}_2\text{Cu}_3\text{O}_{10}$ (Bi2223) (b) phase diagram between Bi2201, Bi2212 and Bi2223 compounds [14].....	6
Figure 1-5. The electronic configuration of $3d^9$ for $\text{Cu}^{2+}$ and $2p^6$ for $\text{O}^{2-}$ in the $\text{CuO}_2$ layer [6]. .....	7
Figure 1-6. Critical current densities ( $J_c$ ) of available superconductors used for magnets [20]. .....	12
Figure 1-7. Typical cross sectional transverse view of (a) single, (b) double restack Bi2212 multifilamentary wire [18].....	14
Figure 1-8. A typical partial melt processing (PMP) profile .....	14
Figure 1-9. SEM micrographs of a transverse sections of a Bi2212 wire after PMP .....	16
Figure 1-10. SEM images of the six types of filaments.] .....	16
Figure 1-11. (a) SEM micrograph of a filament showing micron size Bi2201 grains between Bi2212 grains, (b) high angle annular dark field (HAADF) scanning transmission electron microscopy (STEM) image showing Bi2201 intergrowths within a Bi2212 grain .....	25
Figure 1-12. Schematic of two types of bridges, (a) Type-A bridges form from solidification of the the liquid between filaments during coding, (b) Type-B bridges form from Bi2212 growing into the Ag.....	27
Figure 1-13. The transvers ( $\theta$ ) and longitudinal ( $\alpha$ ) misalignment angles based on filament geometries and Ag–Bi2212 interfaces in Bi2212/Ag tape. ....	28
Figure 1-14. Split melt processing (SMP) heat treatment profile.....	40
Figure 1-15. Saw-tooth processing (STP).....	41
Figure 2-1. Optical images of cross-sections of unreacted Bi2212 wires, (a) wire I, (b) wire II. ....	72
Figure 2-2. Temperature-time schematics (not to scale) of the heat treatment profiles for (a) partial-melt. processing, (b) split-melt processing, (c) saw-tooth processing. ....	74
Figure 2-3. Temperature-time schematics (not to scale) of the heat treatment profiles used for the quench study using wire I. ....	75
Figure 2-4 Cross sectional SEM micrographs of Bi2212/Ag multifilamentary wires after (a) partial-melt processing, (b) split-melt processing, (c) saw-tooth processing (STP1) and (d) saw-tooth processing (STP2). ....	76
Figure 2-5. Cross sectional SEM micrographs of (a) Bi2212/Ag multifilamentary wire after STP2, (b) filament with Bi2201 grains (c) dense, highly textured Bi2212 filament .....	77

Figure 2-6. Transport $J_c$ versus magnetic field for wires heat treated by PMP, SMP, STP1 and STP2.....	78
Figure 2-7. Cross sectional SEM micrographs of Bi2212/Ag multifilamentary wires quenched during STP. Samples are quenched from (a) $T_p = 884$ °C, QTP, (b) $T_{r1} = 882$ °C, QT <sub>R1</sub> , (c) $T_2 = 872$ °C, QT <sub>2</sub> , (d) $T_{r2} = 873$ °C, QSTP-T <sub>R2</sub> , (e) $T_3 = 832$ °C, QSTP-T <sub>3</sub> , (f) $T_4 = 832$ °C, QSTP-T <sub>4</sub> .....	79
Figure 2-8. AEC area fractions as determined by image analysis using the quenched sample SEM micrographs shown in Figure 7. ....	81
Figure 2-9. Differential thermal analysis results showing the effect of each STP heat treatment cycle on the melting behavior.....	82
Figure 2-10. Effect of cycle-1 and cycle-2 on the microstructure, a) cross sectional SEM micrograph after cycle-1, b) cross sectional SEM micrograph after cycle-2, c) AEC content after cycle-1, d) AEC content after cycle-2, and e) FIB cross section image showing the formation of Bi2212 on top of a secondary phase. ....	83
Figure 2-11. Effect of each STP heat treatment cycle on the magnetization behavior.....	84
Figure 2-12. Effect of cooling rate from $T_{r1}$ to $T_2$ on $J_c$ and cross sectional SEM micrographs for a) a cooling rate of 2.5 °C/hr, $J_c = 2760$ A/mm <sup>2</sup> , b) a cooling rate of 5 °C/hr, $J_c = 2443$ A/mm <sup>2</sup> , c) cooling rate of 10 °C/hr, $J_c = 1854$ A/mm <sup>2</sup> .....	85
Figure 2-13. Effect of cooling rate from $T_2$ to $T_{r2}$ on $J_c$ and cross sectional SEM micrographs for a) cooling rate of 80 °C/hr, $J_c = 1880$ A/mm <sup>2</sup> and b) a cooling rate of 160 °C/hr, $J_c = 1550$ A/mm <sup>2</sup> .....	86
Figure 2-14. Effect of heating rate from $T_{r2}$ to $T_{r1}$ on $J_c$ and cross sectional SEM micrographs for a) heating rate of 80 °C/hr, $J_c = 2760$ A/mm <sup>2</sup> , and b) a heating rate of 60 °C/hr, $J_c = 1800$ A/mm <sup>2</sup> .....	87
Figure 2-15. Effect of $T_{r2}$ on the 4.2 K, self-field $J_c$ .....	88
Figure 2-16. Cross sectional SEM micrographs at different $T_{r2}$ s. ....	89
Figure 2-17. Cross sectional SEM micrographs of a) a filament consisting of a noticeable amount of Bi2201 grains, and b) a filament consisting of highly textured Bi2212 grains. ....	90
Figure 3-1. SEM images of the five types of filaments. ....	114
Figure 3-2. (a) A typical SEM micrograph used as input for the Matlab program and (b) the resulting color-coordinated output image from the Matlab program. Red boxes are Bi2212 filaments, green boxes Bi2201 filaments, dark blue boxes are AEC filaments, turquoise boxes are CF filaments and purple boxes are mixed secondary phases filaments.....	115
Figure 3-3. $J_c$ versus the percentage of Bi2212 filaments.....	118
Figure 3-4. $J_c$ versus the percentage of Bi2201 filaments.....	118
Figure 3-5. Area fractions of Bi2201 phase in “Bi2201” filaments and of Bi2212 in “Bi2212” filaments.....	119
Figure 3-6. $J_c$ versus the percentage of AEC filaments.....	119
Figure 3-7. The area fraction of the Bi2212 filaments that is Bi2212 phase, and the area fraction of Bi2201 filaments that is Bi2201 phase.....	120
Figure 3-8. Percentage of Bi2201 filaments versus percentage of Bi2212 filaments.....	120
Figure 3-9. Percentage of AEC filaments versus percentage of Bi2212 filaments.....	121

Figure 3-10. HAADF STEM images of (a) two Bi2212 grains extracted from a Bi2212 filament and (b) a Bi2212 grain extracted from a Bi2201 filament. The black arrow identifies a Bi2201 intergrowth. ....	122
Figure. 4-1. Illustration of the defects and current limiting structures in Bi2212 round wires on multiple length scales. ....	145
Figure. 4-2 Illustration of the defects and current limiting structures in Bi2212 round wires on multiple length scales. ....	147
Figure. 4-3. HAADF-STEM (a) image and (b) EDS-STEM maps of a Bi2212 grain extracted from a “Bi2212 filament”.. ....	148
Figure. 4-4. (a) Cross-sectional SEM image of a “Bi2201 filament” with Bi2212 and Bi2201 area fractions of 88% and 12%, respectively. (b) HAADF-STEM image of a Bi2212 grain extracted from the filament shown in (a). The Bi2201 intergrowths are seen as bright lines. (c) Atomic resolution HAADF-STEM image on the [100] zone showing the crystal structure of Bi2212 and Bi2201. (d) HAADF-STEM image showing diverse Bi2201 intergrowth widths, including a number of half and full-cell. ....	150
Figure. 4-5. (a) Average $J_c(4.2\text{ K})$ as a function of magnetic field for W1 and W2. The magnetic field is applied perpendicular to the wire axis. (b) Magnetic field dependence of the normalized $J_c$ at low magnetic field. Weak links dominate in regions I and II. (c) Magnetic field dependence of the normalized $J_c$ at high magnetic field (region III). Transport is through strong links only and $J_c$ is limited by flux pinning .....	153
Figure 4-S1. XRD of powder obtained by grinding Bi2212 filaments that remain after etching the silver matrix. ....	162
Figure 4-S2. (a) STEM image of a [001] tilt boundary, (b) bright field TEM image of a $8^\circ$ colony boundary, (c) bright field TEM image of an edge on c-axis grain boundary. Schematic drawings of each are also shown. ....	163
Figure 4-S3. (a) Magnetization hysteresis for (a) wire 1 (high $J_c$ ) and (b) wire 2 (low $J_c$ )... ..	163
Figure 5-1 Scanning electron microscope cross-sectional transverse view of unreacted wire .....	174
Figure 5-2 PMP temperature-time profile. The same profile is used for conventional PMP and OP-PMP. ....	174
Figure 5-3 SEM cross sectional view of a) PMP and b) OP-PMP wire. ....	176
Figure 5-4 Interior view of filaments from a) PMP and an b) OP-PMP wires after FIB cross-sectioning. ....	177
Figure 5-5 HAADF STEM images of a) Bi2212 grain colonies from a PMP wire showing porous grain boundaries. b) Well-connected Bi2212 grains in a OP-PMP wire. ....	178
Figure 5-6 HAADF-STEM images of Bi2212 grains extracted from Bi2212 filaments from a) PMP wire, b) OP-PMP wire, and Bi2212 grains extracted from Bi2201 filaments from a c) PMP wire d) OP-PMP wire. ....	180
Figure 5-7 Magnetization as a function of temperature at magnetic fields of 50, 100, 500 and 1000 Oe for a) PMP and b) OP-PMP wire. ....	182
Figure 5-8 A HAADF STEM image of grain colonies extracted from a Bi2212 filament from a PMP wire. This image was used for the EDS semi-quantitative map. ....	183

Figure 5-9 A HAADF STEM image in Bi2212 grains in a Bi2201 filament from an OP-PMP wire. On the left side of the image, the zone axis is close to [100], whereas on the right side of the image the zone axis is close to [010]...... 184

# Chapter 1

## Introduction and overview

### Superconductivity basic principles

Superconductivity was discovered by H. Kamerlingh Onnes in 1911[1]. The most important feature of a superconductor is its ability to carry current without noticeable energy dissipation when cooled below the critical temperature ( $T_c$ ) [2]. Superconducting materials are categorized into two groups based on their  $T_c$ : low temperature superconductors (LTS) with  $T_c$  lower than boiling point of liquid nitrogen 77 K, and high temperature superconductors (HTS) with  $T_c$  above 77 K. With some exceptions like  $MgB_2$  with  $T_c=39$  K [3, 4]. NbTi,  $Nb_3Sn$  are two of the most common LTS materials, compounds of bismuth (Bi-Sr-Ca-Cu-O), yttrium or other RE elements (Y-Ba-Cu-O), thallium (Tl-Ba-Ca-Cu-O) and mercury (Hg-Ba-Ca-Cu-O) are examples of HTS materials [3].

BSC theory by Bardeen, Cooper, and Schrieffer describes the superconductivity phenomenon. Based on this theory the electron pairs, namely the Cooper pairs, form by decreasing the temperature and condense to the lowest energy level at  $T_c$ . Strong interaction between Cooper pairs does not allow scattering of the electrons, resulting to zero resistivity. To break the Cooper pairs a large kinetic energy equivalent to the  $2\Delta$  is needed. Cooper pairs break at temperatures higher than  $T_c$  [5, 6].

Figure 1.1 shows when one electron in the crystal attracts surrounding positive ions, a second electron will be pulled in by positive charges. This generates an attractive force between electrons that overcomes the local Coulombic interaction, and explains the origin of electron

pairs in low temperature superconductors [6]. High temperature superconductors also have Cooper pairs but the interaction mechanism is not fully understood yet. The distance between by which electrons move is called BCS coherence length ( $\xi_0$ ) [6] In a superconductor there are many of the Cooper pairs. These pairs have wave functions with same amplitude and phase, overlapping and resulting in a macroscopic wave function  $\psi$ .

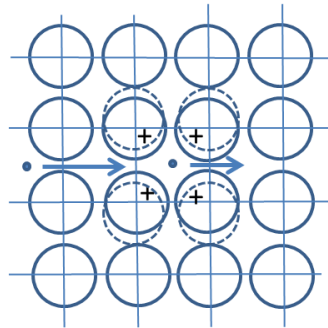


Figure 1-1. Attractive force between electron pairs through the medium [6]

Apart from the transition temperature, there is a critical value of magnetic field,  $H_c$ , above which the superconductivity is destroyed. In superconductors the current flow becomes finite if electric field  $E \neq 0$ . Based on Maxwell equation of (1) one finds that the magnetic field cannot vary with time when  $E = 0$  ( $B$  is the magnetic flux density). Therefore at the presence of magnetic field, in a superconducting state, magnetic fluxes do not penetrate through the material and are completely expelled from the interior of the superconducting material. This phenomenon is called the Meissner effect.

$$\nabla \times \mathbf{E} = -\partial \mathbf{B} / \partial t \quad (1)$$

The motion equation of a superconducting electron is given in equation (2), where the superconducting current density is  $J_s = -n_s e^* V_s$ ;  $V_s$  and  $n_s$  are the speed and the density of the superconducting electron. From these, equation (3) is obtained, which is called the first London equation. Here  $m^*$  and  $-e^*$  are the mass and charge of superconducting electron respectively. Applying the above Maxwell equation (1) one finds equation (4). Combining with  $\nabla \times B = \mu_0 J_s$  we have equation (5), where  $\lambda_L$ , and  $J$  are defined in equations (6) and (7) and  $A$  is the magnetic vector potential.

$$m^* \left( \frac{dV_s}{dt} \right) = -e^* E \quad (2)$$

$$\partial J_s / \partial t = (n_s e^{*2} / m^*) E \quad (3)$$

$$\frac{n_s e^{*2}}{m^*} B + \nabla \times J_s = 0 \quad (4)$$

$$\nabla^2 B = (1/\lambda_L)^2 B \quad (5)$$

$$\lambda_L = (m^* / n_s e^{*2} \mu_0)^{1/2} \quad (6)$$

$$J = - \left( n_s e^{*2} / m^* \right) A \quad (7)$$

This last equation, equation (7), introduces an important phenomenon, at the presence of magnetic field, the stationary supercurrent driven by the vector potential flows to establish the Meissner effect [6].

Based on the Meissner effect, superconductors are categorized in two types, type I and type II [7-9]. Figure 1-3 shows magnetization behavior of type II superconductors in an external magnetic field [10].

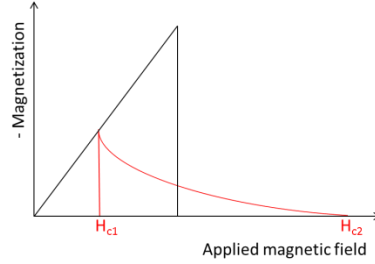


Figure 1-2. Magnetization behavior of type II superconductors in an external magnetic field [6].

If the transition from the superconducting state to the normal state is sharp, then this type of material is called type I superconductor. This behavior normally is observed in pure metal superconductors. In type II superconductors, there are two values of the critical field: the lower critical field ( $H_{c1}$ ) where the field is completely expelled from the superconductor and the upper critical field ( $H_{c2}$ ), where the magnetic field partially penetrates the material. In fields above  $H_{c2}$ , the material transforms to the normal state. The state between  $H_{c1}$  and  $H_{c2}$  is called the mixed state [9, 11]. In the mixed state the superconductivity is maintained up to  $H_{c2}$ . The reason why type II superconductors are practical is their high  $H_{c2}$ .

Ginzburg and Landau (GL) explain the superconductor theory by using the order parameter, equation (8), where the shielding current is the microscopic wave function  $\psi$ ,  $\xi$  is GL coherence length, the spatial change in the order parameter. Note  $\xi_0$  was the characteristic length that shows the extension of the Cooper pairs.  $\lambda_L$  and  $\xi$  are temperature dependent and are related by the GL parameter  $K = \lambda(T) / \xi(T)$ .

$$\psi = |\psi_0| \exp\left(-\frac{x}{\xi}\right) \quad (8)$$

The occurrence of vortices at the presence of magnetic field was predicted by Abrikosov [12]. Abrikosov found a two-dimensional (2D) periodic solution of the Ginzburg–Landau (GL) equations and suggested the periodic arrangement of flux lines, the flux-line lattice (FLL) [12].

The Figure 1-3 shows that when the external magnetic field is applied, vortices are invaded and superconductivity is lost in the  $\xi$  radius area and magnetic field energy is reduced in the  $\lambda$  radius of a flux line. The total free energy is following equation (9), where  $H_e^2$  is the applied magnetic field.

$$\mathbf{G} = \mathbf{G}_{core} + \mathbf{G}_{mag} = \left(\frac{1}{2}\right) \mu_0 H_c^2 \pi \xi^2 - \left(\frac{1}{2}\right) \mu_0 H_e^2 \pi \lambda^2 \quad (9)$$

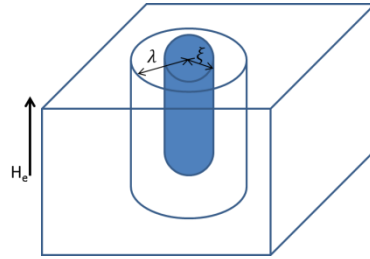


Figure 1-3. Structure of a flux line, at the presence of  $H_e$  where the order parameter is locally lost in  $\xi$  the radius area and the condensation energy increases there. The magnetic field penetrates in the radius and the magnetic energy is decreased. The normal conducting core is surrounded by the magnetic field with the radius of  $\lambda$  [6].

The superconducting shielding current flows in the area of  $\lambda$ . Each flux line (or fluxon, vortex line) carries one quantum of magnetic flux  $\phi_0 = 2.07 \times 10^{-15} \text{ Tm}^2$ , which is caused by the supercurrents circulating in this vortex [6, 12]. When the current  $J$  passes the

superconductor in the mixed state, the current applies the Lorentz force of  $f_l = J \times e_z \Phi_0$ , where  $e_z$  is the unit vector in the z direction. As a result of  $f_l$ , vortices move at a speed of  $v_L$  generating the electric field of  $E = B \times v_L$ . This is called vortex motion. The surrounding friction force limits the speed of flux motion. In the vortex flow state, vortex pinning becomes very important.

Cuprate superconductors: The cuprate superconductors are type II superconductors. The cuprates have a perovskite like crystal structure where the  $CuO_2$  planes represent the basic structural element which are separated by charge reservoirs layers [13].  $Bi_2Sr_2CuO_6$ ,  $Bi_2Sr_2CaCuO_8$  and  $Bi_2Sr_2Ca_2Cu_3O_{10}$  crystal structures are shown in the Figure 1-4a. The corresponding phase diagram is also given in Figure 1-4b [14].

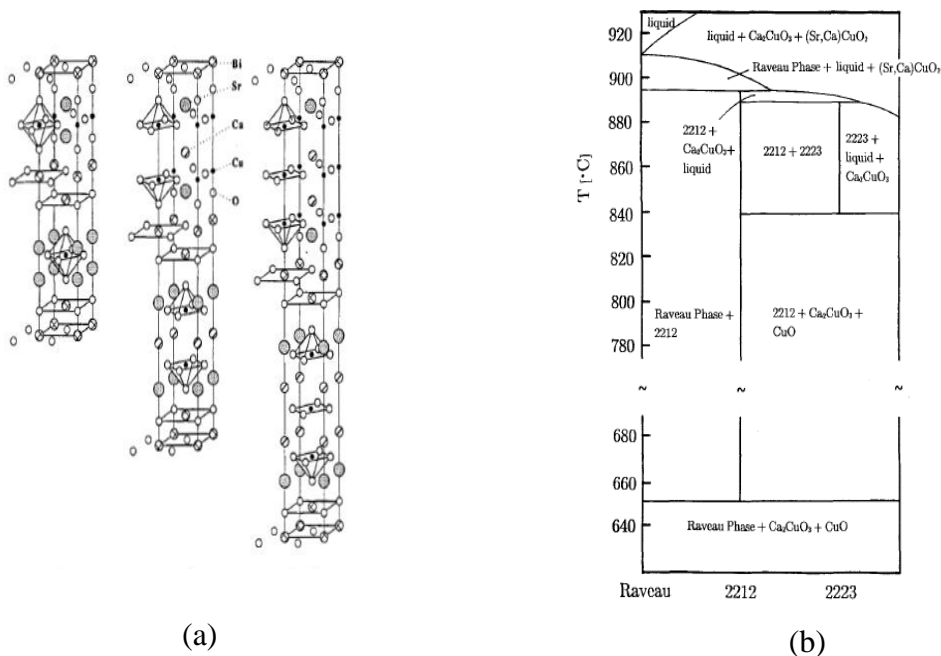


Figure 1-4. (a) Crystal structure of  $Bi_2Sr_2CuO_8$  (Bi2201, Raveau Phase),  $Bi_2Sr_2CaCuO_8$  (Bi2212) and  $Bi_2Sr_2Ca_2Cu_3O_{10}$  (Bi2223) (b) phase diagram between Bi2201, Bi2212 and Bi2223 compounds [14].

In Bi2212, similar to other cuprates  $\text{CuO}_2$  planes are separated by charge reservoirs layers that control the doping of the  $\text{CuO}_2$  planes with charge carriers and control the anisotropy of the physical properties of the conductors [2, 6].

Superconductivity in cuprates is related to the electronic structure of  $\text{CuO}_2$  planes. The  $\text{Cu}^{2+}$  ions have 9 electrons in their  $3d$  orbitals, and a single hole in their  $d_{x^2-y^2}$  orbitals. There is a strong hybridization between  $\text{Cu } 3d$  and  $\text{O } 2p$  orbitals. the Figure 1-5 shows the electronic configuration of  $3d^9$  of  $\text{Cu}^{2+}$  and  $2p^\sigma$  of  $\text{O}^{2-}$  in the  $\text{CuO}_2$  layer . The  $\text{Cu} - \text{O}$  distance is much longer along in the  $c$ -axis than the  $\text{Cu} - \text{O}$  distance in  $\text{CuO}_2$  planes; therefore the bonding along the  $c$ -axis is much weaker than that of the in-plane. This leads to a quasi-2 dimensional electronic structure [6, 13].

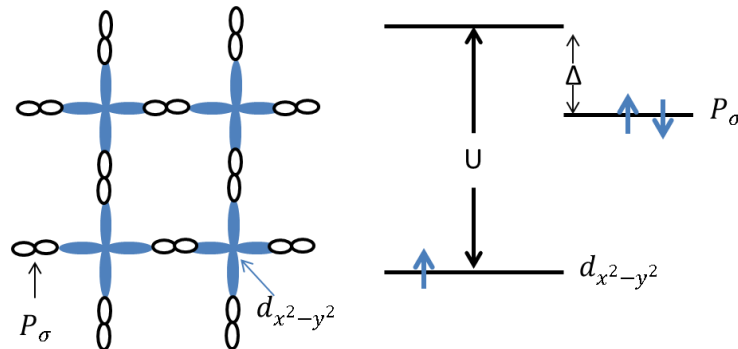


Figure 1-5. The electronic configuration of  $3d^9$  for  $\text{Cu}^{2+}$  and  $2p^6$  for  $\text{O}^{2-}$  in the  $\text{CuO}_2$  layer [6].

The energy of  $d_{x^2-y^2}$  is lower than that of the  $P_\sigma$  orbital. At the presence of other cations, electron on  $\text{O}^{2-}$  are removed and holes are injected into the  $\text{CuO}_2$  layer. Injected holes can freely move and hole pairs are assumed as Cooper pair.

Cuprate superconductors are anisotropic because their effective mass in the  $c$  direction,  $m_c$ , is relatively larger than that of in the  $a$ - $b$  direction the  $m_{ab}$ . Due to the large anisotropy in cuprates the superconducting, coupling between the  $CuO_2$  layers is weak, and at the presence of magnetic field the vertically penetrate vortices bend easily. Coherence length in high temperature superconductors is short, and cores of quantized vortices are small; so that the pinning strength is weak. These features cause that the thermal fluctuation becomes significant and the phase transition between normal state and superconducting state become unclear [6].

### **Applied superconductivity**

In the 1960s, researchers started to build superconducting magnets, which can carry current without resistance at sufficiently low temperatures [15]. High magnetic field research achieved by superconducting materials can be categorized into two groups. First, high fields that create exotic magnetic states in advanced electronic materials. The nature of these states challenges our basic understanding of matter. For instance, in the fractional quantum Hall effect, only accessible in strong magnetic fields, electrons are organized into an irregular state of matter in which new particles appear with electrical charges that have a fraction, one-third or one-fifth, of the charge of an electron. In other magnetic materials, the field creates analogues of the different forms of ice; that only occurs in magnetic matter. Among these states are phases with spin-charge interactions needed in next-generation electronics. Therefore, the accessibility of the highest magnetic fields complements the development of novel materials [16]. Muon Colliders, dipoles and quadrupoles for high energy hadron

colliders beyond the Large Hadron Collider are examples of high magnetic field application in this category [15, 17, 18].

Second group includes biological and chemical systems. In proton beams radiotherapy the beam needs to be focused precisely to small tumors and the depth into tissue, to allow normal surrounding tissues to be spared radiation effects. Other charged particles such as helium, carbon, and neon also have been shown to be effective in the treatment of cancers, specially the lung, liver, and prostate. Since the installation of a patient-based accelerator and the supporting treatment devices and rooms is very expensive, superconducting magnets can play a major role in reducing the physical size and installation costs of the required particle accelerators and beam transport, as well as the operating costs [16].

High-field nuclear magnetic resonance (NMR) has been used extensively to analyze molecular structure and motion in complex molecules. The sensitivity of NMR and magnetic resonance imaging (MRI) strongly depends upon the strength of magnetic field. By access to higher fields new boundaries of biological and medical imaging of human physiology and metabolism are achieved [16].

*Bi2212/Ag round wires state of art:* Conventional NbTi and Nb<sub>3</sub>Sn superconducting wires already have used in MRI, and NMR, and particle accelerators [16, 19]. Today the demand for generating magnetic fields above 20 T is beyond the practical limits of commercial NbTi and Nb<sub>3</sub>Sn wires [15]. It is well established that two high temperature superconductor (HTS), (RE)BaCuO<sub>7-d</sub> (REBCO) coated conductors and Bi2212 round wires (RWs), have the potential to meet this demand because of their very high critical current density ( $J_c$ ) at very high magnetic field [18]. YBa<sub>2</sub>Cu<sub>3</sub>O<sub>7</sub> (YBCO) was discovered in 1987 as the first

superconductor with  $T_c$  of 90 K. YBCO shows a strong anisotropic critical current density in the presence of transverse magnetic fields [16]. Thickness dependence is another limiting factor for YBCO, as the YBCO layer thickness increases YBCO,  $J_c$  decreased significantly [18]. The YBCO coated conductor functions as one filament; any defect that locally interrupts current flow [20]. Strong magneto-electric anisotropy, high costs, limited lengths, low strain tolerance, difficulty at forming superconducting joints and AC loss are the main limitations of YBCO and other rare earth element (REBCO) conductors [18].

In 1988 H. Maeda *et al.* discovered the Bi-Sr-Ca-Cu-O (BSCCO) phases consisting two important compounds,  $\text{Bi}_2\text{Sr}_2\text{Ca}_2\text{Cu}_3\text{O}_{10}$  (Bi-2223) and Bi2212 [21]. Formation of the Bi2223 phase is a slow process requiring a long processing time and severe control over the processing parameters. During processing Bi2223 decomposes into the Bi2212 phase and other secondary phases. Substitution of Bi by Pb is necessary to stabilize Bi2223 [14, 22, 23]. Bi2212 on the other hand is a more stable compound and is therefore easier to form and process [24, 25]. Bi2223 are typically produced in the form of tapes which are anisotropic and show the highest critical current when the magnetic field is applied parallel to the tape and the lowest one when the field is perpendicular to the tape [26].

Figure 1-6 compares the critical current densities ( $J_c$ ) as function of magnetic field  $J_c(B)$  for several state-of-the-art long-length HTS and LTS materials used for magnets at their standard operating temperatures of 4.2 or 1.9 K. Both NbTi and  $\text{Nb}_3\text{Sn}$  clearly show a horizontal  $J_c(B)$  behavior because of their high  $H_{C2}$ . NbTi also operates at 1.9 K. Among all conductors REBCO shows the highest  $J_c$ . However, a high value of  $J_c$  only, does not make a conductor the best candidate for superconducting application. REBCO and Bi2223 performance is

strongly suppressed by the presence of high angle grain boundaries (HAGB). Therefore these conductors need biaxially textured structure. REBCO and Bi2223 tapes show strong anisotropic behavior parallel and perpendicular orientation of magnetic fields, and they only can be made as rectangular tape geometry, whereas all others can be made as round multifilamentary wires. Rectangular conductors are hard to cable for large magnets except in special configurations. From a magnet engineering standpoint, a multifilamentary round wire is superior to a tape, because it is more isotropic in electrical transport properties [18].

In summary, among BSCCO superconductors, Bi2212 is a more promising conductor for high field magnet applications at low operating temperature because of its phase stability, the relative ease of manufacturing long, flexible geometry conductors, and higher  $J_c$  at high magnetic fields. Surprisingly high  $J_c$  in Bi2212 is achieved despite presence of HAGBs and without macroscopic texture. In Bi2212/Ag wires, around 25% of cross-section is Bi2212, which makes their engineering current density ( $J_E$ ) to be the highest among other conductors at fields above 17 T [20, 27, 28].

In 1989 Heine, Tenbrink, and Thoner were the first to demonstrate that Bi2212 round wire can be prepared by “powder-in-tube” (PIT) melt processing with  $J_c$  greater than  $10 \text{ A/cm}^2$  at 26 T, 4.2 K [29]. In 1999 double pancake coils from Bi2212 Ag stacked multifilamentary tapes were fabricated and tested in various backup magnetic fields up to 20 T at the Tsukuba Magnet Laboratory of NRIM [30]. In 2000 Okada *et al.* developed a Bi2212 insert magnet, by multifilamentary tapes, that generates a total magnetic field of 23.42 T, which was the highest magnetic field ever achieved by that time [31]. In 2004 an important milestone in superconducting magnets were passed by Weijers *et al.*, where a Bi2212 superconducting

insert magnet contributed to the generation of a central field of >25 T (5.42 T generated by Bi2212 magnets with a backup field of 18 T) [32]. Recently a small coil that generated

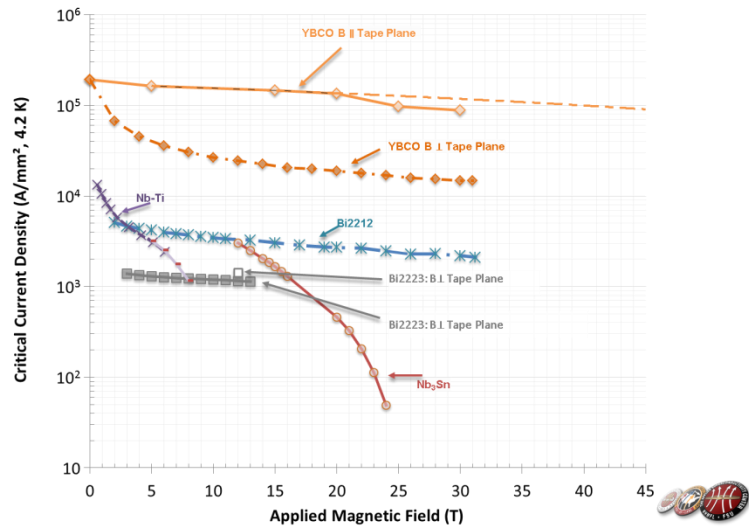


Figure 1-6. Critical current densities ( $J_c$ ) of available superconductors used for magnets [20].

almost 2.6 T in a 31 T background field was made in National High Magnetic Field Laboratory [20].

In the following sections, Bi2212/Ag multifilamentary round wire manufacturing and processing is discussed. A review of underlying challenges is presented with a focus on understanding the processing-microstructure-transport relationships based on the past studies.

### Bi2212/Ag multifilamentary round wire manufacturing

PIT is the most common approach for manufacturing Bi2212/Ag multifilamentary RWs. The reason why Ag is used in the Bi2212 multifilamentary RW is that Ag is a noble metal which

is also permeable to oxygen, moreover Ag is a ductile metal that lowers the melting point of Bi2212 in the heat treatment and acts as substrate helping the radial texture development of Bi2212 grains during the melt processing [5]. An example of a PIT is as following.

The Bi2212 precursor powder has to be calcined to transform the carbonate into an oxide, because carbon is harmful to the thermal processing. Pure Ag tubes are filled with calcined precursor powder by mechanical agitation. Filled tubes are swaged and sealed in one end. The tubes should be cleaned as organic impurities such as oil or grease also introduce carbon into the system. An end cap with evacuation stem is brazed on the fill end. The assembly is then heated to 425°C for 4 hours while pulling a vacuum through the evacuation stem. The stem is sealed after completion of the exhaust cycle to maintain vacuum inside the tube. The tube is then drawn to the restack size, and the wire cleaned and cut to length. The cut monofilaments lengths are put into a silver tube to make the first restack and drawn to the hex restack size. This restack is clean and cut to length and put into an Ag-0.2wt%Mg tube and drawn to the final wire diameter [5, 29-31]. Figure 1-7 shows a typical cross sectional transverse views of a single and a double restack (87×5) Bi2212 multifilamentary wires[18]. Due to the low packing density, because wire drawing requires particle sliding inside the silver tubes, the as drawn wires usually contain 20-30% porosity [32].

Heat treatment of Bi2212/Ag multifilamentary round wires

Partial melt processing: Since Bi2212 has a 2D layered crystal structure, most of the super current flows in the a-b plane, therefore superconducting current requires an oriented well coupled microstructure. The coupled use of silver and partial melt processing (PMP) is

essential to develop a highly textured microstructure and to establish connectivity between Bi2212 grains capable of supporting high  $J_c$  [24, 31, 33-40].

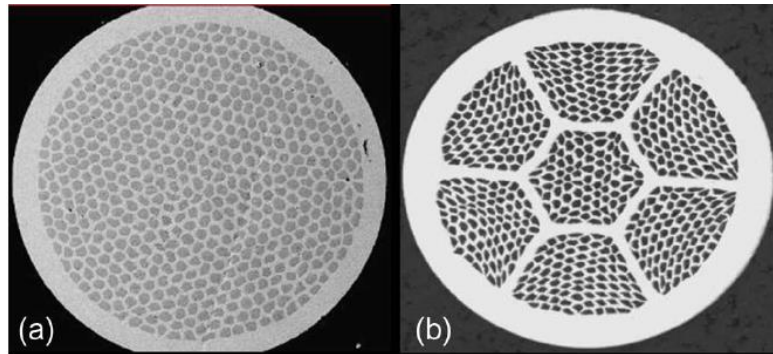


Figure 1-7. Typical cross sectional transverse view of (a) single, (b) double restack Bi2212 multifilamentary wire [18]

Figure 1-8 shows a typical PMP profile. PMP starts with a pre-annealing step, then a heating segment to maximum processing temperature ( $T_{max}$ ), above the Bi2212 peritectic temperature, and a hold for a few minutes ( $t_{max}$ ).  $T_{max}$  is usually between 880-890 °C [41].

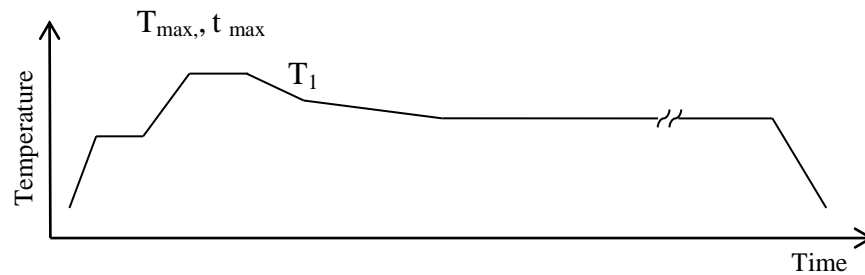


Figure 1-8. A typical partial melt processing (PMP) profile

During the peritectic melt, the single phase Bi2212 starting powder decomposes into alkaline earth cuprate (AEC) and copper free (CF) phases in addition to a liquid; this is shown in equation (10) [42-47].



Ideally, during the cooling, the reverse peritectic reaction reforms the Bi2212 phase into a network of Bi2212 grains with end-to-end connectivity. However, due to the phase separation in the partial-melt and kinetic limitations of resolidification, the reverse reaction is not complete;  $\text{Bi}_2\text{Sr}_2\text{CuO}_x$  (Bi2201) intergrowths and grains form within and beside Bi2212 grains, and a significant amount of AEC and CF phases may remain [48-52].

In as-drawn Bi2212 wires, Bi2212 filament density is around 70% of its theoretical density. The 30% residual void space is distributed within the filaments. During the partial melt the porosity agglomerates in the generated liquid within the filaments and forms bubbles [42, 53, 54]. During the subsequent sintering Bi2212 grain growth, oxygen absorption and further grain coupling occur. Figure 1-9 shows the transvers cross sectional view of a typical Bi2212 wire after PMP.

#### **Filament microstructure after PMP:**

After melt processing, in addition to Bi2212, a number of microstructural defects form; including voids, secondary phases and Bi2201. Usually these defects are large enough to fill a significant portion of a filament cross-section. Therefore, based on the predominant phases, and porosities, filaments cross-sections can be categorized to porous and AEC, CF, Bi2201

filaments as shown in the Figure 1-10. Note. In all of these filaments the primary phase is still Bi2212 but there is no significant other non-Bi2212 phases exist.

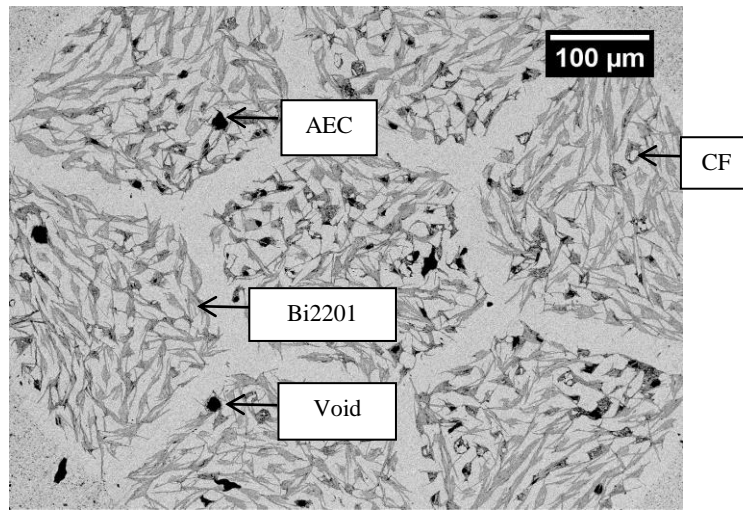


Figure 1-9. SEM micrographs of a transverse section of a Bi2212 wire after PMP

Porous	Bi2201	CF	AEC	Bi2212	Mixed secondary phases

Figure 1-10. SEM images of the six types of filaments.

Filaments with porosity after PMP: Several researches reported transport properties of coils are typically 25–35% less than those of short samples reacted under nominally identical conditions, due to presence of the voids in Bi2212 filaments in long length [52, 55-61]. In as-drawn Bi2212 wires, Bi2212 filament density is around 70% of its theoretical density. Jiang *et al.* showed that the enclosed gas present in the porosity of the as-drawn Bi2212 wire agglomerates into large bubbles that fill the entire filament diameter during the melt phase of the heat treatment. These bubbles remain in Bi2212 filaments of the wire [62].

Enclosed gas in Bi2212/Ag has several sources; absorbed H<sub>2</sub>O and CO<sub>2</sub> from carbon in the precursor powder, and released O<sub>2</sub> from Bi2212 melting. Also if the Bi2212 starting powder is made of nitrate precursors, it contains residual nitrates release NO<sub>2</sub> upon heating. When the enclosed gas exerts a greater force than the restraining force from the Ag sheath, the Ag sheath bubbles outward. Many factors affect bubbling, including the magnitude of the gas pressure, the rate at which the pressure develops, the conductor geometry (flat or round), and the strength and thickness of the Ag sheath. Bubbles from H<sub>2</sub>O form by 700 °C, these from CO<sub>2</sub> form just below Bi2212 melting point, and from O<sub>2</sub> release after Bi2212 peritectic melting begins [63].

A thin silver-sheathed conductor deforms incrementally with zero-strain in response to any gas pressure developed within the conductor upon heating. In the absence of any organic impurities and carbonates, densely packed tapes do not exhibit significant uniform deformation (swelling) during processing. Below 0.001% uniformly distributed carbon content in the precursor powder is tolerable. The swelling due to the carbon content is small

when compared to the swelling due to the air content. Average carbon content is not as critical as the localized accumulation of carbon-containing impurities. To control the deformation of the conductor, the carbon content and the carbon-containing particle size need to be controlled [64]. For PIT RWs containing less than 200 ppm carbon, the effect of trapped gas is less intense [65].

Shen *et al.* used mass spectroscopy to confirm that  $J_e$  degradation with length of Bi2212 wires is because of wire swelling produced by high internal gas pressures at elevated temperatures. Internal gas pressure in long-length wires leads to the Ag sheath to creep during the heat treatment. Creep of Ag expands the wire, reduce the density of Bi2212 filaments, and therefore degrade the  $J_e$  of the wire. The creep rupture of Ag sheath causes the leakage of Bi2212 liquid [65]. Stronger sheath materials or alteration in wire manufacturing eliminate the  $J_e$  degradation [65-67].

Hellstrom *et al.* [63, 68] observed that the extent of Bi2212/Ag tape bubbling varies with the  $pO_2$ , in the surrounding atmosphere during melt processing. Bubbling is more severe in 100%  $O_2$  atmosphere [63, 68].  $CO_2$  partial pressure ( $pCO_2$ ) provides the extra internal pressure causing the deformation. They thermodynamically showed that  $pCO_2$  increases with increasing  $pO_2$ . Changing  $pO_2$ , causes  $pCO_2$  to increase and consequently modifies the physical properties of Ag. The melting point of Ag decreases with increasing  $pO_2$  which reflects the softening of the Ag. Finally they have suggested that carbon content should be minimized in the tape, and oxygen atmosphere ( $P_{total} = 0.1$  MPa) should be maintained between 40% and 50%  $O_2$  [63, 68].

Zhang *et al.* [47] showed that one reason for bubbling is the O<sub>2</sub> release as Bi2212 melts. This problem particularly becomes severe in high oxygen partial pressure (pO<sub>2</sub>) atmospheres, since the melting point of Bi2212 increases by increasing pO<sub>2</sub> and the Ag sheath strength decreases with increasing temperature. A potential method to prevent this bubbling is melting the Bi2212 in an atmosphere with a low pO<sub>2</sub> so that O<sub>2</sub> is released at lower temperature, when Ag is stronger and not so inclined to bubbling [47]. However, PMP in 100% O<sub>2</sub> is more desirable because of a more homogeneous microstructure and a higher J<sub>c</sub> compared to the conductors processed in air [63].

In contrast to and Zhang findings, others found out oxygen solubility to the Ag increases from 0.01 At.% in solid to 0.32 At.% in Ag liquid, and Ag metal is liquid at the partial melt temperature due the presence of the Bi2212 phase. The Ag liquid might accommodate the released oxygen in the melt [69]. Based on a numerical calculation by Kuroda *et al.* oxygen is less responsible for the formation of bubbles in Bi2212 wires comparing to CO<sub>2</sub>. One should note that J<sub>c</sub> values of short samples containing carbon impurity do not reflect the fully detrimental effects of CO<sub>2</sub> on the J<sub>c</sub> of long length wires [58, 70].

Kametani *et al.* studied the microstructure of quenched and fully processed wires. They found an inverse relationship between J<sub>c</sub> and bubble density. Bubbles interrupt the continuous Bi2212 path within each filament and force supercurrent to flow through Bi2212 grains that span the bubbles or through a thin Bi2212 layer at the Ag interface [42].

Patel *et al.* developed a model to determine the degradation in J<sub>c</sub> caused by bubbling. This model evaluates the performance and overall quality of conductors processed under similar

conditions, containing different bubble-type defects. Based on their model  $J_c$  is more sensitive to the width of the defect than its length [71]. Scheuerlein *et al.* used in situ synchrotron micro-tomography and x-ray diffraction (in air) to monitor the void and phase evolution during all PMP steps [72]. They found that early stages of porosity agglomeration occur with eliminating of the Bi2201 phase. Bi2201 decomposes at 850 °C and re-forms during cooling at around 850 °C. Bi2212 nucleation occurs during subsequent cooling between 863–842 °C [72]. This is in contrast with earlier studies arguing that bubbles form only when the Bi2212 melts [42]. Bi2212 phase transformations during PMP are not accompanied with major density variations, therefore the overall void volume in short Bi2212 wire samples does not significantly change during PMP [72].

Rikel *et al.* suggested that to remove the pore from the melt one should remove the gas through the silver. Oxygen diffuses through the silver but not N<sub>2</sub> or Ar. They thought if the PIT billet filled by oxygen before drawing, oxygen is retained in the core. A longer  $t_{\text{melt}}$  is required for O<sub>2</sub> to diffuse out during the melt, however longer  $t_{\text{melt}}$  results to formation of larger secondary phases, change of Cu content, extensive formation of Bi2201 intergrowth. Therefore an optimum  $t_{\text{melt}}$  needs to be found [73]. Researcher used swaging or cold isostatic pressing, (CIP) and over pressure (OP) to densify Bi2212 filaments in the as-drawn wire prior to PMP and along with PMP [20, 42, 62]. Swaging and CIPing (up to 1400 MPa) result to Bi2212 filament densification around 90% of its theoretical density [62]. A 650 MPa CIPed, 1.2 m long sample processed in a 10 bar OP heat treatment gives a  $J_c$  of 550 A/mm<sup>2</sup> at 4.2 K and 15 T [53].

Mia *et al.* used CIP and swaging to increase the filament mass density and reduce filament porosity, where they were able to achieve  $J_c$  of 480 A/mm<sup>2</sup> (at 4.2 K, 15 T) on 1-m-long wires [74]. In their work by 30% area reduction swaging, over 90% of the Bi2212 theoretical density was achieved and no large bubble in the filaments was observed. After 1200 MPa CIPing, over 90% of Bi2212 theoretical density is obtained [74].

Jiang *et al.* believed that swaging is preferred to CIPing because it works better for long length. Swaging increased the Bi2212 filament density of the wires from 3.66 to 5.33 g/cm<sup>3</sup>. The swaged wire after PMP still had some remnant bubbles [75].

Groove-rolling is another technique to densify long length Bi2212 conductors. Groove-rolling is suitable for fabrication of round, square or rectangular shape conductors depending on the application requirements. During groove-rolling, the component of the force transvers to the wire axis is stronger, resulting in a greater powder densification. A 1.1 mm<sup>2</sup> square 37 × 18 groove-rolled wire has a  $J_c$  of 1900 A mm<sup>-2</sup> at 5 T. This result is three times better than that of the drawing process. Groove-rolling densifies the precursor powders and reduces the density and/or size of porosities, while CIP or swaging densify the final as drawn wire [76].

Microcracks formed in the Ag sheath during mechanical processing (swaging, drawing and rolling) of silver tubes could eliminate swelling and bubbles, since these microcracks release the trapped gases during heat treatment. In the absence of microcracks, all gases generated during the PMP are trapped, causing deformation of the conductor [64]. However, microcracks weaken the sheath. Investigations of stronger alloys of silver, which are compatible with Bi2212, are necessary [64, 66, 67].

If one assumes that the gas inside the wire is air and the total gas pressure inside the wire at room temperature (about 300 K) is 1 bar, according to the ideal gas law, the total pressure inside the wire will become about 4 bar when the wire is heated to  $T_{\max}$  (around 890 °C). Since  $O_2$  easily diffuses through the silver sheath, the main internal pressure is induced by  $N_2$  (if the Bi2212 starting powder is made of nitrate precursors) which is about 3.2 bar at 890 °C. A pressure of 5 bar prevents the wire expansion during the PMP [75].

In 1995 Kanai *et al.* [77] developed high gas pressure PMP to eliminate void formation. They suggested two influencing factors on  $J_c$ : 1. the oxygen partial pressure, higher  $pO_2$  depletes the oxygen release during melting, 2. the total gas pressure. They found that PMP  $pO_2$  of 101.3-303.9 kPa and total gas pressures over 303.9 kPa improves the intragrain superconducting properties and eliminates void formation [77].

A hot isostatic press to perform over pressure (OP) processing on Bi2223 tapes was used. OP improves the density and connectivity of Bi2223 filaments and to suppress the lead evaporation from the Bi2223 wires [78-82].

Reeves *et al.* used OP processing to eliminate bubbling and reduce porosity in monocoil and thin multifilamentary Bi2212/Ag tapes. They also used a combination of vacuum annealing at 700 °C and holding for two days at 835 °C in 100%  $O_2$  to reduce the amount of water and  $CO_2$  in the core to prevent bubbling of the silver sheath. Slow cooling rates lead to the Bi2212 decomposition, therefore incorporating fast cooling or modifying the slow cooling process together with over pressure result in even higher  $J_c$  [83, 84].

Recently researchers achieved a significant improvement in transport behavior of Bi2212/Ag RWs. They developed Bi2212/Ag RWs (25% superconductor) with  $J_c$  of as high as that of a REBCO (1% superconductor) and Bi-2223 tape conductors (40% superconductor). They heat treated the wires under over pressure up to 100 atm, and used creep of the Ag under over pressure to fully densify the Bi2212 filaments.  $J_c$  reached to  $4000 \text{ A/mm}^2$  at 4.2 K and 5 [20].

Optimizing the precursor powder composition, optimizing the pre-annealing profile, using stronger or thicker silver sheaths configuration, and applying densification methods are suggested as main routes to overcome the bubbling problems.

*Filaments with impurities after PMP:* Figure 1-10 shows 5 other filament types in addition to the porous filament, filaments containing predominantly Bi2212, filaments containing relatively large Bi2201 grains, filaments containing relatively large AEC grains but no significant other non-Bi2212 phases, filaments containing relatively large CF grains but no other significant non-Bi2212 phases, and filaments containing relatively large AEC and CF grains.

A statistical method, that uses a Matlab program to analyze the SEM micrographs was developed to categorize over 100 filaments within the image [85]. Matlab categorizes the filaments to five filament types based on the predominantly impurity content. The majority of filaments (78% of all filaments classified) are either predominantly Bi2212 or containing-large-Bi2201 grains. Correlating with filament area fraction and  $J_c$  shows that  $J_c$  is directly proportional to the percentage of “predominantly-Bi2212” filaments, and inversely proportional to the percentage of filaments “containing-large-Bi2201 grains”. Unexpectedly,

there is no or weak correlations between  $J_c$  and the other filament types [85]. Based on these one implies that the primary impurity in partial-melt processed multifilamentary Bi2212 RWs is Bi2201.

Thangaraj *et al.* also by using XRD showed that a partially melt proceed tape mainly consist of Bi2212 and Bi2201 phases [24]. In [41], Q.Y. Hu *et al.* assumed that, the Bi2201 intensity in XRD is proportional to residual secondary phases. Bi2212 forms from the peritectic reaction of (Sr,Ca)CuO<sub>2</sub> and liquid phase, and if the liquid is off stoichiometry, the residual Bi2201 remains unreacted [41]. Thermal analysis XRD studies by Shimoyama *et al.* showed that around 600°C, under 1 atm pO<sub>2</sub>, Bi2212 decomposes to CF, Bi2201 and CuO. They suggested that Bi2212 is unstable at low temperature under high pO<sub>2</sub>. The weight increase accompanied with decomposition is due to the oxygen absorption. In Bi-Sr-Ca-O phase, the mean valence of the Bi ions is higher than that in Bi2212 phase resulting in an oxygen absorption during the decomposition [86]. In 1991 Tenbrink *et al.* argued that a two-step annealing procedure is necessary to process high  $J_c$  wires. A long annealing at 840 °C transforms Bi2201 to Bi2212 [87]. Sager *et al.* and Kase *et al.* reported that Bi2201 is the first phase to form during cooling from the partial melt. Bi2201 grains serve as the heterogeneous nucleation sites for Bi2212 crystallization. Reducing the stability of the nuclei leads to large Bi2212 grains formation and low  $J_c$  values in non-textured bulk material [61, 88]. Oka *et al.* used high temperature X-ray measurements to study the crystallization from the melt, in air. They argued that Bi2212 is the first phase to crystalize from the remainder of the liquid around 840 °C and Bi2201 nucleates later at 750 °C [89].

Due to the phase segregating during Bi2212 peritectic melt Bi2201 forms extensively in partially melt processed wires. Figure 1-11 shows Bi2201 forms as mesoscopic grains between Bi2212 grains and nanoscopic intergrowths within Bi2201 intergrowths [85, 90-92].

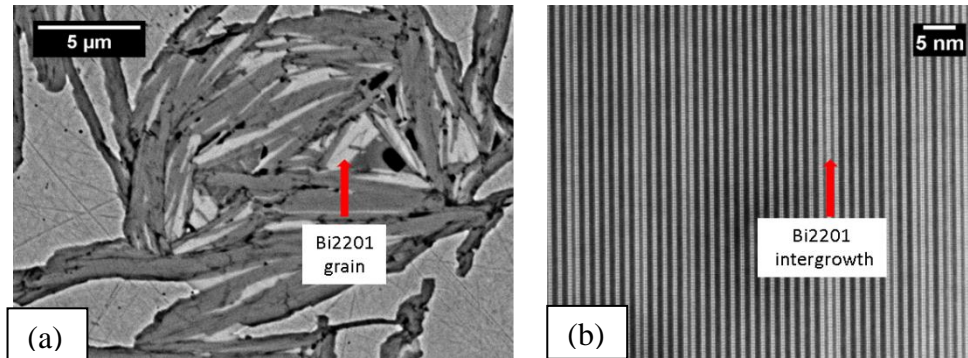


Figure 1-11 (a) SEM micrograph of a filament showing micron size Bi2201 grains between Bi2212 grains, (b) high angle annular dark field (HAADF) scanning transmission electron microscopy (STEM) image showing Bi2201 intergrowths within a Bi2212 grain.

Rikel *et al.* assumed that Bi2201 intergrowth formation results from Bi2212 compositional variations and difficulties in consumption of secondary phases. They thought Bi2201 intergrowths mainly exist in Bi2212 grains which are formed from the melt rather than Bi2212 grains which are formed as result of solid state reaction (consumption of secondary phases) [73].

In a different study Rikel *et al.* [92] predicted that Bi2201 intergrowths strongly affect Bi2212 field-dependent behavior. They found that once Bi2201 intergrowths are formed they are very stable. Their stability relates to the longer diffusion path in the c-axis direction (anisotropy in diffusion). They found that different Bi2212 grains have different Bi2201

intergrowth densities. Bi2212 melt composition is close to Bi2201 and Ca and Cu needed for Bi2212 formation are trapped in the secondary phases. When the secondary phases are larger the diffusion distance is longer. They concluded that the intergrowth density increases with increased texturing [92]. Buhl *et al.* [93] found that by increasing the cooling rate from the melt, Bi2201 intergrowth content increases due to less oxygen uptake during the cooling. Oxygen deficiency results in more Bi2201 intergrowth formation [93].

Ebil *et al.* [94] used high resolution transmission electron microscope to study Bi2201 intergrowths, assuming that the solid state reaction leads to formation of stacking faults on (001) planes. They also observed compositional variations in different regions of the sample, based on the distance from the stacking faults [94].

It was shown that Bi2201 intergrowths and c-axis transport play significant roles in Bi2212 transport behavior. Narrow intergrowths (half- and full-cell) do not act as barriers to transport and they have Josephson-Junction-like behavior at low field and flux pinning at higher field. Wide Bi2201 intergrowths are too large to be flux pinning centers and they cause weak-link behavior. Further improvements in Bi2212 RWs requires the elimination of Bi2201 grains and large intergrowths, however half and full-cell is not problematic [91].

*Interconnection between filaments:* Shen *et al.* [59] performed a systematic microstructural quench study to understand the microstructural evolution focusing on bridge formation during PMP. Bridges form a 3D interconnected filament network of percolative current paths that allows current to avoid obstacles in filaments, enhancing the long-range connectivity and  $J_c$ . After the full heat treatment two bridge types are formed; Type-A bridges that form during melting, composed of single grain Bi2212, Type-B bridges which form between

separated filaments during the cooling and growing stage of Bi2212. Figure 1-12 shows the schematic of these two types of bridges [59]. Later Naderi *et al.* [91] showed that wide bridges, type A, is also composed of several grains with a complex orientation [91].

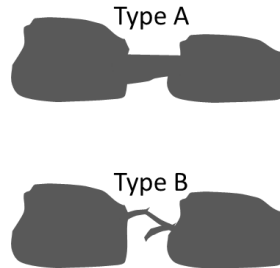


Figure 1-12. Schematic of two types of bridges, (a) Type-A bridges form from solidification of the liquid between filaments during cooling, (b) Type-B bridges form from Bi2212 growing into the Ag.

Slow cooling rate from the melt (2.5 °C/hr) leads to extensive formation of Type-A bridges, and fast cooling (20 °C/hr) results to formation of Type-B bridges. A direct correlation between densities of single grain bridges and  $J_c$  exist in Bi2212 multifilamentary RWs [59].

Texturing: Strong anisotropy in the Bi2212 crystalline structure induces anisotropy in their electromagnetic properties.  $J_c$  strongly depends on grain alignment and long-range texture in Bi2212/Ag conductors. [001] Twist boundaries are the most frequently observed grain boundaries in the thin longitudinal cross-section samples. Bi2212 grains are plate-shaped, which leads to a microstructure composed of colonies of grains having almost parallel c-axes. A colony boundary forms when two colonies with misoriented c-axes impinge [39].

Figure 1-13 shows the transvers ( $\theta$ ) and longitudinal ( $\alpha$ ) misalignment angles based on filament geometries and Ag–Bi2212 interfaces in Bi2212/Ag tape.

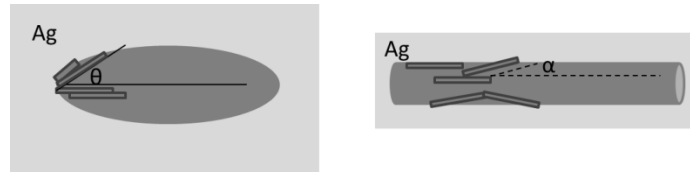


Figure 1-13. The transvers ( $\theta$ ) and longitudinal ( $\alpha$ ) misalignment angles based on filament geometries and Ag–Bi2212 interfaces in Bi2212/Ag tape.

To find the average texture in multifilamentary conductor,  $J_c$  as a function of transvers and longitudinal misalignment angles, temperature and magnetic field can be found [95]. The textured grain growth, mainly in the interfilamentary bridges, plays an important role in electrical transport [96-98]. Rodrigues *et al.* found that slow cooling rate from the melt improves  $J_c$  because of higher degree of texturing [99].

Kumakura *et al.* investigated the grain alignment of Bi2212 layers in Bi2212/Ag tapes. They found out Bi2212 grain alignment at Ag/Bi2212 interface is much better than that of at the Bi2212 free surface. Cooling rate affects Bi2212 grain alignment.  $J_c$  of Bi2212/Ag tape increases with increasing interfacial area and decreasing Bi2212 layer thickness. Cold rolling before heat treatment increases the Bi2212 density and enhances  $J_c$  [40].

High magnetic field is effective to develop texture and to enhance  $J_c$  in mono-core Bi2212/Ag tapes and thick films [100-102]. Magnetic force rotates the paramagnetic Bi2212

grains which are surrounded by a liquid phase, such that the c-axis of the grains orient toward magnetic field direction. Therefore when the magnetic field is applied during the nucleation and early growth stage of Bi2212 grains, a high degree of alignment is developed. Phase assemblage changes in the presence of magnetic field, resulting improved magnetization hysteresis behavior [96]

Villaume *et al.* [96] used magnetic field heat treatment to improve the texture of Bi2212/Ag multifilamentary tapes. The  $I_c$  (self-field, 4.2 K) is increased about 40% for a 5 T melted tape in comparison to a 0 T melted tape [103]. Liu *et al.* [96] studied the effect of magnetic field processing on the texture development in Bi2212/ Ag low aspect ratio rectangular conductors [96].

### **The effects of PMP heat treatment parameters**

Pre-annealing: Holesinger *et al.* [104] studied the effect of pre-annealing in Bi2212 round wire performance. They found that  $J_c$  is more sensitive to the holding time in the pre-anneal than to the temperature. They related the reduced content of secondary phases in longer pre-anneal samples to the grain growth occurring before the precursor melts. If the precursor powder contains some fraction of secondary phases, pre-anneal provides the kinetic energy to promote conditions favoring Bi2212 growth during the resolidification, as opposed to further growth of Bi2201 or CF phase. Prolonged dwells at temperatures near Bi2212 melting point is detrimental to  $J_c$  since it facilitates Cu migration into the Ag-Ag/Mg sheath [104].

Heating rate: Koizumi *et al.* [46] studied the effect of heating rate. At a 10° C/h heating rate, melting starts from central filaments and spreads to the edge-located filaments. However, at a 5 °C/h, melting occurs uniformly. They related this behavior to the oxygen partial pressure; partial pressure of the central filaments is lower than the edge-located filaments. With the 5 °C/h heating rate, oxygen diffuses completely to central filaments, however, with the 10 °C/h heating rate, oxygen does not diffuse completely to central filaments [46]. This was consistent with Nomura *et al.* findings [105].

Maximum processing temperature: Shimoyama *et al.* [106] were one of the first groups who reported the strong relationship between  $J_c$  and  $T_{max}$  [106]. Matsumoto *et al.* [107] found a narrow window for  $T_{max}$  (4 °C). Heat treatment a few °C below the optimized  $T_{max}$  results zero  $J_c$  because no Bi2212 melting occurs at these temperatures. They observed extensive bridging of Bi2212 filaments at temperatures higher than optimized  $T_{max}$ , and related this to lower  $J_c$  values of samples processed far above optimized  $T_{max}$ [107].

Polak *et al.* [45] also reported the narrow window of  $T_{max}$  in Bi2212 tapes proceedings. They argued that formation of macro-pores is responsible for lower  $J_c$  in samples heat treated at temperatures higher than the optimized  $T_{max}$  [45].

Lang *et al.* [35] studied the effect of  $T_{max}$  on transport properties of Bi2212 thick films. They believe that when the optimum temperature is exceeded, nuclei concentration is reduced; liquid is trapped in the gap between Bi2212 platelets. Capillary force drives the liquid from regions without Bi2212 platelets to the regions with many Bi2212 platelets where capillary force is the strongest. This phase segregation results in an incomplete Bi2212 formation. Separated areas remain porous and contain large secondary phases. In optimized  $T_{max}$  the

nuclei density is higher, and the distribution is more homogeneous in the entire film, resulting a more uniform microstructure at the end of processing. PMP with  $T_{\max} \gg T_{\text{optimized}}$  leads to simultaneous loss of Bi, the extreme growth of second phase grains (not dissolving during cooling), or even the loss of liquid through grain boundaries of the silver sheath [35]. At a constant  $pO_2$  increasing  $T_{\max}$  depletes the oxygen content of the melt and consequently changes the phase assemblage of the conductor [108].

Hellstrom *et al.* [37, 109] related  $T_{\max}$  to the CF content in the melt. They thought below the optimized  $T_{\max}$  small grains of CF form whereas above the optimized  $T_{\max}$  large grains of CF form. At the highest temperature, Bi2212 is in equilibrium with liquid, ((Sr,Ca)CuO) (1:1) , and a CF phase exists. Between 885 and 905°C ((Sr,Ca)<sub>2</sub>CuO) (2:1) and some CaO form. CF phase vanishes as temperature increases. At 920 °C only CaO coexists with the liquid [37, 109]. Holesinger *et al.* [110] found that addition of (<1wt.%) ZrO<sub>2</sub> and CaZrO<sub>3</sub> extend the melting processing window with changing Bi2212 phase composition [110].

Time in the melt: Matsumoto *et al.* [111] suggested that the time in the liquid state ( $t_{\text{melt}}$ ) is more critical for Bi2212 grain growth than  $T_{\max}$  [111]. Rikel *et al.* [73] showed that elongating  $t_{\max}$  increases the secondary phases and Bi2201 intergrowth content [73].

Shen *et al.* [112] found that when  $t_{\text{melt}}$  is longer than 2.5 hr,  $J_c$  decreases. As time in the melt passes more filaments bond together due to liquid and Ag transport so the filaments become distorted, small voids agglomerates into larger bubbles, and Cu diffuses out from the liquid. As  $t_{\text{melt}}$  increases, the volume fraction of the AEC grains decreases but their average grain sizes do not change. The grain size and volume fraction of the CF grains, however remains constant. By controlling  $t_{\text{melt}}$ ,  $T_{\max}$  window is 10 degrees wide [112].

Cooling rate from  $T_{max}$ : The cooling rate from  $T_{max}$  affects Bi2122 grain alignment [40, 99]. Buhel and Rodrigues *et al.* showed that slower cooling rate from the melt results higher  $J_c$  [93, 99]. Dietderich *et al.* showed that with a slower cooling rate better texture is achieved in thick Bi2212 films. They also argued that upon reheating to 870 °C, Bi2201 transforms to Bi2212 regardless of the heat treatment history [113]. Lang *et al.* argued that the cooling rate should be sufficiently slow to enable the Bi2212 film to take up oxygen and the secondary phases to dissolve in the liquid [114]. A slow cooling rate helps the oxygen uptake however, and cooling too slowly results in an undesirable macroscopic phase separation [108].

Nachtrab *et al.* recommended a two-stage cooling from  $T_{max}$ , based on the effect of undercooling on the quantity of secondary phases and the rate of nucleation and growth of Bi2212. A two-stage cooling improves  $J_c$ , if the cooling rates are optimized. Bi2212 solidification occurs at a temperature lower than melting point. A certain amount of undercooling is required for Bi2212 nucleation. Nucleation of Bi2212 occurs either heterogeneously at the solid-liquid interfaces or homogeneously in the liquid based on the degree of undercooling. Low initial cooling rates allow more AEC and CF to form before undercooling becomes sufficient for Bi2212 nucleation. At low undercooling, higher  $T_1$ , the driving force for nucleation is low and Bi2212 grains form mainly on heterogeneous sites including the Ag interface. Higher  $T_1$  favors grain growth while producing fewer aligned grains. A higher cooling rate limits AEC and CF grains to grow before Bi2212 grains nucleate. With higher undercooling and lower  $T_1$ , Bi2212 solidifies at a lower temperature, with a higher nucleation rate. In this case, the driving force for nucleation is sufficient for

Bi2212 homogeneous nucleation, resulting in a greater number of smaller, randomly oriented grains and more high-angle boundaries [115].

Annealing time: Long annealing promotes the reaction between secondary phases leading to increases in Bi2212 formation, texture, high-angle grain boundaries connection between Bi2212 grains perpendicular to the growth direction, and oxygen content [116].

Matthiesen *et al.* studied the effects of anneal time and cooling rate in 20%O<sub>2</sub>-80%Ar, on the formation and texturing of Bi2212 films [117]. Longer anneal times increase the volume fraction of the Bi2212 phase while slower cooling rates improves grain growth and texturing. Bi2212 nucleation and growth kinetics during an isothermal anneal are significantly different from that of during cooling. Their results indicated that T<sub>c</sub> of the slowly cooled films is higher than that of the quickly cooled samples. T<sub>c</sub> of samples is mainly determined by the cooling rate, while the sharpness of the superconducting transition is predominantly determined by the anneal time [117].

Cooling from the annealing temperature to room temperature: According to a study by Shimoyama *et al.*, cooling too slowly (20 °C/hr) results in extensive decomposition of Bi2212 to Bi2201 (increasing pO<sub>2</sub> increases the decomposition temperature). Quenching from high temperature was detrimental to J<sub>c</sub> due to crack formation induced by thermal shock (thermal contraction of Ag and Bi2212 filaments are different). However fast cooling suppresses Bi2212 decomposition and improves grain coupling [118].

Based on studies by Kase *et al.* quenched Bi2212/Ag tapes show higher T<sub>c</sub> but lower J<sub>c</sub>. T<sub>c</sub> decreases with decrease of cooling rate [119]. Kase *et al.* showed that T<sub>c</sub> of Bi2212 tapes

quenched from 870 °C (annealing temperature) is 89 K whereas  $T_c$  of slow cooled samples is around 77 K, however  $J_c$  of the latter sample is higher at 4.2 K [34]. Noji *et al.* related the higher  $T_c$  values of quenched samples to lower oxygen content [120].

Post annealing: Shen *et al.* showed that  $J_c$  (5 T, 4.2 K) of Bi2212/Ag multifilamentary wires are doubled by low temperature oxygenation. This was related to an increase in flux pinning, and intergranular connectivity [121]. Nagata *et al.* used a post-annealing step at 810 °C (in air) to improve  $T_c$  and reduce scattering of  $J_c$  by affecting the Bi2212 growth [122]. Buhl *et al.* suggested that to increase  $T_c$  and the  $J_c$  at 77 K, an additional annealing process at lower temperature and lower oxygen partial pressure is helpful [123]. To increase  $T_c$ ,  $N_2$  annealing after PMP is suggested by other researchers [118, 119].

The role of processing atmosphere: Heat treatment atmosphere is another critical factor in Bi2212/Ag processing. Endo *et al.* showed that pure oxygen PMP results to higher  $J_c$  values [68]. Sager *et al.* found that oxygen is needed for the dissolution reaction of secondary phases and consequent Bi2212 crystallization. Oxygen initially diffuses through the melt and then through Bi2212 grains [61]. Sager *et al.* showed that by annealing at low  $pO_2$  (0.1 bar), after solidification, the amount of residual phases is reduced by more than 50% and  $J_c$  of the fully processed samples is increased by 65% compared to samples annealed at high  $pO_2$  (1 bar) [61]. They showed that Bi2201 stability range is slightly reduced by decreasing  $pO_2$ , but can be further reduced by increasing the temperature to 875 °C in  $pO_2$  equal to 1 bar. Post-annealing at high temperatures, 875 °C and 1 bar results in reduced Bi2201 contents, without leading to  $J_c$  improvement [61].

During PMP in air, (SrCa)CuO<sub>x</sub> (1:1) grains form and tend to grow into large grains. Thus, in subsequent cooling, Bi2212 formation does not complete and several tens of micrometer-size (1:1) grains remain. Whereas in tapes PMPed in oxygen, the 14:24 phase is the primary phase coexisting with AEC phase which do not grow into large grains [24, 124]. 14:24 orients parallel to the silver interface [24]. During cooling, Bi2212 grains nucleate from the surface of the 14:24 phase and the silver surface. Thus, a well aligned structure forms even in the inner part of the silver sheathed tape processed in oxygen, compared to air. In addition, 14:24 grains react faster than the 1:1 grains at lower temperatures, increasing the Bi2212 content. Also, oxygen processed tapes exhibit a more uniform microstructure across the tape compared to the tapes heat treated in air. As a result J<sub>c</sub> of the melt processed tapes in oxygen is much higher than those heat treated in air [24]. In electron micrographs by Thangaraj *et al.* a clear difference in the phase assemblage between the tapes heat treated in air and oxygen is observed [24].

Zhang *et al.* also found that the phase assemblages in Bi2212 melt varies with pO<sub>2</sub>, ranging from 0.001 to 1. From 0.001 to 0.01 atm O<sub>2</sub> the melt contains large 2:3 CF grains, these do not fully react during cooling. From 0.075 to 0.30 atm O<sub>2</sub>, the melt contains 1:1 AEC large grains of which also do not fully react during cooling. From 0.40 to 1 atm O<sub>2</sub>, the melt contains small grains of 14:24 AEC and 2:4 CF, these phases react to a great extent during cooling to form Bi2212. Only a few remnant 14:24 AEC or 2:4 CF grains remain in 1 atm fully processed tapes. The remnant grains that are present are quite small [47].

Nomura *et al.* heat treated Bi2212/Ag tapes in different N<sub>2</sub>, air and O<sub>2</sub> atmosphere. Oxygen release and absorption in these atmospheres are different. For the tapes processed in air,

oxygen is reabsorbed into the Bi2212. In N<sub>2</sub>, the released oxygen is not recovered at all during the cooling. In this case, no superconducting Bi2212 phase forms during solidification. For the tapes processed in O<sub>2</sub>, little oxygen is released from Bi2212 and absorbed into Bi2212. These results indicate that the oxygen partial pressure in heat treatment affects the amount of oxygen release from Bi2212. The tape heat treated in O<sub>2</sub> has small void swelling. However, its J<sub>c</sub> is much lower than that of the tapes heat treated in air, because higher oxygen partial pressure results in decomposition of Bi2212 into Bi2201 [105].

Both melting and solidification temperatures increase with pO<sub>2</sub>. In the study by Kumakura the optimum T<sub>max</sub> increases by 35 °C as pO<sub>2</sub> increases from 0.01 to 1 atm. The c-axis lattice parameter of Bi2212 slightly decreases as pO<sub>2</sub> increases. The samples heat treated under 1 atm oxygen partial pressure are in the over-doped state [125].

### **Alternative processes to the PMP**

*Isothermal melt processing (using variable O<sub>2</sub> pressure):* The melting point of Bi2212 is a strong function of pO<sub>2</sub>, decreasing with decreasing pO<sub>2</sub> [126-128]. Isothermal melt processing (IMP) uses this dependence of Bi2212 melting point on the oxygen partial pressure to melt and solidify Bi2212 without a temperature variation. An oxygen-deficient Bi2212 melt solidifies at a constant temperature by simply increasing the oxygen partial pressure [33]. As Bi2212 requires a large undercooling rate for nucleation and growth,

changing  $pO_2$  before the main crystallization has the same effect as increasing the temperature [61].

IMP uses lower processing temperatures compared to the temperatures in conventional melt processing in air [129]. The single processing temperature and the significantly lower processing temperatures (780-850 °C) compared to conventional partial melt processing (870 °C -900 °C) are two desirable characteristics of IMP.  $T_c$  of IMP Bi2212 conductors are in the range of 85-90 K [33, 129, 130].

CaO separation in the melt and extensive formation of Bi2201 is a problem in the IMP[33]. Self- field  $J_c$  (4.2 K) of most IMP samples is on the order of  $10^5$  A/cm<sup>2</sup>. In an IMP attempt of Bi2212 tape,  $J_c$  reached to  $3 \times 10^5$  A/cm<sup>2</sup> (self-field, 4.2 K) [128].

IMP microstructure is mainly studied by Holesinger [7, 129-131]. Funahashi *et al.* also studied the crystallization of IMP tapes [9]. They found that during IMP there are two paths for Bi2212 crystallization, one is the direct precipitation from the liquid phase and the other is the peritectic reaction between the 1:1 phase and the liquid phases. They showed that  $J_c$  strongly depends on the crystallization path.  $J_c$  of tapes obtained by the peritectic reaction is higher than that of tapes obtained by direct precipitation [9, 128].

A significant difference between IMP and PMP is the phase assemblage in the partial melt. In IMP, the present phases in the partial melt, at the start of the oxidation step to form Bi2212, are  $Bi_2Sr_{3-x}Ca_xO_y$ , CaO, and a liquid phase. In PMP the present phases are a relatively oxygen-rich liquid,  $Sr_{14-x}Ca_xCu_{24}O_{41}$  and  $Bi_2Sr_{4-x}Ca_xO_y$  [130, 132].

In [133], IMP was examined on Bi2212 films, and it was found that the temperature range of 770 °C to 790 °C resulting the highest  $J_c$  of  $1.2 \times 10^5$  A/cm<sup>2</sup>. This is because the uniformity

of partial melt formed between 770 °C and 790 °C resulting a uniform composition and distribution of phases. At temperatures lower than 770 °C, the viscosity of the melt is too high to allow for a uniform melt to coat the surface of the substrate. Above 790 °C, phase segregation of the surface of the melt, mostly CaO, leads to the formation of large alkaline-earth cuprate needles. From mass balance considerations, the formation of alkaline-earth cuprates imposes the formation of Bi2201 which is a Bi rich compound [133].

Scanning transmission electron microscope studies by Holsinger *et al.* showed the presence of the amorphous/nano-crystalline lamella within some of the Bi2212 colonies. EDS on these lamella structures showed a slightly bismuth-rich, alkaline earth poor composition relative to Bi2212. They argued that lamella is the last remnants of the liquid during the solidification part of Bi2212 melt-processing [134]. Elsewhere, Holsinger *et al.* showed that with increasing density of intergrowths, the Bi and Sr contents increase while the Cu+Ca content decreases [135].

Split melt processing: Wind and React (W&R) and React and Wind (R&W) are two conventional methods to make superconducting magnets. R&W is mainly used for NbTi and thin conductors since bending strain on round wire is much larger for equal bending radius of thin tapes. W&R is mainly used for brittle wires. In W&R, winding is done before PMP, when conductor is still ductile; bending strain can be relieved during the PMP. The main challenges associated with the W&R include leakage from Bi2212 filaments through the Ag-alloy sheath, thermal and oxygen diffusion, and limited compatibility with insulation and reinforcement material.

To avoid W&R and R&W limitations, a novel approach, React-Wind-Sinter (RWS), is developed. In the RWS approach, the conductor is heat treated through the partial-melt step, and then cooled to room temperature, the winding step is performed and the heat treatment process is continued. With RWS the sensitive partial melt is completed without the large thermal mass and poor oxygen diffusivity of a tightly wound coil. Moreover mechanical damage introduced by winding is eliminated by annealing after winding [49, 50, 136, 137].

Figure 1-14 shows the heat treatment profile for RWS magnets, called split melt processing (SMP). SMP results in a 40% increase in the  $I_c$  of Bi2212 round wires at 4.2 K, indicating that conventional PMP is far from optimized [49, 50, 52, 136-138].

Liu *et al.* used Avrami analysis and showed that Bi2212 grain nucleation is heterogeneous and site-saturation limited. During the first section of SMP, oxygen is fully recovered; Bi2201 and/or Bi2212 nucleation is accelerated. Large, flat Bi2201 grains form from the Bi2201 liquid at the start of the second heat treatment, and subsequently act as Bi2212 grain nucleation sites. During cooling from the return temperature ( $T_r$ ) which is the peak temperature at the beginning of the second heat treatment, Bi2212 grains form via a facilitated solid-liquid reaction by second phase dissolution and cation diffusion.

The most important heat treatment parameter in SMP is  $T_r$  [49]. If  $T_r$  is sufficiently high, the generated liquid reacts with the secondary phases present, result in additional Bi2212 nucleation during cooling [52].  $T_r$  controls the amount of liquid in the second heat treatment. If  $T_r$  is increased above optimum, the volume fraction of Bi2201-based liquid increases due to the higher temperature and  $J_c$  decrease due to the incomplete conversion of Bi2201 to Bi2212 [49].

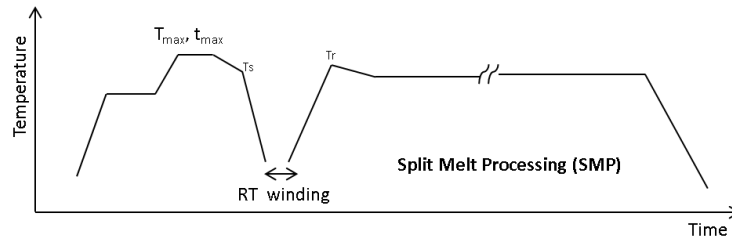


Figure 1-14.. Split melt processing (SMP) heat treatment profile

An explanation by Kametani *et al.* on the strong dependency of  $J_c$  to  $T_r$  suggests that the residual gas in the filament reconnect into large bubbles due to formation of a significant liquid within the filaments [138].

Saw-tooth processing (STP): We developed a newer version of SMP, saw-tooth processing (STP), based upon previous results showing that Bi2212 nucleation is site-saturation limited. Figure 1-15 shows a typical STP heat treatment profile. STP includes multiple heating/cooling cycles.

STP engineers the microstructure by inducing heterogeneous nucleation through controlled, localized melting, during heating cycles, and slow grain growth, during cooling cycles. In STP nucleation and growth is maximized, densely textured Bi2212 grains with minimum Bi2201 and non-superconducting phases are formed. Variations in STP heat treatment parameters affect the morphology and the phase assemblage of Bi2212 filaments [52, 85]. STP increases  $J_c$  by 120% and 70% relative to PMP at 5 T and self-field respectively, and by 65% and 34% relative to SMP [52].

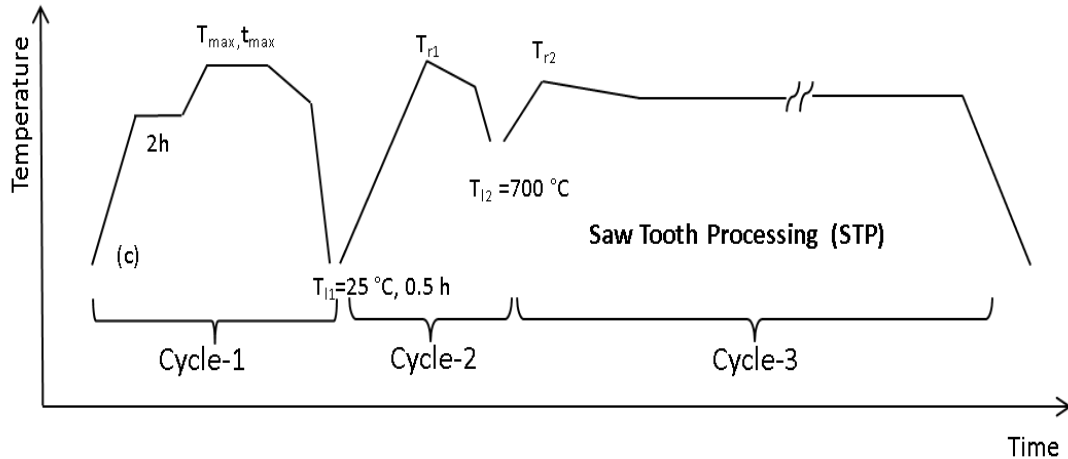


Figure 1-15. Saw-tooth processing (STP)

### Mechanical properties

Due to the very large Lorentz forces associated with very high magnetic fields and the others stress sources causing by fabrication, coil winding, cool down and fault conditions, good mechanical properties of Bi2212/Ag is essential [139].

Large, hard aggregates in the precursor powder form pinhole defects in the sheath of PIT Bi2212 tapes typically thinner than 100  $\mu\text{m}$ . These pinholes become weak spots in the sheath during the mechanical densification process of the green conductor [140].

Bi2212 is brittle, any axial strain ( $\epsilon$ ) beyond an irreversible strain limit ( $\epsilon_{irr}$ ) damages the Bi2212 filaments, causing a significant reduction in  $J_c$ . Improving toughness is also necessary to make the Bi2212 conductors more reliable for magnet applications [141, 142].

Mechanical properties of pure Ag are weak and cannot tolerate high stress levels in high field magnets. For more than 20 years, Ag/0.20wt%Mg alloy has been the most common alloy used for the outer sheath of Bi2212 wires and tapes. Mg strengthens Ag by forming a dispersion of MgO particles in the Ag matrix during PMP through internal oxidation. If Cu diffuses from Bi2212 to the Ag, it will react with Cu, the Mg in Ag/0.20wt%Mg sheath is a sink for Cu. This reaction depletes the Cu content of Bi2212, eliminates the transport properties, and limits its use only to the outer sheath where it is not in direct contact with Bi2212 [67, 139].

Kajbafvala *et al.* suggested that Ag/Al alloy is a strong candidate for Bi2212 wire [66, 67, 142]. They investigated the use of high-elastic-modulus dispersion strengthen silver aluminum alloys for the sheath of Bi2212/Ag wires. They compared mechanical and electrical properties of Ag/0.5-wt.% Al (AgAl) alloy with Ag/0.2-wt.% Mg (AgMg) alloy, which is now the most common alloy used for Bi2212 wires. Transport properties of Bi2212/AgAl wires are as good as Bi2212/AgMg wires. No leakage is observed after PMP of Bi2212/AgAl spirals. After PMP, the Bi2212/AgAl wire has slightly higher yield and tensile stresses than those of Bi2212/AgMg wires, and more importantly they show > 2% elongation, which is several times higher than that of Bi2212/AgMg wires[67]. In a different study they varied the time and temperature of the internal oxidation heat treatment to maximize the strength after Bi2212 PMP. They found out internal oxidation at 650–700 °C for 4 h produces the highest Vickers micro-hardness number for the Ag/Al alloy. After oxidizing at 675 ° C for 4 h the hardness, yield strength and tensile strength of Ag/Al sheath

are 50% higher than the corresponding values of Ag/Mg sheath. Due to the presence of  $\text{Al}_2\text{O}_3$  precipitates, the alloy retains its fine grain structure and strength after PMP [66].

Cheggour *et al.* found a reversible strain effect on  $I_c$  of Bi2212 RWs. They proposed a two-component model based on the presence of mechanically weak and strong Bi2212 components within the wire filaments. Porosity embedded in the weak component initiates cracking under strain  $\varepsilon$ .  $I_c(\varepsilon)$  is irreversible in tension if the weak component contributes to  $I_c$  but becomes reversible once connectivity of the weak component breaks by strain increasing or cycling.  $I_c$  shows reversibility at 4 K, 16 T and up to an irreversible strain limit of about 0.3 % in longitudinal tension. Their results show that the Bi2212 conductor has the potential to sustain mechanical strains generated in high-field magnets. They also suggested a model; in that higher pre-compressive strains improves  $I_c$  if buckling of Bi2212 grains does not occur, and results in a wider  $I_c(\varepsilon)$  plateau in the applied tensile regime without degradation of the initial  $I_c$  [141].

A 2D state-based peridynamic model used to explain the mechanical behavior of Bi2212 RWs at the microstructural level. Using this model, the effects of Ag/Bi2212 interface roughness, bridges and defects of various geometries on Bi2212 mechanical behavior were analyzed. Stress concentrations increases with the defect length or diameter, but decreases with defect width. The stress concentration from porosity or bubbles decreases with decreasing void diameter. Their results predict that critical strain increases as porosity decreases, which is in contrast with experimental data [143].

Gou *et al.* used Weierstrass–Mandelbrot (W–M) fractal function to model and study the fractal behavior of a Bi2212 filament and Bi2212/Ag interfaces. They found that the

interfilamentary bridges are not the cause of electromechanical degradation and failure, and concave tips are the source of large stress concentrations and are the likely causing mechanical failure in Bi2212 RWs [144].

### **Filament diameter**

Motowidlo *et al.* studied the effect of filament diameters, ranging from 11 to 100  $\mu\text{m}$ , on  $J_c$  of Bi2212 RWs. They found  $J_c$  increases with decreasing filament diameter [124]. Their results are consistent with Hasegawa *et al.* findings [145].

Holesinger *et al.* showed that wire geometries with small filament diameters prevent phase segregation during PMP [134]. Natchrab *et al.* found out when the Bi222 filament size is below 12  $\mu\text{m}$ , the filament is unstable during PMP. Small filaments interconnect driven by a reduction in interfacial surface energy. Factors including heat treatment, filament count, Ag/SC ratio, and wire diameter affect the optimum filament diameter. They provided two explanations for the effect of filament size on Bi2212 grain texturing: 1. Similar to the tapes, by increasing the interfacial surface, more nucleation sites are available, resulting in a high degree of alignment. 2. Bi2212 grains grow faster in the a-b direction than c-axis. Based on this only those grains that are oriented parallel to the filament axis grows substantially. According to these explanations one would expect as filament size decreases  $J_c$  increases, however filament contain secondary phases, voids and non-aligned Bi2212 grains, so when these defects are as large as filament diameter, current flow is affected. Also the bridges between filaments use the Bi2212 from the filament and leave voids. Since smaller filaments

have more surface area, they also have a proportionately greater number of bridges in relation to the filament volume compared to larger filaments. In their study, wires with filaments larger than 15  $\mu\text{m}$  diameter are relatively stable and are heat treated at a higher  $T_{\text{max}}$ , however their overall  $J_c$  is lower [146].

Matsumoto *et al.* suggested that filament size and configuration of the multifilamentary wire affects the optimum  $T_{\text{max}}$  and optimum  $T_{\text{max}}$  window [111]. Miao *et al.* discussed that  $J_c$  increases with inverse filament size, because of larger filament-to-silver interface area. Too small filament size is not preferred due to the filament sausaging [27].

## **Conclusions**

One candidate for high-field superconducting magnets conductor is round wire composites of Bi2212 sheathed in an Ag-alloy matrix (Bi2212/Ag). After processing, Bi2212/Ag round wires have a complex heterogeneous microstructures. Improvements in Bi2212/Ag RWs  $J_c$  require a thorough understanding of the processing-structure-properties relationships on multiple length-scales. The most important heat treatment parameter in a partial melt processing is the maximum temperature that controls the peritectic melting behavior of Bi2212. The largest challenges for large scale application of Bi2212 wires were the filament bubbling, a macroscopic scale defects. During partial melt processing porosity agglomerates to voids and causes bubbling which is suppressing their transport properties. However this challenge has been mostly eliminated by using over-pressure partial melt processing.

On the mesoscale, interfilamentary bridging and radial c-axis texturing of grain colonies are the primary structures that influence transport. On the individual filament length scale, porosity and the phase assemblage, including mesoscopic secondary phases and large Bi2201 grains, are the primary challenges. Lastly, the important roles of the intragrain structure and nanoscopic defects remain unknown.

This thesis focusses on answering the following questions:

How a heat treatment can engineer the Bi2212 filament microstructure, such that dense filaments with layered Bi2212 grains form and transport properties improves? (Chapter 2)

How filament microstructure (on the individual filament length scale) and transport properties correlate? What is the most important impurity (on the micron-scale) after heat treatment? (Chapter 3)

How do nanoscale impurities, Bi2201 intergrowths, affect transport? How despite no azimuthal texture current flows between Bi2212 grains in round wires? What is the contribution of c-axis transport? What are the magnetic flux pinning centers? (Chapter 4)

How does over-pressure affect the microstructure on multiple length scales? How to reduce the content of non-superconducting phases and produce dense layered Bi2212 filaments in an over-pressure partial melt processing? How does over-pressure affect the overall and local oxygen content? (Chapter 5)

## REFERENCES

- [1] P. H. E. Meijer, "Kamerlingh Onnes and the discovery of superconductivity," *American Journal of Physics*, vol. 62, pp. 1105-1108, 1994.
- [2] D. A. Cardwell and D. S. Ginley, *Handbook of Superconducting Materials*: Institute of Physics Pub., 2003.
- [3] T. Berlincourt, "Type II superconductivity: Quest for understanding," *IEEE Transactions on Magnetics*, vol. 23, pp. 403-412, 1987.
- [4] J. Nagamatsu, N. Nakagawa, T. Muranaka, Y. Zenitani, and J. Akimitsu, "Superconductivity at 39 K in magnesium diboride," *Nature*, vol. 410, pp. 63-64, 2001.
- [5] B. Lehndorff, *High-Tc Superconductors for Magnet and Energy Technology: Fundamental Aspects*: U.S. Government Printing Office, 2001.
- [6] R. N. Bhattacharya and P. Paranthaman, *High Temperature Superconductors*: Wiley, 2011.
- [7] T. G. Holesinger, D. S. Phillips, J. Y. Coulter, J. O. Willis, and D. E. Peterson, "Isothermal melt processing of Bi-2212 thick films," *Physica C: Superconductivity*, vol. 243, pp. 93-102, 1995.
- [8] J. Sólyom and A. Piróth, *Fundamentals of the Physics of Solids: Volume II: Electronic Properties*: Springer, 2010.
- [9] R. Funahashi, I. Matsubara, K. Ueno, and H. Ishikawa, "Mechanism of Bi<sub>2</sub>Sr<sub>2</sub>CaCu<sub>2</sub>O<sub>x</sub> crystallization and superconducting properties for Bi<sub>2</sub>Sr<sub>2</sub>CaCu<sub>2</sub>O<sub>x</sub>/Ag tapes prepared using isothermal partial melting method," *Physica C: Superconductivity*, vol. 311, pp. 107-121, 1999.
- [10] K. H. Bennemann and J. B. Ketterson, *Superconductivity: Volume 1: Conventional and Unconventional Superconductors Volume 2: Novel Superconductors*: Springer, 2008.

- [11] S. Tanaka, "High-Temperature Superconductor Electronics: Status and Perspectives," *Handbook of High-Temperature Superconductor Electronics*, p. 425, 2003.
- [12] E. H. Brandt, "Vortices in superconductors," *Physica C: Superconductivity*, vol. 369, pp. 10-20, 2002.
- [13] D. Safarali, *Theory of Conventional and Unconventional Superconductivity in the High-Tc Cuprates and Other Systems*: Nova Science Publishers, Incorporated, 2013.
- [14] P. Majewski, "BiSrCaCuO High-Tc Superconductors," *Advanced Materials*, vol. 6, pp. 460-469, 1994.
- [15] H. W. Weijers, U. P. Trociewitz, W. D. Markiewicz, J. Jiang, D. Myers, E. E. Hellstrom, A. Xu, J. Jaroszynski, P. Noyes, Y. Viouchkov, and D. C. Larbalestier, "High Field Magnets With HTS Conductors," *IEEE Transactions on Applied Superconductivity* vol. 20, pp. 576-582, 2010.
- [16] *High Magnetic Field Science and Its Application in the United States: Current Status and Future Directions*: The National Academies Press, 2013.
- [17] E. Barzi, V. Lombardo, D. Turrioni, F. Baca, and T. Holesinger, "BSCCO-2212 wire and cable studies," *Applied Superconductivity, IEEE Transactions on*, vol. 21, pp. 2335-2339, 2011.
- [18] J. Schwartz, T. Effio, X. T. Liu, Q. V. Le, A. L. Mbaruku, H. J. Schneider-Muntau, T. M. Shen, H. H. Song, U. P. Trociewitz, X. R. Wang, and H. W. Weijers, "High field superconducting solenoids via high temperature superconductors," *Ieee Transactions on Applied Superconductivity*, vol. 18, pp. 70-81, Jun 2008.
- [19] W. T. Nachtrab, C. V. Renaud, T. Wong, X. T. Liu, T. M. Shen, U. P. Trociewitz, and J. Schwartz, "Development of High Superconductor Fraction Bi<sub>2</sub>Sr<sub>2</sub>CaCuO<sub>x</sub>/Ag Wire for MRI," *Ieee Transactions on Applied Superconductivity*, vol. 18, pp. 1184-1187, 2008.
- [20] D. C. Larbalestier, J. Jiang, U. P. Trociewitz, F. Kametani, C. Scheuerlein, M. Dalban-Canassy, M. Matras, P. Chen, N. C. Craig, P. J. Lee, and E. E. Hellstrom,

- "Isotropic round-wire multifilament cuprate superconductor for generation of magnetic fields above 30 T," *Nature Materials*, vol. 13, pp. 375-381, 2014.
- [21] H. Maeda, Y. Tanaka, M. Fukutomi, and T. Asano, "A New High-  $T_c$  Oxide Superconductor without a Rare Earth Element," *Japanese Journal of Applied Physics*, vol. 27, p. L209, 1988.
- [22] K. R. Marken, W. Dai, L. Cowey, S. Ting, and S. Hong, "Progress in BSCCO-2212/silver composite tape conductors," *Applied Superconductivity, IEEE Transactions on*, vol. 7, pp. 2211-2214, 1997.
- [23] T. H. Tiefel, S. Jin, G. W. Kammlott, J. E. Graebner, R. B. van Dover, and N. D. Spencer, "Fabrication of thin-film superconductors by bulk processing," *Applied Physics Letters*, vol. 58, pp. 1917-1919, 1991.
- [24] K. Thangaraj, A. N. Iyer, L. Zhang, and K. Salama, "Heat treatment studies on Bi-2212/Ag tapes fabricated using a powder-in-tube technique," *Superconductor Science and Technology*, vol. 13, p. 1035, 2000.
- [25] R. Müller, T. Schweizer, P. Bohac, R. O. Suzuki, and L. J. Gauckler, "Compositional range of the  $\text{Bi}_2\text{Sr}_2\text{CaCu}_2\text{O}_x$  HTc-superconductor and its surrounding phases," *Physica C: Superconductivity*, vol. 203, pp. 299-314, 1992.
- [26] D. Turrioni, E. Barzi, M. J. Lamm, R. Yamada, A. V. Zlobin, and A. Kikuchi, "Study of HTS Wires at High Magnetic Fields," *Applied Superconductivity, IEEE Transactions on*, vol. 19, pp. 3057-3060, 2009.
- [27] H. Miao, K. R. Marken, M. Meinesz, B. Czabaj, S. Hong, M. O. Rikel, and J. Bock, "Studies of Precursor Composition Effect on  $J_c$  in Bi-2212/Ag Wires and Tapes," *AIP Conference Proceedings*, vol. 824, pp. 673-682, 2006.
- [28] P. Majewski, H.-L. Su, and B. Hettich, "The High- $T_c$  superconducting solid solution  $\text{Bi}_{2+x}(\text{Sr,Ca})_3\text{Cu}_2\text{O}_{8+d}$  (2212 Phase)—chemical composition and superconducting properties," *Advanced Materials*, vol. 4, pp. 508-511, 1992.

- [29] L. R. Motowidlo, P. Haldar, S. Jin, and N. D. Spencer, "Multifilament BPSCCO superconductor: fabrication and heat treatment study," *Applied Superconductivity, IEEE Transactions on*, vol. 3, pp. 942-945, 1993.
- [30] L. Motowidlo, "powder-in-tube process and method of manufacture," ed: Google Patents, 2010.
- [31] K. Heine, J. Tenbrink, and M. Thöner, "High-field critical current densities in  $\text{Bi}_2\text{Sr}_2\text{Ca}_1\text{Cu}_2\text{O}_{8+x}/\text{Ag}$  wires," *Applied Physics Letters*, vol. 55, pp. 2441-2443, 1989.
- [32] M. Karuna, J. A. Parrell, and D. C. Larbalestier, "Study of powder density, Ag:superconductor ratio, and microhardness of BSCCO-2212 Ag-sheathed wires and tapes during wire drawing and rolling," *Applied Superconductivity, IEEE Transactions on*, vol. 5, pp. 1279-1282, 1995.
- [33] T. G. Holesinger, D. J. Miller, H. K. Viswanathan, K. W. Dennis, L. S. Chumbley, P. W. Winandy, and A. C. Youngdahl, "Directional isothermal growth of highly textured  $\text{Bi}_2\text{Sr}_2\text{CaCu}_2\text{O}_y$ ," *Applied Physics Letters*, vol. 63, pp. 982-984, 1993.
- [34] J.-i. Kase, K. Togano, H. Kumakura, D. R. Dietderich, N. Irisawa, T. Morimoto, and H. Maeda, "Partial Melt Growth Process of  $\text{Bi}_2\text{Sr}_2\text{Ca}_1\text{Cu}_2\text{O}_x$  Textured Tapes on Silver," *Japanese Journal of Applied Physics*, vol. 29, p. L1096, 1990.
- [35] T. Lang, D. Buhl, and L. J. Gauckler, "Influence of the maximum temperature during partial melt-processing of Bi-2212 thick films on microstructure and  $j_c$ ," *Physica C: Superconductivity*, vol. 294, pp. 7-16, 1998.
- [36] J. Kase, N. Irisawa, T. Morimoto, K. Togano, H. Kumakura, D. R. Dietderich, and H. Maeda, "Improvement in critical current density of  $\text{Bi}_2\text{Sr}_2\text{Ca}_1\text{Cu}_2\text{O}_x$  tapes synthesized by doctor-blade casting and melt growth," *Applied Physics Letters*, vol. 56, pp. 970-972, 1990.
- [37] W. Zhang and E. E. Hellstrom, "The development of an aligned microstructure during melt processing of  $\text{Bi}_2\text{Sr}_2\text{CaCu}_2\text{O}_x$  (BSCCO-2212) doctor-bladed films," *Physica C: Superconductivity*, vol. 218, pp. 141-152, 1993.

- [38] T. D. Aksenova, P. V. Bratukhin, S. V. Shavkin, V. L. Melnikov, E. V. Antipova, N. E. Khlebova, and A. K. Shikov, "Texture formation in  $\text{Bi}_2\text{Sr}_2\text{Ca}_1\text{Cu}_2\text{O}_x/\text{Ag}$  tapes prepared by partial melt process," *Physica C: Superconductivity*, vol. 205, pp. 271-279, 1993.
- [39] Y. Feng, K. E. Hautanen, Y. E. High, D. C. Larbalestier, R. Ray Li, E. E. Hellstrom, and S. E. Babcock, "Microstructural analysis of high critical current density Ag-clad  $\text{Bi}_2\text{Sr}_2\text{Ca}_2\text{Cu}_2\text{O}$  (2:2:1:2) tapes," *Physica C: Superconductivity*, vol. 192, pp. 293-305, 1992.
- [40] H. Kumakura, H. Kitaguchi, K. Togano, T. Muroga, J. Sato, and M. Okada, "Influence of Ag substrates on grain alignment and critical current density of Bi-2212 tape conductors," *Applied Superconductivity, IEEE Transactions on*, vol. 9, pp. 1804-1807, 1999.
- [41] Q. Y. Hu, P. V. P. S. S. Sastry, U. P. Trociewitz, and J. Schwartz, "Microstructure and critical currents in AgMg-sheathed multifilamentary  $\text{Bi}_2\text{Sr}_2\text{CaCu}_2\text{O}_8$  tapes," *Applied Superconductivity, IEEE Transactions on*, vol. 9, pp. 1876-1879, 1999.
- [42] F. Kametani, T. Shen, J. Jiang, C. Scheuerlein, A. Malagoli, M. D. Michiel, Y. Huang, H. Miao, J. A. Parrell, E. E. Hellstrom, and D. C. Larbalestier, "Bubble formation within filaments of melt-processed Bi2212 wires and its strongly negative effect on the critical current density," *Superconductor Science and Technology*, vol. 24, p. 075009, 2011.
- [43] J. Polonka, M. Xu, Q. Li, A. I. Goldman, and D. K. Finnemore, "Insitu x-ray investigation of the melting of  $\text{Bi}_2\text{Sr}_2\text{Ca}_1\text{Cu}_2\text{O}$  phases," *Applied Physics Letters*, vol. 59, pp. 3640-3642, 1991.
- [44] T. Hasegawa, T. Kitamura, H. Kobayashi, H. Kumakura, H. Kitaguchi, and K. Togano, "High-temperature x-ray diffraction analysis for  $\text{Bi}_2\text{Sr}_2\text{CaCu}_2\text{O}_y$ ," *Applied Physics Letters*, vol. 60, pp. 2692-2694, 1992.
- [45] M. Polak, W. Zhang, A. Polyanskii, A. Pashitski, E. E. Hellstrom, and D. C. Larbalestier, "The effect of the maximum processing temperature on the microstructure and electrical properties of melt processed Ag-sheathed  $\text{Bi}_2\text{Sr}_2\text{CaCu}_2\text{O}_2$  tape," *IEEE Transactions on Applied Superconductivity*, vol. 7, pp. 1537-1540, 1997.

- [46] T. Koizumi, T. Hasegawa, J. Nishioka, Y. Hikichi, T. Nakatsu, H. Kumakura, H. Kitaguchi, A. Matsumoto, and S. Nagaya, "Bi-2212 phase formation process in multifilamentary Bi-2212/Ag wires and tapes," *Applied Superconductivity, IEEE Transactions on*, vol. 15, pp. 2538-2541, 2005.
- [47] W. Zhang and E. E. Hellstrom, "The effects of oxygen on melt-processing Ag-sheathed  $\text{Bi}_2\text{Sr}_2\text{CaCu}_2\text{O}_8$  conductors," *Superconductor Science and Technology*, vol. 8, p. 430, 1995.
- [48] W. Zhang, E. A. Goodilin, and E. E. Hellstrom, "Composition studies for Ag-sheathed  $\text{Bi}_2\text{Sr}_2\text{CaCu}_2\text{O}_8$  conductors processed in 100%  $\text{O}_2$ ," *Superconductor Science and Technology*, vol. 9, p. 211, 1996.
- [49] X. T. Liu, Q. V. Le, and J. Schwartz, "Influencing factors on the electrical transport properties of split-melt processed  $\text{Bi}_2\text{Sr}_2\text{CaCu}_2\text{O}_x$  round wires," *Superconductor Science and Technology*, vol. 25, p. 075008, 2012.
- [50] X. T. Liu, W. T. Nachtrab, T. Wong, and J. Schwartz, "Effect of Resolidification Conditions on  $\text{Bi}_2\text{Sr}_2\text{CaCu}_2\text{O}_x$  /Ag/AgMg Coil Performance," *Ieee Transactions on Applied Superconductivity*, vol. 19, pp. 2232-2236, 2009.
- [51] W. T. Nachtrab, C. V. Renaud, T. Wong, X. T. Liu, T. M. Shen, U. P. Trociewitz, and J. Schwartz, "Development of High Superconductor Fraction  $\text{Bi}_2\text{Sr}_2\text{CaCu}_2\text{O}_x$ /Ag Wire for MRI," *IEEE Transactions on Applied Superconductivity*, vol. 18, pp. 1184-1187, 2008.
- [52] G. Naderi, X. Liu, W. Nachtrab, and J. Schwartz, "Understanding processing–microstructure–properties relationships in  $\text{Bi}_2\text{Sr}_2\text{CaCu}_2\text{O}_x$ /Ag round wires and enhanced transport through saw-tooth processing," *Superconductor Science and Technology*, vol. 26, p. 105010, 2013.
- [53] H. Miao, Y. Huang, S. Hong, M. Gerace, and J. Parrell, "Bi-2212 round wire development for high field applications," *Journal of Physics: Conference Series*, vol. 507, p. 022020, 2014.
- [54] A. Malagoli, F. Kametani, J. Jiang, U. P. Trociewitz, E. E. Hellstrom, and D. C. Larbalestier, "Evidence for long range movement of Bi-2212 within the filament

- bundle on melting and its significant effect on  $J_c$ ," *Superconductor Science and Technology*, vol. 24, p. 075016, 2011.
- [55] H. W. Weijers, Q. Y. Hu, Y. S. Hascicek, A. Godeke, Y. Vouchkov, E. Celik, J. Schwartz, K. Marken, W. Dai, and J. Parrell, "Development of 3 T class Bi-2212 insert coils for high field NMR," *Applied Superconductivity, IEEE Transactions on*, vol. 9, pp. 563-566, 1999.
- [56] C. M. Friend, M. Hanping, H. Yibing, Z. Melhem, F. Domptail, M. Meinesz, H. Seung, E. A. Young, and Y. Yifeng, "The Development of High Field Magnets Utilizing Bi-2212 Wind & React Insert Coils," *Applied Superconductivity, IEEE Transactions on*, vol. 20, pp. 583-586, 2010.
- [57] M. Dalban-Canassy, D. A. Myers, U. P. Trociewitz, J. Jiang, E. E. Hellstrom, Y. Viouchkov, and D. C. Larbalestier, "A study of the local variation of the critical current in Ag-alloy clad, round wire  $\text{Bi}_2\text{Sr}_2\text{CaCu}_2\text{O}_{8+x}$  multi-layer solenoids," *Superconductor Science and Technology*, vol. 25, p. 115015, 2012.
- [58] T. Kuroda, Y. Tanaka, K. Togano, Y. Suga, T. Sakamoto, Y. Abe, K. Miura, T. Yanagiya, and M. Ishizuka, "Critical current densities of AgCu-sheathed Bi-2212 multifilamentary round wires in long length," *Physica C: Superconductivity*, vol. 357-360, Part 2, pp. 1098-1101, 2001.
- [59] T. Shen, J. Jiang, F. Kametani, U. P. Trociewitz, D. C. Larbalestier, J. Schwartz, and E. E. Hellstrom, "Filament to filament bridging and its influence on developing high critical current density in multifilamentary  $\text{Bi}_2\text{Sr}_2\text{CaCu}_2\text{O}_x$  round wires," *Superconductor Science and Technology*, vol. 23, p. 025009, 2010.
- [60] B. Callaway, G. Naderi, and J. Schwartz, "Statistical analysis of the relationship between electrical transport and filament microstructure in multifilamentary  $\text{Bi}_2\text{Sr}_2\text{CaCu}_2\text{O}_x/\text{Ag}/\text{Ag-Mg}$  round wires," *Superconductor Science and Technology*, vol. 27 044020 2014.
- [61] D. Sager, M. Koch, B. Hallstedt, L. J. Gauckler, and M. Chen, "Enhanced residual secondary phase dissolution by atmosphere control in Bi-2212 superconductors," *Physica C: Superconductivity*, vol. 405, pp. 103-116, 2004.

- [62] J. Jiang, W. L. Starch, M. Hannion, F. Kametani, U. P. Trociewitz, E. E. Hellstrom, and D. C. Larbalestier, "Doubled critical current density in Bi-2212 round wires by reduction of the residual bubble density," *Superconductor Science and Technology*, vol. 24, p. 082001, 2011.
- [63] E. E. Hellstrom and W. Zhang, "Formation and prevention of bubbles when melt processing Ag-sheathed  $\text{Bi}_2\text{Sr}_2\text{CaCu}_2\text{O}_x$  (2212) conductors," *Superconductor Science and Technology*, vol. 8, p. 317, 1995.
- [64] S. Patel, T. Haugan, and D. T. Shaw, "Deformation of silver-sheathed oxide superconducting tapes by trapped gases," *Cryogenics*, vol. 34, pp. 1031-1037, 1994.
- [65] T. Shen, A. Ghosh, L. Cooley, and J. Jiang, "Role of internal gases and creep of Ag in controlling the critical current density of Ag-sheathed  $\text{Bi}_2\text{Sr}_2\text{CaCu}_2\text{O}_x$  wires," *Journal of Applied Physics*, vol. 113, pp. -, 2013.
- [66] A. Kajbafvala, W. Nachtrab, R. Kumar, F. Hunte, T. Wong, and J. Schwartz, "High strength oxide dispersion strengthened silver aluminum alloys optimized for  $\text{Bi}_2\text{Sr}_2\text{CaCu}_2\text{O}_{8+x}$  round wire," *Superconductor Science and Technology*, vol. 26, p. 125012, 2013.
- [67] A. Kajbafvala, W. Nachtrab, L. Xi Feng, F. Hunte, L. Xiaotao, N. Cheggour, T. Wong, and J. Schwartz, "Dispersion-Strengthened Silver Alumina for Sheathing  $\text{Bi}_2\text{Sr}_2\text{CaCu}_2\text{O}_{8+x}$  (Bi2212) Multifilamentary Wire," *Applied Superconductivity, IEEE Transactions on*, vol. 22, pp. 8400210-8400210, 2012.
- [68] A. Endo and S. Nishikida, "Effects of heating temperature and atmosphere on critical current density of  $\text{Bi}_2\text{Sr}_2\text{Ca}_1\text{Cu}_2/\text{Ag}_{0.8}/\text{O}_y/\text{Ag}$ -sheathed tapes," *Applied Superconductivity, IEEE Transactions on*, vol. 3, pp. 931-934, 1993.
- [69] T. Kanai and T. Kamo, "Control of oxygen release from Bi-2212 phase in a partial melt process," *Superconductor Science and Technology*, vol. 6, p. 510, 1993.
- [70] T. Kuroda, T. Nakane, H. Kumakura, Y. Suga, and K. Miura, "The influence of carbon on the critical current densities of melt processed AgCu-sheathed Bi-2212 wires," *Physica C: Superconductivity*, vol. 412-414, Part 2, pp. 1167-1173, 2004.

- [71] S. Patel, T. Haugan, S. Chen, F. Wong, E. Narumi, and D. T. Shaw, "Predictive model for critical current density of Ag-sheathed  $\text{Bi}_2\text{Sr}_2\text{Ca}_1\text{Cu}_2\text{O}_8$  composite tapes with fabrication defects," *Cryogenics*, vol. 34, pp. 537-542, 1994.
- [72] C. Scheuerlein, M. D. Michiel, M. Scheel, J. Jiang, F. Kametani, A. Malagoli, E. E. Hellstrom, and D. C. Larbalestier, "Void and phase evolution during the processing of Bi-2212 superconducting wires monitored by combined fast synchrotron microtomography and x-ray diffraction," *Superconductor Science and Technology*, vol. 24, p. 115004, 2011.
- [73] M. O. Rikel, D. Wesolowski, Y. Yuan, and E. E. Hellstrom, "Competitiveness of porosity and phase purity in melt processed Bi2212/Ag conductors," *Physica C: Superconductivity*, vol. 354, pp. 321-326, 2001.
- [74] M. Hanping, H. Yibing, H. Seung, and J. A. Parrell, "Recent Advances in Bi-2212 Round Wire Performance for High Field Applications," *Applied Superconductivity, IEEE Transactions on*, vol. 23, pp. 6400104-6400104, 2013.
- [75] J. Jianyi, M. Hanping, H. Yibing, H. Seung, J. A. Parrell, C. Scheuerlein, M. Di Michiel, A. K. Ghosh, U. P. Trociewitz, E. E. Hellstrom, and D. C. Larbalestier, "Reduction of Gas Bubbles and Improved Critical Current Density in Bi-2212 Round Wire by Swaging," *Ieee Transactions on Applied Superconductivity*, vol. 23, pp. 6400206-6400206, 2013.
- [76] A. Malagoli, V. Braccini, M. Vignolo, X. Chaud, and M. Putti, "Groove-rolling as an alternative process to fabricate Bi-2212 wires for practical applications," *Superconductor Science and Technology*, vol. 27, p. 055022, 2014.
- [77] T. Kanai and N. Inoue, "Development of gas pressure melting (GPM) method for Ag-sheathed Bi-2212 wires," *Journal of Materials Science*, vol. 30, pp. 3200-3206, 1995/06/01 1995.
- [78] S. Kobayashi, K. Yamazaki, T. Kato, K. Ohkura, E. Ueno, K. Fujino, J. Fujikami, N. Ayai, M. Kikuchi, K. Hayashi, K. Sato, and R. Hata, "Controlled over-pressure sintering process of Bi2223 wires," *Physica C: Superconductivity*, vol. 426-431, Part 2, pp. 1132-1137, 2005.

- [79] T. Kato, S. Kobayashi, K. Yamazaki, K. Ohkura, M. Ueyama, N. Ayai, J. Fujikami, E. Ueno, M. Kikuchi, K. Hayashi, and K. Sato, "Development of high performance Ag sheathed Bi2223 wire," *Physica C: Superconductivity*, vol. 412–414, Part 2, pp. 1066-1072, 2004.
- [80] N. Ayai, M. Kikuchi, K. Yamazaki, S. Kobayashi, S. Yamade, E. Ueno, N. J. Fujikami, T. Kato, K. Hayashi, K. Sato, R. Hata, J. Ihara, K. J. Yamaguchi, and J. Shimoyama, "The Bi-2223 Superconducting Wires With 200A-Class Critical Current," *IEEE Transactions on Applied Superconductivity*, vol. 17, pp. 3075-3078, 2007.
- [81] Y. Yuan, J. Jiang, X. Y. Cai, S. Patnaik, A. A. Polyanskii, E. E. Hellstrom, D. C. Larbalestier, R. K. Williams, and Y. Huang, "Microstructure and  $J_c$  improvements in overpressure processed Ag-sheathed Bi-2223 tapes," *IEEE Transactions on Applied Superconductivity*, vol. 13, pp. 2921-2925, 2003.
- [82] M. O. Rikel, R. K. Williams, X. Y. Cai, A. A. Polyanskii, J. Jiang, D. Wesolowski, E. E. Hellstrom, D. C. Larbalestier, K. DeMoranville, and G. N. Riley, Jr., "Overpressure processing Bi2223/Ag tapes," *IEEE Transactions on Applied Superconductivity*, vol. 11, pp. 3026-3029, 2001.
- [83] J. L. Reeves, E. E. Hellstrom, V. Irizarry, and B. Lehdorff, "Effects of overpressure processing on porosity in Ag-sheathed Bi-2212 multifilamentary tapes with various geometries," *Applied Superconductivity, IEEE Transactions on*, vol. 9, pp. 1836-1839, 1999.
- [84] J. L. Reeves, M. Polak, W. Zhang, E. E. Hellstrom, S. E. Babcock, D. C. Larbalestier, N. Inoue, and M. Okada, "Overpressure processing of Ag-sheathed Bi-2212 tapes," *Applied Superconductivity, IEEE Transactions on*, vol. 7, pp. 1541-1543, 1997.
- [85] E. B. Callaway, G. Naderi, Q. V. Le, and J. Schwartz, "Statistical analysis of the relationship between electrical transport and filament microstructure in multifilamentary  $\text{Bi}_2\text{Sr}_2\text{CaCu}_2\text{O}_x/\text{Ag}/\text{Ag-Mg}$  round wires," *Superconductor Science and Technology*, vol. 27, p. 044020, 2014.
- [86] J. Shimoyama, J. Kase, T. Morimoto, J. Mizusaki, and H. Tagawa, "Oxygen nonstoichiometry and phase instability of  $\text{Bi}_2\text{Sr}_2\text{CaCu}_2\text{O}_{8+\delta}$ ," *Physica C: Superconductivity*, vol. 185–189, Part 2, pp. 931-932, 1991.

- [87] J. Tenbrink, M. Wilhelm, K. Heine, and H. Krauth, "Development of high- $T_c$  superconductor wires for magnet applications," *Magnetics, IEEE Transactions on*, vol. 27, pp. 1239-1246, 1991.
- [88] J. Kase, T. Morimoto, K. Togano, H. Kumakura, D. R. Dietderich, and H. Maeda, "Preparation of the textured Bi-based oxide tapes by partial melting process," *Magnetics, IEEE Transactions on*, vol. 27, pp. 1254-1257, 1991.
- [89] Y. Oka, N. Yamamoto, H. Kitaguchi, K. Oda, and J. Takada, "Crystallization Behavior and Partially Melted States in Bi-Sr-Ca-Cu-O," *Japanese Journal of Applied Physics*, vol. 28, p. L213, 1989.
- [90] B. Heeb, L. J. Gauckler, H. Heinrich, and G. Kostorz, "From imperfect to perfect  $\text{Bi}_2\text{Sr}_2\text{CaCu}_2\text{O}_x$  (Bi-2212) grains," *Journal of Materials Research*, vol. 8, pp. 2170-2176, 1993.
- [91] G. Naderi and J. Schwartz, "On the roles of  $\text{Bi}_2\text{Sr}_2\text{CuO}_x$  intergrowths in  $\text{Bi}_2\text{Sr}_2\text{CaCu}_2\text{O}_x/\text{Ag}$  round wires: c-axis transport and magnetic flux pinning," *Applied Physics Letters*, vol. 104, pp. 152602-152602-5, 2014.
- [92] M. O. Rikel and E. E. Hellstrom, "Development of 2201 intergrowths during melt processing Bi2212/Ag conductors," *Physica C: Superconductivity*, vol. 357-360, Part 2, pp. 1081-1090, 2001.
- [93] D. Buhl, T. Lang, M. Cantoni, D. Risold, B. Hallstedt, and L. J. Gauckler, "Critical current densities in Bi-2212 thick films," *Physica C: Superconductivity*, vol. 257, pp. 151-159, 1996.
- [94] O. Eibl, "Crystal defects in  $\text{Bi}_2\text{Sr}_2\text{Ca}_{n-1}\text{Cu}_n\text{O}_{4+2n+\delta}$  ceramics," *Physica C: Superconductivity*, vol. 168, pp. 249-256, 1990.
- [95] D. Bourgault, E. Flahaut, A. Antonevici, C. E. Bruzek, N. Lallouet, J. L. Soubeyroux, and R. Tournier, "Misalignment angles and the 2D-3D temperature crossover in Bi2212 multifilaments studied using transport critical current densities," *Superconductor Science and Technology*, vol. 17, p. 463, 2004.

- [96] X. Liu and J. Schwartz, "On the influence of magnetic field processing on the texture, phase assemblage and properties of low aspect ratio  $\text{Bi}_2\text{Sr}_2\text{CaCu}_2\text{O}_x/\text{AgMg}$  wire," *Science and Technology of Advanced Materials*, vol. 10, p. 014605, 2009.
- [97] S. Labdi, H. Raffy, O. Laborde, and P. Monceau, "Angular dependence of critical currents in  $\text{Bi}_2\text{Sr}_2\text{CaCu}_2\text{O}_8$  thin films predominant role of the transverse magnetic field component," *Physica C: Superconductivity*, vol. 197, pp. 274-282, 1992.
- [98] P. H. Kes, J. Aarts, V. M. Vinokur, and C. J. van der Beek, "Dissipation in highly anisotropic superconductors," *Physical Review Letters*, vol. 64, pp. 1063-1066, 1990.
- [99] D. Rodrigues, Jr., A. R. Bigansolli, E. Cursino, and P. S. Papini, "Phase formation and evolution, texturing and current transport in Ag/Bi2212 PIT monofilamentary tapes," *Applied Superconductivity, IEEE Transactions on*, vol. 15, pp. 2546-2549, 2005.
- [100] H. Maeda, K. Ohya, M. Sato, W. P. Chen, K. Watanabe, M. Motokawa, A. Matsumoto, H. Kumakura, and J. Schwartz, "Microstructure and critical current density of Bi2212 tapes grown by magnetic melt-processing," *Physica C: Superconductivity*, vol. 382, pp. 33-37, 2002.
- [101] H. B. Liu, P. J. Ferreira, and J. B. Vander Sande, " $J_c$  enhancement of  $\text{Bi}_2\text{Sr}_2\text{CaCu}_2\text{O}_8/\text{Ag}$  thick films melt-grown under an elevated magnetic field (0–10 T)," *Physica C: Superconductivity*, vol. 316, pp. 261-266, 1999.
- [102] E. Cecchetti, P. J. Ferreira, and J. B. Vander Sande, "The influence of elevated magnetic fields on the texture formation of melt-processed Bi-2212," *Physica C: Superconductivity*, vol. 336, pp. 192-198, 2000.
- [103] A. Villaume, D. Bourgault, L. Porcar, A. Girard, C. E. Bruzek, and P. F. Sibeud, "Misalignment angles' reduction in Bi2212 multifilaments melted by dynamic heat treatment under a magnetic field," *Superconductor Science and Technology*, vol. 20, p. 691, 2007.
- [104] F. J. Baca, T. G. Holesinger, J. Y. Coulter, H. Miao, Y. Huang, J. Parrell, S. Campbell, J. Searcy, E. Sooby, J. Kennison, R. DePaula, I. Apodaca, and K. Marken,

- "Effect of pre-annealing in thermal processing of Bi-2212 round wires," *AIP Conference Proceedings*, vol. 1435, pp. 340-345, 2012.
- [105] K. Nomura, M. Seido, H. Kitaguchi, H. Kumakura, K. Togano, and H. Maeda, "Fabrication conditions and superconducting properties of Ag-sheathed Bi-Sr-Ca-Cu-O tapes prepared by partial melting and slow cooling process," *Applied Physics Letters*, vol. 62, pp. 2131-2133, 1993.
- [106] J.-i. Shimoyama, N. Tomita, T. Morimoto, H. Kitaguchi, H. Kumakura, K. Togano, H. Maeda, K. Nomura, and M. Seido, "Improvement of Reproducibility of High Transport  $J_c$  for  $\text{Bi}_2\text{Sr}_2\text{CaCu}_2\text{O}_y/\text{Ag}$  Tapes by Controlling Bi Content," *Japanese Journal of Applied Physics*, vol. 31, p. L1328, 1992.
- [107] A. Matsumoto, H. Kitaguchi, H. Kumakura, J. Nishioka, and T. Hasegawa, "Improvement of the microstructure and critical current densities of Bi-2212 round wires with a precisely controlled heat treatment," *Superconductor Science & Technology*, vol. 17, pp. 989-992, Aug 2004.
- [108] B. Heeb, L. J. Gauckler, H. Heinrich, and G. Kostorz, "Microstructure and properties of melt-processed Bi-2212 ( $\text{Bi}_2\text{Sr}_2\text{CaCu}_2\text{O}_x$ )," *Journal of Electronic Materials*, vol. 22, pp. 1279-1283, 1993/10/01 1993.
- [109] E. E. Hellstrom and W. Zhang, "Important parameters for processing long lengths of Ag-sheathed  $\text{Bi}_2\text{Sr}_2\text{CaCu}_2\text{O}_x$  conductors," *Physica B: Condensed Matter*, vol. 216, pp. 252-254, 1996.
- [110] T. G. Holesinger, M. Hanping, M. Meinesz, H. Yibing, J. Parrell, J. A. Kennison, K. R. Marken, and S. Campbell, "Analysis of High  $I_c$  and  $J_c$  Bi-2212 Conductors With Dilute Second Phase Additions," *IEEE Transactions on Applied Superconductivity*, vol. 21, pp. 2791-2794, 2011.
- [111] A. Matsumoto, H. Kitaguchi, H. Kumakura, J. Nishioka, and T. Hasegawa, "Improvement of the microstructure and critical current densities of Bi-2212 round wires with a precisely controlled heat treatment," *Superconductor Science and Technology*, vol. 17, p. 989, 2004.

- [112] T. Shen, J. Jiang, F. Kametani, U. P. Trociewitz, D. C. Larbalestier, and E. E. Hellstrom, "Heat treatment control of Ag–Bi<sub>2</sub>Sr<sub>2</sub>CaCu<sub>2</sub>O<sub>x</sub> multifilamentary round wire: investigation of time in the melt," *Superconductor Science and Technology*, vol. 24, p. 115009, 2011.
- [113] D. R. Dietderich, B. Ullmann, H. C. Freyhardt, J. Kase, H. Kumakura, K. Togano, and H. Maeda, "Textured Thick Films of Bi<sub>2</sub>Sr<sub>2</sub>Ca<sub>1</sub>Cu<sub>2</sub>O<sub>x</sub>," *Japanese Journal of Applied Physics*, vol. 29, p. L1100, 1990.
- [114] T. Lang, D. Buhl, S. Al-Wakeel, D. Schneider, and L. J. Gauckler, "Phase assemblage and morphology during the partial melt processing of Bi-2212 thick films," *Physica C: Superconductivity*, vol. 281, pp. 283-292, 1997.
- [115] W. T. Nachtrab, X. T. Liu, T. Wong, and J. Schwartz, "Effect of Solidification Conditions on Partial Melt Processed Bi<sub>2212</sub>/Ag Round Wire," *IEEE Transactions on Applied Superconductivity*, vol. 21, pp. 2795-2799, Jun 2011.
- [116] H. M. Chow, X. P. Jiang, M. J. Cima, J. S. Haggerty, H. D. Brody, and M. C. Flemings, "Effects of Annealing on the Microstructure and Phase Chemistry of Directionally Solidified Bi<sub>2</sub>Sr<sub>2</sub>CaCu<sub>2</sub>O<sub>8</sub>," *Journal of the American Ceramic Society*, vol. 74, pp. 1391-1396, 1991.
- [117] M. M. Matthiesen, J. M. Graybeal, T. P. Orlando, J. B. Vander Sande, and D. A. Rudman, "The effects of anneal time and cooling rate on the formation and texture of Bi<sub>2</sub>Sr<sub>2</sub>CaCu<sub>2</sub>O<sub>8</sub> films," *Magnetics, IEEE Transactions on*, vol. 27, pp. 1223-1226, 1991.
- [118] J.-i. Shimoyama, J.-i. Kase, T. Morimoto, H. Kitaguchi, H. Kumakura, K. Togano, and H. Maeda, "Effect of Cooling Rate on Critical Current Density for Bi<sub>2</sub>Sr<sub>2</sub>CaCu<sub>2</sub>O<sub>8+δ</sub>/Ag Composite Tapes," *Japanese Journal of Applied Physics*, vol. 31, p. L1167, 1992.
- [119] H. Noji, W. Zhou, B. A. Glowacki, and A. Oota, "Influence of cooling and annealing procedure on the intergranular coupling of Ag-Bi<sub>2</sub>Sr<sub>2</sub>CaCu<sub>2</sub>O<sub>x</sub> screen-printed tape," *Physica C: Superconductivity*, vol. 205, pp. 397-405, 1993.

- [120] H. Noji and A. Oota, "The influence of sintering conditions on the critical current density and the microstructure of Ag-sheathed  $\text{Bi}_2\text{Sr}_2\text{CaCu}_2\text{O}_x$  superconducting tapes," *Superconductor Science and Technology*, vol. 5, p. 269, 1992.
- [121] T. Shen, J. Jiang, A. Yamamoto, U. P. Trociewitz, J. Schwartz, E. E. Hellstrom, and D. C. Larbalestier, "Development of high critical current density in multifilamentary round-wire  $\text{Bi}_2\text{Sr}_2\text{CaCu}_2\text{O}_{8+\delta}$  by strong overdoping," *Applied Physics Letters*, vol. 95, p. 152516, 2009.
- [122] A. Nagata, S. Yamauchi, S. Kamada, K. Sugawara, C. Takahashi, M. Nagano, Y. Wakiya, and S. Hanada, "Effect of post annealing on superconducting properties and microstructures of Bi(2212)/Ag tapes," *Applied Superconductivity, IEEE Transactions on*, vol. 5, pp. 1853-1856, 1995.
- [123] D. Buhl, T. Lang, and L. J. Gauckler, "Critical current density of Bi-2212 thick films processed by partial melting," *Superconductor Science and Technology*, vol. 10, p. 32, 1997.
- [124] L. R. Motowidlo, G. Galinski, G. Ozeryansky, W. Zhang, and E. E. Hellstrom, "Dependence of critical current density on filament diameter in round multifilament Ag-sheathed  $\text{Bi}_2\text{CaCu}_2\text{O}_x$  wires processed in  $\text{O}_2$ ," *Applied Physics Letters*, vol. 65, pp. 2731-2733, 1994.
- [125] H. Kumakura, H. Kitaguchi, K. Togano, and N. Sugiyama, "Effect of high oxygen partial pressure heat treatment on the superconducting properties of  $\text{Bi}_2\text{Sr}_2\text{CaCu}_2\text{O}_x/\text{Ag}$  tapes," *Journal of Applied Physics*, vol. 80, pp. 5162-5168, 1996.
- [126] P. Strobel, W. Korczak, and T. Fournier, "A thermal analysis study of the system Bi-Sr-Ca-Cu-O at variable oxygen pressure," *Physica C: Superconductivity*, vol. 161, pp. 167-174, 1989.
- [127] MacManus, x, J. L. Driscoll, P. Wang, Chin, J. C. Bravman, and R. B. Beyers, "Phase equilibria and melt processing of  $\text{Bi}_2\text{Sr}_2\text{Ca}_1\text{Cu}_2\text{O}_{8+x}$  tapes at reduced oxygen partial pressures," *Applied Physics Letters*, vol. 65, pp. 2872-2874, 1994.
- [128] R. Funahashi, I. Matsubara, T. Ogura, K. Ueno, and H. Ishikawa, "Critical current density for  $\text{Bi}_2\text{Sr}_2\text{CaCu}_2\text{O}_x/\text{Ag}$  tapes prepared using an isothermal partial melting

- method under controlled atmospheres," *Physica C: Superconductivity*, vol. 273, pp. 337-341, 1997.
- [129] T. C. Holesinger, P. S. Baldonado, V. Nghia Van, D. Weiming, K. R. Marken, and H. Seungok, "Isothermal melt processing of Bi-2212 tapes," *Applied Superconductivity, IEEE Transactions on*, vol. 9, pp. 1800-1803, 1999.
- [130] T. G. Holesinger, J. M. Johnson, J. Y. Coulter, H. Safar, D. S. Phillips, J. F. Bingert, B. L. Bingham, M. P. Maley, J. L. Smith, and D. E. Peterson, "Isothermal melt processing of  $\text{Bi}_2\text{Sr}_2\text{CaCu}_2\text{O}_y$  round wire," *Physica C: Superconductivity*, vol. 253, pp. 182-190, 1995.
- [131] T. G. Holesinger, "Al<sub>2</sub>O<sub>3</sub> additions for isothermal melt processing of  $\text{Bi}_2\text{Sr}_2\text{CaCu}_2\text{O}_y$ ," *Journal of Materials Research*, vol. 11, pp. 2135-2141, 1996.
- [132] R. D. Ray II and E. E. Hellstrom, "Ag-clad Bi-Sr-Ca-Cu-O wires: II. Important factors in supersolidus phase studies," *Physica C: Superconductivity*, vol. 175, pp. 255-260, 1991.
- [133] T. G. Holesinger, D. S. Phillips, J. O. Willis, and D. E. Peterson, "Relationships between processing temperature and microstructure in isothermal melt processed Bi-2212 thick films," *Applied Superconductivity, IEEE Transactions on*, vol. 5, pp. 1939-1942, 1995.
- [134] T. G. Holesinger, J. A. Kennison, K. R. Marken, M. Hanping, M. Meinesz, and S. Campbell, "Compositional and microstructural analysis of high  $I_c$  Bi-2212 conductors," *Applied Superconductivity, IEEE Transactions on*, vol. 15, pp. 2562-2565, 2005.
- [135] T. G. Holesinger, D. J. Miller, and L. S. Chumbley, "Solid solution region of the  $\text{Bi}_2\text{Sr}_2\text{CaCu}_2\text{O}_y$  superconductor," *Physica C: Superconductivity*, vol. 217, pp. 85-96, 1993.
- [136] T. M. Shen, X. T. Liu, U. P. Trociewitz, and J. Schwartz, "Electromechanical behavior of  $\text{Bi}_2\text{Sr}_2\text{CaCu}_2\text{O}_x$  conductor using a split melt process for react-wind-sinter magnet fabrication," *Ieee Transactions on Applied Superconductivity*, vol. 18, pp. 520-524, Jun 2008.

- [137] J. Schwartz and G. A. Merritt, "Proof-of-principle experiments for react–wind–sinter manufacturing of  $\text{Bi}_2\text{Sr}_2\text{CaCu}_2\text{O}_x$  magnets," *Superconductor Science and Technology*, vol. 20, p. L59, 2007.
- [138] F. Kametani, E. G. Lee, T. Shen, P. J. Lee, J. Jiang, E. E. Hellstrom, and D. C. Larbalestier, "An explanation of how split melt processing can enhance the critical current density of Bi2212 round wires based on examination of bubble size and density formed in the melt," *Superconductor Science and Technology*, vol. 27, p. 055004, 2014.
- [139] R. Navarro, "Silver alloys used in composite BSCCO tapes: development of electrical and mechanical properties during manufacture," *Superconductor Science and Technology*, vol. 13, p. R147, 2000.
- [140] T. Haugan, S. Chen, S. Patel, F. Wong, P. Bush, and D. T. Shaw, "Pinhole defects in Ag sheath of PIT Bi-2212 tapes," *Cryogenics*, vol. 35, pp. 853-859, 1995.
- [141] N. Cheggour, X. F. Lu, T. G. Holesinger, T. C. Stauffer, J. Jiang, and L. F. Goodrich, "Reversible effect of strain on transport critical current in  $\text{Bi}_2\text{Sr}_2\text{CaCu}_2\text{O}_{8+x}$  superconducting wires: a modified descriptive strain model," *Superconductor Science and Technology*, vol. 25, p. 015001, 2012.
- [142] Amir, " $\text{Bi}_2\text{Sr}_2\text{CaCu}_2\text{O}_{8+x}$  round wires with Ag/Al oxide dispersion strengthened sheaths: microstructure–properties relationships, enhanced mechanical behavior and reduced Cu depletion " 2014.
- [143] Quang, "Two-dimensional peridynamic simulation of the effect of defects on the mechanical behavior," 2014.
- [144] X. Gou and J. Schwartz, "Fractal analysis of the role of the rough interface between  $\text{Bi}_2\text{Sr}_2\text{CaCu}_2\text{O}_x$  filaments and the Ag matrix in the mechanical behavior of composite round wires," *Superconductor Science and Technology*, vol. 26, p. 055016, 2013.
- [145] T. Hasegawa, T. Koizumi, Y. Hikichi, T. Nakatsu, R. M. Scanlan, N. Hirano, and S. Nagaya, "HTS conductors for magnets," *Applied Superconductivity, IEEE Transactions on*, vol. 12, pp. 1136-1140, 2002.

- [146] W. T. Nachtrab, T. Wong, X. T. Liu, and J. Schwartz, "The Effect of Filament Diameter on  $J_c$  in High Filament Count Bi2212/Ag Round Wire," *Applied Superconductivity, IEEE Transactions on*, vol. 19, pp. 3061-3066, 2009.

## **Chapter 2**

### **Understanding processing - microstructure – properties relationships in**

#### **Bi<sub>2</sub>Sr<sub>2</sub>CaCu<sub>2</sub>O<sub>x</sub>/Ag round wires and enhanced transport through saw-tooth processing**

Golsa Naderi<sup>1</sup>, Xiaotao Liu<sup>1</sup>, William Nachtrab<sup>2</sup>, Justin Schwartz<sup>1</sup>

<sup>1</sup>Department of Materials Science and Engineering, North Carolina State University, Raleigh,  
NC 27695-7907, U.S.A.

<sup>2</sup>Supercon Inc., Shrewsbury, Massachusetts, MA 01545, U.S.A

Supercond. Sci. Technol. 26 (2013) 105010 (15pp)

<http://iopscience.iop.org/0953-2048/26/10/105010/>

#### **Abstract**

Superconducting magnets generating magnetic fields above 25 T are needed for many scientific applications. Due to fundamental limitations to NbTi and Nb<sub>3</sub>Sn, such high-field superconducting magnets require alternative high-field conductors. One candidate conductor is round wire composites of Bi<sub>2</sub>Sr<sub>2</sub>CaCu<sub>2</sub>O<sub>x</sub> sheathed in an Ag-alloy matrix (Bi2212/Ag). The performance of such wires is sensitive to the heat treatment, so improvements in the critical current density ( $J_c$ ) require a thorough understanding of the processing-structure-properties relationships. Here we present a two-part study. In Part I, a new heat treatment approach, saw-tooth processing (STP), is introduced based upon previous results showing that Bi2212 nucleation is site-saturation limited. The microstructural evolution of Bi2212 filaments during processing is discussed and results from STP are compared with those from other processes. STP is shown to increase  $J_c$  by 120% and 70% relative to partial-melt

processing at 5 T and self-field respectively, and by 65% and 34% relative to split-melt processing. Yet STP also complicates the heat treatment by introducing a number of new heat treatment variables that affect the grain morphology, phase assemblage and oxygen content of the Bi2212 filaments and thus the transport properties. In Part II, the effects of STP heat treatment parameters on the microstructure and transport properties are discussed. It is shown that wires with the highest transport critical current densities primarily have filaments with two types of microstructures, one comprised primarily highly textured Bi2212 grains, and another with a noticeable amount of  $\text{Bi}_2\text{Sr}_2\text{CuO}_x$  with the Bi2212.

## **Introduction**

Superconducting magnets generating magnetic fields above 25 T are needed for future dipoles and quadrupoles for high energy hadron colliders beyond the Large Hadron Collider, solenoids for muon cooling in a neutrino factory or a muon collider, and for future nuclear magnetic resonance spectrometers [1-3]. Due to fundamental limits in low temperature superconductors such as NbTi and  $\text{Nb}_3\text{Sn}$ , such very high field magnets require high temperature superconductor (HTS) because of their very high irreversibility field at 4.2 K. Among HTS materials capable of high transport critical current density ( $J_c$ ) in the low temperature and high magnetic field regime, round, multifilamentary  $\text{Bi}_2\text{Sr}_2\text{CaCu}_2\text{O}_x$  (Bi2212) wire in a Ag/Ag-alloy matrix has received much attention due to its high engineering critical current density ( $J_e$ ) [2, 4-6]. Moreover, as the only HTS conductor available as a round wire, Bi2212/Ag may be preferred for magnets that require isotropic electromagnetic behavior and for magnets that require a high current cable [3, 6-9].

Bi2212 round wires are manufactured using the powder-in-tube (PIT) method. After deforming the tube into a wire, partial-melt processing (PMP) is required to obtain high  $J_c$  and  $J_e$ . During PMP, Bi2212/Ag wire is heated above the Bi2212 peritectic temperature, around 890 °C, decomposing the single-phase Bi2212 starting powder [10] into alkaline earth cuprate (AEC) and copper free (CF) phases in addition to liquid; this is shown in equation (1).



In the subsequent resolidification, the reverse peritectic reaction reforms the Bi2212 phase in a network of grains and grain colonies with end-to-end connectivity. Due to phase separation in the partial-melt and kinetic limitations of resolidification, the reverse reaction is not complete;  $\text{Bi}_2\text{Sr}_2\text{CuO}_x$  (Bi2201) intergrowths and grains form within and beside Bi2212 grains, and AEC and CF phases may remain [11-14].

From a number of studies of PMP of Bi2212 wires and tapes, there is some understanding of the correlations between the complex microstructure of Bi2212 wires, heat treatment variables and transport properties. In [7, 15, 16], the effect of maximum processing temperature was discussed and an optimal range was determined. Oxygen partial pressure was also studied as an important variable [17, 18]. The effects of hold time and temperature in the melt,  $t_{\text{melt}}$  and  $T_{\text{max}}$ , were studied [7, 19, 20]. High  $J_c$  was obtained by controlling  $t_{\text{melt}}$ ; when  $t_{\text{melt}}$  was longer than 2.5 h,  $J_c$  decreased linearly [21]. In [14], two-stage cooling from  $T_{\text{max}}$  was recommended based on the effect of undercooling on the quantity of secondary phases and the rate of nucleation and growth of Bi2212. It was also shown that Ag and impurities such as C affect the melt temperature of Bi2212 [22]. Moreover, it has been shown

that the Sr/Ca ratio has a strong effect on both the Bi2212 melt temperature and phase assemblage after PMP [23, 24].

One of the main barriers to transport current in long wires is the residual porosity in the Bi2212 filaments after PMP. One mechanism that has been proposed for the source of porosity is bubble agglomeration during PMP from gas within the filaments [10, 21, 25-27]. Using cold isostatic pressure and swaging, the bubble density and size have been reduced and  $J_c$  increased [10, 28].

Despite these efforts to optimize PMP and Bi2212 wire performance, it is likely that  $J_c$  can be significantly improved further through better understanding of the processing-structure-properties relationships. In particular, there are two primary limitations to  $J_c$  in Bi2212 wires: porosity and Bi2212 phase purity. This paper focuses on the understanding and control of the phase transformation kinetics to solve the latter limitation.

One approach to better controlling the transformation kinetics of Bi2212 wires is split-melt processing (SMP) [8, 29, 30]. In SMP, the PMP heat treatment is separated into two parts. In the first part, the wire is heated above the peritectic melt temperature. After this step is completed, the wire is cooled to room temperature and can be wound into the final magnet geometry. In the second step, the rest of the PMP heat treatment schedule is followed, including a long solid state sintering in the last step. The SMP approach resulted in a 40% increase in  $J_c$  and  $J_e$  at 4.2 K [6, 30, 31].

Further study of SMP [12] showed that the enhanced transport is a result of creating more recrystallization sites for the Bi2212 phase. This work showed [12] that the phase transformation kinetics of the resolidification of Bi2212 wires during non-isothermal cooling,

at a constant cooling rate, obeys the Avrami equation. Based on a physically significant special case studied by Cahn [32], where the phase transformation kinetics follow the Avrami equation, nucleation occurs early in the course of the transformation and is site-saturation limited. Also in [12], the values obtained for the Avrami exponents indicate that the formation of Bi2212 is associated with a diffusion mechanism for both the nucleation and the growth of Bi2212 plate-like grains. Rapid cation diffusion at the early stage of solidification causes the rapid formation of Bi2201 and/or Bi2212 grains, resulting in larger Avrami exponents. As the temperature decreases, the nucleation of Bi2201 and Bi2212 grains ceases and as Bi2212 and Bi2201 grains grow, edge impingement of the large plate-like grains occurs. The large Bi2201 and Bi2212 phases grow and form a network-like microstructure during further cooling. The impingement among Bi2201 and/or Bi2212 grains in the latter growth stage, results from the retardation of cation diffusion and the decreased growth dimension of the Bi2201 and Bi2212 grains. The slower cation diffusion, after the liquid is consumed, results in the low Avrami exponent for this stage of cooling [12].

Bi2212 can form via several mechanisms during a melt and resolidification process, including heterogeneous and homogeneous nucleation from the melt [14, 21, 33-37], a liquid-solid reaction between the melt and secondary phases during solidification [12, 14, 21, 38], and a solid-state reaction between the secondary phases and Bi2201 after solidification and during sintering [30, 37, 39, 40].

The work reported here is predicated on the hypothesis that additional nucleation sites for Bi2212 are created through additional heat-cool-heat cycles during processing, activating Bi2212 formation by liquid-solid reactions. This new heat treatment approach is called saw-

tooth processing (STP), during which the heat treatment is split into multiple heat-cool-heat cycles. After the first cycle, existing secondary phases act as nucleation sites and heterogeneous nucleation is encouraged at these imperfections. Moreover, additional heat-cool-heat cycles induce additional localized melting, and the resulting liquid facilitates Bi2212 formation by increasing the rate of cation diffusion.

This paper is organized into two parts. First, STP is introduced and results are compared with those from PMP and SMP. Relative to wires heat treated with PMP, wires processed with STP showed a 70% enhancement in  $J_c$  in self-field and a 120% improvement at 5 T, and the microstructural evolution of Bi2212 filaments during STP is discussed. Subsequently, the effects of varying the STP heat treatment parameters within each cycle on the microstructure and transport properties are reported in greater detail, to better understand the processing-structure-properties relationships in Bi2212 wires, and to further improve the transport behavior of Bi2212 wires.

### **Experimental procedures**

Two single-restack multifilamentary Bi2212 round wires are manufactured by the PIT method. Cross-sectional optical images of wires taken by an Olympus SC30 after deformation but before heat treatment are seen in Figure 2-1. The wire used in Part I, wire I, has a 0.787 mm outer diameter, 357 filaments, 31.4% fill factor and a relatively large filament size, 25.2  $\mu\text{m}$ . A previous study showed that the optimum filament size for maximizing transport is about 15  $\mu\text{m}$ ; therefore these wires are not expected to have as high a  $J_c$  as some previously reported wires [41]. The wire used in Part II, wire II, has a 0.787 mm outer diameter, 928 filaments, 54.7% fill factor, and a nominal 20  $\mu\text{m}$  filament size. Each

wire contains the same Nexans Superconductor starting powder with chemical composition of  $\text{Bi}_{2.19}\text{Sr}_{1.95}\text{Ca}_{0.88}\text{Cu}_{1.98}\text{O}_x$ . The filaments are in a pure Ag matrix contained within an Ag–0.2wt% Mg alloy outer sheath.

Heat treatments are performed on 4-5 cm long wires in 1 bar flowing oxygen in a quartz tube within a horizontal tube furnace instrumented with R-type thermocouples monitored with programmable controllers. A monitoring thermocouple is placed close to the samples and the temperature–time data is recorded every 30 seconds using Labview. The temperature variation is controlled within 0.5 °C of the set value.

Heat treatment profiles, which are used to heat treat wire I, are shown in Figure 2-2 (axes not to scale). The PMP temperature-time profile is shown in Figure 2-2(a) with  $T_p = 884$  °C; this value is selected based on differential thermal analysis (DTA) results on a green wire in comparison with previous studies [8, 13, 30]. Several SMP heat treatments are performed and that which resulted in the highest  $J_c$  is the basis for further studies; the SMP temperature-time profile is shown in Figure 2-2(b). After determining the common heat treatment parameters, STP heat treatment studies are established; this is illustrated in Figure 2-2(c). Note that the three parts of STP are labeled on cycle-1, cycle 2, and cycle 3. In STP,  $T_{11}$  is as low as room temperature, and  $T_{12}$  is 700 °C, which is low enough to ensure solidification of all liquid and high enough to remain in the single phase region of Bi2212 [42]. Heat treatment parameters common to PMP, SMP and STP including  $T_p$ ,  $T_1$ ,  $T_s$ ,  $T_{r1}$ , and ramping and cooling rates, are chosen based on previous studies and presented in Figure 2-2 [8, 13, 30]. Two different cooling rates, ( $R_{23}$ ), 2.5 and 1 °C/hr, are used for cooling from  $T_{r2}$  to  $T_3$  during STP; these heat treatments are referred to as STP1 and STP2. Furthermore, the microstructural evolution

of wire I, during STP1 is studied by quenching samples into room temperature brine by dropping them from the hot-zone of a vertical furnace. The quench temperatures are illustrated in Figure 2-3.

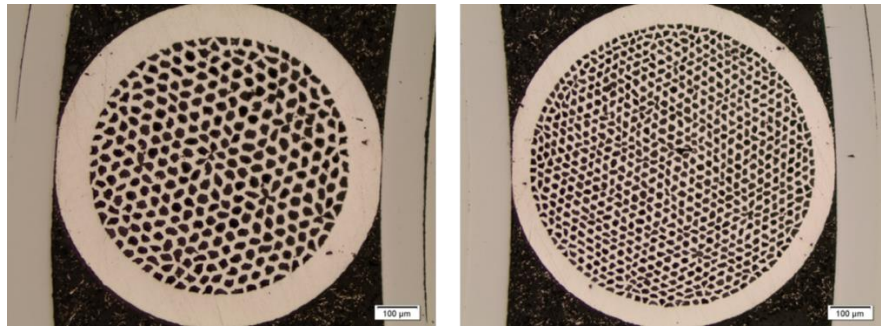


Figure 2-1. Optical images of cross-sections of unreacted Bi2212 wires, (a) wire I, (b) wire II.

To study STP in greater detail, samples of wire II are heat treated using STP2 and characterized after each cycle. To investigate the effects of varying some of the STP2 heat treatment parameters on wires that have experienced all three cycles, certain individual heat treatment parameters are varied in subsequent heat treatments. Parameters varied (and the values studied) include: cooling rate from  $T_{r1}$  to  $T_2$ ,  $R_{r12}$ , (2.5, 5 and 10 °C/hr), cooling rate from  $T_2$  to  $T_{l2}$ ,  $R_{2l2}$ , (80 and 160 °C/hr), heating rate from  $T_{l2}$  to  $T_{r2}$ ,  $R_{l2r2}$ , (80 and 160 °C/hr),  $T_{r2}$  (867, 869, 871, 873, 874, 875, 877, 878, 879 °C).

Samples are prepared for cross-sectional imaging in a scanning electron microscopy (SEM) by mounting small pieces of wire using a Durocit cold mounting liquid with graphite added so that the mounting is conductive. Mounted samples are polished using SiC paper, 1.0  $\mu\text{m}$  and 0.3  $\mu\text{m}$  alumina suspensions. Different phases within a multiphase sample are observed

via two SEMs, a Hitachi S3200 and a Hitachi TM3000, both in backscatter (BSE) mode. Phase identification is carried out using energy dispersive spectrometer (EDS) attached to the Hitachi S3200. A FEI Quanta 3D field emission gun (FEG), a dual beam instrument that combines a traditional field emission scanning electron microscope (FESEM) column with a focused ion beam (FIB) column, is used to investigate sample microstructures.

For quantitative image analysis on SEM micrographs of the quenched samples, AEC and CF grains are selected via the “magic wand” and “quick selection” tools of Photoshop and the area fraction of these grains is calculated using the “analyze particle” feature of imageJ. The measurement is averaged over several SEM micrographs of each sample.

Differential thermal analysis (DTA) on wire II is carried out on a green wire, a wire after cycle-1, after cycle-2, and after cycle-3 (fully processed wire). DTA is performed using a STA6000 (Perkin Elmer) under 20 ml/min of flowing oxygen and a 5 °C/min heating rate while the sample held in an alumina crucible. Pt is used as the reference material. Each sample is several pieces of wire, about 3 mm in length and  $40 \pm 10$  mg in mass. The onset of melting is found using the intersection of the baseline and the tangent line to the steepest slope. SEM micrographs of the samples after each cycle of STP2 are analyzed quantitatively using the same approach used for quenched samples.

Critical current ( $I_c$ ) is measured using the four-probe method in liquid helium (4.2 K) in magnetic fields up to 5 T generated using a 200 mm warm-bore superconducting magnet. A  $10^{-6}$  V cm<sup>-1</sup> electric field criterion, with 20 mm voltage tap spacing, is used to determine  $I_c$ . Each measurement is performed on at least three samples.  $J_c$  is calculated by dividing  $I_c$  by the superconductor area in the cross-section of the wire as measured on the green wire. The  $J_c$

values reported are the average of at least three samples for each heat treatment with a maximum variance less than 10%.

A Quantum Design superconducting quantum interface device (SQUID) is used to measure the superconducting-to-normal transition temperature upon warming in a 100 G magnetic field parallel to the wire. The magnetization measurements are performed on 5 mm long samples cut from the green wire and from wires after each heat treatment cycle.

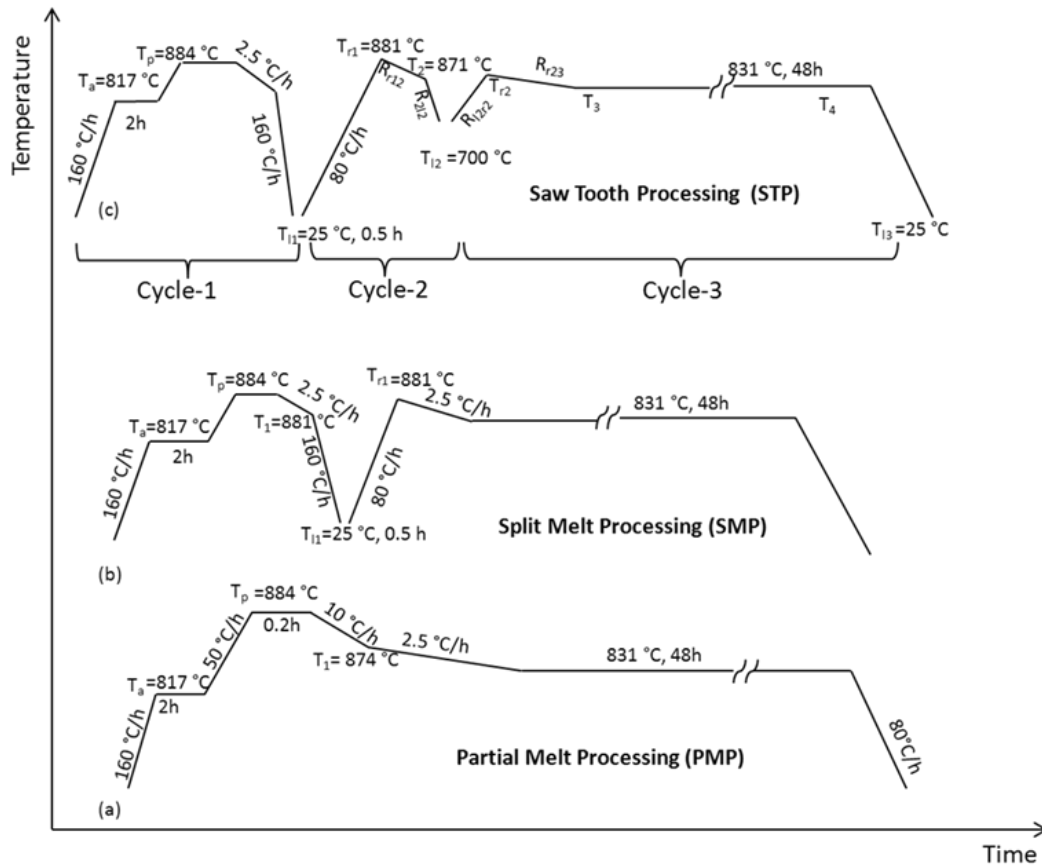


Figure 2-2. Temperature-time schematics (not to scale) of the heat treatment profiles for (a) partial-melt processing, (b) split-melt processing, (c) saw-tooth processing.

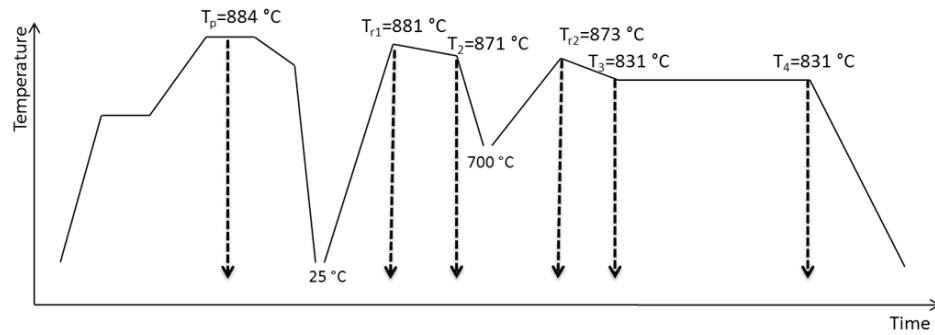


Figure 2-3. Temperature-time schematics (not to scale) of the heat treatment profiles used for the quench study using wire I.

## Results

### Part I

Cross sectional SEM images, of (a) PMP, (b) SMP, (c) STP1 and (d) STP2 samples of wire I are shown in Figure 2-4. Multiple filament types are distinguishable in all samples; filaments containing AEC, CF, and Bi2201 phases are observed, along with filaments containing mostly well-textured Bi2212 grains. The most commonly seen phases are Bi2212 and Bi2201. Figure 2-5 shows higher magnification images from the interior of two filaments from a STP2 wire; one with a mixture of Bi2212 and Bi2201 and another with highly textured, dense Bi2212. These images show that the STP2-processed sample has a larger number of filaments with such high-density, well-textured Bi2212 grains than other samples.  $J_c$  as a function of magnetic field for each sample type is plotted in Figure 2-6. Each data point is the average of at least three samples and in no case was the sample-to-sample variance greater than 10%. As reported previously, SMP wires show improved  $J_c$  relative to PMP; here the increase is 34 % at self -field. Interestingly, the transport behavior of STP1

wires is similar to that of SMP wires. There is a significant increase in transport in STP2 wires compared to all others. At 5 T,  $J_c$  of STP2 wires is increased by 120% relative to that of the PMP wires and 65% relative to SMP and STP1 wires.

Figure 2-7 shows SEM images of samples that are quenched as illustrated in Figure 2-3. Note that the image in Figure 2-7(a) is representative of PMP, SMP, STP1 and STP2, and those in Figure 2-7(b, c) are representative of SMP and STP1. Images in Figure 2-7(d-f) show the microstructural evolution in STP1 at  $T_{r2}$ ,  $T_3$ , and  $T_4$ . Temperatures  $T_3$  and  $T_4$  are the same but represent different stages of the heat treatment;  $T_4$  is 48 hours after  $T_3$ .

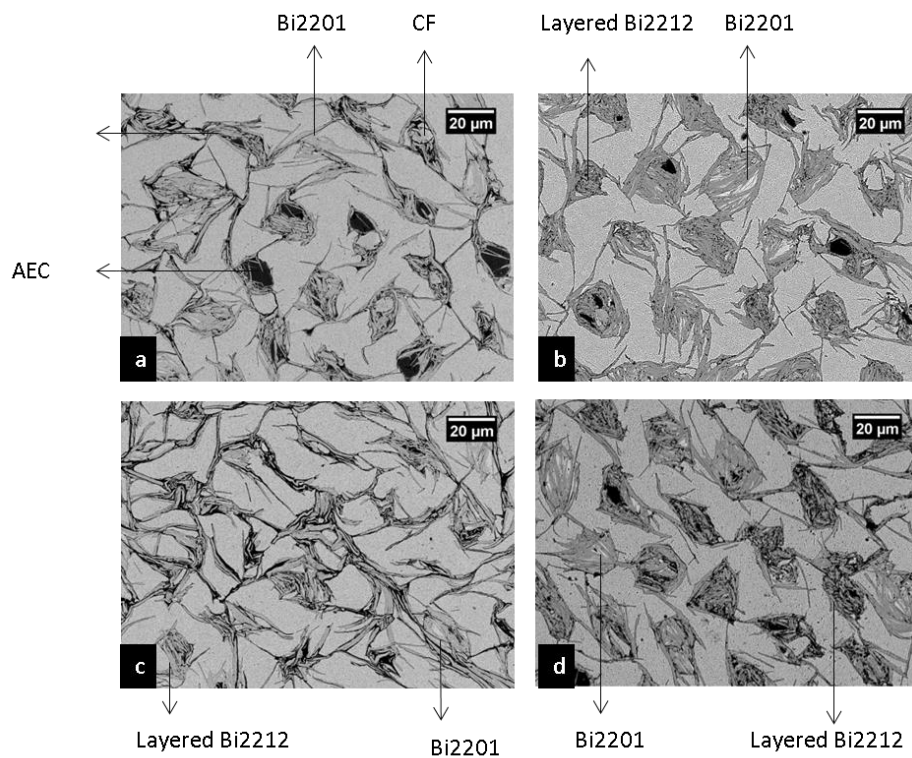


Figure 2-4 Cross sectional SEM micrographs of Bi2212/Ag multifilamentary wires after (a) partial-melt processing, (b) split-melt processing, (c) saw-tooth processing (STP1) and (d) saw-tooth processing (STP2).

The sample illustrated by Figure 2-7(a) is quenched after a 6 minute hold at the peak temperature and is named QTP. AEC, CF and voids, formed during peritectic melting, are clearly seen, confirming the melt. In Figure 2-7(b), which is a sample quenched after reheating to  $T_{r1}$ , the amount of crystalline phases is increased. Figure 2-7(c), a sample quenched at  $T_2$  ( $QT_2$ ), shows that during cooling from  $T_{r1}$ , liquid converts to Bi2212 and large grains of secondary phases are also formed. SEM image of  $QSTP-T_{r2}$ , Figure 2-7(d), as compared to  $QT_2$ , Figure 2-7(c), show that the second cool-heat cycle results in less secondary phases and an increase in the number of interfilamentary bridges.

The next step in the STP1 heat treatments is slow cooling,  $2.5\text{ }^\circ\text{C/hr}$ , from  $T_{r2}$  to  $T_3$ . In  $QSTP-T_3$ , Figure 2-7(e), the AEC and CF phases content decrease greatly relative to what is seen in Figures 2-7(d). Lastly, Figure 2-7(f) shows the microstructures after 48 hours at  $830\text{ }^\circ\text{C}$ . The filaments are strongly connected with wide bridge, and the amount of secondary phases is reduced further.

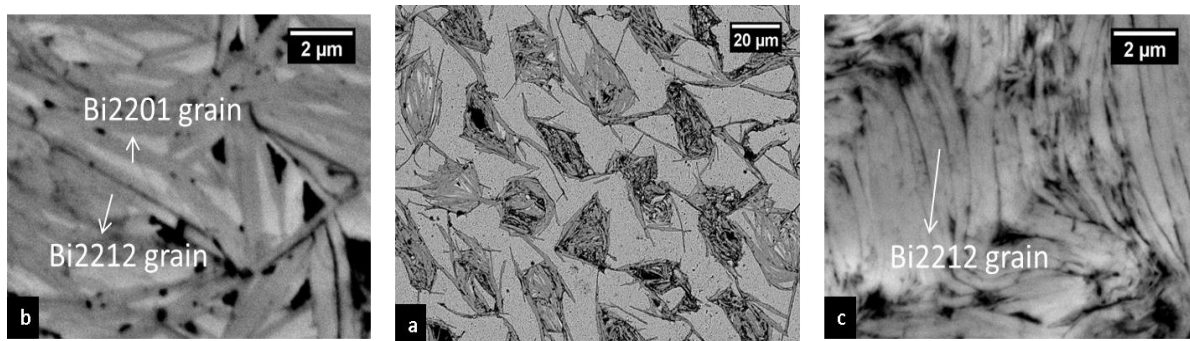


Figure 2-5. Cross sectional SEM micrographs of (a) Bi2212/Ag multifilamentary wire after STP2, (b) filament with Bi2201 grains (c) dense, highly textured Bi2212 filament.

A quantitative comparison of the AEC and CF phase content from STP1 quench studies is shown in Figure 2-8. Large secondary phase grains grow while smaller ones are consumed during slow cooling to  $T_2$ . Therefore the AEC and CF area fractions do not change significantly at this stage. From  $T_2$  to  $T_{r2}$ , however, the AEC and CF phase contents decrease by 50% and 70% respectively. There is an additional 70% decrease in the AEC content and 50% decrease in the CF content during the slow cooling step from  $T_{r2}$  and  $T_3$ . At  $T_3$ , the AEC content is very low and decreases slightly in the final sintering step, from  $T_3$  to  $T_4$ . In the fully processed sample the AEC phase content reaches a minimum compared to the previous stages. The CF phase content increases slightly, relative to the previous step, during the final heat treatment step.

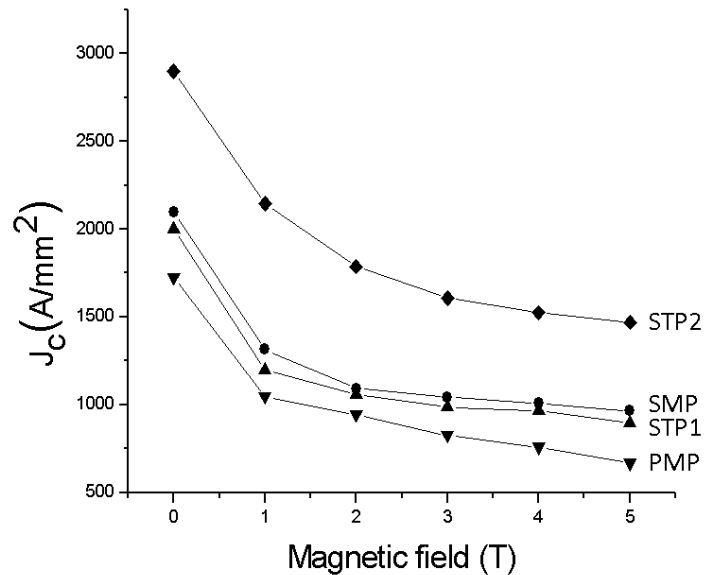


Figure 2-6. Transport  $J_c$  versus magnetic field for wires heat treated by PMP, SMP, STP1 and STP2.

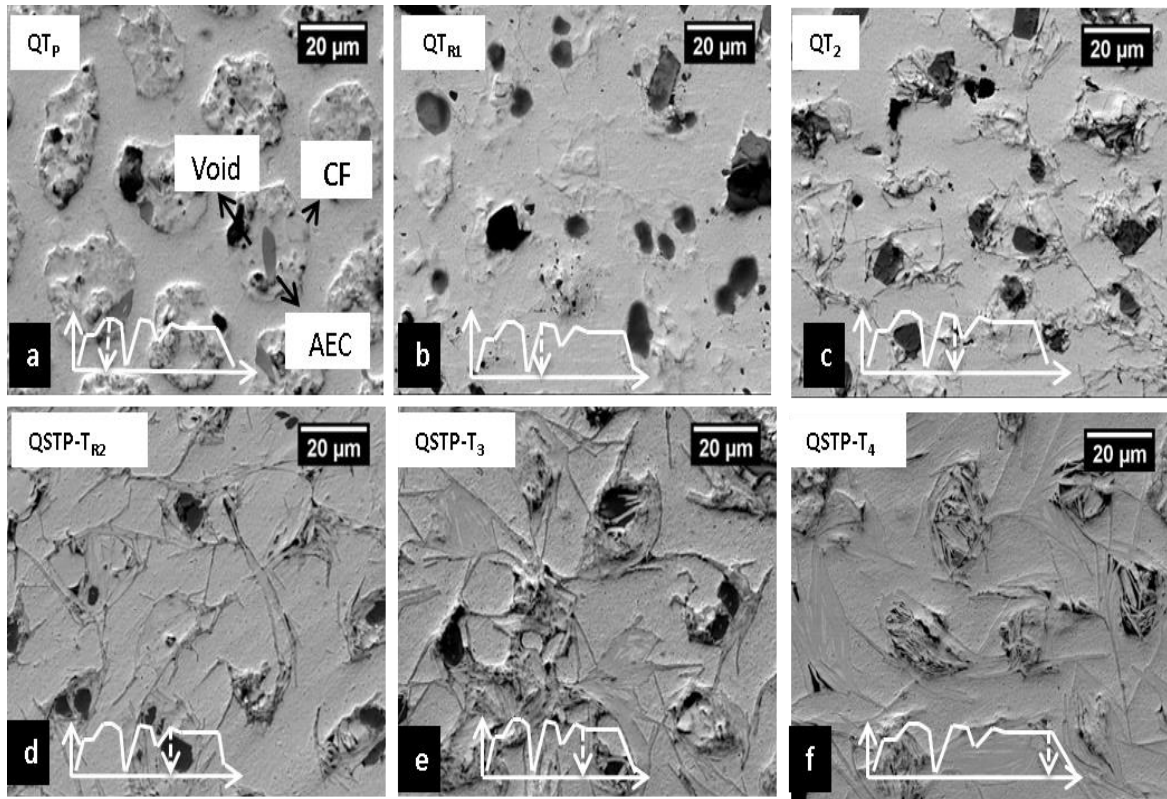


Figure 2-7. Cross sectional SEM micrographs of Bi2212/Ag multifilamentary wires quenched during STP. Samples are quenched from (a)  $T_p=884$  °C, QT<sub>p</sub>, (b)  $T_{r1}=882$  °C, QTR<sub>1</sub>, (c)  $T_2=872$  °C, QT<sub>2</sub>, (d)  $T_{r2}=873$  °C, QSTP-TR<sub>2</sub>, (e)  $T_3=832$  °C, QSTP-T<sub>3</sub>, (f)  $T_4=832$  °C, QSTP-T<sub>4</sub>.

## Part II

### *Thermal analysis and magnetic measurements*

Thermal analysis of wire II is performed to understand the melting behavior of the Bi2212 filaments after each STP cycle in STP2 of wire II. Figure 2-9 shows the DTA results on a green wire, and wires after the first, second and third heat treatment cycles. The onset of melting in the green wire is  $878 \pm 0.5$  °C, whereas after the cycle-1 the onset temperature is reduced to  $862 \pm 1$ °C. After cycle-2, the onset of melting increases to  $871 \pm 1$ °C, and after

cycle-3 it increases further to  $881\pm 1^\circ\text{C}$ . Melt behavior characteristic of a single phase material, including a sharp endothermic peak, is observed for the green wire and the fully processed wire, whereas after cycle-1 and cycle-2 the melting peaks are broad and accompanied by a side peak, typical of a multiphase sample. These side peaks point to the existence of other phases within the filaments, a large quantity of AEC and CF, as shown in Figure 2-10(a, b), as well as possible oxygen inhomogeneities within the Bi2212 grains.

Comparing the thermal analysis data from the green wire with that from the wires heat treated after cycle-1, cycle-2 and cycle-3 (fully processed, STP2), together with the magnetization results in Figure 2-11, provides insight into the relationship between melting and oxygen content through the heat treatment. One indicator of changes in oxygen content within the Bi2212 is  $T_c$ . Figure 2-11 shows the magnetization versus temperature for a green wire and wires heat treated through cycle-1, cycle-2 and cycle-3. The magnitude of the magnetization at low temperature which is an indicative of the Bi2212 content and grain connectivity, increases significantly after each cycle. When magnetization is normalized to the maximum magnetization of each sample, (inset in Figure 2-11), the critical temperature ( $T_c$ ) is found as the intersection of the baseline and the tangent line to the steepest slope. Here  $T_c$  is likely indicative of oxygen content. These results show that  $T_c$  decreases after each heat treatment cycle from  $80 \pm 1$  K for the green wire to  $72 \pm 1$  K for fully processed (STP2) wire. Figure 2-10(a, b) shows SEM micrographs of wires after cycle-1 and cycle-2. These images are converted by Photoshop into the images seen in Figure 2-10(c, d), which only show the AEC grains.

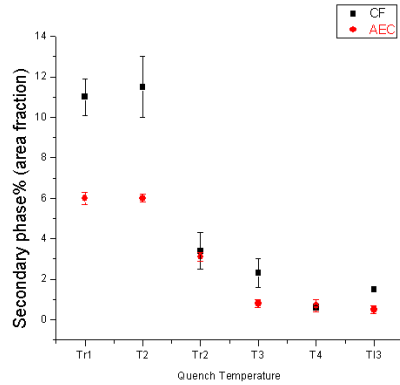


Figure 2-8. AEC area fractions as determined by image analysis using the quenched sample SEM micrographs shown in Figure 7.

After cycle-1, AEC grains are found in almost every filament, but this is not the case after cycle-2, which has fewer but larger AEC grains. After cycle-1, the AEC area fraction is  $4.1 \pm 0.1\%$ , whereas after cycle-2 it is  $3.8 \pm 0.1\%$ . After cycle-1, due the large number of secondary phases and weak interfilamentary coupling, there is no transport current, whereas after cycle-2,  $J_c$  is  $1040 \text{ A/mm}^2$ . Figure 2-10(e) shows a Bi2212 grain that is formed atop an AEC grain during cycle-2.

### ***Heat treatment variations***

Small variations in processing temperatures can lead to substantial changes in the phase distribution and microstructure of Bi2212 filaments [38, 43-45]. Here the effects of a number of heat treatment variables are studied on wire II within each cycle of STP2. Note that for all of the  $J_c$  results shown, each data point is again the average of at least three samples and in no case was the sample-to-sample variance greater than 10%.

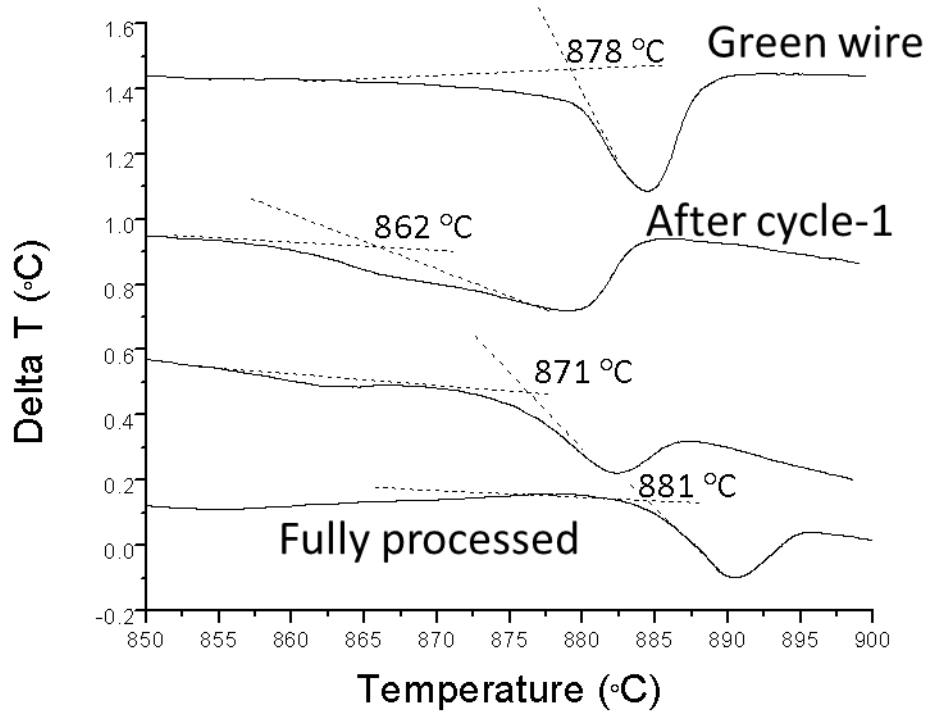


Figure 2-9. Differential thermal analysis results showing the effect of each STP heat treatment cycle on the melting behavior

The effects of varying two parameters within cycle-2 are studied. The effect of cooling from  $T_{r1}$  to  $T_2$  is shown in Figure 2-11, which illustrates cross-sectional SEM images and the corresponding self-field  $J_c$  values. As the cooling rate increases,  $J_c$  decreases linearly. In the cooling stage at the end of cycle-2, from  $T_2$  to  $T_{l2}$ , two cooling rates, 80 and 160 °C/hr are considered. Cross-sectional SEM images together with self-field transport properties are presented in Figure 2-13. As the cooling rate increases from 80 to 160 °C/hr, the critical current density decreases by less than 20%.

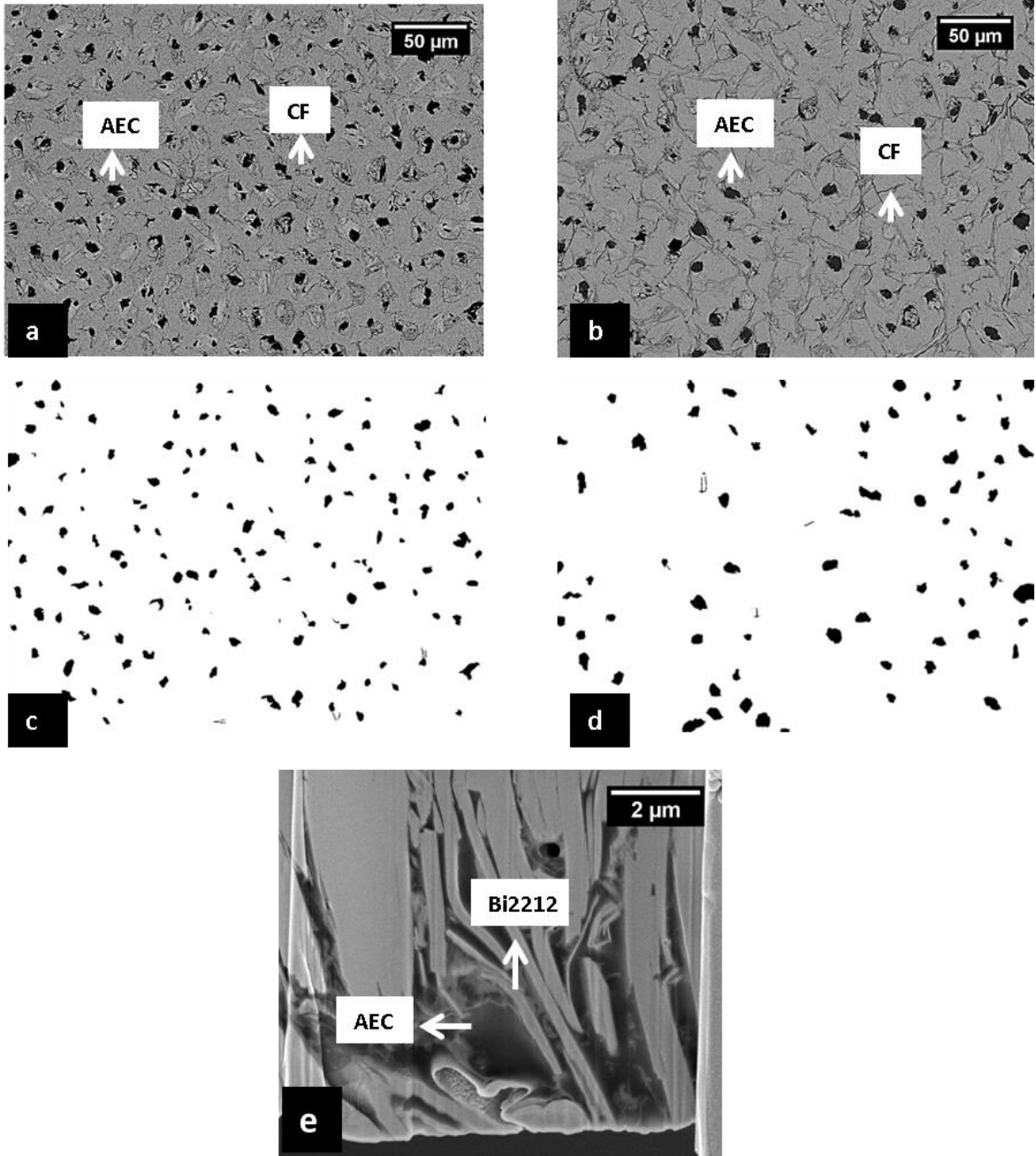


Figure 2-10. Effect of cycle-1 and cycle-2 on the microstructure, a) cross sectional SEM micrograph after cycle-1, b) cross sectional SEM micrograph after cycle-2, c) AEC content after cycle-1, d) AEC content after cycle-2, and e) FIB cross section image showing the formation of Bi2212 on top of a secondary phase.

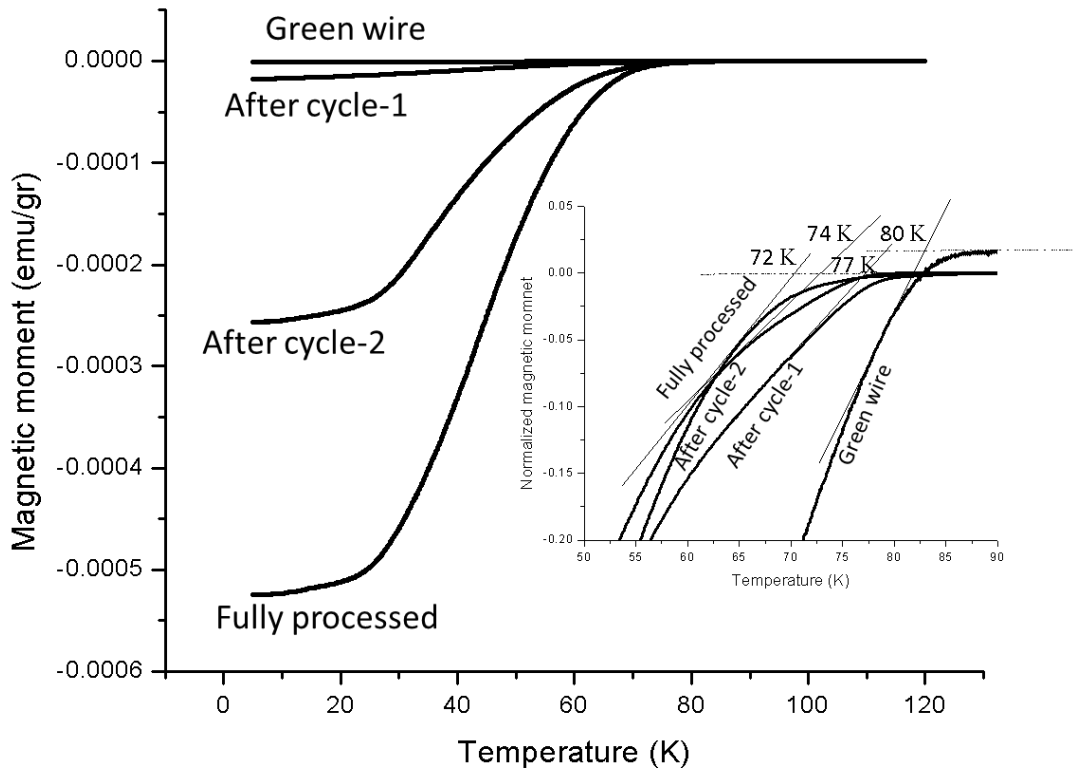


Figure 2-11. Effect of each STP heat treatment cycle on the magnetization behavior.

The effects of varying two parameters within cycle-3 are also studied. Heating rates from  $T_{12}$  to  $T_{r2}$  of 80 and 160 °C/hr are considered; cross-sectional SEM images and self-field  $J_c$  are seen in Figure 2-14. At this stage, slower heating rate results in significantly higher  $J_c$ . The effects of varying  $T_{r2}$  are seen in Figure 2-15 ( $J_c$ ) and Figure 2-16 (SEM images). The effect on  $J_c$  is strong with a clear peak.

Higher magnification images of two filaments from the highest- $J_c$  sample are shown in Figure 2-17. Similar to results from wire I, two types of filament microstructures are seen; one with a considerable amount of Bi2212 and Bi2201, and another with primarily highly textured Bi2212.

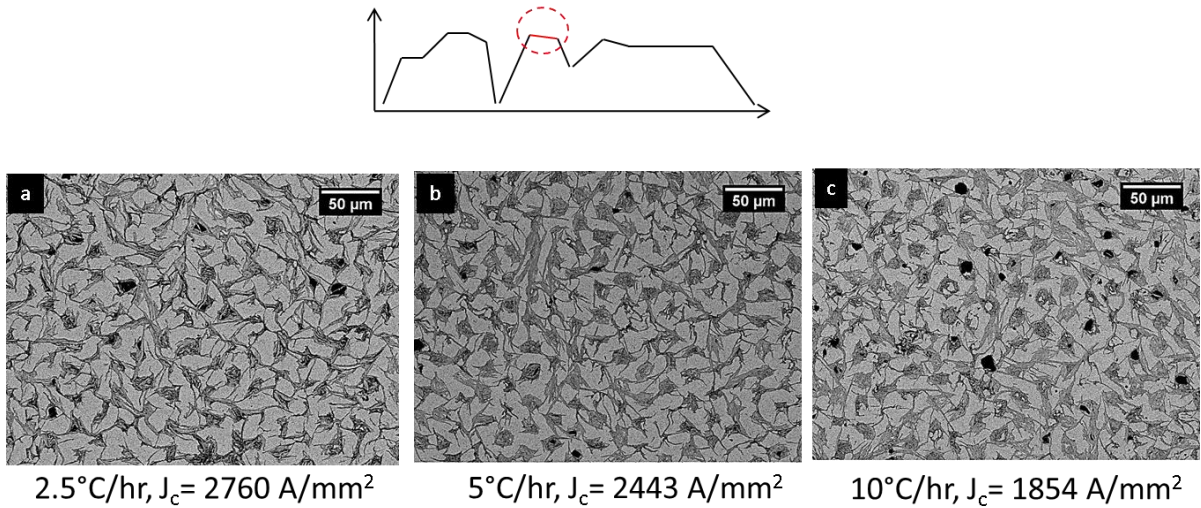


Figure 2-12. Effect of cooling rate from  $T_{r1}$  to  $T_2$  on  $J_c$  and cross sectional SEM micrographs for a) a cooling rate of  $2.5^{\circ}\text{C/hr}$ ,  $J_c = 2760 \text{ A/mm}^2$ , b) a cooling rate of  $5^{\circ}\text{C/hr}$ ,  $J_c = 2443 \text{ A/mm}^2$ , c) cooling rate of  $10^{\circ}\text{C/hr}$ ,  $J_c = 1854 \text{ A/mm}^2$ .

## Discussion

### Comparison of PMP, SMP and STP

It was shown previously that the phase transformation kinetics of Bi2212 during non-isothermal cooling at a constant cooling rate obey the Avrami equation and that Bi2212 formation during PMP and SMP is a site-saturation limited phenomenon. Thus, nucleation occurs early in the transformation and the nucleation sites are depleted as the reaction

proceeds [12, 32]. Due to a lack of nucleation sites and insufficient mass transport to nucleated grains not all reactants are converted to Bi2212. Thus, to maximize Bi2212 formation, more nucleation sites and improved mass transport are needed.

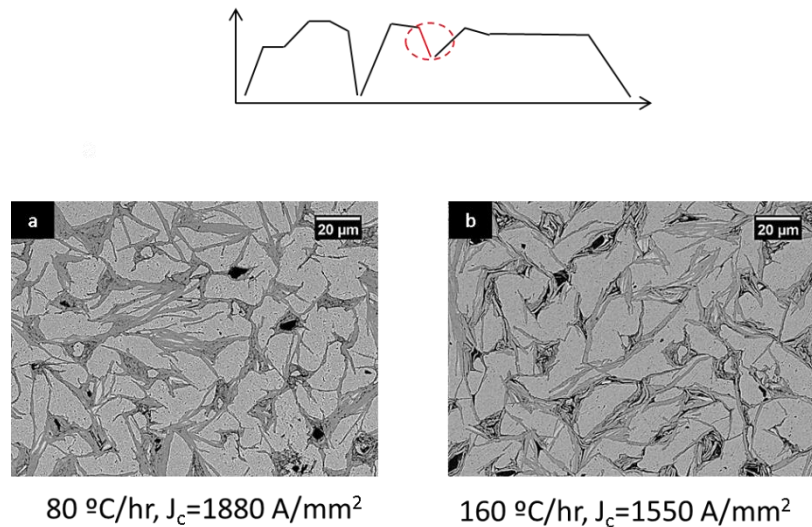


Figure 2-13. Effect of cooling rate from  $T_2$  to  $T_{12}$  on  $J_c$  and cross sectional SEM micrographs for a) cooling rate of 80 °C/hr,  $J_c=1880 \text{ A/mm}^2$  and b) a cooling rate of 160 °C/hr,  $J_c=1550 \text{ A/mm}^2$ .

Any solid interface within filaments is a potential site for heterogeneous nucleation due to the effective elimination of the positive part of the free energy [46]. The liquid phase generated by reheating to sufficiently high  $T_r$  during SMP reacts with the secondary phases present, resulting in additional Bi2212 nucleation during cooling, partially overcoming the site-saturation limitations of PMP [12]. During cooling from  $T_r$ , SMP is also likely site-saturation limited for the same reasons as PMP. Under the right STP conditions, additional heating-cooling cycles create further nucleation sites beyond those created by SMP, facilitating

heterogeneous nucleation of Bi2212 and a greater degree of Bi2212 formation and filament densification. The cross-sectional SEM micrographs in Figure 2-4 show that the PMP wires have large AEC and CF grains not found in SMP or STP wires, indicating a higher level of diffusion in SMP and STP wires and supporting the hypothesis that secondary phases act as Bi2212 nucleation sites in the presence of the additional liquid that forms during the additional heating cycles in SMP and STP.

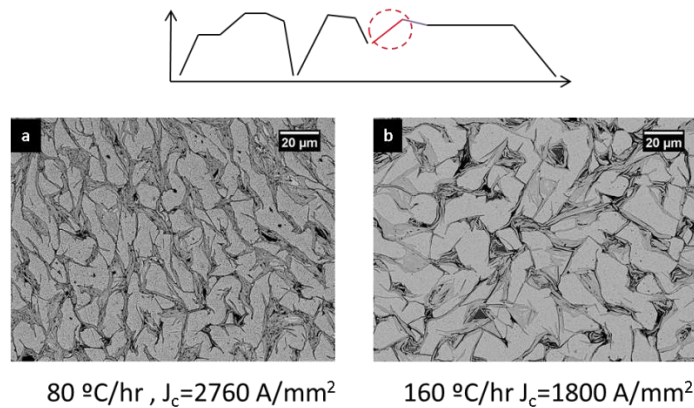


Figure 2-14. Effect of heating rate from  $T_{12}$  to  $T_{r2}$  on  $J_c$  and cross sectional SEM micrographs for a) heating rate of  $80\text{ }^{\circ}\text{C/hr}$ ,  $J_c=2760\text{ A/mm}^2$ , and b) a heating rate of  $60\text{ }^{\circ}\text{C/hr}$ ,  $J_c=1800\text{ A/mm}^2$ .

The increase in  $J_c$  in the SMP wire relative to PMP is consistent with previous studies [12, 30]. The improved  $J_c$  in the STP2 wires relative to the STP1 and SMP wires is a result of the relatively slow Bi2212 growth kinetics. During the third heating cycle that differentiates STP from SMP, a relatively small amount of liquid is formed and diffusion limits the liquid-solid Bi2212 reaction. The slower cooling rate of STP2 provides the additional time required for the growth of dense Bi2212 grains and the consumption of secondary phases; this is similar

to the time-in-the-melt explanation of PMP processing by Shen *et al.*[21]. If this slow cooling rate is not provided, such as with STP1, Bi2212 formation and the consumption of secondary phases will not occur and transport properties will not be improved relative to SMP. This is supported by the SEM images in Figure 2-4 which show larger number of highly layered Bi2212 filaments in STP2 as compared to the micrographs from the other wires.

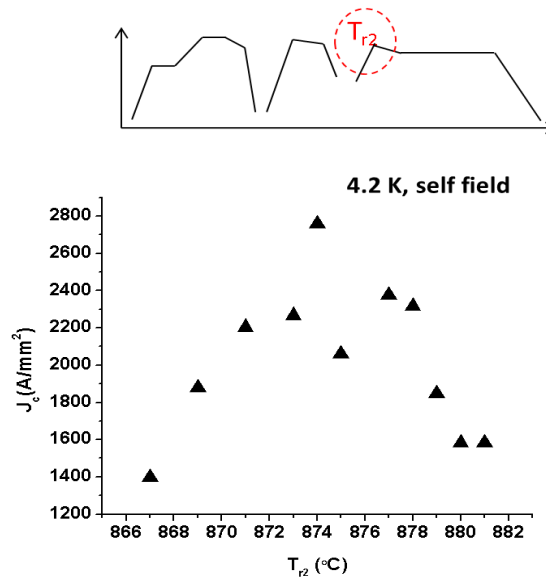


Figure 2-15. Effect of  $T_{r2}$  on the 4.2 K, self-field  $J_c$ .

Figure 2-4 also shows that a variety of dominant microstructures are found within the filaments of wires from each heat treatment approach. In the STP2 wire, two filament structure types are predominant; these are illustrated in Figure 2-5. As seen in Figure 2-5(b), one structure contains a considerable amount of Bi2201 embedded Bi2212 grains. Based on the grain orientations seen, this filament structure is most likely formed from a eutectic

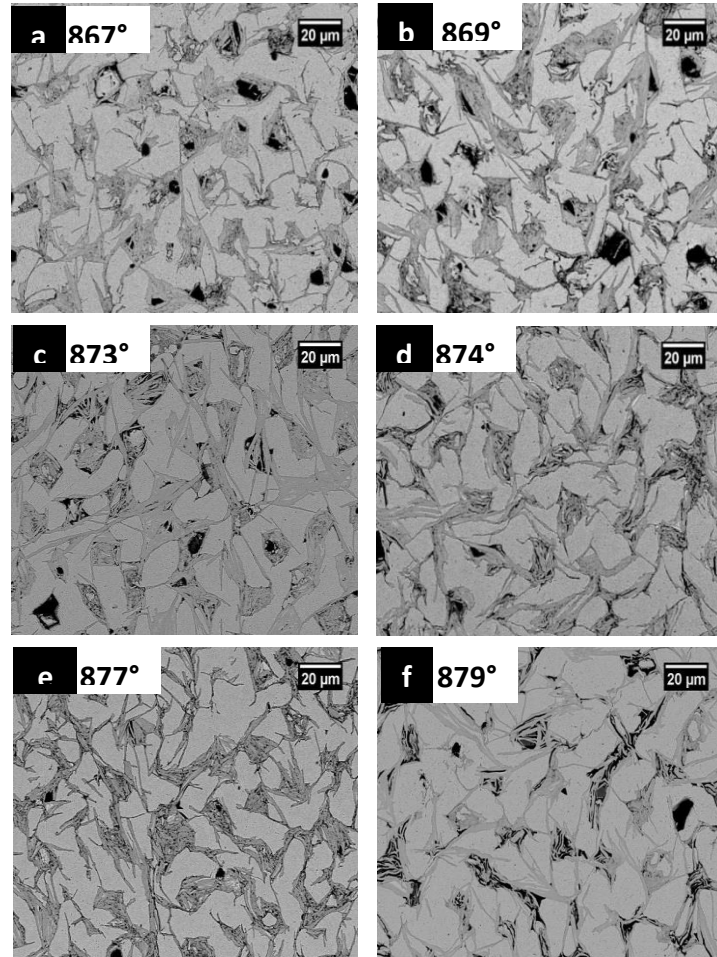


Figure 2-16. Cross sectional SEM micrographs at different  $T_{12s}$ .

solidification, with Bi2212 and Bi2201 grains growing layer-by-layer. Figure 2-5(c) shows that the other structure consists of highly textured Bi2212, with minimal other phases seen. It is unclear if this microstructure nucleated heterogeneously on a secondary phase, such as an AEC grain, and formed a layered structure through step-wise growth while completely consuming the secondary phase, or if Bi2212 nucleated directly at the Ag surface and formed a textured colony of grains naturally. TEM studies are required for more detailed analysis of

the differences between these two structures, their likely origins, and to determine the extent to which Bi2201 intergrowths are present within the highly layered Bi2212 seen in Figure 2-5(c).

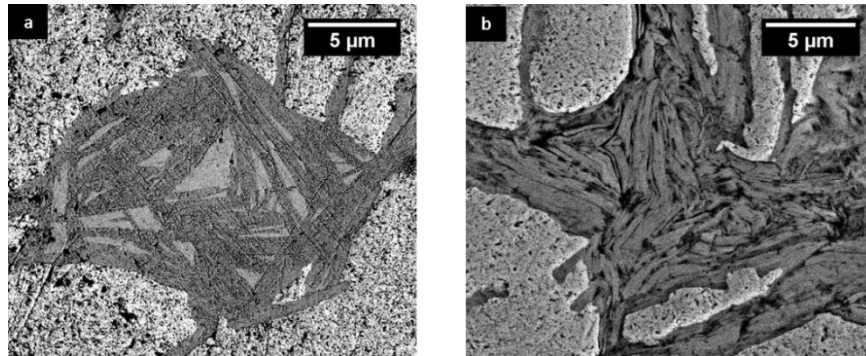


Figure 2-17. Cross sectional SEM micrographs of a) a filament consisting of a noticeable amount of Bi2201 grains, and b) a filament consisting of highly textured Bi2212 grains.

It is also important to note that, although both of these filament structures are seen in wires from all heat treatment approaches, the highly layered structures are more likely to be observed in STP2 wires, consistent with the significantly higher  $J_c$  observed.

### **Microstructural evolution during STP**

Figure 2-7(a) shows the AEC and CF phases that result from the peritectic melt. After the first partial melt, the presence of AEC grains causes the liquid to be deficient in copper and the alkaline earths; this leads to Bi2201 crystallization in competition with Bi2212. In next cycles, these fine Bi2201 grains can also act as nucleation sites, and the presence of (Ca,

Sr)O inhibits  $(\text{Sr}, \text{Ca})_x\text{Cu}_y\text{O}_z$  formation and so the liquid remains rich in copper, facilitating further Bi2212 crystallization [12, 34].

It is expected that selection of the  $T_r$ s is particularly important for STP; this has been previously shown for SMP. The underlying hypothesis is that, to avoid complete partial-melting within the filaments,  $T_r$  should not be as high as  $T_p$ ; otherwise the second and third heating cycles would be similar to the initial partial melt.  $T_r$  should, however, be sufficiently high to cause local melting of high-energy boundaries and low melting point phases within the filaments, facilitating further diffusional nucleation and growth of Bi2212.

The SEM image of the wire quenched from  $T_{r1}$  in Figure 2-7(b) indicates that local melting occurred. Localized melting occurs in grains adjacent to the silver interface or Bi2212 grain boundaries [12]. The melt at this stage leads to recrystallization of Bi2212 and reactivates the rapid growth mechanism. The quantitative analysis of secondary phase formation, AEC and CF, in Figure 2-8 shows that the quantity of AEC grains formed after local melting at  $T_{r1}$  does not change during the slow cooling to  $T_2$ . Instead, some of the larger grains grow and some of the smaller ones are consumed. Analogous to PMP [14, 20, 47], CF grains are small immediately after melting and grow during slow cooling, therefore the area fraction of CF increases from  $T_{r1}$  to  $T_2$ . Furthermore this is a nucleation step and neither Bi2212 growth nor consumption of secondary phases has started. Additional Bi2212 grains also form during cooling from  $T_{r1}$  via a solid-liquid reaction since secondary phases now act as nucleation sites and the presence of liquid facilitates cation diffusion. At this stage, Bi2201 absorbs more Ca and Cu, enhancing Bi2212 formation according to equation (2) and as observed in Figure 2-8(c).



Due to variations in the stoichiometry, oxygen content, silver content and silver contact area, the melting point within a filament varies. Therefore in the second heat treatment cycle, where  $T_{12}$  is 873 °C, some local melting of Bi2212 is expected. When Bi2212 melts locally, small Bi2201 grains act as nucleation sites for Bi2212 formation. Moreover, when liquid is present, Ca and Cu diffusion is faster and more Bi2212 forms [48]. Thus, in this cycle, secondary phase grains do not grow but instead they are consumed as illustrated in Figure 2-8. At  $T_{12}$  CF area fraction drops significantly relative to  $T_2$  indicating that small CF grains are consumed more readily than large, separated AEC grains. It is also clear that, as Bi2212 grains grow, the number and size of AEC and CF grains are reduced; thus Bi2212 growth is not simply solidification from the liquid. In general, to achieve a homogenous microstructure, the grain size of secondary phases must be small, facilitating their conversion to Bi2212. When the secondary phases are large, they confine the elements needed for Bi2212 formation. Furthermore, from a transport perspective, they obstruct the flow of superconducting current.

### **Oxygen content in cycle-1**

During cycle-1, oxygen is released during the Bi2212 peritectic melt and recovered during cooling [16, 38, 49, 50]. It has been shown that oxygen is fully recovered after the first cycle in SMP [12]. Excess oxygen occupies sites within the BiO bilayers, expands the lattice, and decreases  $T_c$  [43, 50-54]. Lower  $T_c$  of the wire after cycle-1, in comparison with that of the green wire, confirms oxygen recovery. After the cycle-1, however, the wire does not carry

superconducting transport current because of insufficient grain connectivity and large secondary phases found almost in every filament.

### **Melting behavior and heat treatment variables during cycle-2**

Secondary phase grains formed in cycle-1 act as nucleation sites in cycle-2; this is seen in Figure 2-10(e) where a Bi2212 grain has formed atop an AEC grain. The crystal structure of an AEC or Bi2201 grain, or even a CF grain, is closer to the crystal structure of Bi2212 than that of Ag. So these defects are preferred nucleation sites for Bi2212 relative to the Ag interfaces. Furthermore, because Bi2212 has a reduced melt temperature at the Ag interface, Bi2212 formation during cooling is more likely to occur at the interface of a phase with a higher melt temperature.

After cycle-1, the onset of melting shifts to a lower temperature; therefore,  $T_{r1}$  is lower than  $T_p$  in order to reduce the amount of liquid formed in cycle-2. The effect of  $T_{r1}$  on the microstructure and transport properties is extensively discussed in [12]. Too much liquid results in excessive oxygen release and formation of large secondary phases. As a result of cycle-2, the melting point increases by 9 °C. Competing factors, including oxygen content, silver content, and phase assemblage, affect the melting temperature changes seen here. The Bi2212 melting point strongly depends on the oxygen content, varying by 40 °C as a function of oxygen partial pressure [12, 30, 49, 51, 52]. According to the inset plot in the Figure 2-12, the oxygen content increases after cycle-2, thus increasing the melting point of Bi2212 filaments. Furthermore, EDS on several Bi2212 filaments indicates the presence of Ag within the filaments, which is a direct result of the increased Ag diffusion and solubility within Bi2212 at elevated temperature. The presence of Ag within the Bi2212 further reduces the

Bi2212 melt temperature. After cycle-2 the reactions proceed further and Bi2212 grains and filaments are connected; a  $J_c$  of 1040 A/mm<sup>2</sup> is obtained.

Varying the cooling rate from  $T_{r1}$  to  $T_2$  (2.5 °C/hr and 5 °C/hr) has a small effect on  $J_c$  [21]. Generally, when crystallization begins, a change in cooling rate is directly related to the amount of under-cooling. At this stage, however, there are many secondary phases available to act as nucleation sites and, therefore, a large under-cooling is not needed for Bi2212 nucleation.

Through further cooling, Bi2212 grains have nucleated and the reaction becomes primarily growth, with the growth rate the primary result of under-cooling. Bi2212 crystals flow in the peritectic liquid until they encounter a surface, e.g. an AEC, CF, or Ag grain, to which they align [25]. More energetically favorable contact between Bi2212 crystals is between their  $c$  planar surfaces because crystallographic parameters of Bi2212 differ greatly along the  $a$ ,  $b$  and  $c$  axes. Therefore, the growth rates in the  $a$  and  $b$  directions are much faster than in the  $c$  direction [28, 35]. A slow cooling rate maximizes the textured growth because slow cooling rates favor growth in the preferred orientation. In the case of a 2.5 °C/hr cooling rate, however, the amount of under cooling is not significant, and the slow growth of Bi2212 results in enhanced transport properties.

Slow oxygen uptake during solidification is another factor that favors a slower cooling rate to form Bi2212 instead of Bi2201. The cooling rate must be slower than the recovery rate of oxygen [55]. When oxygen is available, Bi2212 formation proceeds and less secondary phases remain in the filaments. This is verified by the SEM images in Figure 2-12, where samples are heat treated with different cooling rates. For the faster cooling rate, 10 °C/hr,

large secondary phase grains remain in the filaments. Growth of dense Bi2212 grains and the consumption of secondary phases are consistent with the time-in-the-melt explanation of PMP processing by Shen *et al* [21].

In agreement with the Avrami results, a number of studies [12, 14, 37, 55, 56] indicate that there are two primary stages governing the kinetics of Bi2212 growth during re-solidification. During the initial period, growth is rapid due to mass transfer in the liquid. The second, slower stage is dominated by solid-state mass transfer. At  $T_2$ , the second growth stage is activated. Different cooling rates, 80 and 160 °C/hr, are examined in this stage and the slower cooling rate is shown to facilitate Bi2212 grain growth. Therefore, an 80 °C/hr cooling rate results in a higher ( $J_c=1880 \text{ A/mm}^2$ ) than a 160 °C/hr cooling rate ( $J_c=1550 \text{ A/mm}^2$ ). In the SEMs shown in Figure 2-13, porous filaments are clearly seen in Figure 2-13(b) whereas filaments are relatively dense in Figure 2-13(a).

### **Melting behavior and heat treatment variables in cycle-3**

To achieve high transport  $J_c$ , reactions in cycle-3 must include the consumption of secondary phases formed in previous cycles, Bi2212 phase formation, and improved grain connectivity. To consume secondary phases and form additional Bi2212 through a solid-liquid reaction, heating to a sufficiently high  $T_{r2}$  is required. The heating rate to  $T_{r2}$  is important since there is a drawback with either fast or slow heating rates. As Bi2212 melts,  $O_2$  is released from the Bi2212 filaments and must diffuse through the Ag sheath to avoid the formation of additional porosity [10, 21, 27]. A slower heating rate facilitates  $O_2$  diffusion by providing additional time. Conversely, with a slow heating rate, secondary phase grains formed in previous cycles grow and become more difficult to consume. Therefore, to avoid further growth of these

grains, a faster heating rate is preferred. Two different heating rates to  $T_{r2}$  are studied and it is found that with a faster heating rate, cross-sectional SEM images in Figure 2-14 of Bi2212 filaments do not appear as dense as compared to SEM images of the sample heated with a slower rate. This shows providing additional time for oxygen diffusion is more important for Bi2212 formation than avoiding the additional growth of secondary phases; higher  $J_c$  is thus achieved when the heating rate is slower.

Variations of  $T_{r2}$  significantly change the Bi2212 filament microstructure which is understood through two different approaches. Firstly, the equilibrium phase diagram [45, 57] of the Bi-Sr-Ca-Cu-O system is used to realize why  $T_{r2}$  is very effective in changing of the transport properties and microstructure as seen in Figures 2-15 and Figure 2-16. Based on the phase diagram [45], when calcium is between 0.8 and 1, there is a narrow window for the pure Bi2212 phase. At temperatures slightly above or below that narrow window,  $873 \pm 2^\circ\text{C}$ , the phase assemblage differs. This temperature range corresponds to  $T_{r2}$ . Above this range, Bi2212+Bi<sub>2</sub>Sr<sub>3</sub>Cu<sub>2</sub>O<sub>x</sub> (Bi2302)+SrCaCuO<sub>2</sub>+liquid phases are present. Bi2302 is more stable at higher temperatures in comparison with Bi2201, but transforms more readily to Bi2212 during solidification [58]. Below that range, Bi2212+Sr<sub>3</sub>Bi<sub>2</sub>O<sub>6</sub>+Sr<sub>14</sub>Cu<sub>24</sub>O<sub>41-x</sub> are stable. When the phases are different at elevated temperatures, final microstructure will also be different.

Secondly, at  $T_{r2}$ , in the  $874 \pm 3^\circ\text{C}$  range, a few localized melting events are expected instead of a complete melt inside the filaments. These local melting events occur at positions with higher energy levels such as grain boundaries, or at the Ag/Bi2212 interface. At higher temperatures, increased melt is probable; whereas at lower temperatures less liquid is

available and more solid state reactions are activated. Similar to  $T_{r1}$ , at  $T_{r2}$  increased melt causes increased oxygen release and changes to the phase assemblage [12]. This is consistent with the SEM image of the sample at 879 °C seen in Figure 2-16(f); filaments are porous due to the extended formation of melt within filaments. At lower temperatures, such as 867 °C and 869 °C (Figure 2-16(a, b)) more secondary phases such as AEC grains are found due to the incomplete consumption of secondary phases as a result of the reduction in liquid content due to lower  $T_{r2}$ s. Therefore, a certain amount of melt is optimum for phase purity and better transport properties.

At  $T_{r2}$ , there are many potential nucleation sites, including AEC grains and fine Bi2201 needles. Thus, with the right amount of melt and with high nucleation density, textured, dense Bi2212 grains form where the wire was previously weakly linked, such as grain boundaries. Similar to results from wire I, in the wire II sample with the highest  $J_c$ , two types of filaments are primarily found. One type, seen in Figure 2-17(a), contains a noticeable amount of Bi2201 with a pearlite-like structure. The other type, seen in Figure 2-17(b), consists of highly textured Bi2212 grains. SEM images in Figure 2-16 show that the ratio of one filament type versus the other changes noticeably with  $T_{r2}$ . In the sample with  $T_{r2}=873$  °C, Figure 2-16(c) filaments with Bi2201 grains are seen primarily as a result of a partial liquid-solid reaction. The secondary phase grains formed at this temperature consume the elements required for the formation of Bi2212 versus Bi2201 [45, 57]. In the samples with  $T_{r2}=874$  °C and  $T_{r2}=877$  °C (Figure 2-16 (d, e)), layered Bi2212 filaments are found primarily due to the higher content of Bi2212 phase formation and sufficient melt within the filaments. Consistent with results from wire I, highly layered filament structures are more likely to be

observed in higher  $J_c$  wires. Further understanding of differences between these two filament types requires more detailed microstructural studies.

Lastly, to improve grain connectivity, a long sintering time is essential. The magnetic moment at low temperature comprises both inter and intra-granular contributions and denotes some average size of the current loops [59, 60]. Based on this, Figure 2-11 suggests that grain connectivity, oxygen homogeneity, and Bi2212 grain size are increased after cycle-3. Improved oxygen absorption and homogeneity also improves grain connectivity through the cycles of the heat treatment. Comparing Figure 2-12(a) to Figure 2-10, one finds that after cycle-3 a more uniform microstructure results because large secondary phases, which are observed in almost every filament after cycle-1 and in many of the filaments after cycle-2, are reacted and consumed. Longer exposure to the elevated temperatures enlarges the Bi2212 grain size in fully processed samples in comparison with other samples. These all contribute to the improved magnetization behavior of the sample after cycle-3.

From a technological perspective, the sensitivity of  $J_c$  upon  $T_{r2}$  is a potential limitation of STP for wind-and-react heat treatment of coils. This is similar, however, to the sensitivity of PMP to the peak heat treatment temperature  $T_p$ , yet PMP has been effectively used to heat treat high field insert coils. Using a furnace with strong temperature stability over a sufficient volume, and minimizing the coil winding thickness, are important for both PMP and STP. Furthermore, through better understanding of the processing-properties relationships for Bi2212, it is expected that the sensitivity to key processing temperatures like  $T_p$  and  $T_{r2}$  can be reduced.

## **Summary**

Previous studies of the correlations between processing, microstructure, and transport properties of Bi2212 round wires has led to the development of a new heat treatment approach that includes multiple heating/cooling cycles, saw tooth processing (STP). In STP, the microstructure is engineered to maximize the nucleation and growth of dense, textured Bi2212 grains while minimizing the formation of Bi2201 and non-superconducting phases that are barriers to transport current. This is achieved by inducing heterogeneous nucleation through controlled, localized melting that occurs during heating cycles and slow grain growth during cooling cycles. With the right heat treatment parameters STP wires show a 120% increase of  $J_c$  (4.2 K, 5 T) relative to wires heat treated with a standard PMP heat treatment and a 65% increase relative to SMP wires. STP significantly improves texture, density, and  $J_c$  in multifilamentary Bi2212 wire. Variations in the heat treatment parameters affect the grain morphology and the phase assemblage of Bi2212 filaments. Microstructures of STP Bi2212 wires are correlated with  $J_c$  measurements to ascertain the reasons for the improved performance of these wires.

An optimum value for  $T_{r2}$  is found which results in the highest  $J_c$  ( $2760 \text{ A/mm}^2$ ) among all heat treated wires. In the sample with the highest  $J_c$  mainly two types of filaments (with the greater ratio of the second type) are seen, one containing a large amount of Bi2201 grains and the other containing purely layered Bi2212 grains.

## **Acknowledgments**

This work was supported by the US Department of energy, office of High Energy Physics. The authors would like to thank Dr. Frank Hunte, Dr. Safoura Seifikar, Dr. Sasha Ismael,

and Quang Ye, Liyang Ye, Yun Zhang, Amir Kajbafvala, Raj Kumar, Christian Roach, Davide Cruciani, Ben Callaway, Jonathan Butler and Mary Conrad from North Carolina State University, for many useful discussions and help with the experimental work. Some of the microstructural characterization was performed at the NC State University Analytical Instrumentation Facility.

## REFERENCES

- [1] H. W. Weijers, U. P. Trociewitz, W. D. Markiewicz, J. Jiang, D. Myers, E. E. Hellstrom, A. Xu, J. Jaroszynski, P. Noyes, Y. Viouchkov, and D. C. Larbalestier, "High Field Magnets With HTS Conductors," *IEEE Transactions on Applied Superconductivity* vol. 20, pp. 576-582, 2010.
- [2] S. A. Kahn, M. Alsharo'a, R. P. Johnson, M. Kuchnir, R. C. Gupta, R. B. Palmer, E. Willen, and D. J. Summers, "A high field HTS solenoid for muon cooling," in *Particle Accelerator Conference, 2007. PAC. IEEE, 2007*, pp. 446-448.
- [3] M. Okada, K. Tanaka, T. Wakuda, K. Ohata, J. Sato, T. Kiyoshi, H. Kitaguchi, and H. Wada, "Bi-2212/Ag high-field magnets," *Physica C: Superconductivity*, vol. 335, pp. 61-64, 2000.
- [4] K. Kitazawa, "Physical properties of the high temperature superconductor: the mysterious goddess," *Physica C: Superconductivity*, vol. 341-348, Part 1, pp. 19-24, 2000.
- [5] M. Chen, L. Donzel, M. Lakner, and W. Paul, "High temperature superconductors for power applications," *Journal of the European Ceramic Society*, vol. 24, pp. 1815-1822, 2004.
- [6] J. Schwartz, T. Effio, X. T. Liu, Q. V. Le, A. L. Mbaruku, H. J. Schneider-Muntau, T. M. Shen, H. H. Song, U. P. Trociewitz, X. R. Wang, and H. W. Weijers, "High field superconducting solenoids via high temperature superconductors," *IEEE Transactions on Applied Superconductivity*, vol. 18, pp. 70-81, Jun 2008.
- [7] A. Matsumoto, H. Kitaguchi, H. Kumakura, J. Nishioka, and T. Hasegawa, "Improvement of the microstructure and critical current densities of Bi-2212 round wires with a precisely controlled heat treatment," *Superconductor Science & Technology*, vol. 17, pp. 989-992, Aug 2004.
- [8] J. Schwartz and G. A. Merritt, "Proof-of-principle experiments for react-wind-sinter manufacturing of  $\text{Bi}_2\text{Sr}_2\text{CaCu}_2\text{O}_x$  magnets," *Superconductor Science and Technology*, vol. 20, p. L59, 2007.

- [9] H. Miao, K. R. Marken, M. Meinesz, B. Czabaj, H. Seung, A. Twin, P. Noonan, U. P. Trociewitz, and J. Schwartz, "High Field Insert Coils From Bi-2212/Ag Round Wires," *IEEE Transactions on Applied Superconductivity*, vol. 17, pp. 2262-2265, 2007.
- [10] F. Kametani, T. Shen, J. Jiang, C. Scheuerlein, A. Malagoli, M. D. Michiel, Y. Huang, H. Miao, J. A. Parrell, E. E. Hellstrom, and D. C. Larbalestier, "Bubble formation within filaments of melt-processed Bi2212 wires and its strongly negative effect on the critical current density," *Superconductor Science and Technology*, vol. 24, p. 075009, 2011.
- [11] W. Zhang, E. A. Goodilin, and E. E. Hellstrom, "Composition studies for Ag-sheathed  $\text{Bi}_2\text{Sr}_2\text{CaCu}_2\text{O}_8$  conductors processed in 100%  $\text{O}_2$ ," *Superconductor Science and Technology*, vol. 9, p. 211, 1996.
- [12] X. T. Liu, Q. V. Le, and J. Schwartz, "Influencing factors on the electrical transport properties of split-melt processed  $\text{Bi}_2\text{Sr}_2\text{CaCu}_2\text{O}_x$  round wires," *Superconductor Science and Technology*, vol. 25, p. 075008, 2012.
- [13] X. T. Liu, W. T. Nachtrab, T. Wong, and J. Schwartz, "Effect of Resolidification Conditions on  $\text{Bi}_2\text{Sr}_2\text{CaCu}_2\text{O}_x$  /Ag/AgMg Coil Performance," *IEEE Transactions on Applied Superconductivity*, vol. 19, pp. 2232-2236, 2009.
- [14] W. T. Nachtrab, X. T. Liu, T. Wong, and J. Schwartz, "Effect of Solidification Conditions on Partial Melt Processed Bi2212/Ag Round Wire," *IEEE Transactions on Applied Superconductivity*, vol. 21, pp. 2795-2799, 2011.
- [15] T. Lang, D. Buhl, and L. J. Gauckler, "Influence of the maximum temperature during partial melt-processing of Bi-2212 thick films on microstructure and  $j_c$ ," *Physica C: Superconductivity*, vol. 294, pp. 7-16, 1998.
- [16] T. Kanai, N. Inoue, and T. Kamo, "Effect of oxygen partial pressure and melting temperature on Ag sheathed Bi-2212 wires," *Journal of Materials Research*, vol. 9, pp. 1363-1368, 1994.

- [17] E. E. Hellstrom and W. Zhang, "Important parameters for processing long lengths of Ag-sheathed  $\text{Bi}_2\text{Sr}_2\text{CaCu}_2\text{O}_x$  conductors," *Physica B: Condensed Matter*, vol. 216, pp. 252-254, 1996.
- [18] T. Lang, D. Buhl, and L. J. Gauckler, "Melting of Bi-2212 under controlled oxygen partial pressures with silver," *Physica C: Superconductivity*, vol. 275, pp. 284-292, 1997.
- [19] T. C. Holesinger, P. S. Baldonado, V. Nghia Van, D. Weiming, K. R. Marken, and H. Seungok, "Isothermal melt processing of Bi-2212 tapes," *Ieee Transactions on Applied Superconductivity*, vol. 9, pp. 1800-1803, 1999.
- [20] T. Shen, J. Jiang, F. Kametani, U. P. Trociewitz, D. C. Larbalestier, J. Schwartz, and E. E. Hellstrom, "Filament to filament bridging and its influence on developing high critical current density in multifilamentary  $\text{Bi}_2\text{Sr}_2\text{CaCu}_2\text{O}_x$  round wires," *Superconductor Science and Technology*, vol. 23, p. 025009, 2010.
- [21] T. Shen, J. Jiang, F. Kametani, U. P. Trociewitz, D. C. Larbalestier, and E. E. Hellstrom, "Heat treatment control of Ag- $\text{Bi}_2\text{Sr}_2\text{CaCu}_2\text{O}_x$  multifilamentary round wire: investigation of time in the melt," *Superconductor Science and Technology*, vol. 24, p. 115009, 2011.
- [22] L. Margulies, K. W. Dennis, R. J. Hofer, M. J. Kramer, and R. W. McCallum, "The effect of carbon on the peritectic melting of Bi2212 and Bi2212 + Ag," *Physica C: Superconductivity*, vol. 264, pp. 133-136, 1996.
- [23] W. Zhang, O. V. Pupyshova, Y. Ma, M. Polak, E. E. Hellstrom, and D. C. Larbalestier, "Study of the effect of the Sr/Ca ratio on the microstructure and critical current density of BSCCO 2212 Ag-sheathed tapes," *IEEE Transactions on Applied Superconductivity*, vol. 7, pp. 1544-1547, 1997.
- [24] M. O. Rikel, S. Arsac, E. Soileux, J. Ehrenberg, J. Bock, K. Marken, H. Miao, C.-E. Bruzek, S. Pavard, A. Matsumoto, E. E. Hellstrom, and L. Motowidlo, "Effect of composition on the melting behaviour of Bi2212-Ag conductors," *Journal of Physics: Conference Series*, vol. 43, p. 51, 2006.

- [25] J. Jiang, W. L. Starch, M. Hannion, F. Kametani, U. P. Trociewitz, E. E. Hellstrom, and D. C. Larbalestier, "Doubled critical current density in Bi-2212 round wires by reduction of the residual bubble density," *Superconductor Science and Technology*, vol. 24, p. 082001, 2011.
- [26] C. Scheuerlein, M. D. Michiel, M. Scheel, J. Jiang, F. Kametani, A. Malagoli, E. E. Hellstrom, and D. C. Larbalestier, "Void and phase evolution during the processing of Bi-2212 superconducting wires monitored by combined fast synchrotron microtomography and x-ray diffraction," *Superconductor Science and Technology*, vol. 24, p. 115004, 2011.
- [27] E. E. Hellstrom and W. Zhang, "Formation and prevention of bubbles when melt processing Ag-sheathed  $\text{Bi}_2\text{Sr}_2\text{CaCu}_2\text{O}_x$  (2212) conductors," *Superconductor Science and Technology*, vol. 8, p. 317, 1995.
- [28] J. Jiang, H. Miao, H. Yibing, H. Seung, J. A. Parrell, C. Scheuerlein, M. Di Michiel, A. K. Ghosh, U. P. Trociewitz, E. E. Hellstrom, and D. C. Larbalestier, "Reduction of Gas Bubbles and Improved Critical Current Density in Bi-2212 Round Wire by Swaging," *Ieee Transactions on Applied Superconductivity*, vol. 23, pp. 6400206-6400206, 2013.
- [29] A. Godeke, D. Cheng, D. R. Dietderich, C. D. English, H. Felice, C. R. Hannaford, S. O. Prestemon, G. Sabbi, R. M. Scanlan, Y. Hikichi, J. Nishioka, and T. Hasegawa, "Development of Wind-and-React Bi-2212 Accelerator Magnet Technology," *Ieee Transactions on Applied Superconductivity*, vol. 18, pp. 516-519, 2008.
- [30] X. T. Liu, T. M. Shen, U. P. Trociewitz, and J. Schwartz, "React-Wind-Sinter Processing of High Superconductor Fraction  $\text{Bi}_2\text{Sr}_2\text{CaCu}_2\text{O}_x/\text{AgMg}/\text{AgMg}$  Round Wire," *IEEE Transactions on Applied Superconductivity*, vol. 18, pp. 1179-1183, 2008.
- [31] T. M. Shen, X. T. Liu, U. P. Trociewitz, and J. Schwartz, "Electromechanical behavior of  $\text{Bi}_2\text{Sr}_2\text{CaCu}_2\text{O}_x$  conductor using a split melt process for react-wind-sinter magnet fabrication," *IEEE Transactions on Applied Superconductivity*, vol. 18, pp. 520-524, Jun 2008.
- [32] J. W. Cahn, "Transformation kinetics during continuous cooling," *Acta Metallurgica*, vol. 4, pp. 572-575, 1956.

- [33] P. Prieto, G. Zorn, R. R. Arons, S. Thierfeldt, M. E. Gomez, B. Kabius, W. Sybertz, and K. Urban, "Formation of highly textured  $\text{Bi}_2\text{Sr}_2\text{Ca}_1\text{Cu}_2\text{O}$  superconducting thick films by a rapid melting process," *Solid State Communications*, vol. 69, pp. 235-240, 1989.
- [34] D. P. Matheis, S. T. Mixture, and R. L. Snyder, "Melt-texture processing and high-temperature reactions of Bi-2212 thick films," *Physica C: Superconductivity*, vol. 217, pp. 319-324, 1993.
- [35] E. Cecchetti, P. J. Ferreira, and J. B. V. Sande, "A model for texture development in BSCCO high-  $T_c$  superconductors," *Superconductor Science and Technology*, vol. 13, p. 1270, 2000.
- [36] K. Thangaraj, A. N. Iyer, L. Zhang, and K. Salama, "Heat treatment studies on Bi-2212/Ag tapes fabricated using a powder-in-tube technique," *Superconductor Science and Technology*, vol. 13, p. 1035, 2000.
- [37] T. Koizumi, T. Hasegawa, J. Nishioka, Y. Hikichi, T. Nakatsu, H. Kumakura, H. Kitaguchi, A. Matsumoto, and S. Nagaya, "Bi-2212 phase formation process in multifilamentary Bi-2212/Ag wires and tapes," *Ieee Transactions on Applied Superconductivity*, vol. 15, pp. 2538-2541, 2005.
- [38] B. Heeb, S. Oesch, P. Bohac, and L. J. Gauckler, "Microstructure of melt-processed  $\text{Bi}_2\text{Sr}_2\text{CaCu}_2\text{O}_y$  and reaction mechanisms during post heat treatment," *Journal of Materials Research*, vol. 7, pp. 2948-2955, 1992.
- [39] A. Nagata, S. Yamauchi, S. Kamada, K. Sugawara, C. Takahashi, M. Nagano, Y. Wakiya, and S. Hanada, "Effect of post annealing on superconducting properties and microstructures of Bi(2212)/Ag tapes," *Ieee Transactions on Applied Superconductivity*, vol. 5, pp. 1853-1856, 1995.
- [40] M. O. Rikel and E. E. Hellstrom, "Development of 2201 intergrowths during melt processing Bi2212/Ag conductors," *Physica C: Superconductivity*, vol. 357-360, Part 2, pp. 1081-1090, 2001.

- [41] W. T. Nachtrab, T. Wong, X. T. Liu, and J. Schwartz, "The Effect of Filament Diameter on  $J_c$  in High Filament Count Bi2212/Ag Round Wire," *Ieee Transactions on Applied Superconductivity*, vol. 19, pp. 3061-3066, 2009.
- [42] E. Flahaut, D. Bourgault, and J. L. Soubeyrou, "In situ high temperature neutron study of the Bi2212 phase formation in Ag-sheathed tapes," *Physica B: Condensed Matter*, vol. 350, pp. E339-E341, 2004.
- [43] P. Majewski, "BiSrCaCuO High-Tc Superconductors," *Advanced Materials*, vol. 6, pp. 460-469, 1994.
- [44] M. D. Judith L, P. Wang, Chin, J. C. Bravman, and R. B. Beyers, "Phase equilibria and melt processing of  $\text{Bi}_2\text{Sr}_2\text{Ca}_1\text{Cu}_2\text{O}_{8+x}$  tapes at reduced oxygen partial pressures," *Applied Physics Letters*, vol. 65, pp. 2872-2874, 1994.
- [45] P. Majewski, "Phase diagram studies in the system Bi - Pb - Sr - Ca - Cu - O - Ag," *Superconductor Science and Technology*, vol. 10, p. 453, 1997.
- [46] K. F. Kelton, *Nucleation in condense matter*, 15 ed., 2010.
- [47] D. Rodrigues, Jr., A. R. Bigansolli, E. Cursino, and P. S. Papini, "Phase formation and evolution, texturing and current transport in Ag/Bi2212 PIT monofilamentary tapes," *Ieee Transactions on Applied Superconductivity*, vol. 15, pp. 2546-2549, 2005.
- [48] "ChemInform Abstract: Phase Diagram Studies in the System Bi-Pb-Sr-Ca-Cu-O-Ag," *ChemInform*, vol. 28, p. no, 2010.
- [49] T. Kanai and T. Kamo, "Control of oxygen release from Bi-2212 phase in a partial melt process," *Superconductor Science and Technology*, vol. 6, p. 510, 1993.
- [50] R. Funahashi, I. Matsubara, K. Ueno, and H. Ishikawa, "Mechanism of  $\text{Bi}_2\text{Sr}_2\text{CaCu}_2\text{O}_x$  crystallization and superconducting properties for  $\text{Bi}_2\text{Sr}_2\text{CaCu}_2\text{O}_x/\text{Ag}$  tapes prepared using isothermal partial melting method," *Physica C: Superconductivity*, vol. 311, pp. 107-121, 1999.

- [51] K. Shibutani, T. Hase, Y. Fukumoto, S. Hayashi, E. Inoue, R. Ogawa, and Y. Kawate, "Improvement of  $J_c$  in Bi-2212-Ag composite superconductor by controlling  $PO_2$  on the partial melt process," *IEEE Transactions on Applied Superconductivity*, vol. 5, pp. 1849-1852, 1995.
- [52] Y. Fukumoto, A. R. Moodenbaugh, M. Suenaga, D. A. Fischer, K. Shibutani, T. Hase, and S. Hayashi, "Effect of oxygen partial pressure during postheat treatment on  $Bi_2Sr_2CaCu_2O_y/Ag$  tapes," *Journal of Applied Physics*, vol. 80, pp. 331-335, 1996.
- [53] M. Babaei pour, D. K. Ross, P. A. Gorgiev, B. Khoshnevisan, and A. Yazdani, "Oxygen non-stoichiometry of bismuth-based  $Bi_2Sr_2CaCu_2O_{8+x}$  (Bi-2212) high-temperature superconductor," *Physica C: Superconductivity*, vol. 391, pp. 289-297, 2003.
- [54] H. P. Roeser, F. Hetfleisch, F. M. Huber, M. F. von Schoenermark, M. Stepper, A. Moritz, and A. S. Nikoghosyan, "Correlation between oxygen excess density and critical transition temperature in superconducting Bi-2201, Bi-2212 and Bi-2223," *Acta Astronautica*, vol. 63, pp. 1372-1375, 2008.
- [55] A. Narlikar, *Studies of High-Temperature Superconductors: Advances in Research and Applications: Studies of Josephson Junction Arrays* vol. 39: Nova Science Publishers, 2002.
- [56] A. Y. Ilyushechkin, T. Yamashita, and I. D. R. Mackinnon, "Re-melting of Bi-2212/Ag laminated tapes by partial melting process," *Physica C: Superconductivity*, vol. 377, pp. 362-371, 2002.
- [57] J. Assal, B. Hallstedt, and L. J. Gauckler, "Thermodynamic Optimization of the Silver—Bismuth—Strontium—Calcium—Copper—Oxygen (Ag-Bi-Sr-Ca-Cu-O) System," *Journal of the American Ceramic Society*, vol. 83, pp. 911-914, 2000.
- [58] M. Mamiya, T. Suzuki, M. Hasegawa, and H. Takei, "In situ observation of the thermal stability field of  $Bi_2Sr_3Cu_2O_8$ ," *Physica C-Superconductivity and Its Applications*, vol. 295, pp. 271-276, 1998.

- [59] R. H. Patel, A. Nabialek, and M. Niewczas, "Characterization of superconducting properties of BSCCO powder prepared by attrition milling," *Superconductor Science & Technology*, vol. 18, pp. 317-324, Mar 2005.
- [60] M. Dhalle, M. Cuthbert, M. D. Johnston, J. Everett, R. Flukiger, S. X. Dou, W. Goldacker, T. Beales, and A. D. Caplin, "Experimental assessment of the current-limiting mechanisms in BSCCO/Ag high-temperature superconducting tapes," *Superconductor Science & Technology*, vol. 10, pp. 21-31, Jan 1997.

## Chapter 3

### **Statistical analysis of the relationship between electrical transport and filament microstructure in multifilamentary $\text{Bi}_2\text{Sr}_2\text{CaCu}_2\text{O}_x/\text{Ag}/\text{Ag-Mg}$ round wires**

Evan Benjamin Callaway, Golsa Naderi, Quang Van Le, Justin Schwartz

Department of Materials Science and Engineering, North Carolina State University,

Raleigh, NC 27695-7907, U.S.A.

Supercond. Sci. Technol. **27** (2014) 044020 (8pp)

<http://dx.doi.org/10.1088/0953-2048/27/4/044020>

#### **Abstract**

After processing, multifilamentary  $\text{Bi}_2\text{Sr}_2\text{CaCu}_2\text{O}_x$  (Bi2212) round wires have complex microstructures. In this study, the microstructures are analyzed quantitatively using a new statistical method in which filaments are categorized based on the predominant phases observed by cross-sectional scanning electron microscopy (SEM). A Matlab program is created to analyze the SEM micrographs and categorize over 100 filaments within the image. In total, 26 wires, each heat treated differently so as to vary the critical current density ( $J_c$ ), are studied. In some wires, two distinct cross-sectional areas are analyzed, so a total of 41 cross-sections and 5506 filaments are characterized. Five filament types are defined: filaments containing predominantly Bi2212, filaments containing relatively large  $\text{Bi}_2\text{Sr}_2\text{CuO}_x$  (Bi2201) grains, filaments containing relatively large alkaline earth cuprate (AEC) grains but no significant other non-Bi2212 phases, filaments containing relatively large copper-free

(CF) grains but no other significant non-Bi2212 phases, and filaments containing relatively large AEC and CF grains. The majority of filaments (78% of all filaments classified) are either predominantly Bi2212 or containing-large-Bi2201 grains. Clear correlations between the number of these two types of filaments and the wire  $J_c$  are found;  $J_c$  is directly proportional to the percentage of “predominantly-Bi2212” filaments. Although typically 70-90% of the containing-large-Bi2201 filament cross-sections is actually Bi2212 phase,  $J_c$  is inversely proportional to the percentage of this type of filament. Surprisingly, the correlations between  $J_c$  and the other filament types are weak or non-existent. Furthermore, using high-angle annular dark-field imaging in a scanning transmission electron microscopy, Bi2201 intergrowths are found within Bi2212 grains, and results suggest possible differences in the Bi2201 intergrowth densities within Bi2212 grains extracted from a predominantly Bi2212 filaments than from Bi2201-containing filaments. These results indicate that significant enhancements in Bi2212 wire performance require either avoiding the formation of Bi2201, or ensuring complete conversion of Bi2201 to Bi2212.

## **Introduction**

There is a growing demand for superconducting magnets generating magnetic fields above 20 T, which is beyond the practical limits of commercial NbTi and Nb<sub>3</sub>Sn wires. It is well established that two high temperature superconductor (HTS) technologies, (RE)BaCuO<sub>7-d</sub> (REBCO) coated conductors and Bi<sub>2</sub>Sr<sub>2</sub>CaCu<sub>2</sub>O<sub>x</sub> (Bi2212) round wires, have the potential to meet this demand, as they have demonstrated very high critical current density ( $J_c$ ) at very high magnetic field [1-8]. At present, REBCO conductor development has progressed such that the superconducting REBCO layer itself is well understood and highly engineered; the

challenges for REBCO high field magnets are elsewhere [9]. Future progress in the development of round, multifilamentary Bi2212 wire, however, whose primary advantage over REBCO is that it is round, depends on better understanding and controlling the complex Bi2212 microstructure [3, 9-14].

Bi2212 round wires (RWs) are formed using the powder-in-tube (PIT) method with a Ag innermost sheath and either one or two restacks using with an oxide-dispersion strengthened (ODS) outer sheath. In most Bi2212 RWs the ODS element is Mg, although recent work has shown significant improvements with the use of Al [15, 16]. After deformation to a final diameter, the wires are processed using partial-melt processing (PMP) or variants thereof. In PMP, the wire is heated above the Bi2212 peritectic temperature of  $\sim 890$  °C, leading to the decomposition of the Bi2212 powder into a liquid and a mixture of solid alkaline earth cuprate (AEC) and copper free (CF) phases [17]. As the wire is cooled, Bi2212 resolidifies into a network of grains with end-to-end connectivity. Some AEC and CF phases remain, as well as  $\text{Bi}_2\text{Sr}_2\text{CuO}_x$  (Bi2201) intergrowths and grains; the reverse peritectic reaction is not completed due to phase segregation in the partial-melt and the kinetics of the resolidification reaction [18-21]. The effects of AEC, CF and Bi2201 are discussed in [22, 23].

One heat-treatment variant, split-melt processing (SMP), divides the PMP into two segments. Like PMP, in SMP the wire is heated above the peritectic melt temperature, but it is then cooled to room temperature and subsequently reheated to complete the remainder of the PMP sequence. The SMP heat treatment increases  $J_c$  by improving the transformation kinetics and increasing the content of dense Bi2212 grains [9, 11, 22, 24-26]. A previous study has shown that Bi2212 nucleation is site saturation limited and the SMP heat-cool-heat cycle provides

additional nucleation sites that enhance Bi2212 formation [19]. Another variant of PMP, saw-tooth processing (STP), builds on the SMP concept and consists of multiple heat-cool-heat cycles. The additional cycles provide new heterogeneous nucleation sites in the regions of Bi2201, AEC and CF phases, as well as increasing the rate of diffusion through localized melting, further enhancing Bi2212 formation [26].

This study focuses on the relationship between the microstructure, and in particular the phase assemblages of filaments, and the  $J_c$  of Bi2212 round wire. A Matlab program is developed that analyzes each filament from cross-sectional SEM images of a large number of wires and the results are correlated to the transport behavior.

### **Experimental Procedure**

Two different multifilamentary Bi2212 round wires are produced by Supercon, Inc. using the PIT method. Both wires are single restacks with an outer diameter of 0.787 mm; one has 357 filaments and a 31.4% fill factor, while the other has 928 filaments and a 54.7% fill factor. Cross-sectional images of the green wires are seen in [26]. The chemical composition of the starting powder, obtained from Nexans Superconductor, is  $\text{Bi}_{2.19}\text{Sr}_{1.95}\text{Ca}_{0.88}\text{Cu}_{1.98}\text{O}_x$ ; the same powder is used for each wire. The inner sheath is pure Ag and the outer sheath is Ag–0.2wt% Mg. Short samples, 40 mm in length, are cut from each wire and heat treated using PMP, SMP and STP, with the heat treatment details varied to obtain varying electrical performance. Details of the heat treatments and how they affect  $J_c$  for these wires has been published previously [26]; here the focus is on a quantitative correlation of the relationships between the microstructure and  $J_c$ . In this study, 26 wires are selected for image analysis. Of the 26, 2 were heat treated by PMP, 1 by SMP and 23 by STP. Note that three short samples

from the same batch of wire were heat treated together for each heat treatment. The self-field critical current ( $I_c$ ) was measured using the four-probe method in liquid helium (4.2 K). A  $10^{-4}$  V m<sup>-1</sup> electric field criterion, with 20 mm voltage tap spacing, was used to identify  $I_c$ . All samples were measured and the results from the three identical samples were averaged.  $I_c$  values from the three samples varied by less than 10% in all cases. The average  $I_c$  was divided by wire cross-sectional area and the fill factor to determine  $J_c$ .

A small section of each wire is cut and mounted using Durocit cold mounting liquid and graphite as conductive filler. The samples are polished with 180 to 1200 grit SiC paper and 1.0  $\mu$ m and 0.3  $\mu$ m alumina suspensions. A Hitachi S3200 SEM and a Hitachi TM3000 SEM in backscatter mode are used to image the wire cross-sections. For consistency, all micrographs are captured at a magnification of 500X; there are approximately 125 filaments per micrographs. When possible, multiple micrographs of each wire are taken to increase the amount of data available (without imaging the same filament more than once).

A Matlab program is written to quickly and accurately analyze each SEM micrograph. The program requires two input images, the grayscale SEM micrograph and a black and white (binary) image in which the filaments are black and the Ag is white. The binary images are created through the “Threshold” function in ImageJ, followed by the “Smooth” function, and finally filling in any small holes by hand. The SEM micrographs are taken at various times with two different SEMs, leading to varying levels of contrast and brightness. Using ImageJ, the “Brightness/Contrast” is adjusted to normalize all images to the same brightness level. To improve the accuracy of the results, the Ag portion of the image is adjusted to an average color of 180 on the 8-bit grayscale of 0 to 255 and the filaments are between 120 and 130.

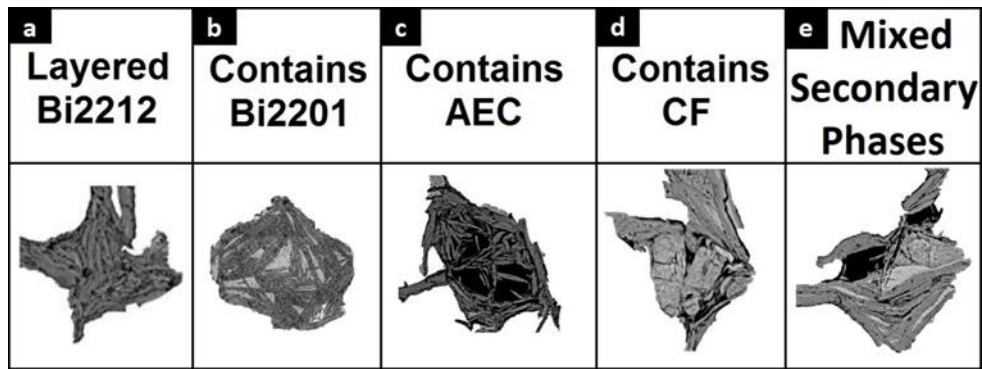


Figure 3-1. SEM images of the five types of filaments.

The Matlab program consists of two main sections. First, using the binary image, the filament bridges are eliminated, leaving only the main filaments as black and the remainder of the cross-section as white. This second binary image gives the coordinates of every pixel in each of the main filaments in the grayscale image. The second section of the program analyzes each filament individually. The wire cross-sections contain regions or individual grains of AEC, CF, Bi2201 and high-purity layered regions of Bi2212. All filaments contain Bi2212 and one of these other three phases; a small percentage contain Bi2212 and both AEC and CF grains. A significant amount of all four phases is not seen in any individual filament. Therefore, the Matlab code classifies each filament as being one of five filament types: (1) filaments containing predominantly Bi2212, “Bi2212”, (2) filaments containing relatively large  $\text{Bi}_2\text{Sr}_2\text{CuO}_x$  grains, “Bi2201”, (3) filaments containing relatively large alkaline earth cuprate grains but no significant other non-Bi2212 phases, “AEC”, (4) filaments containing relatively large copper-free grains but no other significant non-Bi2212 phases, “CF”, and filaments containing relatively large AEC and CF grains, “mixed secondary phases”. The Bi2212 filaments, shown in Figure 3-1a, are dense and contain only

small amounts of non-Bi2212 grains (as observable at 500x in the SEM). Examples of the other four filament types are also seen in Figure 3-1. In Figure 3-1b, the small bright regions in the filament are Bi2201 grains whereas the dark areas are Bi2212. Filaments seen in Figure 3-1c and d have large areas of AEC or CF phase, while the remainder of the filament is Bi2212. AECs are the solid black regions and CFs are the large bright regions. It is important to note that, although the filaments are referred to as “Bi2201”, “AEC”, “CF” and “AEC+CF” for simplicity, these classifications refer to the predominant non-Bi2212 phase present; Bi2212 is the majority phase in every filament studied.

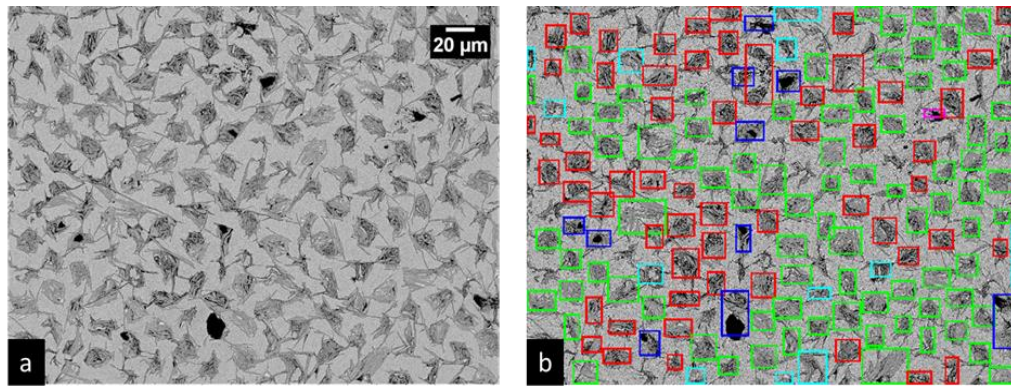


Figure 3-2. (a) A typical SEM micrograph used as input for the Matlab program and (b) the resulting color-coordinated output image from the Matlab program. Red boxes are Bi2212 filaments, green boxes Bi2201 filaments, dark blue boxes are AEC filaments, turquoise boxes are CF filaments and purple boxes are mixed secondary phases filaments.

The identification and quantification of secondary phase(s) present is determined by measuring the largest connected area of pixels that are very dark (less than 5) or very bright (greater than 160). A significant challenge in this process is distinguishing Bi2201 grains

from CF grains, because their brightness is similar, and distinguishing AEC grains from voids. The Bi2201 and CF are differentiated primarily by their shape. CF grains tend to be significantly larger than Bi2201 grains, on the order of 5-15  $\mu\text{m}$ , and rectangularly shaped. The Bi2201 tend to be triangular or highly elongated (plate-like). Similarly, AEC grains tend to be larger, on the order of 4-15  $\mu\text{m}$ , with sharp corners, whereas voids are typically irregular, especially when found between grains. So, although it is relatively straightforward to differentiate these phases visually, it is more challenging to create a Matlab program to automate the process. Based on the analysis of a number of filaments during the development of the image analysis procedure, it was found that to be classified as AEC, the largest individual dark spot in the cross section must be greater in size than 4% of the filament area; AEC grains observed in 500X SEM micrographs are always at least this large. Through a similar non-automated process, the corresponding threshold value for a bright spot to be a CF grain is 6.5% of the filament area. If both threshold values are met within one filament, then the filament is labeled as “mixed secondary phases”. If neither AEC nor CF meets their respective threshold in a filament, then the Matlab program begins searching for Bi2201 grains. Filaments containing significant Bi2201 grains are characterized by having many small bright regions (Bi2201 grains) within the dark filament. If the combined area of the bright regions in one filament is greater than 1.5% of the filament cross-sectional area, and no one spot is greater than 6.5%, then the filament is labeled as “Bi2201”. Finally, if a filament does not meet the threshold for AEC, CF or Bi2201 grains, it is classified as “Bi2212”. All of the Bi2212 filaments show the dense, layered Bi2212 grain structures seen in Figure 3-1.

Forty-one SEM cross-sectional images from 26 different wires are analyzed through the Matlab program to determine the number of each type of filament. In total, 5506 filaments are analyzed in this study. For wires with multiple images, the results are averaged and the range is found. The program output states the number of filaments of each type and produces an image that has color coordinated boxes surrounding each filament corresponding to the filament type. The output image is checked manually to verify the accuracy of the program. The percentage of each filament type is plotted with  $J_c$  values using OriginLab to identify relationships between  $J_c$  and the microstructure.

Electron transparent samples are made from “2212” and “2201” filaments via a lift-out technique using a FEI Quanta 3D focused ion beam (FIB). The samples are then imaged using a FEI Titan 80-300 probe aberration corrected, monochromated scanning transmission electron microscope (STEM).

## **Results**

Figure 3-2 illustrates a typical SEM micrograph used as input to the Matlab program and the corresponding color-coded output image. In Figure 3-2b, the red boxes are “Bi2212” filaments and the green boxes are the “Bi2201” filaments; these are the most commonly seen filaments types, accounting for 70% – 90% of the filaments in any image. Note that the CF, AEC and AEC+CF filaments show no detectable Bi2201 phase. In total, 5506 filaments were characterized, including 2452 Bi2212 (45%), 1863 Bi2201 (34%), 619 AEC (11%), 463 CF (8%) and 109 mixed secondary phases (2%).

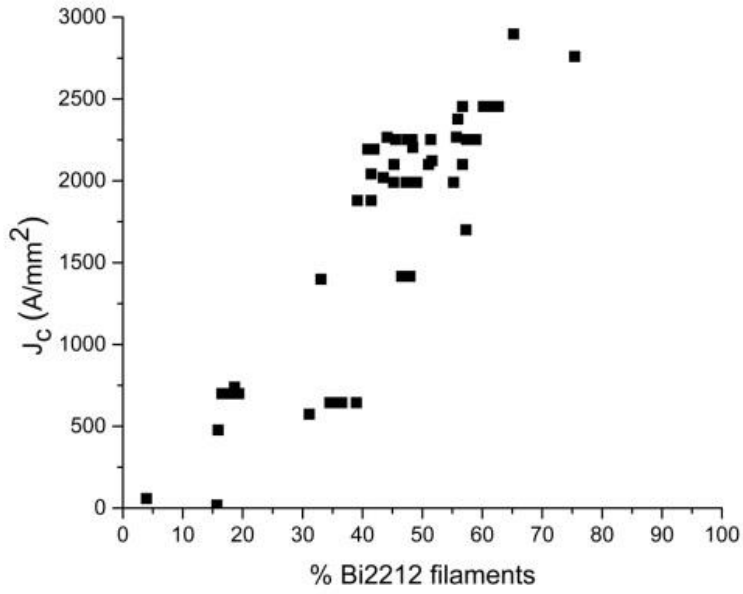


Figure 3-3.  $J_c$  versus the percentage of Bi2212 filaments.

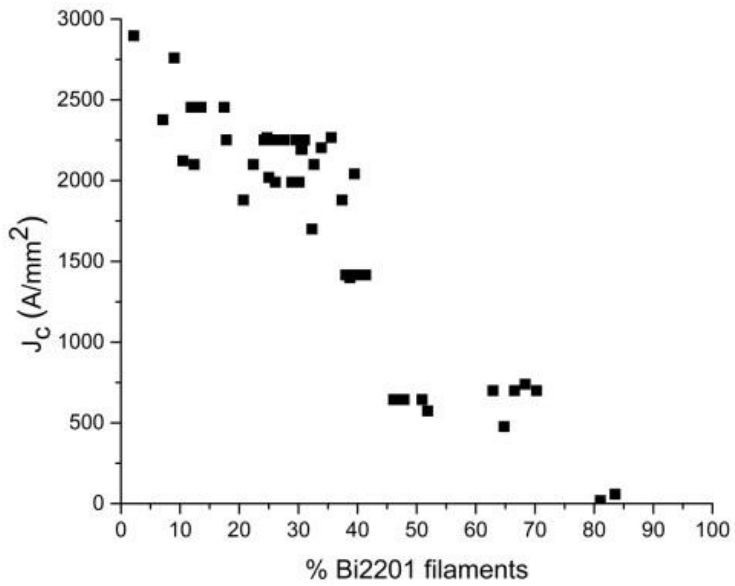


Figure 3-4.  $J_c$  versus the percentage of Bi2201 filaments.

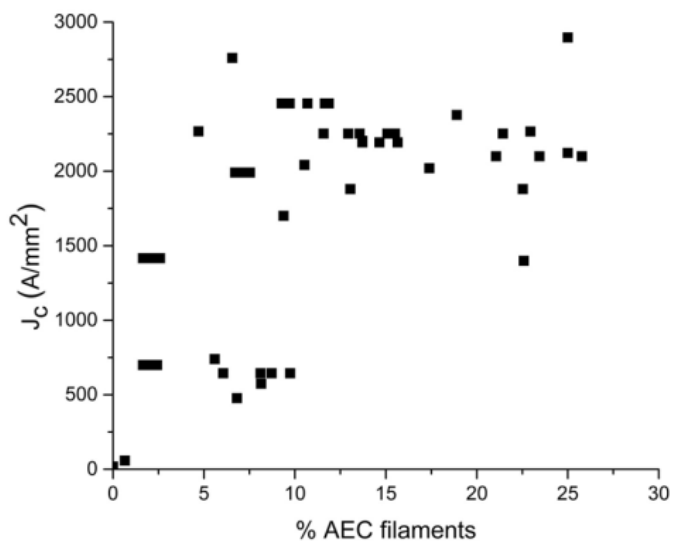


Figure 3-5. Area fractions of Bi2201 phase in “Bi2201” filaments and of Bi2212 in “Bi2212” filaments.

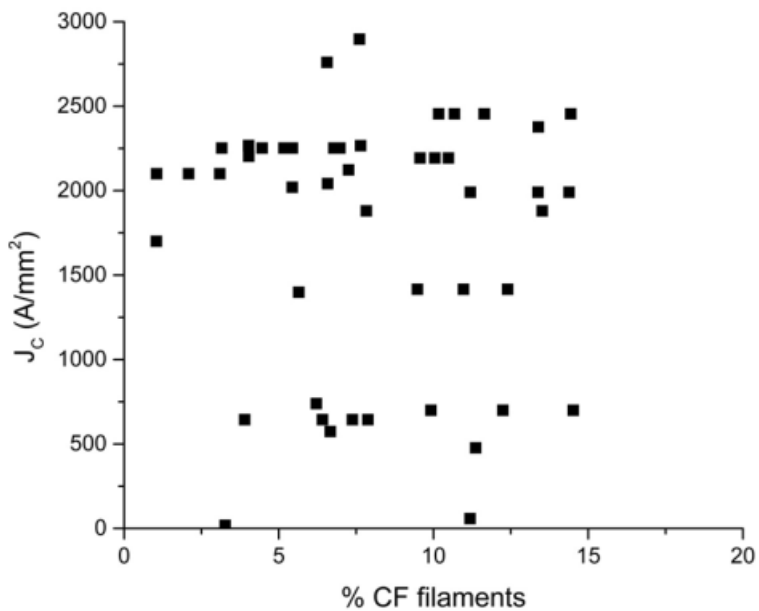


Figure 3-6.  $J_c$  versus the percentage of CF filaments.

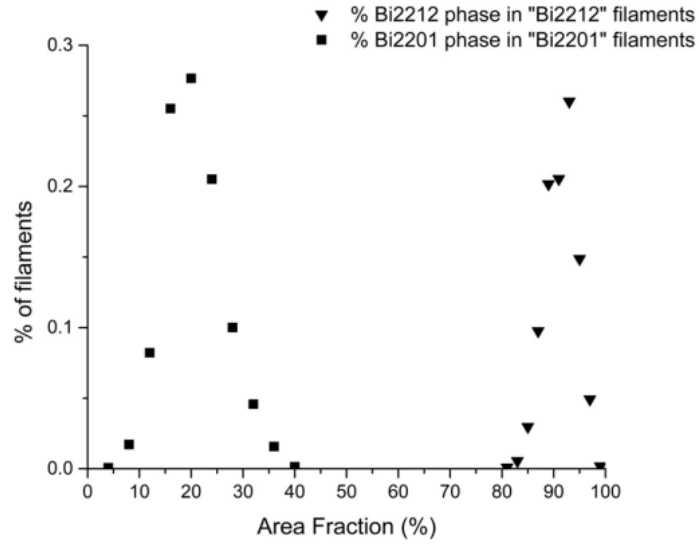


Figure 3-7. The area fraction of the Bi2212 filaments that is Bi2212 phase, and the area fraction of Bi2201 filaments that is Bi2201 phase.

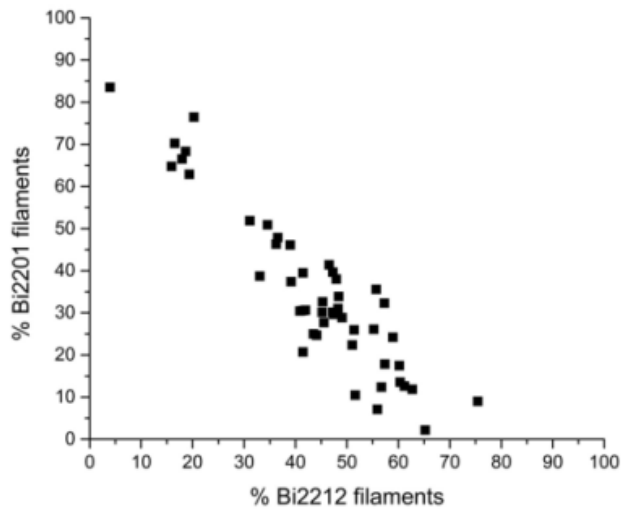


Figure 3-8. Percentage of Bi2201 filaments versus percentage of Bi2212 filaments.

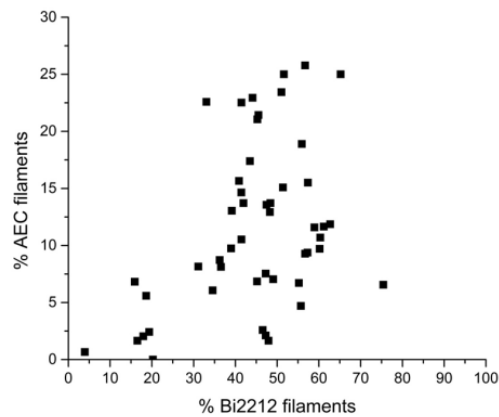


Figure 3-9. Percentage of AEC filaments versus percentage of Bi2212 filaments.

By codifying the complex Bi2212 wire microstructure into the five filament categories, correlations between the phases present and  $J_c$  are identified. The total number of each of the five types of filaments is calculated for every image and the percentage of each is plotted as the independent variable with  $J_c$  as the dependent variable; results are seen in Figures 3-6. Figure 3-3 shows that  $J_c$  increases linearly with percentage of Bi2212 filaments with a slope of  $44 \text{ A/mm}^2/\%$  (calculated over the range of 5% Bi2212 to 80% Bi2212). Figure 3-4 shows  $J_c$  decreases linearly with the percentage of Bi2201 filaments with a slope of  $-36 \text{ A/mm}^2/\%$  (calculated over the range of less than 5% Bi2201 to over 80% Bi2201).

Figure 3-5 shows the relationship between  $J_c$  and the percentage of AEC filaments, and Figure 3-6 shows the corresponding relationship with the percentage of CF filaments. Surprisingly, for small values of %AEC (0 to  $\sim 10\%$ ),  $J_c$  increases with %AEC. Above 10%  $J_c$  is independent of %AEC, with only one wire having above 25% AEC filaments. The

relationship between  $J_c$  and %CF appears random, with the %CF ranging from about 1% to 15%. Thus, although CF phases have previously been shown to negatively impact  $J_c$  [27], it is not a dominant factor in the context of the heat treatment variations in this study. The relatively low content of CF is consistent with other studies [28, 29]. Lastly, filaments containing mixed secondary phases are rarely found; only 2% of filaments analyzed are classified as such. Thus, this filament type is not considered further.

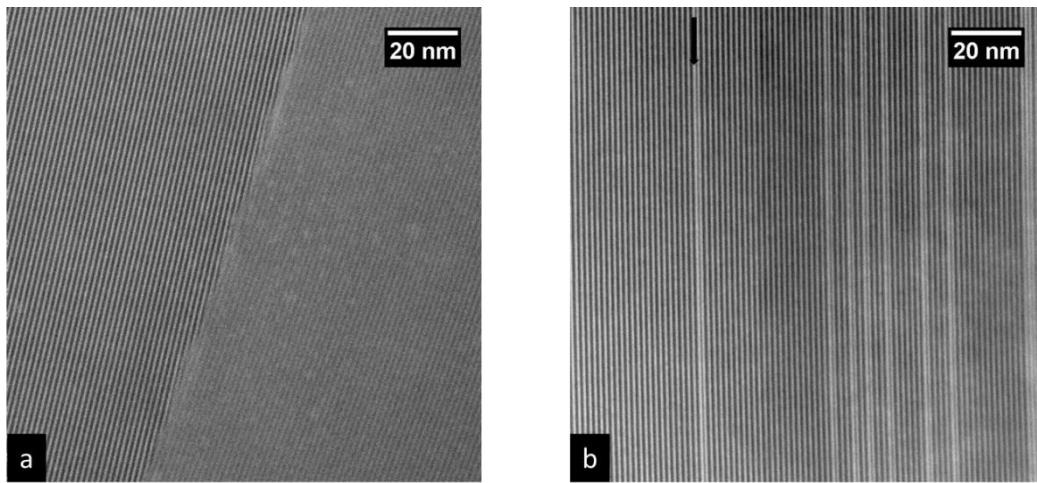


Figure 3-10. HAADF STEM images of (a) two Bi2212 grains extracted from a Bi2212 filament and (b) a Bi2212 grain extracted from a Bi2201 filament. The black arrow identifies a Bi2201 intergrowth.

A more detailed analysis of the Bi2201 filament and Bi2212 filament cross-sectional images quantifies the phase assemblage within each of these filament types. Figure 3-7 plots the area fraction of the Bi2212 filaments that is Bi2212 phase, and similarly the area fraction of Bi2201 filaments that is Bi2201 phase. The results are plotted as distribution functions, with

the abscissa indicating the area fraction of the respective phase and the ordinate indicating the percentage of filaments with that area fraction. For each phase, the filaments are grouped such all filaments are classified within ten increments along the abscissa. Thus, the Bi2212 filaments are grouped in increments of 2% and the Bi2201 filaments are grouped in increments of 4%. The results show that the filaments codified as “Bi2201” contain only 5%-40% Bi2201 phase, with the remaining 60%-95% of the cross-sectional area being Bi2212 phase. The filaments codified as “Bi2212” contain 80%-100% Bi2212 phase, with the remaining 0-20% being primarily porosity and Bi2201. Both the Bi2212 and Bi2201 distributions are highly peaked, with over 75% of the filaments within one increment from the mean value.

Figure 3-10 shows Z-contrast high angle annular dark field (HAADF)-STEM images from two samples. In Figure 3-10(a), two Bi2212 grains are imaged from a Bi2212 filament. In Figure 3-10(b), a Bi2212 grain extracted from a Bi2201 filament shows a high density of Bi2201 intergrowths.

## **Discussion**

Phase transformations accompanied with phase separation during the heat treatment of Bi2212 wires result in diverse filament microstructures with different phase assemblages and grain morphologies. Strong correlations between filament microstructure and  $J_c$  are observed. As expected,  $J_c$  increases with the percentage of Bi2212 filaments. In fact, the two predominant filaments types, Bi2212 and Bi2201, have strong correlations with  $J_c$ , and as seen in Figure 3-8, with each other as well. With a slope of -1.2, Figure 3-8 shows that there is a direct competition between the formation of Bi2201 and Bi2212 filaments, which is a

key factor in determining wire  $J_c$ . It is important to note that the Bi2201 filaments correlate negatively with  $J_c$  even though most of these filaments contain 70%-90% Bi2212 phase. The presence of Bi2201 phase has a strong negative impact on  $J_c$ .

The surprising relationship between  $J_c$  and %AEC grains is understood through Figure 3-9, which shows a positive trend in the correlation between the %AEC filaments and the %Bi2212 filaments. The results in Figure 3-9 imply that the conditions that avoid the formation of Bi2201 result in the formation of both Bi2212 and AEC filaments.

Consistent with the results presented here, x-ray diffraction results in [17] show that, consistent with the phase diagram, Bi2201 is the major impurity in Bi2212 wires. Bi2201 is in equilibrium with Bi2212 and thus it remains present after full heat treatment [30]. When large Bi2201 grains form, even if they occupy a relatively small fraction of the cross-sectional area of a filament, they are detrimental to the transport properties because they reduce Bi2212 grain connectivity and confine the elements needed for Bi2212 growth.

Previous studies have shown that Bi2201 forms as grains and intergrowths [30-33]. The STEM images in Figure 3-10 show a significant presence of Bi2201 intergrowths in a Bi2212 grain extracted from a Bi2201 filament and the absence of intergrowths in a Bi2212 grain extracted from a Bi2212 filament. This can be understood from a thermodynamic point of view; in the regions closer to Bi2201 grains there is a deficiency of the elements needed for Bi2212 formation and therefore Bi2212 grains lower their energy by producing Bi2201 intergrowths [31, 32, 34]. A more thorough STEM study is needed to confirm this observation and to better understand how Bi2201 intergrowths impact  $J_c$  in Bi2212 RWs.

It is important to recognize that, although porosity plays an important role limiting  $J_c$  in Bi2212 wires [17, 35-37], this analysis does not evaluate the porosity in the wire cross-sections; the analysis approach used here would not give accurate results for porosity. Porosity and phase assemblage are two independent factors influencing  $J_c$ ; there is no evidence that the high- $J_c$  wires obtained by reducing the porosity do not continue to have a similar phase assemblage to more porous wires; variations in porosity from wire to wire in this study are the likely cause of scatter in the data shown in Figures 3-3 and 3-4.

Similar to Bi2223 wires, the secondary phases in Bi2212 wires are discontinuous grains that do not run along the entire wire length [27]. These grains block the superconducting transport current, but in the CF and AEC filaments there is a large amount of Bi2212 present so the current bypasses these grains either within the filament or through interfilamentary bridges [27, 38]. As a result, each individual filament has a phase assemblage that varies along its length and filaments that are codified as, for example, “Bi2201” in one cross-section, may be “AEC” or “CF” or “Bi2212” elsewhere along the wire length. From the perspective of image analysis, this variance is addressed by using a statistical analysis of a large number of wire cross-sections. From the perspective of understanding electrical transport in Bi2212 wires, these results further support the argument that interfilamentary bridges are essential for high  $J_c$  [38], and Bi2212 wires that are multifilamentary with respect to magnetic behavior will not be obtainable until there are significant improvements in Bi2212 phase purity.

The statistical results found here imply that research to increase the  $J_c$  of Bi2212 wires should focus on eliminating the presence of Bi2201 grains, either by preventing Bi2201 formation or completing its conversion to Bi2212. In a previous study, it was shown that by varying the

heat treatment parameters, for example through STP, the nucleation growth of Bi2212 filaments is encouraged in lieu of Bi2201. Further heat treatment optimization, variations in the starting stoichiometry, or other wire processing studies, should focus on the competition between Bi2201 and Bi2212.

### **Conclusion**

After heat treatment, both low- $J_c$  and high- $J_c$  multifilamentary Bi2212 wires have complex, multiphasic microstructures. Here, a new statistical method is introduced to categorize individual filaments in the cross-section based on the predominant non-Bi2212 phase(s) present in order to correlate the microstructure to the transport  $J_c$ . Image analysis shows that there are strong relationships between the two types of filaments and the wire  $J_c$ ;  $J_c$  is directly proportional to the percentage of “predominantly-Bi2212” filaments and inversely proportional to the percentage of “containing-large-Bi2201” filaments, even though those filaments contain 70-85% Bi2212 phase by area-fraction. The correlations between  $J_c$  and the other filament types are weak or non-existent. These results indicate the significant enhancements in Bi2212 wire performance requires either avoiding the formation of Bi2201, or ensuring complete conversion of Bi2201 to Bi2212.

### **Acknowledgements**

This work was supported by the US Department of Energy, Office of Science, Office of High Energy Physics, through the SBIR/STTR program. Microstructural characterization was performed at the NC State University Analytical Instrumentation Facility, which is supported by the State of North Carolina and the National Science Foundation. The authors thanks Dr.

Yi Liu of the NC State University Analytical Instrumentation Facility for his assistance with TEM sample preparation and microscopy.

## REFERENCES

- [1] H. W. Weijers, U. P. Trociewitz, W. D. Markiewicz, J. Jiang, D. Myers, E. E. Hellstrom, A. Xu, J. Jaroszynski, P. Noyes, Y. Viouchkov, and D. C. Larbalestier, "High Field Magnets With HTS Conductors," *IEEE Transactions on Applied Superconductivity* vol. 20, pp. 576-582, 2010.
- [2] S. A. Kahn, M. Alsharo'a, R. P. Johnson, M. Kuchnir, R. C. Gupta, R. B. Palmer, E. Willen, and D. J. Summers, "A high field HTS solenoid for muon cooling," in *Particle Accelerator Conference, 2007. PAC. IEEE, 2007*, pp. 446-448.
- [3] M. Okada, K. Tanaka, T. Wakuda, K. Ohata, J. Sato, T. Kiyoshi, H. Kitaguchi, and H. Wada, "Bi-2212/Ag high-field magnets," *Physica C: Superconductivity*, vol. 335, pp. 61-64, 2000.
- [4] H. W. Weijers, B. ten Haken, H. H. J. ten Kate, and J. Schwartz, "Field dependence of the critical current and its relation to the anisotropy of BSCCO conductors and coils," *IEEE Transactions on Applied Superconductivity*, vol. 15, pp. 2558-2561, Jun 2005.
- [5] H. W. Weijers, B. ten Haken, H. H. J. ten Kate, and J. Schwartz, "Critical currents in Bi-Sr-Ca-Cu-O superconductors up to 33 T at 4.2 K," *Ieee Transactions on Applied Superconductivity*, vol. 11, pp. 3956-3959, Mar 2001.
- [6] H. W. Weijers, U. P. Trociewitz, K. Marken, M. Meinesz, H. Miao, and J. Schwartz, "The generation of 25.05 T using a 5.11 T Bi<sub>2</sub>Sr<sub>2</sub>CaCu<sub>2</sub>O<sub>x</sub> superconducting insert magnet," *Superconductor Science & Technology*, vol. 17, pp. 636-644, Apr 2004.
- [7] K. Koyanagi, M. Ono, S. Hanai, K. Watanabe, S. Awaji, T. Hamajima, T. Kiyoshi, and H. Kumakura, "Design of a 30 T Superconducting Magnet Using a Coated Conductor Insert," *Ieee Transactions on Applied Superconductivity*, vol. 19, pp. 1617-1620, Jun 2009.

- [8] D. W. Hazelton, V. Selvamanickam, J. M. Duval, D. C. Larbalestier, W. D. Markiewicz, H. W. Weijers, and R. L. Holtz, "Recent Developments in 2G HTS Coil Technology," *Ieee Transactions on Applied Superconductivity*, vol. 19, pp. 2218-2222, Jun 2009.
- [9] J. Schwartz, T. Effio, X. T. Liu, Q. V. Le, A. L. Mbaruku, H. J. Schneider-Muntau, T. M. Shen, H. H. Song, U. P. Trociewitz, X. R. Wang, and H. W. Weijers, "High field superconducting solenoids via high temperature superconductors," *IEEE Transactions on Applied Superconductivity*, vol. 18, pp. 70-81, Jun 2008.
- [10] A. Matsumoto, H. Kitaguchi, H. Kumakura, J. Nishioka, and T. Hasegawa, "Improvement of the microstructure and critical current densities of Bi-2212 round wires with a precisely controlled heat treatment," *Superconductor Science & Technology*, vol. 17, pp. 989-992, Aug 2004.
- [11] J. Schwartz and G. A. Merritt, "Proof-of-principle experiments for react-wind-sinter manufacturing of  $\text{Bi}_2\text{Sr}_2\text{CaCu}_2\text{O}_x$  magnets," *Superconductor Science and Technology*, vol. 20, p. L59, 2007.
- [12] H. MiaO, K. R. Marken, M. Meinesz, B. Czabaj, H. Seung, A. Twin, P. Noonan, U. P. Trociewitz, and J. Schwartz, "High Field Insert Coils From Bi-2212/Ag Round Wires," *IEEE Transactions on Applied Superconductivity*, vol. 17, pp. 2262-2265, 2007.
- [13] M. Abbasi, M. Naderi, and A. Saeed-Akbari, "Isothermal versus non-isothermal hot compression process: A comparative study on phase transformations and structure-property relationships," *Materials & Design*, vol. 45, pp. 1-5, Mar 2013.
- [14] X. Liu, Q. V. Le, and J. Schwartz, "Influencing factors on the electrical transport properties of split-melt processed  $\text{Bi}_2\text{Sr}_2\text{CaCu}_2\text{O}_x$  round wires," *Superconductor Science & Technology*, vol. 25, p. 075008, 2012.
- [15] A. Kajbafvala, W. Nachtrab, T. Wong, and J. Schwartz, "A. Kajbafvala, W. Nachtrab, T. Wong and J. Schwartz, "High strength oxide dispersion strengthened silver aluminum alloys optimized for  $\text{Bi}_2\text{Sr}_2\text{CaCu}_2\text{O}_{8+x}$  round wire," *Superconductor Science & Technology*, 2013 (accepted).

- [16] A. Kajbafvala, W. Nachtrab, X. F. Lu, F. Hunte, X. Liu, N. Cheggour, T. Wong, and J. Schwartz, "Dispersion-Strengthened Silver Alumina for Sheathing  $\text{Bi}_2\text{Sr}_2\text{CaCu}_2\text{O}_{8+x}$  Multifilamentary Wire," *IEEE Transactions on Applied Superconductivity*, vol. 22, pp. 8400210-8400210, 2012.
- [17] F. Kametani, T. Shen, J. Jiang, C. Scheuerlein, A. Malagoli, M. D. Michiel, Y. Huang, H. Miao, J. A. Parrell, E. E. Hellstrom, and D. C. Larbalestier, "Bubble formation within filaments of melt-processed Bi2212 wires and its strongly negative effect on the critical current density," *Superconductor Science and Technology*, vol. 24, p. 075009, 2011.
- [18] W. Zhang, O. V. Pupyshva, Y. Ma, M. Polak, E. E. Hellstrom, and D. C. Larbalestier, "Study of the effect of the Sr/Ca ratio on the microstructure and critical current density of BSCCO 2212 Ag-sheathed tapes," *IEEE Transactions on Applied Superconductivity*, vol. 7, pp. 1544-1547, 1997.
- [19] X. T. Liu, Q. V. Le, and J. Schwartz, "Influencing factors on the electrical transport properties of split-melt processed  $\text{Bi}_2\text{Sr}_2\text{CaCu}_2\text{O}_x$  round wires," *Superconductor Science and Technology*, vol. 25, p. 075008, 2012.
- [20] X. T. Liu, W. T. Nachtrab, T. Wong, and J. Schwartz, "Effect of Resolidification Conditions on  $\text{Bi}_2\text{Sr}_2\text{CaCu}_2\text{O}_x$  /Ag/AgMg Coil Performance," *IEEE Transactions on Applied Superconductivity*, vol. 19, pp. 2232-2236, 2009.
- [21] W. T. Nachtrab, X. T. Liu, T. Wong, and J. Schwartz, "Effect of Solidification Conditions on Partial Melt Processed Bi2212/Ag Round Wire," *IEEE Transactions on Applied Superconductivity*, vol. 21, pp. 2795-2799, Jun 2011.
- [22] X. T. Liu, T. M. Shen, U. P. Trociewitz, and J. Schwartz, "React-Wind-Sinter Processing of High Superconductor Fraction  $\text{Bi}_2\text{Sr}_2\text{CaCu}_2\text{O}_x$ /AgMg/AgMg Round Wire," *IEEE Transactions on Applied Superconductivity*, vol. 18, pp. 1179-1183, 2008.
- [23] G. Villard, F. Legendre, S. Poissonnet, P. Régnier, C. Bifulco, and G. Giunchi, "Enhancement in  $J_c$  of Bi-2212/Ag tapes," *Physica C: Superconductivity*, vol. 355, pp. 312-324, 2001.

- [24] T. M. Shen, X. T. Liu, U. P. Trociewitz, and J. Schwartz, "Electromechanical behavior of  $\text{Bi}_2\text{Sr}_2\text{CaCu}_2\text{O}_x$  conductor using a split melt process for react-wind-sinter magnet fabrication," *IEEE Transactions on Applied Superconductivity*, vol. 18, pp. 520-524, Jun 2008.
- [25] A. Godeke, D. Cheng, D. R. Dietderich, C. D. English, H. Felice, C. R. Hannaford, S. O. Prestemon, G. Sabbi, R. M. Scanlan, Y. Hikichi, J. Nishioka, and T. Hasegawa, "Development of Wind-and-React Bi-2212 Accelerator Magnet Technology," *Applied Superconductivity, IEEE Transactions on*, vol. 18, pp. 516-519, 2008.
- [26] G. Naderi, X. Liu, W. Nachtrab, and J. Schwartz, "Understanding processing–microstructure–properties relationships in  $\text{Bi}_2\text{Sr}_2\text{CaCu}_2\text{O}_x$  /Ag round wires and enhanced transport through saw-tooth processing," *Superconductor Science and Technology*, vol. 26, p. 105010, 2013.
- [27] U. Welp, D. O. Gunter, G. W. Crabtree, W. Zhong, U. Balachandran, P. Haldar, R. S. Sokolowski, V. K. Vlasko-Vlasov, and V. I. Nikitenko, "Imaging of transport currents in superconducting  $(\text{Bi, Pb})_2\text{Sr}_2\text{Ca}_2\text{Cu}_3\text{O}_x$  composites," *Nature*, vol. 376, pp. 44-46, 1995.
- [28] T. Shen, J. Jiang, F. Kametani, U. P. Trociewitz, D. C. Larbalestier, and E. E. Hellstrom, "Heat treatment control of Ag– $\text{Bi}_2\text{Sr}_2\text{CaCu}_2\text{O}_x$  multifilamentary round wire: investigation of time in the melt," *Superconductor Science and Technology*, vol. 24, p. 115009, 2011.
- [29] M. O. Rikel, D. Wesolowski, Y. Yuan, and E. E. Hellstrom, "Competitiveness of porosity and phase purity in melt processed Bi2212/Ag conductors," *Physica C: Superconductivity*, vol. 354, pp. 321-326, 2001.
- [30] P. Majewski, A. Sotelo, H. Szillat, S. Kaesche, and F. Aldinger, "Phase diagram studies in the system Ag– $\text{Bi}_2\text{Sr}_2\text{CaCu}_2\text{O}_8$ ," *Physica C: Superconductivity*, vol. 275, pp. 47-51, 1997.
- [31] B. Heeb, L. J. Gauckler, H. Heinrich, and G. Kostorz, "From imperfect to perfect  $\text{Bi}_2\text{Sr}_2\text{CaCu}_2\text{O}_x$  (Bi–2212) grains," *Journal of Materials Research*, vol. 8, pp. 2170-2176, 1993.

- [32] B. Heeb, L. J. Gauckler, H. Heinrich, and G. Kostorz, "Microstructure and properties of melt-processed Bi-2212 ( $\text{Bi}_2\text{Sr}_2\text{CaCu}_2\text{O}_x$ )," *Journal of Electronic Materials*, vol. 22, pp. 1279-1283, 1993/10/01 1993.
- [33] M. O. Rikel and E. E. Hellstrom, "Development of 2201 intergrowths during melt processing Bi2212/Ag conductors," *Physica C-Superconductivity and Its Applications*, vol. 357, pp. 1081-1090, Aug 2001.
- [34] T. Holesinger, J. Bingert, M. Teplitsky, Q. Li, R. Parrella, M. Rupich, and G. Riley, "Spatial variations in composition in high-critical-current-density Bi-2223 tapes," *Journal of Materials Research*, vol. 15, pp. 285-295, 2000.
- [35] J. Jiang, W. L. Starch, M. Hannion, F. Kametani, U. P. Trociewitz, E. E. Hellstrom, and D. C. Larbalestier, "Doubled critical current density in Bi-2212 round wires by reduction of the residual bubble density," *Superconductor Science and Technology*, vol. 24, p. 082001, 2011.
- [36] A. Malagoli, F. Kametani, J. Jiang, U. P. Trociewitz, E. E. Hellstrom, and D. C. Larbalestier, "Evidence for long range movement of Bi-2212 within the filament bundle on melting and its significant effect on  $J_c$ ," *Superconductor Science and Technology*, vol. 24, p. 075016, 2011.
- [37] C. Scheuerlein, M. D. Michiel, M. Scheel, J. Jiang, F. Kametani, A. Malagoli, E. E. Hellstrom, and D. C. Larbalestier, "Void and phase evolution during the processing of Bi-2212 superconducting wires monitored by combined fast synchrotron microtomography and x-ray diffraction," *Superconductor Science and Technology*, vol. 24, p. 115004, 2011.
- [38] T. Shen, J. Jiang, F. Kametani, U. P. Trociewitz, D. C. Larbalestier, J. Schwartz, and E. E. Hellstrom, "Filament to filament bridging and its influence on developing high critical current density in multifilamentary  $\text{Bi}_2\text{Sr}_2\text{CaCu}_2\text{O}_x$  round wires," *Superconductor Science and Technology*, vol. 23, p. 025009, 2010.

## APPENDICES

## Appendix A

This Matlab code is written by Evan Benjamin Callaway is added to the thesis by his permission.

```
clear
%% Part 1: Input Greyscale SEM Image and Black & White Image %%

string = input('What image would you like to analyze? ', 's');
micron = input('How many pixels are there per micrometer? ');

Imginfo = imfinfo(string);
I = imread(string);
rgbImage = repmat(I,[1 1 3]);
Outlined_Image=rgbImage;
GW = Imginfo.Width;
GH = Imginfo.Height;

%% Defining Variables Used Later %%
AEC = 0;
maxarea = 0;
maxblack = 0;
too_small = 0;
too_big = 0;
iter = 0;
contains_bi2201 = 0;
porous_bi2212 = 0;
layered_bi2212 = 0;
CF = 0;
mixed_secondary_phase = 0;
unknown = 0;
AEC_Area = zeros(20,1);
CF_Area = zeros(20,1);
total_filament_area_no_bridges = 0;
bi2212_in_AEC_and_CF = 0;
bi2212_filaments = 0;
bi2201_grains_in_bi2212 = 0;
bi2212_in_filaments_containing_bi2201_grains = 0;

%% Black and White Binary Image Input %%
prompt = 'Do you have a black and white image? Y/N: ';
Answer = input(prompt,'s');
Answer

%% If the user's response is not "Y" or "N", then the question will be repeated %%
if Answer ~= 'Y' && Answer ~= 'N'
    for i=1:9999999999
        prompt = 'Please answer Y or N: ';
        Answer = input(prompt,'s');
        Answer
        if Answer == 'Y' || Answer == 'N'
            break
        end
    end
end
end
```

```

%% Input the binary image if there is one and fill in any small holes %%
if Answer == 'Y'
    string3 = input('Enter the black and white image where black is the filaments and white is the silver: ', 's');
    bw = imread(string3);
    % all pixels along the edge are set to a value of 1 so that they appear
    % to be white
    for i=1:GH
        bw(i,1) = 1;
        bw(i,GW) = 1;
    end
    for j=1:GW
        bw(1,j) = 1;
        bw(GH,j) = 1;
    end
    level = graythresh(bw);
    bw1 = im2bw(bw,level);
    % fill in all holes less than 3.5 microns squared
    bw2 = bwareaopen(bw1, (3.5*micron)^2);
    bw3 = medfilt2(bw2);
    bw4 = imcomplement(bw3);
    [r5, c5] = find(bw3 == 0);
    rc5 = [r5 c5]; % rc5 is an array with the coordinates (row,column) of all filament pixels
    total_filament_area = size(rc5,1); % Total number of pixels in the filaments
end

%% Part 2: Convert Grayscale Image to Black and White Image %%

vec = zeros(GW*GH,1);
for i=1:GH
    for j=1:GW
        k = (i-1)*GW+j;
        vec(k,1)=I(i,j);
    end
end
image_mean = mean(vec) % Mean of the entire image
image_median = median(vec); % Median of the entire image
threshold = image_median;
I2 = I;
range = 4;
k=1;
m=1;
silver = zeros(GH*GW,1);
filaments = zeros(GH*GW,1);

%% for input with binary image %%
if Answer == 'Y'
    for i=1:GH
        for j=1:GW
            if bw3(i,j) == 1
                silver(k,1) = I(i,j); % silver is a vector with values of all pixels that are
                k = k + 1;
            else
                filaments(m,1) = I(i,j); % filaments is a vector with values of all pixels that are in the
                m = m + 1;
            end
        end
    end
end

```

```

        end
    end
end
filaments(filaments==0)=[];
mean_filaments = mean(filaments);
median_filaments = median(filaments);
max_filaments = max(filaments);
mode_filaments = mode(filaments);
mean_filaments % mean value of the filaments needs to be between 120 and 140

silver(silver==0)=[];
mean_silver = mean(silver);
mean_silver % mean value of the silver needs to be between 170 and 190
median_silver = median(silver);
min_silver = min(silver);
mode_silver = mode(silver);
end

%% for no binary image %%
if Answer == 'N'
    for i=1:GH % creating a black and white iamge pixel by pixel
        for j=1:GW
            if I(i,j) > image_mean
                lowi = i-range;
                highi = i+range;
                if lowi < 1
                    lowi = 1;
                end
                if highi > GH
                    highi = GH;
                end
                lowj = j-range;
                highj = j+range;
                if lowj < 1
                    lowj = 1;
                end
                if highj > GW
                    highj = GW;
                end
                if mean(mean(I(lowi:highi,lowj:highj))) > ...
                    2*image_median-image_mean
                    I2(i,j) = 255;
                    silver(k,1) = I(i,j);
                    k = k + 1;
                end
            end
            if I2(i,j) < 200
                I2(i,j) = 0;
                filaments(m,1) = I(i,j);
                m = m + 1;
            end
        end
    end
end
filaments(filaments==0)=[];
mean_filaments = mean(filaments);
median_filaments = median(filaments);
max_filaments = max(filaments);
mode_filaments = mode(filaments);

```

```

mean_filaments % mean value of the filaments needs to be between 120 and 140

silver(silver==0)=[];
mean_silver = mean(silver);
mean_silver % mean value of the silver needs to be between 170 and 190
median_silver = median(silver);
min_silver = min(silver);
mode_silver = mode(silver);

level = graythresh(I2);
bw = im2bw(I2,level);
for i=1:GH
    bw(i,1) = 1;
    bw(i,GW) = 1;
end
for j=1:GW
    bw(1,j) = 1;
    bw(GH,j)= 1;
end
bw2 = imcomplement(bw);
bw3 = medfilt2(bw2);
bw4 = bwareaopen(bw3, (5.5*micron)^2);
end

%% Warning if filaments or silver mean is outside of the preferred value %%
if mean_silver < 170
    disp('The silver region is too dark. Adjust the image in ImageJ for better results')
end
if mean_silver > 190
    disp('The silver region is too bright. Adjust the image in ImageJ for better results')
end
if mean_filaments < 120
    disp('The filament region is too dark. Adjust the image in ImageJ for better results')
end
if mean_filaments > 140
    disp('The filament region is too bright. Adjust the image in ImageJ for better results')
end

%% Part 2: Remove Bridges %%
LF1 = (20*micron)^2;
LF2 = (17.5*micron)^2;
SF1 = (7.5*micron)^2;
SF2 = (6*micron)^2;
max_allowed_size = LF1;
min_allowed_size = SF1;
for m=1:6
    maxarea = 0;
    R = (1+0.5*m)*micron;
    cc = bwconncomp(bw4);
    bw5 = imcomplement(bw4);
    bw7 = bw5;
    stats = regionprops(cc, 'Area');
    idx = find([stats.Area] > 50*micron^2);
    bw6 = ismember(labelmatrix(cc), idx);
    L = bwlabel(bw6, 4);
    maxl = max(L,[],2);
    filament_number = max(maxl);
end

```



```

%% Part 3: Analyze Each Filament %%

data = zeros(1,8);
for i=1:filament_number
    [r, c] = find(L==i);
    rc = [r c]; % coordinates of the pixels of the filament beign analyzed
    Area = size(rc,1); % area of the filament
    rmax = max(r);
    rmin = min(r);
    cmax = max(c);
    cmin = min(c);
    filament_values = zeros(Area,1);
    filament_values_plus_1 = zeros(Area,1);
    if Area > maxarea
        maxarea = Area;
    end
    if min_allowed_size < Area && Area < max_allowed_size
        iter = iter + 1;
        total_filament_area_no_bridges = total_filament_area_no_bridges + Area;
        number_of_filaments = number_of_filaments + 1;
        % determine percent of pixels that are black (=0 or close to 0)
        [r0, c0] = find(I(rmin:rmax,cmin:cmax)<=5); % black pixels are either voids or AEC
        rc0 = [r0 c0];
        black = size(rc0,1);
        percentblack = black/Area;
        if percentblack > maxblack
            maxblack = percentblack;
        end
        for j=1:Area
            filament_values(j,1)=I(rc(j,1),rc(j,2));
            filament_values_plus_1(j,1)=filament_values(j,1)+1;
        end
        [row, col] = find(filament_values > (mean_silver-20));
        rowcol = [row, col];
        data(iter,3) = ceil(size(rowcol,1)/Area*10000); % area of bright spots in filament
        data(iter,4) = ceil(percentblack*10000); % area of black spots in filament
        data(iter,1) = ceil(iter); % Filament #
        data(iter,8) = Area;
        I3 = I;
        for k=rmin:rmax
            for l=cmin:cmax
                if L(k,l)==i
                    I3(k,l) = I(k,l);
                else
                    I3(k,l) = 0;
                end
            end
        end
        end
        BW = im2bw(I3(rmin:rmax,cmin:cmax),((mean_silver+image_mean)/510));
        CC = bwconncomp(BW,4);
        numPixels = cellfun(@numel,CC.PixelIdxList);
        white_spot = max(numPixels);
        data(iter,6) = ceil(white_spot/Area*10000);
        data(iter,7) = white_spot;
        if percentblack > 0.075 % black area is AEC or voids (porous Bi2212)
            BW2 = im2bw(I(rmin:rmax,cmin:cmax),0.01);
            BWC = imcomplement(BW2);
            CC = bwconncomp(BWC,4);
        end
    end
end

```

```

numPixels = cellfun(@numel,CC.PixelIdxList);
black_spot = max(numPixels);
data(iter,5) = ceil(black_spot/Area*10000);
if black_spot/Area*100 > 4 % If there is a large black spot above the threshold value (4% of
the filament), then it is AEC
    AEC = AEC + 1;
    data(iter,2) = ceil(4444);
    bi2212_in_AEC_and_CF = bi2212_in_AEC
_and_CF + Area - black_spot;
    % Blue for AEC
    Outlined_Image(rmin:rmax,cmin:cmin+4,1) = 0;
    Outlined_Image(rmin:rmax,cmax-4:cmax,1) = 0;
    Outlined_Image(rmin:rmin+4,cmin:cmax,1) = 0;
    Outlined_Image(rmax-4:rmax,cmin:cmax,1) = 0;
    Outlined_Image(rmin:rmax,cmin:cmin+4,2) = 0;
    Outlined_Image(rmin:rmax,cmax-4:cmax,2) = 0;
    Outlined_Image(rmin:rmin+4,cmin:cmax,2) = 0;
    Outlined_Image(rmax-4:rmax,cmin:cmax,2) = 0;
    Outlined_Image(rmin:rmax,cmin:cmin+4,3) = 255;
    Outlined_Image(rmin:rmax,cmax-4:cmax,3) = 255;
    Outlined_Image(rmin:rmin+4,cmin:cmax,3) = 255;
    Outlined_Image(rmax-4:rmax,cmin:cmax,3) = 255;
    if ceil(white_spot/Area*10000) > 400 % If there is also a large white spot, then there
is CF and AEC
        mixed_secondary_phase = mixed_secondary_phase + 1;
        AEC = AEC - 1;
        CF_Area(CF + mixed_secondary_phase,1) = white_spot;
        bi2212_in_AEC_and_CF = bi2212_in_AEC_and_CF - white_spot;
        data(iter,2) = ceil(666666);
        % Purple for mixed_secondary_phase
        Outlined_Image(rmin:rmax,cmin:cmin+4,1) = 255;
        Outlined_Image(rmin:rmax,cmax-4:cmax,1) = 255;
        Outlined_Image(rmin:rmin+4,cmin:cmax,1) = 255;
        Outlined_Image(rmax-4:rmax,cmin:cmax,1) = 255;
        Outlined_Image(rmin:rmax,cmin:cmin+4,2) = 0;
        Outlined_Image(rmin:rmax,cmax-4:cmax,2) = 0;
        Outlined_Image(rmin:rmin+4,cmin:cmax,2) = 0;
        Outlined_Image(rmax-4:rmax,cmin:cmax,2) = 0;
        Outlined_Image(rmin:rmax,cmin:cmin+4,3) = 255;
        Outlined_Image(rmin:rmax,cmax-4:cmax,3) = 255;
        Outlined_Image(rmin:rmin+4,cmin:cmax,3) = 255;
        Outlined_Image(rmax-4:rmax,cmin:cmax,3) = 255;
    end
    AEC_Area(AEC + mixed_secondary_phase,1) = black_spot;
else
    if ceil(white_spot/Area*100) > 6.5 || white_spot > (3.5*micron)^2 % If there is no
large black spot (AEC) but there is a large white spot, then it is CF
        data(iter,2) = ceil(55555);
        CF = CF + 1;
        bi2212_in_AEC_and_CF = bi2212_in_AEC_and_CF + Area -
white_spot;
        CF_Area(CF + mixed_secondary_phase,1) = white_spot;
        % Teal for CF
        Outlined_Image(rmin:rmax,cmin:cmin+4,1) = 0;
        Outlined_Image(rmin:rmax,cmax-4:cmax,1) = 0;
        Outlined_Image(rmin:rmin+4,cmin:cmax,1) = 0;
        Outlined_Image(rmax-4:rmax,cmin:cmax,1) = 0;
        Outlined_Image(rmin:rmax,cmin:cmin+4,2) = 255;

```

```

        Outlined_Image(rmin:rmax,cmax-4:cmax,2) = 255;
        Outlined_Image(rmin:rmin+4,cmin:cmax,2) = 255;
        Outlined_Image(rmax-4:rmax,cmin:cmax,2) = 255;
        Outlined_Image(rmin:rmax,cmin:cmin+4,3) = 255;
        Outlined_Image(rmin:rmax,cmax-4:cmax,3) = 255;
        Outlined_Image(rmin:rmin+4,cmin:cmax,3) = 255;
        Outlined_Image(rmax-4:rmax,cmin:cmax,3) = 255;
    else
        porous_bi2212 = porous_bi2212 + 1; % If there is significant black
regions, no large black or white spots, then it is porous Bi2212
        data(iter,2) = ceil(22);
        bi2212_filaments = bi2212_filaments + Area;
        % Yellow for porous bi2212
        Outlined_Image(rmin:rmax,cmin:cmin+4,1) = 255;
        Outlined_Image(rmin:rmax,cmax-4:cmax,1) = 255;
        Outlined_Image(rmin:rmin+4,cmin:cmax,1) = 255;
        Outlined_Image(rmax-4:rmax,cmin:cmax,1) = 255;
        Outlined_Image(rmin:rmax,cmin:cmin+4,2) = 255;
        Outlined_Image(rmin:rmax,cmax-4:cmax,2) = 255;
        Outlined_Image(rmin:rmin+4,cmin:cmax,2) = 255;
        Outlined_Image(rmax-4:rmax,cmin:cmax,2) = 255;
        Outlined_Image(rmin:rmax,cmin:cmin+4,3) = 0;
        Outlined_Image(rmin:rmax,cmax-4:cmax,3) = 0;
        Outlined_Image(rmin:rmin+4,cmin:cmax,3) = 0;
        Outlined_Image(rmax-4:rmax,cmin:cmax,3) = 0;
    end
end
else
    if ceil(white_spot/Area*100) > 6.5 || white_spot > (3.5*micron)^2 % if no significant black
regions and there is a large white spot, then it is CF
        data(iter,2) = ceil(55555);
        % Teal for CF
        CF = CF + 1;
        CF_Area(CF + mixed_secondary_phase,1) = white_spot;
        bi2212_in_AEC_and_CF = bi2212_in_AEC_and_CF + Area - white_spot;
        Outlined_Image(rmin:rmax,cmin:cmin+4,1) = 0;
        Outlined_Image(rmin:rmax,cmax-4:cmax,1) = 0;
        Outlined_Image(rmin:rmin+4,cmin:cmax,1) = 0;
        Outlined_Image(rmax-4:rmax,cmin:cmax,1) = 0;
        Outlined_Image(rmin:rmax,cmin:cmin+4,2) = 255;
        Outlined_Image(rmin:rmax,cmax-4:cmax,2) = 255;
        Outlined_Image(rmin:rmin+4,cmin:cmax,2) = 255;
        Outlined_Image(rmax-4:rmax,cmin:cmax,2) = 255;
        Outlined_Image(rmin:rmax,cmin:cmin+4,3) = 255;
        Outlined_Image(rmin:rmax,cmax-4:cmax,3) = 255;
        Outlined_Image(rmin:rmin+4,cmin:cmax,3) = 255;
        Outlined_Image(rmax-4:rmax,cmin:cmax,3) = 255;
    else
        if ceil(size(rowcol,1)/Area*10000) > cf_cutoff && ...
percentblack < 0.05 % if there are many small bright regions
then it is Bi2201 grains
            data(iter,2) = ceil(333);
            bi2201_grains_in_bi2212 = bi2201_grains_in_bi2212 + size(rowcol,1);
            bi2212_in_filaments_containing_bi2201_grains =
bi2212_in_filaments_containing_bi2201_grains ...
+ Area - size(rowcol,1);
            % Green for contains bi2201
            contains_bi2201 = contains_bi2201 + 1;

```

```

    Outlined_Image(rmin:rmax,cmin:cmin+4,1) = 0;
    Outlined_Image(rmin:rmax,cmax-4:cmax,1) = 0;
    Outlined_Image(rmin:rmin+4,cmin:cmax,1) = 0;
    Outlined_Image(rmax-4:rmax,cmin:cmax,1) = 0;
    Outlined_Image(rmin:rmax,cmin:cmin+4,2) = 255;
    Outlined_Image(rmin:rmax,cmax-4:cmax,2) = 255;
    Outlined_Image(rmin:rmin+4,cmin:cmax,2) = 255;
    Outlined_Image(rmax-4:rmax,cmin:cmax,2) = 255;
    Outlined_Image(rmin:rmax,cmin:cmin+4,3) = 0;
    Outlined_Image(rmin:rmax,cmax-4:cmax,3) = 0;
    Outlined_Image(rmin:rmin+4,cmin:cmax,3) = 0;
    Outlined_Image(rmax-4:rmax,cmin:cmax,3) = 0;
else % if there are no CF, AEC, Bi2201, or voids, then it is layered Bi2212

    data(iter,2) = ceil(1);
    % Red for layered bi2212
                                bi2212_filaments = bi2212_filaments + Area;
    layered_bi2212 = layered_bi2212 + 1;
    Outlined_Image(rmin:rmax,cmin:cmin+4,1) = 255;
    Outlined_Image(rmin:rmax,cmax-4:cmax,1) = 255;
    Outlined_Image(rmin:rmin+4,cmin:cmax,1) = 255;
    Outlined_Image(rmax-4:rmax,cmin:cmax,1) = 255;
    Outlined_Image(rmin:rmax,cmin:cmin+4,2) = 0;
    Outlined_Image(rmin:rmax,cmax-4:cmax,2) = 0;
    Outlined_Image(rmin:rmin+4,cmin:cmax,2) = 0;
    Outlined_Image(rmax-4:rmax,cmin:cmax,2) = 0;
    Outlined_Image(rmin:rmax,cmin:cmin+4,3) = 0;
    Outlined_Image(rmin:rmax,cmax-4:cmax,3) = 0;
    Outlined_Image(rmin:rmin+4,cmin:cmax,3) = 0;
    Outlined_Image(rmax-4:rmax,cmin:cmax,3) = 0;
end
end
end
end
if min_allowed_size > Area
    too_small = too_small + 1;
end
if Area > max_allowed_size
    too_big = too_big + 1;
end
end
end

%% Output Data %%

too_small
too_big
figure, imshow(Outlined_Image), title('red for layered bi2212, yellow for porous, green contains bi2201, blue for AEC, teal
for CF, purple for mixed secondary phases');
label = {'number','type','% > silver', '% black','% b spot','% w spot','# w spot','area'};
%label
%data
number_of_filaments

layered_bi2212
porous_bi2212
contains_bi2201
AEC
CF

```

mixed\_secondary\_phase

AEC\_Total = sum(AEC\_Area);

CF\_Total = sum(CF\_Area);

Area\_Fraction\_AEC = AEC\_Total/(GW\*GH)

Area\_Fraction\_CF = CF\_Total/(GW\*GH)

Area\_Fraction\_Secondary\_Phases = Area\_Fraction\_CF + Area\_Fraction\_AEC

%total\_filament\_area

%total\_filament\_area\_no\_bridges

bi2212\_in\_AEC\_and\_CF\_Filaments

bi2201\_grains\_in\_bi2212

bi2212\_in\_filaments\_containing\_bi2201\_grains

bi2212\_filaments

Area\_Fraction\_total\_bi2212 = (bi2212\_in\_AEC\_and\_CF + bi2212\_in\_filaments\_containing\_bi2201\_grains + bi2212\_filaments)/(GW\*GH)

Area\_Fraction\_bi2201 = bi2201\_grains\_in\_bi2212/(GW\*GH)

## Chapter 4

### On the roles of $\text{Bi}_2\text{Sr}_2\text{CuO}_x$ intergrowths in $\text{Bi}_2\text{Sr}_2\text{CaCu}_2\text{O}_x/\text{Ag}$ round wires: c-axis transport and magnetic flux pinning

G. Naderi<sup>a</sup> and J. Schwartz

Department of Materials Science and Engineering, North Carolina State University

Raleigh, NC 27695-7907, U.S.A.

Appl. Phys. Lett. **104**, 152602 (2014); <http://dx.doi.org/10.1063/1.4871805>

Despite progress in the performance of  $\text{Bi}_2\text{Sr}_2\text{CaCu}_2\text{O}_x$  (Bi2212)/Ag multifilamentary round wires, understanding the impact of microstructural defects on multiple length scales on electrical transport remains a significant challenge. Many recent studies have focused on porosity, but porosity is not the only factor in determining  $J_c$ . The primary impurity in partial-melt processed multifilamentary Bi2212 wires is  $\text{Bi}_2\text{Sr}_2\text{CuO}_x$  (Bi2201), which forms as mesoscopic grains and nanoscopic intergrowths. Previously, we showed the destructive effect of Bi2201 grains on transport. Here, we relate scanning transmission electron microscopy results to the Bi2212 coherence length, anisotropic magnetization behavior and magnetic-field dependent transport to study c-axis transport and the effects of Bi2201 intergrowths on magnetic flux pinning. We show that wide Bi2201 intergrowths are barrier to c-axis transport within Bi2212 grains, whereas narrow (half- and full-cell) Bi2201 intergrowths are not detrimental to c-axis transport and are likely magnetic flux pinning centers. These results have significant impact on the understanding of Bi2212/Bi2201 systems and provide important physical insight towards future improvements in devices based upon wires, film and junctions.

Significant progress in the critical current density ( $J_c$ ) of  $\text{Bi}_2\text{Sr}_2\text{CaCu}_2\text{O}_x$  (Bi2212)/Ag multifilamentary round wires (RWs) has led to growing interest in high field dipoles and quadrupoles for high energy hadron colliders, solenoids for muon cooling and nuclear magnetic resonance magnets.[1-7] Recently, Bi2212 wire development has focused on reducing porosity, and indeed this has resulted in increased  $J_c$ . Porosity, however, is not the only current limiting mechanism in Bi2212 RWs. Due to the complex, heterogeneous Bi2212 microstructures, the performance of Bi2212 RWs remains far from maximized and improvements remain dependent upon understanding the remaining microstructure-transport relationships on multiple length-scales.[2, 5, 8] Figure. 4-1 illustrates the five key length scales that affect transport in Bi2212 multifilamentary RWs and their respective defects. On the macroscopic scale, bubbles[1, 3, 4, 9] and leakage[10, 11] are the primary issues, but these have been mostly eliminated. On the mesoscale, interfilamentary bridging[12, 13] and radial c-axis texturing of grain colonies[14-17] are the primary structures that influence transport. On the individual filament length scale, porosity and the phase assemblage, including mesoscopic secondary phases and large  $\text{Bi}_2\text{Sr}_2\text{CuO}_x$  (Bi2201) grains, are the primary challenges.<sup>[8, 13, 18, 19]</sup> Previously we showed that  $J_c$  is directly proportional to the fraction of predominantly-Bi2212 filaments and inversely proportional to the percentage of filaments containing large Bi2201 grains; for simplicity these filaments are called “Bi2212 filaments” and “Bi2201 filaments”.[18] On the grain-to-grain scale, grain colony orientation and grain boundaries dictate local behavior.[20, 21] Lastly, the important roles of the intragrain structure and nanoscopic defects remain unknown with many unanswered

questions: *how do Bi2201 intergrowths affect transport? Does c-axis transport contribute to  $J_c$ ? What are the magnetic flux pinning centers?* Here we begin to answer those questions by focusing on nanoscale features of Bi2212 RWs that have previously not been studied extensively. The small Bi2212 coherence length emphasizes the importance of nanoscale studies.[22-26]

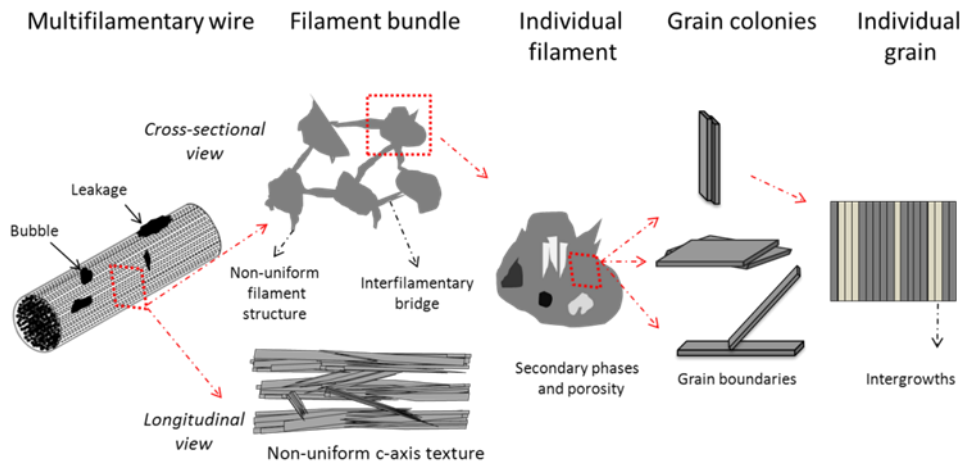


Figure 4-1. Illustration of the defects and current limiting structures in Bi2212 round wires on multiple length scales.

We consider the role of Bi2201 intergrowths,[7, 27-29] focusing on the role of c-axis transport, due to Josephson-Junction-like behavior, and magnetic flux pinning.[30, 31] Previously we studied a series of 26 melt processed Bi2212 RWs with  $J_c$ (self-field, 4.2 K) ranging from 60 - 2900 A/mm<sup>2</sup>. Our previous study showed that  $J_c$  is directly proportional to the fraction of “Bi2212 filaments” and inversely proportional to the percentage of “Bi2201 filaments” within the wire cross-section.[18] Note that 70-90% of the cross-sectional area of

"Bi2201 filaments" is actually Bi2212 phase;[18] a large quantity of Bi2201 grains is not required to significantly reduce  $J_c$  and the reduction in  $J_c$  is much greater than expected based upon a simple area-fraction basis, indicating that other current-limiting factors that correlate with the presence of Bi2201 grains may be significant. Initial STEM results showed that the density of Bi2201 intergrowths in a Bi2212 grain extracted from a "Bi2212 filament" is less than that within a Bi2212 grain extracted from a "Bi2201 filament". Thus, the impact of Bi2201 on  $J_c$  may be influenced by the coexistence of Bi2201 grains and Bi2201 intergrowths.

Here, we study one of these wires with  $J_c$  (5 T, 4.2 K) = 1500 A/mm<sup>2</sup> at greater depth. For experimental details see supplementary material.[32] Figure. 4-2a shows a cross-sectional scanning electron microscope (SEM) image and Supplementary Figure. 4-S1 shows the corresponding x-ray diffraction (XRD) pattern for one of this wire, confirming that Bi2201 is the major impurity phase. Figure. 4-2b displays a longitudinal SEM image of the wire shown in Figure 2a. Within each filament, most of the Bi2212 grains are oriented with the a-b direction almost parallel to the wire axis and filaments are connected via interfilamentary bridges. Figure. 4-3a shows a high angle annular dark field (HAADF) STEM image of one Bi2212 grain extracted from a "Bi2212 filament" (this filament is 96% Bi2212 and 2% Bi2201 by cross-sectional area) via a focused ion beam lift-out technique and thinned to electron transparency along the preferred [010] zone axis. The energy dispersive x-ray spectroscopy (EDS) map seen in Figure. 4-3b confirms the presence of Bi2201 intergrowths within the Bi2212 grain. Figure. 4a shows a cross-sectional SEM image of a "Bi2201

filament" from the same wire. This filament has large Bi2201 grains, but 88% of the cross-sectional area is Bi2212 and 12% is Bi2201.

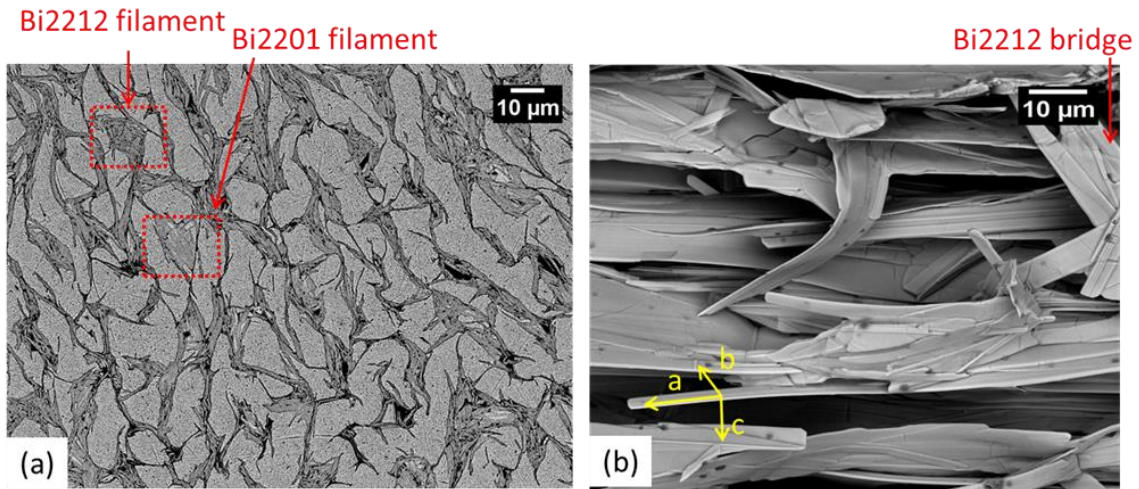


Figure 4-2. Cross-sectional SEM images of a Bi2212/Ag multifilamentary wire. (a) Transverse cross-section and (b) longitudinal cross-section. In (b), the silver has been etched.

Figures. 4-4(b-d) show HAADF STEM images of a Bi2212 grain extracted from this filament. Multiple Bi2201 intergrowths of varying sizes, including half-cell (1.3 nm wide), full-cell (2.5 nm wide) and wide bands (15-25 nm), are observed. Comparing HAADF STEM images in Figures. 4-3 and 4-4, the intergrowth density is larger in Bi2212 grains extracted from the “Bi2201 filament” than that from the “Bi2212 filament”, increasing the likelihood of finding more merged intergrowths and wide Bi2201 bands. Note that Bi2201 a-b planes of half- or full-cell intergrowths are parallel to the Bi2212 a-b planes, forming a coherent boundary that does not distort the crystalline lattice. The wide Bi2201 intergrowth in Figure. 4-4b, however, has a Bi2212/Bi2201 interface that is less smooth.

The coherence length ( $\xi$ ) of Bi2212 is calculated using equation 1; for critical temperature ( $T_c$ ) values ranging from of 70 K – 90 K[8] and  $\xi_0 = 3$  nm (0 K),  $\xi(4.2$  K) ranges from 3.09 nm – 3.07 nm, slightly larger than the width of a full cell Bi2201.[26, 33]

$$\xi(T) = \xi_0 \sqrt{\frac{T_c}{(T_c - T)}} \quad (1)$$

The dimensional similarity of thin intergrowths (half- and full-cells) and  $\xi$ , and the smooth Bi2212/Bi2201 thin intergrowth interfaces, suggest that half- and full-cell Bi2201 intergrowths are not barriers to transport. Supercurrent passes through these thin intergrowths via a Josephson Junction (JJ) mechanism, similar to intrinsic JJs associated with the layered crystal structure of the Bi2212 unit cell.[30, 31]

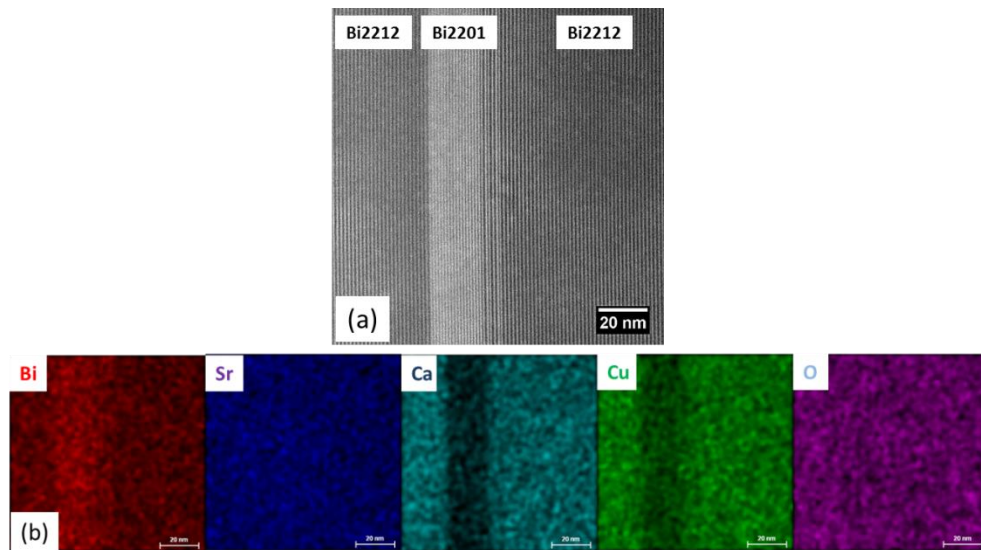


Figure 4-3. HAADF-STEM (a) image and (b) EDS-STEM maps of a Bi2212 grain extracted from a “Bi2212 filament”.

The crystallographic orientation of thin Bi2201 intergrowths implies that they contribute to transport through the c-axis. Figure. 4-2b shows that Bi2212 grains align nearly parallel to the silver interface in the a-b direction with their c-axes perpendicular to the wire axis. Thus, one can ask if there is considerable c-axis transport in Bi2212 wires. In the simplified bridge microstructure presented previously,[13] where wide bridges were assumed to be single grains, it is argued that when supercurrent reaches a barrier it continues its path by passing through these single grain bridges. The longitudinal SEM image in Figure. 4-2b shows that bridges are not single Bi2212 grains but are composed of several grains with a complex orientation. Bi2212 grains are connected over a variety of grain boundary angles and form multiple branches along the length of the wire. Thus, to understand the c-axis contribution to long-range transport, the transport behavior of each type of grain boundary must be understood.

Figure. 4-S2 shows the three most common grain boundary types with corresponding schematics.[15, 20, 21] Bi2212 grains are plate-like with large a-and b- dimensions. During solidification, Bi2212 grains align through a shared c-axis with some degree of tilting relative to the a- or b- directions. The TEM images show extensive formation of dislocations associated with the formation of the high angle grain boundaries (HAGBs). Previous studies have shown that dislocation cores block supercurrent, behaving as insulators.[21, 34] Due to the existence of HAGBs and associated dislocations at the basal-plane-faced grains, supercurrent moves from strongly conducting a-b directions to the poorly conducting c

direction. This is similar to the current percolation mechanisms in  $(\text{Bi,Pb})_2\text{Sr}_2\text{Ca}_2\text{Cu}_3\text{O}_x$  tapes.[35]

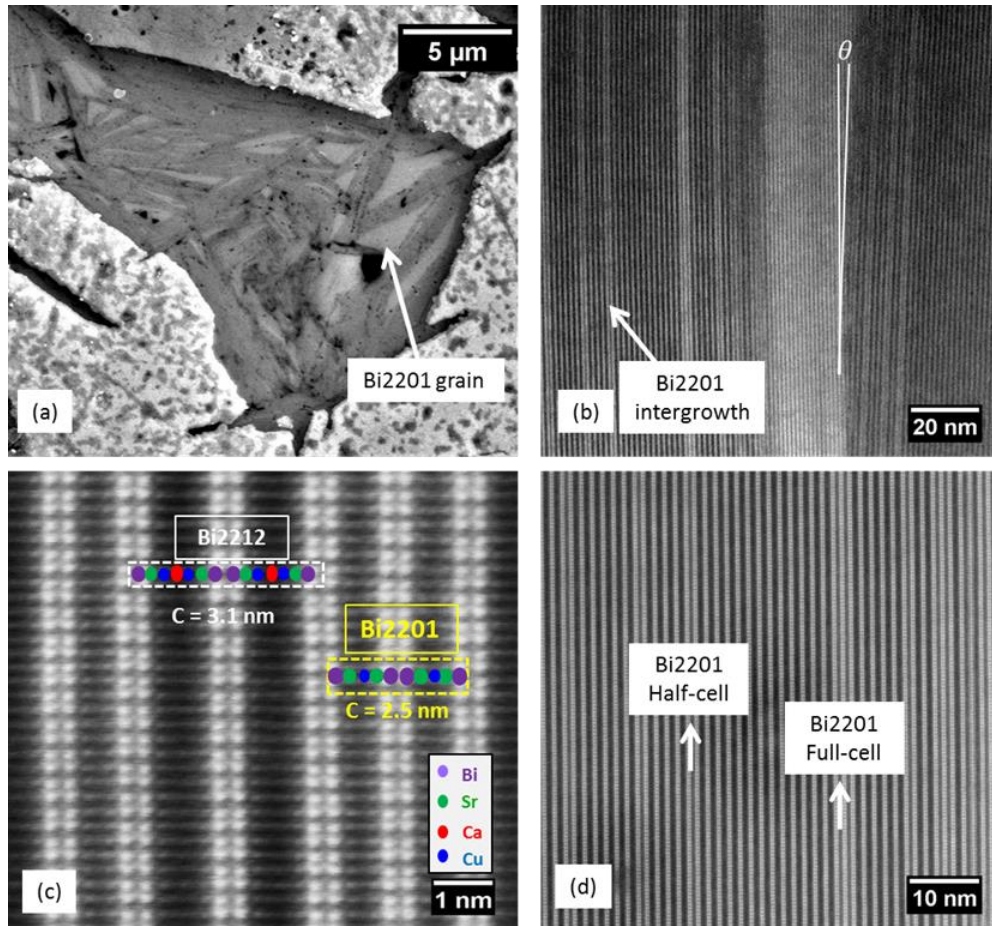


Figure 4-4. (a) Cross-sectional SEM image of a “Bi2201 filament” with Bi2212 and Bi2201 area fractions of 88% and 12%, respectively. (b) HAADF-STEM image of a Bi2212 grain extracted from the filament shown in (a). The Bi2201 intergrowths are seen as bright lines. (c) Atomic resolution HAADF-STEM image on the [010] zone showing the crystal structure of Bi2212 and Bi2201. (d) HAADF-STEM image showing diverse Bi2201 intergrowth widths, including a number of half and full-cell.

Magnetization hysteresis for magnetic fields between  $\pm 2$  T is measured on two representative Bi2212/Ag wires with significantly different in Bi2201 filament contents and  $J_c$ ; sample details are given in Table I. Hysteresis is measured with each sample oriented parallel and perpendicular to the magnetic field. Supplementary Figure. 4-S3 shows a higher magnetic response when the wire axis is perpendicular to the magnetic field, because the magnetic moment in this orientation reflects the current density within the a-b planes. When the magnetic field is parallel to the wire axis (a-b planes), in addition to a-b transport, there is a c-axis contribution. To study the anisotropic behavior of Bi2212 wires,  $\alpha$  is calculated as defined in equation 2 and summarized in Table I.

$$\alpha = \Delta M(H \perp \text{wire axis}) / \Delta M(H \parallel \text{wire axis}) \quad (2)$$

Table 4.1: Characteristics of representative wires 1 and 2 used for magnetization and transport studies.  $H_p$  is the magnetic field with maximum magnetic field penetration. The anisotropy parameter  $\alpha$  is obtained from magnetization hysteresis measurements at 4.2 K at fields of  $H_p$  and 2 T using equation 2.

	Wire 1	Wire 2
$J_c$ (self-field 4.2 K), A/mm <sup>2</sup>	2450	460
Percentage of “Bi2212 filaments”	60	31
Percentage of “Bi2201 filaments”	14	52
$\alpha$ at $H_p$	6.0	15.2
$\alpha$ at 2 T	4.3	10.9

$H_p$  is the magnetic field at full penetration and thus the maximum magnetization  $(\Delta M)_{\max}$ . [36] Comparing  $\alpha$  in Bi2212 wires at full penetration and 2 T, one finds that  $\alpha$  of wire 1 is only about 40% that of wire 2, indicating that wire 1, with higher  $J_c$ , is more isotropic than wire 2. Wire 2 has more c-axis aligned Bi2201 grains, reducing c-axis transport and increasing anisotropy.

To study the effect of Bi2201 on transport,  $J_c$  of six wires, with a significant variance in Bi2201 content, is measured at low magnetic field in small magnetic field increments, 0.02 to 0.05 T, for fields up to 1 T. Figure. 4-5 shows  $J_c(H)$  in applied magnetic fields up to 8 T for W1 and W2; results for other wires showed similar behavior. In Figure. 4-5a, dashed lines at 0.4 T and 0.8 T separate three distinct regions. The difference in self-field  $J_c$  is mainly due to the difference in the number of “Bi2201 filaments”. Figure. 4-5b and c show the relative change in  $J_c(H)$  normalized by the self-field  $J_c$ . A rapid decrease in  $J_c$  at low magnetic fields (i.e., “weak-link” behavior) relates to Josephson-Junction-like c-axis transport.<sup>[31, 35, 37-39]</sup> Other common weak links include Bi2212/impurity interfaces and HAGBs; each affects  $J_c$  at low magnetic field.<sup>[21, 35, 37-39]</sup> Weak links dominate dissipation at low magnetic field whereas intragranular flux motion dominates dissipation at high magnetic field.[35, 39] Considering the magnetic field dependence,  $J_c$  decreases by 30% at  $\sim 0.2$  T in W2, yet only by  $\sim 5\%$  in W1, suggesting a correlation between increased Bi2201 filament content and weak-link behavior.

Figure. 4-5b can be viewed as a flux-pinning energy landscape, with each minima corresponding to the decoupling of a specific type of weak link at a particular magnetic field.

Figure. 4-4b shows a wide Bi2201 intergrowth in a Bi2212 grain extracted from a Bi2212 filament. Wide Bi2201 intergrowths (~ 20 nm width) are ~ 7 times larger than the Bi2212 coherence length, and the interface between Bi2212 and wide Bi2201 intergrowths is not smooth. Thus, these intergrowths act as weak-links.

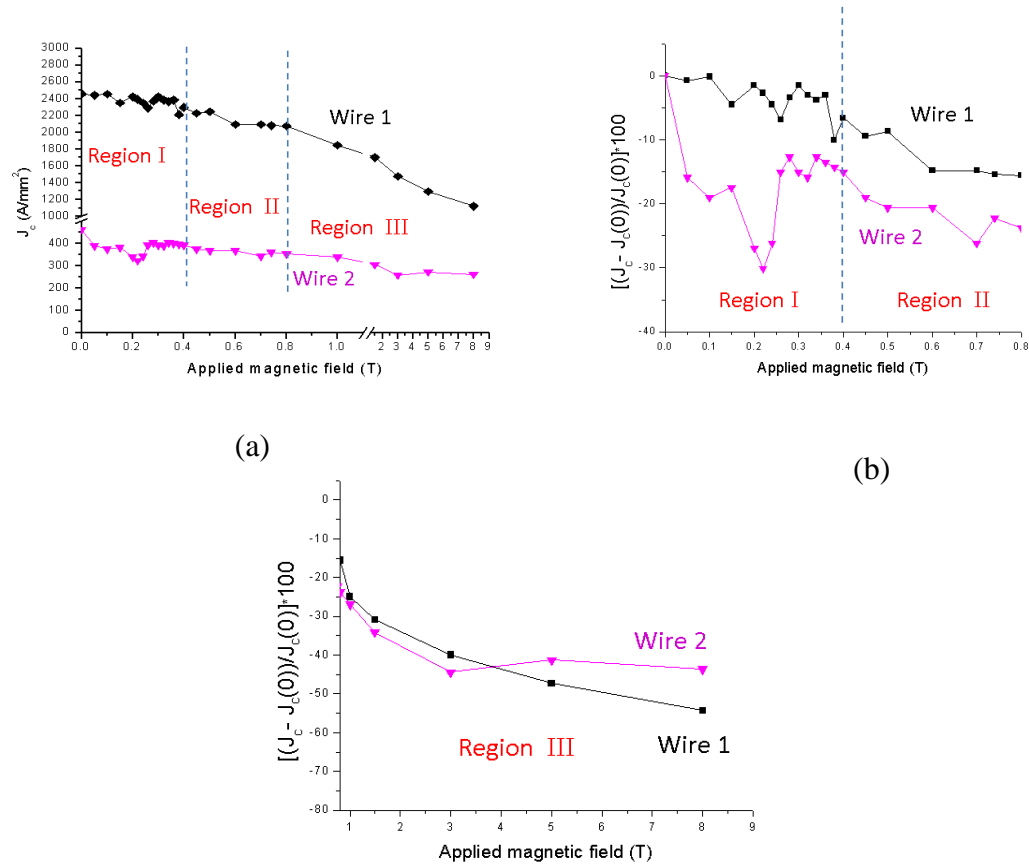


Figure. 4-5. (a) Average  $J_c(4.2\text{ K})$  as a function of magnetic field for W1 and W2. The magnetic field is applied perpendicular to the wire axis. (b) Magnetic field dependence of the normalized  $J_c$  at low magnetic field. Weak links dominate in regions I and II. (c) Magnetic field dependence of the normalized  $J_c$  at high magnetic field (region III). Transport is through strong links only and  $J_c$  is limited by flux pinning.

Figure. 4-5 suggests that when the magnetic field increases above  $\sim 0.2$  T, the Bi2201/Bi2212 interfaces are decoupled, magnetic flux penetrates the Bi2212 grains, and the half-cell and full-cell intergrowths become flux-pinning centers. Thus, as the magnetic field increases,  $J_c$  in W2 increases slightly due to the improved pinning.

The ideal size of magnetic flux pinning centers is on the order of  $\xi$ . [20, 40] The half- and full-cell Bi2201 intergrowth widths are smaller than  $\xi(4.2$  K) but sufficiently large to provide at least weak pinning. Moreover, the lattice parameter ( $c$ ) in a Bi2201 unit cell is 75% of a Bi2212 unit cell, so the presence of a Bi2201 intergrowth reduces the distance between Bi2212 Cu-O planes, locally increasing the effectiveness of Bi2201 intergrowths as flux pinning centers. We expect that HAGBs have similar behavior to Bi2212/Bi2201 interfaces but are decoupled at slightly higher fields and are thus another source of weak-link behavior. We see this, for example, in the W2 behavior at 0.32 T. There is no physical reason for any difference in the HAGB content in the two wire types, and therefore the field-dependence is similar. This behavior continues until all weak links decouple at around 0.4 T. In region II,  $J_c$  decreases gradually with increasing magnetic field. The contribution of the weakly-linked network diminishes at intermediate magnetic fields and disappears at higher magnetic fields. This semi-plateau region illustrates the intragranular intrinsic  $J_c(H)$  behavior of the Bi2212 grains. Unlike weak links, the percolation path in the plateau region is not decoupled by magnetic field. [37]

In region III ( $H > 0.8$  T),  $J_c(H)$  is mainly governed by flux pinning [37] and we observe a slow, consistent decline. As seen in Figure. 4-5c,  $J_c$  decreases more slowly in W2 than W1.

W2 has higher “Bi2201 filament” content and higher Bi2201 intergrowth density within the Bi2212 grains and therefore a higher density of pinning centers. The weaker dependence of  $J_c$  upon  $H$  in W2 is thus a result of the additional flux pinning induced by Bi2201 intergrowths. Previous work has shown that nanotube and nanorod inclusions, ranging from 5-50 nm in diameter, act as extrinsic flux pinning centers in Bi2212, even though they are much larger than  $\xi$ . [27, 28] Intrinsic flux pinning centers are preferred, however, due to their chemical compatibility and stability.

Nanostructural, magnetization and transport studies indicate that Bi2201 intergrowths and  $c$ -axis transport play important roles in Bi2212 transport behavior. The smaller size of half- and full-cell Bi2201 intergrowths, as compared to the Bi2212 coherence length, and their smooth interface with Bi2212, imply that these narrow intergrowths are not barriers to transport. Instead, Bi2201 intergrowths show Josephson-Junction-like behavior at low field and flux pinning at higher field. [31, 41] Wide Bi2201 intergrowths, however, not only provide flux pinning, but also cause weak-link behavior. These results indicate that future improvements in Bi2212 wires and films require the elimination of Bi2201 grains and large intergrowths, but that the presence of half- and full-cell intergrowths is not problematic. More generally, these results provide insight into the types of defects that should be engineered into the structure and as Bi2212 processing matures, an increased focus on engineering the nanostructure in concert with the microstructure is required.

## **ACKNOWLEDGMENTS**

This work was supported by the U.S. Department of Energy, Office of Science, Office of

High Energy Physics, through the SBIR/STTR program. Microstructural characterization was performed at the NC State University Analytical Instrumentation Facility, which is supported by the State of North Carolina and the National Science Foundation. The authors thanks Dr. Yi Liu, formerly of the NC State University Analytical Instrumentation Facility, for his assistance with TEM sample preparation and microscopy. The authors thank William Nachtrab (Supercon) and Frank Hunte (NC State University) for useful discussions.

## REFERENCES

- [1] J. Jiang, H. Miao, Y. Huang, S. Hong, J. A. Parrell, C. Scheuerlein, M. Di Michiel, A. K. Ghosh, U. P. Trociewitz, and E. E. Hellstrom, "Reduction of gas bubbles and improved critical current density in Bi-2212 round wire by swaging," in *Applied Superconductivity, IEEE Transactions on* vol. 23, ed, 2013, pp. 6400206-6400206.
- [2] M. Hanping, H. Yibing, H. Seung, and J. A. Parrell, "Recent Advances in Bi-2212 Round Wire Performance for High Field Applications," *Applied Superconductivity, IEEE Transactions on*, vol. 23, pp. 6400104-6400104, 2013.
- [3] J. Jiang, W. L. Starch, M. Hannion, F. Kametani, U. P. Trociewitz, E. E. Hellstrom, and D. C. Larbalestier, "Doubled critical current density in Bi-2212 round wires by reduction of the residual bubble density," *Superconductor Science and Technology*, vol. 24, p. 082001, 2011.
- [4] T. Shen, A. Ghosh, L. Cooley, and J. Jiang, "Role of internal gases and creep of Ag in controlling the critical current density of Ag-sheathed Bi<sub>2</sub>Sr<sub>2</sub>CaCu<sub>2</sub>Ox wires," *Journal of Applied Physics*, vol. 113, pp. 213901-10, 2013.
- [5] D. Christen, "Superconductors - Current limits to wire technology," *Nature*, vol. 392, pp. 862-863, Apr 30 1998.
- [6] D. Larbalestier, A. Gurevich, D. M. Feldmann, and A. Polyanskii, "High-Tc superconducting materials for electric power applications," *Nature*, vol. 414, pp. 368-377, 2001.

- [7] S. R. Foltyn, L. Civale, J. L. Macmanus-Driscoll, Q. X. Jia, B. Maiorov, H. Wang, and M. Maley, "Materials science challenges for high-temperature superconducting wire," *Nature Materials*, vol. 6, pp. 631-642, Sep 2007.
- [8] G. Naderi, X. Liu, W. Nachtrab, and J. Schwartz, "Understanding processing–microstructure–properties relationships in  $\text{Bi}_2\text{Sr}_2\text{CaCu}_2\text{O}_x$  /Ag round wires and enhanced transport through saw-tooth processing," *Superconductor Science and Technology*, vol. 26, p. 105010, 2013.
- [9] F. Kametani, T. Shen, J. Jiang, C. Scheuerlein, A. Malagoli, M. Di Michiel, Y. Huang, H. Miao, J. A. Parrell, E. E. Hellstrom, and D. C. Larbalestier, "Bubble formation within filaments of melt-processed Bi2212 wires and its strongly negative effect on the critical current density," *Superconductor Science & Technology*, vol. 24, Jul 2011.
- [10] A. Kajbafvala, W. Nachtrab, L. Xi Feng, F. Hunte, L. Xiaotao, N. Cheggour, T. Wong, and J. Schwartz, "Dispersion-Strengthened Silver Alumina for Sheathing  $\text{Bi}_2\text{Sr}_2\text{CaCu}_2\text{O}_{8+x}$  (Bi2212) Multifilamentary Wire," *Applied Superconductivity, IEEE Transactions on*, vol. 22, pp. 8400210-8400210, 2012.
- [11] A. Godeke, P. Acosta, D. Cheng, D. R. Dietderich, M. G. T. Mentink, S. O. Prestemon, G. L. Sabbi, M. Meinesz, S. Hong, Y. Huang, H. Miao, and J. Parrell, "Wind-and-react Bi-2212 coil development for accelerator magnets," *Superconductor Science & Technology*, vol. 23, Mar 2010.
- [12] X. T. Liu, Q. V. Le, and J. Schwartz, "Influencing factors on the electrical transport properties of split-melt processed  $\text{Bi}_2\text{Sr}_2\text{CaCu}_2\text{O}_x$  round wires," *Superconductor Science and Technology*, vol. 25, p. 075008, 2012.
- [13] T. Shen, J. Jiang, F. Kametani, U. P. Trociewitz, D. C. Larbalestier, J. Schwartz, and E. E. Hellstrom, "Filament to filament bridging and its influence on developing high critical current density in multifilamentary  $\text{Bi}_2\text{Sr}_2\text{CaCu}_2\text{O}_x$  round wires," *Superconductor Science and Technology*, vol. 23, p. 025009, 2010.
- [14] W. Zhang and E. E. Hellstrom, "The Development of an Aligned Microstructure during Melt Processing of  $\text{Bi}_2\text{Sr}_2\text{CaCu}_2\text{O}_x$  (BSCCO-2212) Doctor-Bladed Films," *Physica C-Superconductivity and Its Applications*, vol. 218, pp. 141-152, Dec 1 1993.

- [15] E. Cecchetti, P. J. Ferreira, and J. B. Vander Sande, "A model for texture development in BSCCO high-T<sub>c</sub> superconductors," *Superconductor Science & Technology*, vol. 13, pp. 1270-1278, Aug 2000.
- [16] B. Ozcelik, B. Ozkurt, M. E. Yakinci, A. Sotelo, and M. A. Madre, "Relationship Between Annealing Time and Magnetic Properties in Bi-2212 Textured Composites," *Journal of Superconductivity and Novel Magnetism*, vol. 26, pp. 873-878, Apr 2013.
- [17] A. Villaume, D. Bourgault, L. Porcar, A. Girard, C. E. Bruzek, and P. F. Sibeud, "Misalignment angles' reduction in Bi2212 multifilaments melted by dynamic heat treatment under a magnetic field," *Superconductor Science & Technology*, vol. 20, pp. 691-696, Jul 2007.
- [18] E. B. Callaway, G. Naderi, Q. V. Le, and J. Schwartz, "Statistical analysis of the relationship between electrical transport and filament microstructure in multifilamentary Bi<sub>2</sub>Sr<sub>2</sub>CaCu<sub>2</sub>O<sub>x</sub>/Ag/Ag-Mg round wires," *Superconductor Science and Technology*, vol. 27, p. 044020, 2014.
- [19] D. Sager, M. Koch, B. Hallstedt, L. J. Gauckler, and M. Chen, "Enhanced residual secondary phase dissolution by atmosphere control in Bi-2212 superconductors," *Physica C: Superconductivity*, vol. 405, pp. 103-116, 2004.
- [20] B. Heeb, L. J. Gauckler, H. Heinrich, and G. Kostorz, "From imperfect to perfect Bi<sub>2</sub>Sr<sub>2</sub>CaCu<sub>2</sub>O<sub>x</sub> (Bi-2212) grains," *Journal of Materials Research*, vol. 8, pp. 2170-2176, 1993.
- [21] S. Graser, P. J. Hirschfeld, T. Kopp, R. Gutser, B. M. Andersen, and J. Mannhart, "How grain boundaries limit supercurrents in high-temperature superconductors," *Nature Physics*, vol. 6, pp. 609-614, Aug 2010.
- [22] M. R. Koblishka and U. Hartmann, "Analysis of high-T<sub>c</sub> superconductor compounds on the nanometre scale," *physica status solidi (c)*, vol. 2, pp. 1726-1731, 2005.
- [23] A. Llodes, A. Palau, J. Gazquez, M. Coll, R. Vlad, A. Pomar, J. Arbiol, R. Guzman, S. Ye, V. Rouco, F. Sandiumenge, S. Ricart, T. Puig, M. Varela, D. Chateigner, J. Vanacken, J. Gutierrez, V. Moshchalkov, G. Deutscher, C. Magen, and X. Obradors,

- "Nanoscale strain-induced pair suppression as a vortex-pinning mechanism in high-temperature superconductors," *Nature Materials*, vol. 11, pp. 329-336, Apr 2012.
- [24] M. Nishiyama, G. Kinoda, Y. Zhao, T. Hasegawa, Y. Itoh, N. Koshizuka, and M. Murakami, "Nanometre-sized inhomogeneity in high-J(c) Bi<sub>2</sub>Sr<sub>2</sub>CaCu<sub>2</sub>O<sub>8+delta</sub> superconductors," *Superconductor Science & Technology*, vol. 17, pp. 1406-1410, Dec 2004.
- [25] J. Sosnowski, "Critical current problems in HTc superconductors with nanoscale pinning centers," *7th European Conference on Applied Superconductivity (Eucas'05)*, vol. 43, pp. 659-662, 2006.
- [26] G. Blatter, M. V. Feigel'man, V. B. Geshkenbein, A. I. Larkin, and V. M. Vinokur, "Vortices in high-temperature superconductors," *Reviews of Modern Physics*, vol. 66, pp. 1125-1388, 1994.
- [27] H. Yamasaki and K. Endo, "Nanostructural defects for effective flux pinning in high-quality Bi<sub>2</sub>Sr<sub>2</sub>CaCu<sub>2</sub>O<sub>8+x</sub> epitaxial thin films with high critical current density," *Superconductor Science and Technology*, vol. 24, p. 10, 2014.
- [28] P. Yang and C. M. Lieber, "Nanorod-Superconductor Composites: A Pathway to Materials with High Critical Current Densities," *Science*, vol. 273, pp. 1836-1840, September 27, 1996 1996.
- [29] K. Fossheim, E. D. Tuset, T. W. Ebbesen, M. M. J. Treacy, and J. Schwartz, "Enhanced flux pinning in Bi<sub>2</sub>Sr<sub>2</sub>CaCu<sub>2</sub>O<sub>8+x</sub> superconductor with embedded carbon nanotubes," *Physica C: Superconductivity*, vol. 248, pp. 195-202, 1995.
- [30] C. Pegrum, "High-Temperature Superconductivity - Natural Josephson-Junctions," *Nature*, vol. 358, pp. 193-193, Jul 16 1992.
- [31] R. A. Klemm, "Bi<sub>2</sub>212 c-axis twist bicrystal and artificial and natural cross-whisker Josephson junctions: Strong evidence for s-wave superconductivity and incoherent c-axis tunneling," *Journal of Superconductivity*, vol. 18, pp. 697-700, Nov 2005.
- [32] U. w. b. i. b. AIP.

- [33] T. Örd, K. Rågo, and A. Vargunin, "Critical and Non-Critical Coherence Lengths in a Two-Band Superconductor," *Journal of Superconductivity and Novel Magnetism*, vol. 25, pp. 1351-1356, 2012/07/01 2012.
- [34] D. Agassi, D. K. Christen, and S. J. Pennycook, "Flux pinning and critical currents at low-angle grain boundaries in high-temperature superconductors," in *Applied Physics Letters* vol. 81, ed, 2002, pp. 2803-2805.
- [35] X. Cai, A. Polyanskii, Q. Li, G. Riley, and D. Larbalestier, "Current-limiting mechanisms in individual filaments extracted from superconducting tapes," *Nature*, vol. 392, pp. 906-909, 1998.
- [36] C. P. Bean, "Magnetization of High-Field Superconductors," *Reviews of Modern Physics*, vol. 36, pp. 31-&, 1964.
- [37] D. C. Van der Laan, J. Schwartz, B. ten Haken, M. Dhalle, and H. J. N. van Eck, "Limits to the critical current in  $\text{Bi}_2\text{Sr}_2\text{Ca}_2\text{Cu}_3\text{O}_x$  tape conductors: The parallel path model," *Physical Review B*, vol. 77, Mar 2008.
- [38] H. W. Weijers, B. ten Haken, H. H. J. ten Kate, and J. Schwartz, "Field dependence of the critical current and its relation to the anisotropy of BSCCO conductors and coils," *Ieee Transactions on Applied Superconductivity*, vol. 15, pp. 2558-2561, Jun 2005.
- [39] B. Xu, J. H. Su, and J. Schwartz, "Dependence of transport critical current of magnetic field processed  $\text{B}_2\text{Sr}_2\text{CaCu}_2\text{O}_8/\text{AgMg}$  tapes on the background magnetic field and magnetic field direction," *Superconductor Science & Technology*, vol. 18, pp. 503-507, Apr 2005.
- [40] D. Larbalestier, "High-Temperature Superconductors - Critical Currents Pinned Down," *Nature*, vol. 343, pp. 210-211, Jan 18 1990.
- [41] R. Kleiner and P. Müller, "Intrinsic Josephson effects in high- $T_c$  superconductors," *Physical Review B*, vol. 49, pp. 1327-1341, 1994.

## APPENDICES

Supplementary information

**On the roles of  $\text{Bi}_2\text{Sr}_2\text{CuO}_x$  intergrowths in  $\text{Bi}_2\text{Sr}_2\text{CaCu}_2\text{O}_x/\text{Ag}$  round wires: c-axis transport and magnetic flux pinning**

Golsa Naderi and Justin Schwartz

Department of Materials Science and Engineering, North Carolina State University

Raleigh, NC 27695-7907, U.S.A.

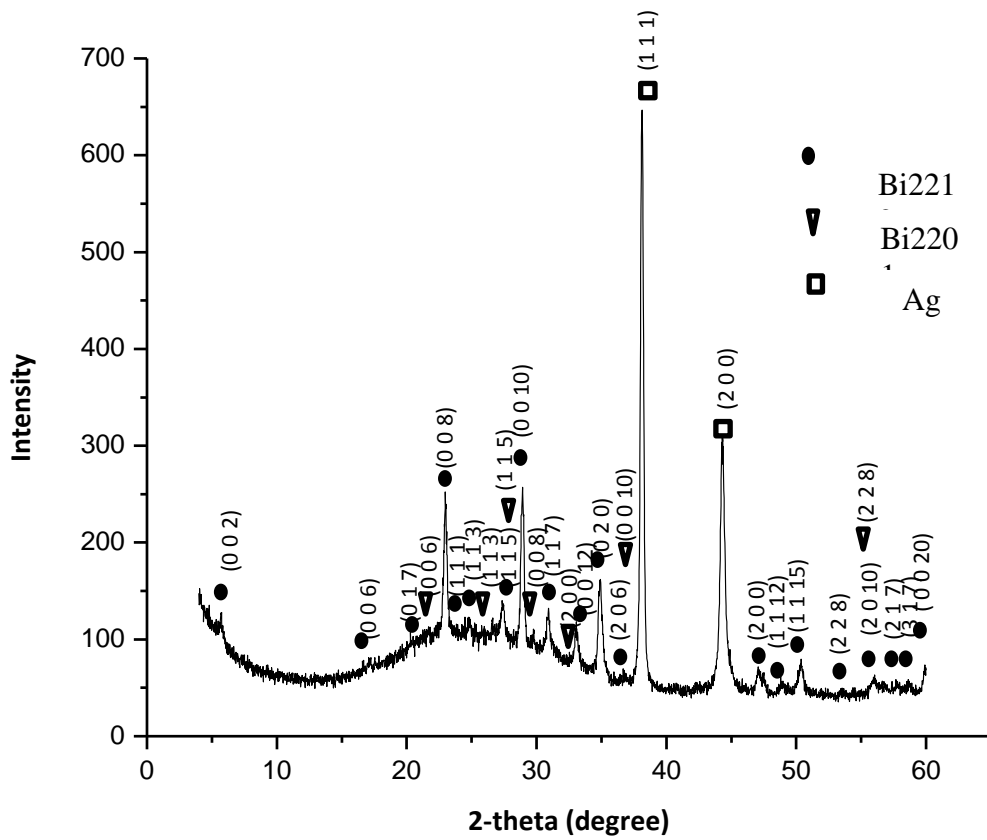


Figure 4-S1. XRD of powder obtained by grinding Bi2212 filaments that remain after etching the silver matrix.

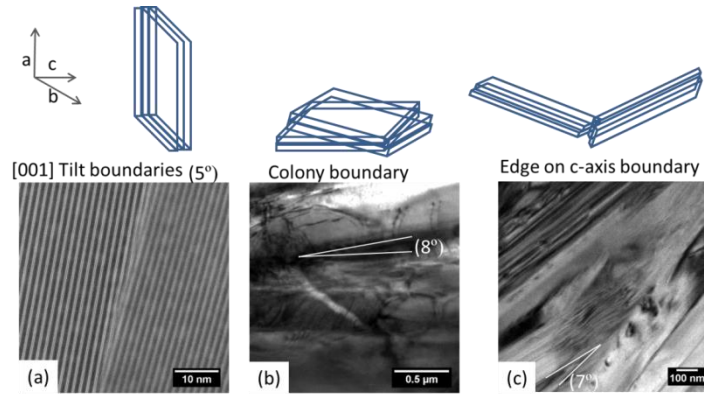


Figure 4-S2. (a) STEM image of a [001] tilt boundary, (b) bright field TEM image of a 8° colony boundary, (c) bright field TEM image of an edge on c-axis grain boundary. Schematic drawings of each are also shown

Bi2212 grains are plate-like with large a- and b- dimensions. During solidification these grains are aligned such that they share a common c-axis with some degree of sliding and tilting relative to the a or b directions. The HAADF-STEM image in Figure. 4-S2a is an example of a 5° [001] tilt boundary. [001] twist and tilt boundaries are thus the most common grain boundary types, and as a result stacks of Bi2212 plates form colonies. Figure 4-2Sb shows a typical bright field (BF) TEM image of an 8° colony boundary and Figure. 4-2Sc demonstrates an edge-on c-axis grain boundary, where two grains collide at a 7° angle through their c axes.

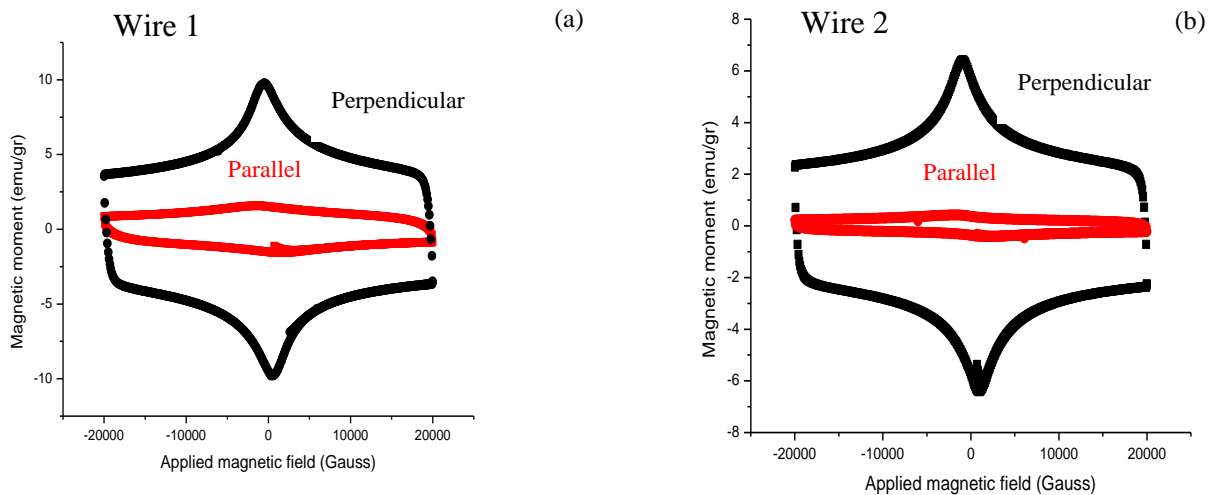


Figure 4-S3. (a) Magnetization hysteresis for (a) wire 1 (high  $J_c$ ) and (b) wire 2 (low  $J_c$ ).

## Experimental Section

Bi2212/Ag wire is made by Supercon, Inc., by the powder-in-tube method. The wire outer diameter is 0.787 mm and contains 928 filaments, each nominally 20  $\mu\text{m}$  in diameter. Detailed wire characteristics and heat treatment profiles have been reported previously.<sup>[8]</sup> Critical current ( $I_c$ ) is measured using the four-probe method in liquid helium (4.2 K) in magnetic fields up to 8 T generated by a 200 mm warm-bore superconducting magnet. A  $10^{-8}$   $\text{V m}^{-1}$  electric field criterion, with 20 mm voltage tap spacing, is used to determine  $I_c$ . Each measurement is performed on at least three samples, and  $J_c$  is calculated by dividing the average  $I_c$  by the superconductor area in the green-wire cross-section. XRD is carried out by Rigaku RadB system having  $\text{CuK}\alpha$  radiation ( $\lambda=1.5405 \text{ \AA}$ ) with a 0.002 step size. The time at each step is 5 s. To have sufficient Bi2212 counts in the XRD, the outer Ag sheath is chemically etched in a  $\text{NH}_4\text{OH}/\text{H}_2\text{O}_2$  solution and then the Bi2212 filaments are ground to powder. Two SEMs, a Hitachi S3200 and a FEI Quanta 3D field emission gun, both in backscatter mode, are used to image the microstructure. Samples are prepared for SEM by mounting small pieces of wire using a Durocit cold mounting liquid with graphite added so that the mounting is conductive. Mounted samples are polished using SiC paper, 1.0  $\mu\text{m}$  and 0.3  $\mu\text{m}$  alumina suspensions. Longitudinal SEM imaging uses chemically etched samples. Complete removal of Ag is not possible because Ag also fills the intrafilamentary space. A Focused Ion Beam lift-out technique is used to produce electron transparent samples from specific filaments. The region of interest (RoI) is found in the electron column of FEI Quanta 3D, Pt is deposited to protect the RoI, followed by bulk milling and cross-sectional clean up to fix the wedge effect at the bottom of the milled area while the sample is tilted to 52°. By

tilting the sample to  $7^\circ$ , a U shape cut is performed and the Omni probe is used to cut free and lift out the sample. The sample then is attached to a Mo grid and final polishing is performed with lower ion beam currents until the sample is sufficiently thin. The FEI Titan 80-300 probe aberration corrected STEM with monochromator is used to study Bi2201 intergrowths within Bi2212 grains in both filament types. The JEOL 2000FX TEM is used for bright field imaging. A Quantum Design superconducting quantum interface device is used to measure the magnetization hysteresis at 4.2 K with a step-size of 0.01 T in the range of 0 to 2 T on 5 mm long samples orientated parallel and perpendicular to the magnetic field.

## Chapter 5

### **Multiscale studies of processing-microstructure-transport relationships in over-pressure processed $\text{Bi}_2\text{Sr}_2\text{CaCu}_2\text{O}_x/\text{Ag}$ multifilamentary round wire**

G. Naderi<sup>a</sup> and J. Schwartz

Department of Materials Science and Engineering, North Carolina State University  
Raleigh, NC 27695-7907, U.S.A.

**Abstract:** Recently, significantly improved transport properties in  $\text{Bi}_2\text{Sr}_2\text{CaCu}_2\text{O}_x/\text{Ag}$  ( $\text{Bi}2212/\text{Ag}$ ) multifilamentary round wire (RW) has been achieved by applying 100 atm over-pressure (OP) during partial melt processing (PMP). Despite this significant progress, the microstructural details and phase evolution during the high pressure partial melt processing are poorly understood, and previous studies have focused solely on densification. Here we investigate the processing-microstructure-transport relationships of OP-PMP RWs by comparing the filament microstructure of a PMP wire with that of an OP-PMP wire on multiple length scales. OP affects the microstructure differently in each stage of PMP: it causes grain growth during pre-annealing, increases the peritectic melting temperature in the partial melt, improves oxygen uptake during solidification, and enhances grain connectivity during sintering. It is also found that OP-PMP wire is related to increase in filament density. Yet OP-PMP wire shows higher area fraction of filaments with large  $\text{Bi}2201$  grains. Thus, to further improve transport, optimization of OP-PMP is essential; in particular the maximum heat treatment temperature should be increased, consistent with the increase in peritectic melt temperature, such that less  $\text{Bi}2201$  grains form during processing.

## Introduction

High magnetic field is needed to create exotic magnetic states in advanced electronic materials and to improve resolution and performance of biological and chemical analysis systems [1]. Dipoles and quadrupoles for high energy hadron colliders beyond the Large Hadron Collider, solenoids for muon cooling in a neutrino factory or a muon collider and high-field nuclear magnetic resonance spectrometers are example applications of high field ( $> 25$  T) superconducting magnets [2-4]. Among technical high temperature superconductors, only  $\text{Bi}_2\text{Sr}_2\text{CaCu}_2\text{O}_x/\text{Ag}$  (Bi2212/Ag) multifilamentary round wires (RWs) show isotropic electromagnetic behavior and high current density ( $J_c$ ) at high magnetic field, so they are of particular technological interest [5-7].

*Partial melt processing:* Partial melt processing (PMP) in 1 atm oxygen partial pressure ( $p\text{O}_2$ ) is the most common heat treatment approach to obtain  $J_c$  in Bi2212/Ag RWs. In 1 atm  $p\text{O}_2$ , Bi2212 melts peritectically into a liquid and two solid phases,  $(\text{Sr,Ca})_{14}\text{Cu}_{24}\text{O}_x$  (AEC) and  $\text{Bi}_2(\text{Sr,Ca})_2\text{O}_x$  (CF). During PMP, after a pre-annealing step, the Bi2212/Ag wire is heated to a maximum temperature ( $T_{\text{max}}$ ) above the Bi2212 peritectic temperature ( $T_p$ ), held for a few minutes ( $t_{\text{max}}$ ) at  $T_{\text{max}}$ , cooled using a two-step process, and finally sintered for a 48 hrs [7-11].

The liquid created in the Bi2212 peritectic melt is ionic. The oxidation state of Cu is between +1 and +2 and that of Bi is +3 or lower. In solid Bi2212 and secondary phases, the oxidation state of Cu can exceed +2 and of Bi can exceed +3. Thus, Bi2212 peritectic melting is

accompanied by oxygen release, which decreases if the oxygen partial pressure in the processing atmosphere increases [12-15].

During the first stage of cooling from the melt, Bi2212 reforms through two routes: direct solidification from the melt and a reverse peritectic reaction between the liquid and solid phases. Due to phase segregation, however, the direct solidification forms  $\text{Bi}_2\text{Sr}_2\text{CuO}_x$  (Bi2201) grains and intergrowths between and within Bi2212 grains. Likewise, the reverse reaction is not always complete and some AEC and CF phases remain after full processing [7-11]. When AEC and CF grains are absent locally, direct solidification is dominant and filaments with large Bi2201 grains are common. In both solidification routes, the oxygen content must be recovered [16, 17].

In previous studies filaments within Bi2212 RWs were analyzed and categorized based upon the area fraction of grains of the multiple phases present. For example, filaments with area fractions greater than 10% Bi2201 were labeled as “Bi2201 filaments” and similarly for other phases. Results showed that “Bi2201 filaments” are more detrimental to transport properties than any other secondary phase present [11, 17]. Previous works also showed that Bi2201 forms as intergrowths within Bi2212 grains and plays several roles in Bi2212 wire transport [11]. Bi2201 intergrowths form in multiple widths: half-cell, full-cell and “wide” (10-20 nm). The size of half- and full-cell Bi2201 intergrowths as compared to the Bi2212 coherence length, and their smooth interface with Bi2212, imply that these narrow intergrowths are not barriers to transport. Instead, they show Josephson-Junction-like behavior at low magnetic field and flux pinning at higher magnetic field. Wide Bi2201 intergrowths, however, not only

provide flux pinning, but also cause weak-link behavior [11, 18, 19]. After solidification, in the second stage of cooling and during sintering, the solid state reaction between Bi2201 and secondary phases increases the Bi2212 content; but in no case is phase-pure Bi2212 found in fully-PMPed Bi2212 RW.

Porosity: Bi2212/Ag RWs are manufactured by the powder-in-tube (PIT) method using phase-pure Bi2212 starting powder. After wire deformation, the density of the Bi2212 powder in the filaments is less than 70% of theoretical density. Initially, the 30-40% void or gas is uniformly distributed, but during PMP it agglomerates and forms voids (porosity) which reduces electrical transport.

Kametani *et al.* studied the microstructure of both quenched and fully processed wires and found an inverse relationship between  $J_c$  and bubble density [20]. Bubbling, and the corresponding low density of Bi2212 filaments, are a significant challenge to increased  $J_c$  and thus applications of Bi2212/Ag RWs [5, 20-22].

Grain connectivity: Ideally, after PMP, the Bi2212 phase reforms into a network of Bi2212 grains with end-to-end connectivity [9, 16]. In polycrystalline superconductors, if the misorientation angle is small then those grains will be connected electrically, but if high angle and/or porous grain boundaries exist, the boundaries act as weak-links, greatly reducing transport [23]. Clem suggested a model in which a weak link is a Josephson (J) medium such that Josephson vortices form and the intergranular coupling is weak. Based on this, there is an initial flux penetration field,  $H_{C1}^J$ , which is less than the magnetic field of initial flux penetration into the grains themselves,  $H_{C1}^G$ . This description is consistent with our

previous observations that in the magnetic energy landscape each minima corresponds to the decoupling of a specific type of weak link [11]. In this scenario, flux penetration into such a granular sample occurs in several steps. The magnetic field is completely shielded until  $H_{C1}^J$ ; at  $H_{C1}^J$  flux enters the sample in the form of Josephson vortices into the granular area and strongly superconducting grains are shielded. When  $H_{C1}^G$  is reached, Abrikosov vortices form inside the superconducting grains, which are then completely decoupled from each other [23, 24].

Over-pressure processing: The application of hot isostatic pressure (HIP) to high temperature superconductors was first studied by Landingham *et al.* [25]. HIP was shown to improve the transport properties by increasing the grain boundary coupling [26, 27]. Typically, the primary effects of HIPping on the microstructure are porosity elimination and grain growth. The driving force for densification is to decrease the surface area and surface energy of the pores [28]. The internal pressure in the pores opposes the driving force for the shrinkage. As the pores shrink, the gas dissolves into the matrix [28].

Previously, a HIP was used to perform over-pressure (OP) processing on Bi2223 tapes [29-33]. OP increases the density and connectivity of Bi2223 filaments and suppresses Pb evaporation from Bi2223 wires [29-33]. More recently, OP has been used to reduce bubbling and porosity in PMP Bi2212/Ag RWs [5, 21, 34]. Sufficiently high OP uses creep of the silver matrix to densify Bi2212 filaments and increase wire transport [5, 21]. It was shown that a 100 atm OP significantly densifies Bi2212 filaments in Bi2212/Ag RWs, resulting in a significant increase in Bi2212/Ag RW transport [5].

Since OP increases the filament density in Bi2212/Ag RWs, the significant in transport properties is understandable. What remain unknown, however, are the effects of OP on phase transformations during PMP. For example, a large area fraction of Bi2201 filaments is found in Bi2212/Ag wire after OP-PMP. Therefore, to better understand the effects of OP on phase transformations in Bi2212/Ag RWs, we compare the structures of wire cross-sections and Bi2212 filaments extracted from PMP and OP-PMP wires on multiple length scales.

### **Experimental approach**

The Bi2212/Ag wire studied is prepared by Supercon, Inc., using the powder-in-tube method. Figure 5-1 shows a cross-sectional image of the green wire with an outer diameter of 0.8 mm and 1050 filaments, each nominally 14.4  $\mu\text{m}$  in diameter. The wire is heat treated with the PMP temperature-time profile shown in Figure 5-2. OP-PMP is performed at the National High Magnetic Field Laboratory using the same temperature-time profile.

Critical current ( $I_c$ ) is measured using the four-probe method in liquid helium (4.2 K) in a 5 T magnetic field generated by a 200 mm warm-bore superconducting magnet. A  $10^{-8}$  V  $\text{m}^{-1}$  electric field criterion, with 20 mm voltage tap spacing, is used to determine  $I_c$ . Note that  $I_c$  of the OP-PMP wire is measured at the National High Magnetic Field Laboratory using the same approach. All  $I_c$  values are the average of three samples; sample-to-sample variations are less than 10%.  $J_c$  is calculated by dividing the average  $I_c$  of the three samples by the superconductor area in the green-wire cross-section. A Quantum Design superconducting quantum interface device (SQUID) is used to measure the superconducting-to-normal transition temperature upon warming in 50, 100, 500, and 1000 Oe magnetic fields parallel to

the wire. The magnetization measurements are performed on 3 mm long samples cut from wires after PMP and OP-PMP. Critical transition temperatures of the two wires are compared based on their normalized magnetization (normalized to the maximum magnetic moment) as a function of temperature.

A Hitachi S3200 scanning electron microscope (SEM) in backscatter mode is used to image the wire microstructures. Samples are prepared by mounting small pieces of wire using a Durocit cold mounting liquid with graphite added so that the mounting is conductive. Mounted samples are polished using SiC paper, 1.0  $\mu\text{m}$  and 0.3  $\mu\text{m}$  alumina suspensions. The interior filament structure is studied using a focused-ion beam (FIB) in a FEI Quanta 3D. A  $20\times 2\times 2$   $\mu\text{m}$  Pt bar is deposited on the region of interest (RoI) while a 30 kV, 15 nA Ga ion is used for rectangular milling and 3 nA is used for the cleaning cross-section. After the rectangular milling, the SEM is used for imaging the interior of the filaments.

A FIB lift-out technique is used to produce electron transparent samples from specific filaments. The RoI is found in the electron column of the FEI Quanta 3D, a  $15\times 2\times 2$  Pt bar is deposited to protect the RoI, followed by ion bulk milling (15 nA) and ion cross-sectional clean-up (7 nA) to fix the wedge effect at the bottom of the milled area while the sample is tilted to  $52^\circ$ . At  $0^\circ$  tilt, a U shape cut by a 3 nA ion beam is performed and the Omni probe is used to cut free and lift out the sample. The sample then is attached to a Mo grid and final polishing is performed with lower ion beam currents (0.3 to 0.1 nA) until the sample is sufficiently thin. The FEI Titan 80-300 probe aberration corrected scanning transmission electron microscopy (STEM) with monochromator is used to study Bi2201 intergrowths

within Bi2212 grains. The Titan SuperX Energy Dispersive Spectrometry (SuperX EDS) system, equipped with the four Bruker Silicon Drift Detectors, is used to collect characteristic X-Ray signals at different specimen sections. To reduce beam damage, an 80 kV accelerating voltage is used for STEM EDS studies. Areas adjacent to the Bi2201 grains are avoided to exclude the effect of Bi2201 in EDS quantification of Bi2212.

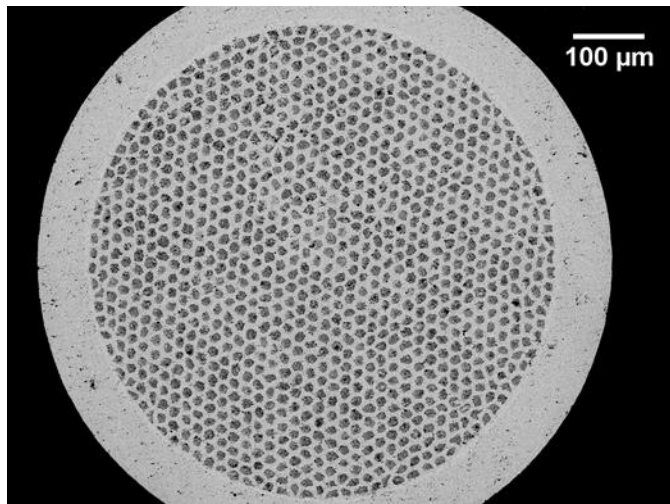


Figure 5-1 Scanning electron microscope cross-sectional transverse view of unreacted wire

## Results

Table 5-1 summarizes the  $I_c$  and  $J_c$  results for the PMP and OP-PMP Bi2212/Ag wires. OP increases transport of the PMP wires by almost 70%. Figure 5-3 compares SEM cross-sectional images of PMP and OP-PMP wires. Using the same image analysis protocols reported previously [17], the area fraction of filaments containing large Bi2201 grains

(“Bi2201 filaments”) in the PMP cross-section is 32% whereas in the OP-PMP wire it is 65%. Note that the criteria defined previously is such that if the Bi2201 area fraction within a filament is more than 10%, that filament is termed a “Bi2201 filament”, even if the primary phase is a Bi2212 [17].

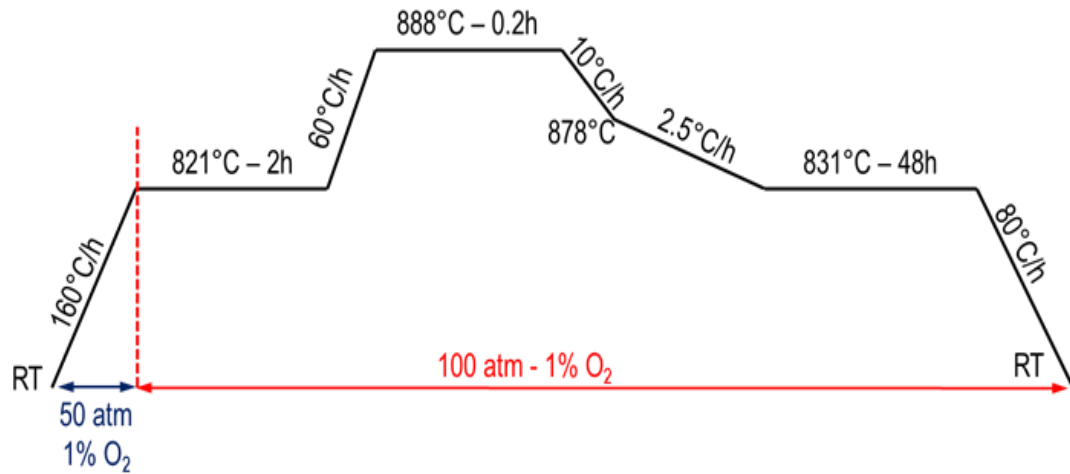


Figure 5-2 PMP temperature-time profile. The same profile is used for conventional PMP and OP-PMP.

Table 5-1  $I_c$  and  $J_c$  at 4.2 K, 5 T, for the PMP and OP-PMP Bi2212/Ag wires

	$I_c$ (A)	$J_c$ (A/mm <sup>2</sup> )
PMP	157	908
OP-PMP	264	1560

Figure 5-4 shows interior views of filaments from PMP and OP-PMP wires after FIB cross-sectioning. Significantly less voids are seen in the OP-PMP wire, yet some voids clearly remain. Large Bi2201 grains are also clear in the OP-PMP wire that are not as prevalent in the PMP wire. The high angle annular dark field (HAADF)-STEM image in Figure 5-5 shows the existence of porous grain boundaries in the PMP wire, whereas the OP-PMP wire does not contain such porous boundaries. Figure 5-6 shows the HAADF-STEM images of different Bi2212 grains extracted from Bi2212 and Bi2201 filaments of PMP and OP-PMP wires. Consistent with our previous results [11], Bi2201 intergrowth densities are higher in Bi2212 grains extracted from Bi2201 filaments than those extracted from Bi2212 filaments; this is the case for both PMP and OP-PMP wires; Bi2201 intergrowths in Bi2212 grains of a Bi2201 filament in an OP-PMP wire, however are more uniformly distributed than those in the PMP wire. Semi-quantitative EDS results of the four samples shown in Figure 5-6 are summarized in Table 5-2; each data point is the average of more than five different regions in each specimen obtained from  $\sim 20 \times 60 \text{ nm}^2$  hyper maps. Areas adjacent to the Bi2201 grains are avoided to exclude the effect of Bi2201 in EDS quantification of Bi2212 grains. Note that presence of heavy elements suppresses oxygen detection with EDS, so in all samples the O atomic percentage (at%) is below stoichiometric, influencing the at% of all other cations. Ca is the most consistent element with only small variations in different areas of the sample. EDS results near a Bi2201 grain, however, show that the Ca content increases with the distance from the Bi2201 grain until  $\sim 50 \text{ nm}$  and then remains fairly constant. Sr deficiency is observed in all samples, which is beneficial for transport because strontium deficiency is charge-compensated by the creation of electron holes in the  $\text{CuO}_2$  layer [35]. The standard

deviations in all elements of both OP-PMP samples are much less than those of PMP samples, indicating improved compositional homogeneity on the nanoscale.

Figure 5-7 plots the magnetization versus temperature in magnetic fields ranging from 50-1000 Oe for PMP and OP-PMP wires. For both wire types,  $T_c(100 \text{ Oe})$  is 75 K and decreases with increasing magnetic field. Figure 5-8 shows grain colonies extracted from a Bi2212 filament of the PMP wire that is selected for the hyper map; the semi-quantitative EDS-STEM results from this area are given in Table 5-3. The sample thickness, tilt angle, and grain orientation affect the oxygen count significantly; therefore grains with similar orientation and thickness are studied and very thin or thick areas are avoided. Figure 5-9 shows a HAADF STEM image of Bi2212 grains; on the left side of the image zone axis is close to [100], whereas on the right side the zone axis is closer to [010]. The observed modulation in the [010] zone of Figure 5-9 is caused by extra oxygen atoms located in the Bi-O layers in every five sub-cells [35, 36].

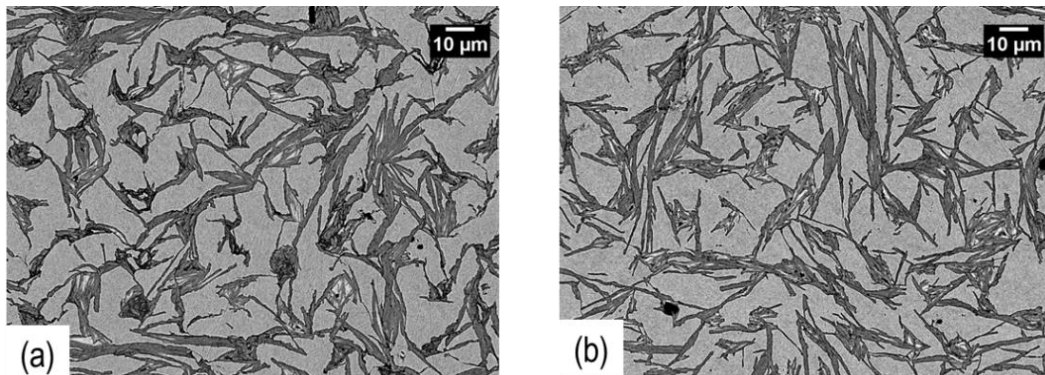


Figure 5-3 SEM cross sectional view of a) PMP and b) OP-PMP wire.

## Discussion

OP densifies Bi2212 filaments on multiple length scales: Comparing the microstructures of the PMP and OP-PMP wires in Figure 5-4 one observes that the density is improved in OP-PMP wire; this is the primary reason for the improvement in  $J_c$  in OP-PMP wires. In the SEM image of Figure 5-4b, however, smaller than 2  $\mu\text{m}$  size triangular voids are observed between Bi2212 grains. These voids appear to be the empty spaces between the plate-like Bi2212 grains. Due to the geometrical limitations, these voids are unavoidable unless the Bi2212 grains stack perfectly. If grains were smaller, then the voids are would be correspondingly smaller but still present. Therefore, high pressure does not result in 100% dense filaments throughout the wire and other phase transformation routes are required if further densification is sought.

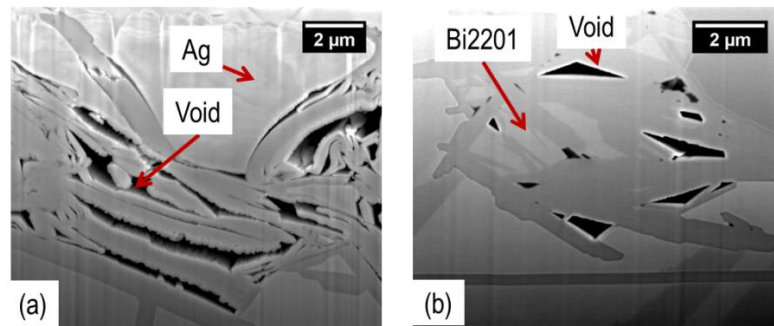


Figure 5-4 Interior view of filaments from a) PMP and an b) OP-PMP wires after FIB cross-sectioning

The HAADF-STEM images shown in Figure 5-5 show the extensive presence of porous grain boundaries in Bi2212 grain colonies of the PMP sample, but well coupled Bi2212

grains of OP-PMP. Thus, OP-PMP reduces porosity on multiple length scales. As observed in prior studies, high pressure heat treatment improves diffusion across grain boundaries due to the stress gradients between the grain boundaries and pores [25, 28, 37, 38]. This leads to a better connectivity between Bi2212 grains and reduces the formation of porous grain boundaries in Bi2212 filaments of the OP-PMP wire.

OP affects Bi2212 peritectic melting behavior and the filament structure: Extensive Bi2212 grain growth is expected during the OP-PMP pre-annealing step [38]. With a 100 atm pressure, this step can be likened to an intermediate HIPping. Because the 100 atm pressure is far below the yield strength of Ag, AgMg and Bi2212, no rapid densification (yielding) and limited power-law creep is expected; instead significant grain growth by long-range diffusion is more probable [28, 39].

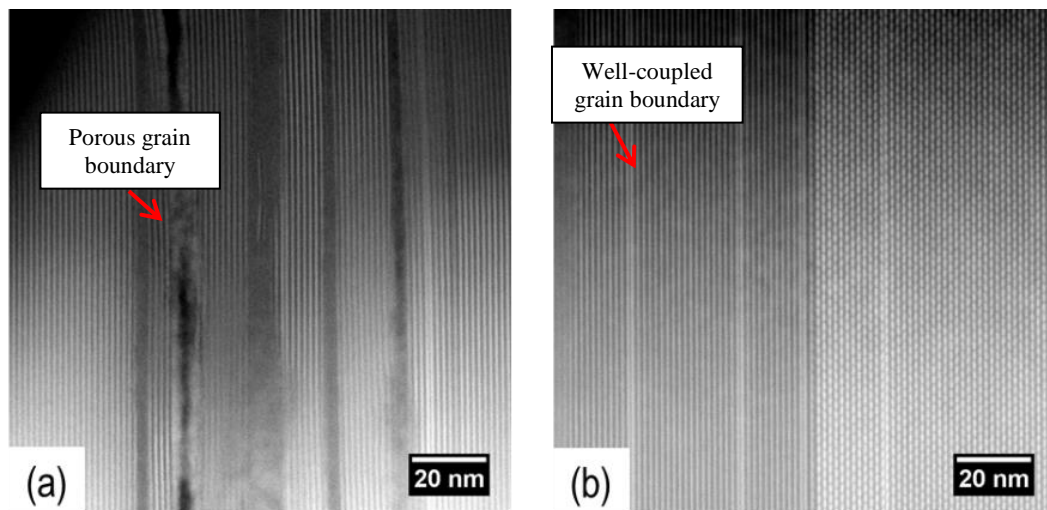


Figure 5-5 HAADF STEM images of a) Bi2212 grain colonies from a PMP wire showing porous grain boundaries. b) Well-connected Bi2212 grains in a OP-PMP wire

In general, for materials that increase in density during solidification, isostatic pressure increases the melting point. Thus, 100 atm of isostatic pressure likely changes the peritectic melting point ( $T_p$ ) of Bi2212 by a few °C. Furthermore, grain growth during the OP pre-annealing step can also increase the  $T_p$  of Bi2212. Several studies have shown that the maximum heat treatment temperature ( $T_{max}$ ) during PMP should be carefully chosen, such that it is sufficiently above  $T_p$  to ensure melting but not so high as to result in excessive phase segregation. A change of only a few °C in  $T_{max}$  relative to  $T_p$  alters the phase evolution during solidification and reduces the resulting  $J_c$  [40-48].

If  $T_{max}$  is optimally chosen relative to  $T_p$ , then during cooling sufficient liquid and secondary phases react to form filaments with layered Bi2212 grains (“Bi2212 filament”) instead of filaments with large Bi2201 grains (“Bi2201 filament”). This was not considered in the OP-PMP however, and the same  $T_{max}$  was used for both PMP and OP-PMP. As a result, since the optimum  $T_{max}$  is related to  $T_p$ , the OP-PMP wire was heat treated with a  $T_{max}$  that was likely several °C lower than optimum, altering the generation of liquid and secondary phases during the peritectic melt.

Analyzing the SEM images in Figure 5-3, one finds that in a typical OP-PMP cross-section, the percentage of Bi2201 filaments is doubled compared to that of typical PMP wire. Increased Bi2201 filament content was shown previously to decrease wire  $J_c$  [11, 17]. Therefore, for OP-PMP, increased  $T_{max}$  would lead to increased liquid and secondary phases, thus favoring the reverse peritectic reaction over direct solidification and the formation of preferred Bi2212 filaments over Bi2201 filaments [40, 42-48]. Consistent with our results in

the previous chapter, here OP wire with more Bi2201 filaments shows higher an-isotropic behavior in magnetic measurement with similar approach as Chapter 4 [11]. Improved density and improved a-b transport could be another factor for the an-isotropic behavior.

OP affects the nanoscale structure: Consistent with STEM results in [11] the density of Bi2201 intergrowths in Bi2212 grains extracted from Bi2201 filaments is higher in both PMP and OP-PMP wires as compared to samples extracted from layered Bi2212 filaments. The wide-band intergrowths seen in [11], however are absent in the wires in this study. The formation of wider intergrowths may be related to the several melting events in the cyclic heat treatment (saw-tooth-processing) used in that study [11, 16].

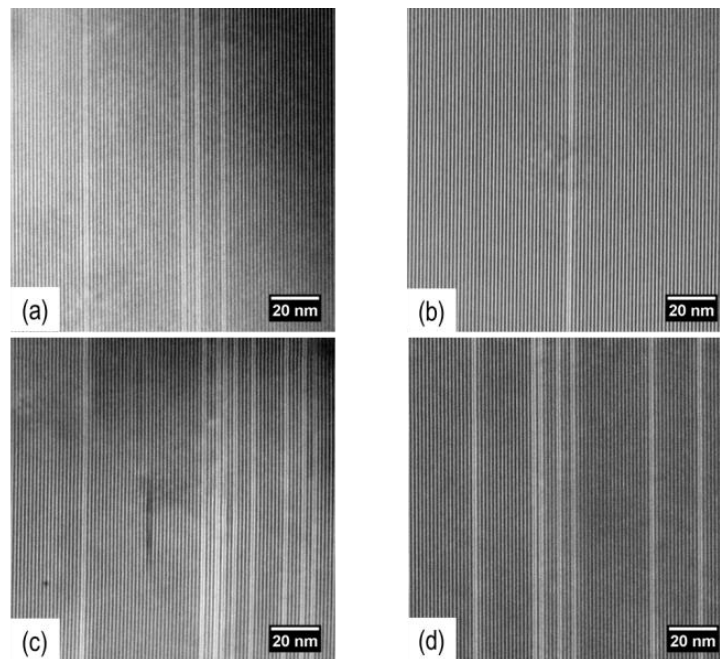


Figure 5-6 HAADF-STEM images of Bi2212 grains extracted from Bi2212 filaments from a) PMP wire, b) OP-PMP wire, and Bi2212 grains extracted from Bi2201 filaments from a c) PMP wire d) OP-PMP wire.

STEM EDS results summarized in Table 5-2 indicate that the oxygen distribution in different filaments of both wires is not uniform. Based on the smaller standard deviations, OP-PMP wire shows less oxygen inhomogeneity compared to that of the PMP wire. Oxygen content in Bi2212 grains depends upon their solidification route.

Table 5-2 Semi-quantitative EDS results of the corresponding four samples (shown in Figure 5-6)

Element	PMP Bi2201 Filament		PMP Bi2212 Filament		OP-PMP Bi2201 Filament		OP-PMP Bi2212 Filament	
	at.%	standard deviation	at.%	standard deviation	at.%	standard deviation	at.%	standard deviation
Bi	19.9	0.95	22.2	2.01	18.0	0.48	21.7	0.39
Sr	17.8	0.79	20.3	1.20	16.0	0.70	20.2	0.41
Ca	6.3	0.45	6.0	0.56	6.8	0.29	5.8	0.30
Cu	19.7	1.25	19.8	0.77	18.7	0.55	21.6	0.53
O	36.2	3.20	32.3	2.99	40.2	1.95	30.4	1.2

In both PMP and OP-PMP wires, Bi2201 filaments which form directly from the liquid contain higher oxygen content than Bi2212 filaments which form by a peritectic reaction between the liquid and the secondary phases. This is understood as oxygen diffusion in the melt being faster than in solid secondary phases. Moreover, the oxygen diffusion coefficient in Bi2212 is anisotropic; diffusion parallel to the c-direction via vacancies is much slower than parallel to ab-plane via an interstitial mechanism [49, 50]. In Figure 5-9, Bi2212 grains with their zone axis closer to [010] show 4±1% less O at% than those grains closer to the [100] zone. This is because diffusion in the ab-plane is also anisotropic; the diffusion

coefficient in the “a” direction is larger than in the “b” direction [49]. Moreover, Bi2212 grains from Bi2201 filaments in the OP-PMP wire show higher oxygen content than that of the PMP wire; this is understood as improved oxygen uptake in OP-PMP because of higher oxygen diffusion rates in 100 atm.

Porous grain colonies are found at several locations in the PMP wire; one is presented in Figure 5-9. Semi-quantitative EDS shows that the O at% is lower than in regular colonies in PMP wires. This may be related to poor oxygen recovery during solidification. Diffusional activities are improved in OP-PMP, therefore areas like this are not found in the samples extracted from the OP-PMP wire.

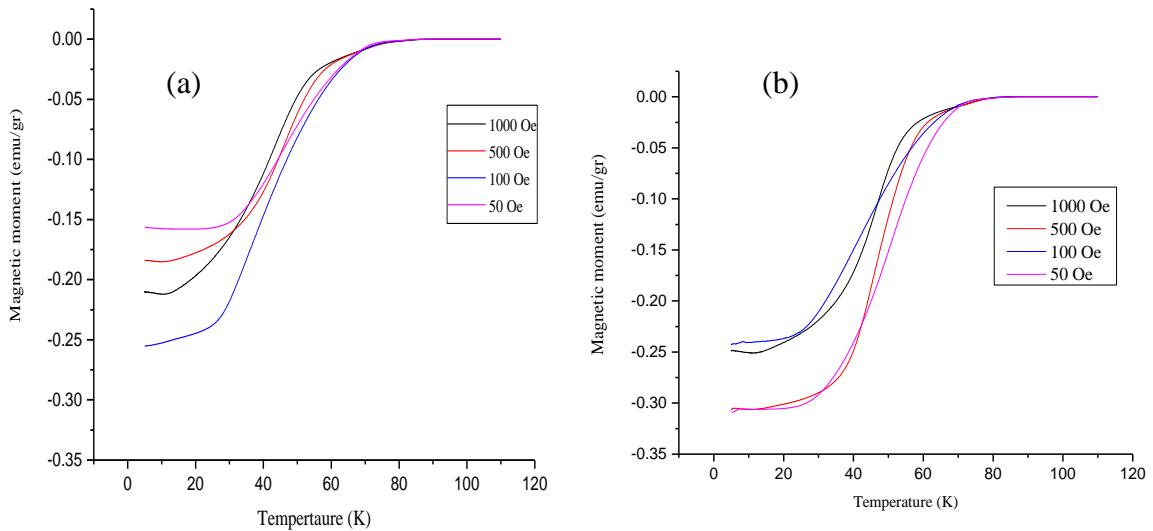


Figure 5-7 Magnetization as a function of temperature at magnetic fields of 50, 100, 500 and 1000 Oe for a) PMP and b) OP-PMP wire. The oxygen content of Bi2212 directly influences  $T_c$  [51]. Based on the magnetization behavior shown in Figure 5-7, a significant difference in overall oxygen content of the Bi2212/Ag wires after PMP and OP-PMP is not seen. Since in both heat treatments  $pO_2$  is 1 atm, the similarity of the overall oxygen content is understood. In both wires, onset of  $T_c$  decreases as magnetic field increases.

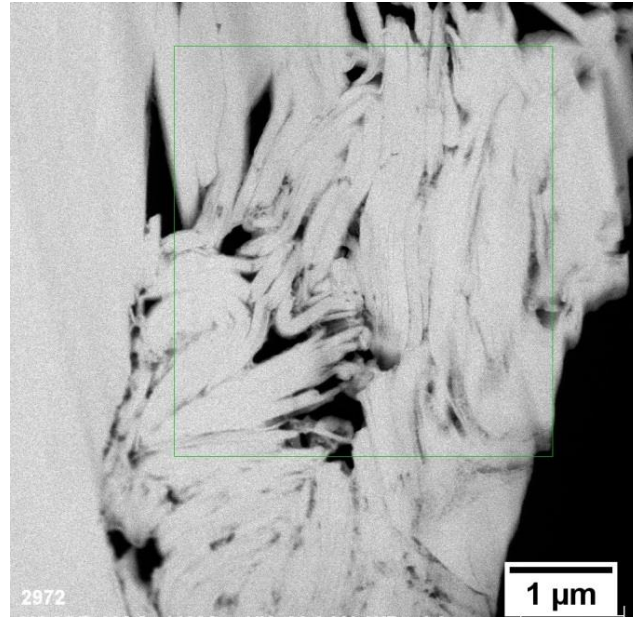


Figure 5-8 A HAADF STEM image of grain colonies extracted from a Bi2212 filament from a PMP wire. This image was used for the EDS semi-quantitative map

Table 5-3 Semi-quantitative EDS-STEM results of the Bi2212 colony shown in Figure 5-8

Element	at. %	error in wt. %
Bi	25.3	1.2
Sr	22.2	0.5
Ca	5.6	0.1
Cu	19.8	0.3
O	27.0	0.1

The magnitude of the diamagnetic moments seen in Figure 5-7 depend upon phase purity, grain connectivity, grain size, texturing and magnetic flux pinning [23]. In the PMP wire, the weakest magnetization moment corresponds to magnetization at 50 Oe, implying that  $H_{C1}^J$  is

around 50 Oe. The OP-PMP at 50 Oe shows much stronger magnetic moment due to the better intergrain connectivity which is also seen in the STEM image in Figure 5-5. At 100 Oe ( $H_{C1}^G$ ), both wires show the same order-of-magnitude magnetic moment, since  $H_{C1}^G$  mainly depends upon intragrain properties. Above  $H_{C1}^G$  (at 500 and 1000 Oe), the grain size and pinning mechanisms primarily determine the magnitude of magnetization because grains are completely decoupled from each other [23]. As Bi2212 grains in Bi2201 filaments are larger than Bi2212 grains in Bi2212 filaments, and contain a higher density of intergrowths, the OP-PMP wire shows larger magnetization at 500 Oe and 1000 Oe due to the higher content of Bi2201 filaments.

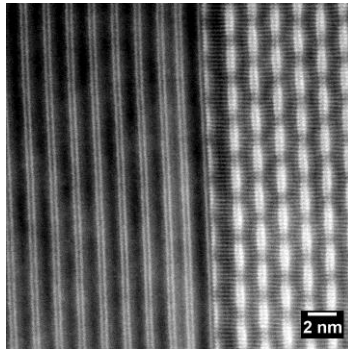


Figure 5-9 A HAADF STEM image in Bi2212 grains in a Bi2201 filament from an OP-PMP wire. On the left side of the image, the zone axis is close to [100], whereas on the right side of the image the zone axis is close to [010].

## Conclusions

Results here show that OP-PMP increases transport through increased filament density and improved grain connectivity on the nanoscale. Yet OP-PMP also increases the percentage of

Bi2201 filaments compared to PMP. Bi2201 filaments with  $\mu\text{m}$ -sized Bi2201 grains are detrimental to transport. A processing schedule that provides densification and connectivity but avoids formation of Bi2201 filaments would increase  $J_c$  significantly. Furthermore, results here show that the increased percentage of Bi2201 filaments in OP-PMP is a result of reduced liquid and secondary phases during the peritectic melt which is caused by increased  $T_p$  during OP-PMP compared to PMP. The EDS results, which are consistent with magnetization measurements, show that the overall oxygen content of PMP and OP-PMP wires is similar.

### **Acknowledgments**

This work was supported by North Carolina State University. Microstructural characterization was performed at the NC State University Analytical Instrumentation Facility, which is supported by the State of North Carolina and the National Science Foundation. The authors thank Professor David C. Larbalestier and Dr. Jianyi Jiang at the National High Magnetic Field Laboratory, Florida State University, for performing OP-PMP and  $I_c$  measurements on OP-PMP wires, and Dr. William Nachtrab (Supercon) for useful discussions.

## REFERENCES

- [1] *High Magnetic Field Science and Its Application in the United States: Current Status and Future Directions*: The National Academies Press, 2013.
- [2] H. W. Weijers, U. P. Trociewitz, W. D. Markiewicz, J. Jiang, D. Myers, E. E. Hellstrom, A. Xu, J. Jaroszynski, P. Noyes, Y. Viouchkov, and D. C. Larbalestier, "High Field Magnets With HTS Conductors," *IEEE Transactions on Applied Superconductivity* vol. 20, pp. 576-582, 2010.
- [3] S. A. Kahn, M. Alsharo'a, R. P. Johnson, M. Kuchnir, R. C. Gupta, R. B. Palmer, E. Willen, and D. J. Summers, "A high field HTS solenoid for muon cooling," in *Particle Accelerator Conference, 2007. PAC. IEEE, 2007*, pp. 446-448.
- [4] M. Okada, K. Tanaka, T. Wakuda, K. Ohata, J. Sato, T. Kiyoshi, H. Kitaguchi, and H. Wada, "Bi-2212/Ag high-field magnets," *Physica C: Superconductivity*, vol. 335, pp. 61-64, 2000.
- [5] D. C. Larbalestier, J. Jiang, U. P. Trociewitz, F. Kametani, C. Scheuerlein, M. Dalban-Canassy, M. Matras, P. Chen, N. C. Craig, P. J. Lee, and E. E. Hellstrom, "Isotropic round-wire multifilament cuprate superconductor for generation of magnetic fields above 30 T," *Nature Materials*, vol. 13, pp. 375-381, 2014.
- [6] J. Schwartz, T. Effio, X. T. Liu, Q. V. Le, A. L. Mbaruku, H. J. Schneider-Muntau, T. M. Shen, H. H. Song, U. P. Trociewitz, X. R. Wang, and H. W. Weijers, "High field superconducting solenoids via high temperature superconductors," *Ieee Transactions on Applied Superconductivity*, vol. 18, pp. 70-81, Jun 2008.
- [7] W. T. Nachtrab, C. V. Renaud, T. Wong, X. T. Liu, T. M. Shen, U. P. Trociewitz, and J. Schwartz, "Development of High Superconductor Fraction  $\text{Bi}_2\text{Sr}_2\text{CaCu}_2\text{O}_x/\text{Ag}$  Wire for MRI," *IEEE Transactions on Applied Superconductivity*, vol. 18, pp. 1184-1187, 2008.
- [8] W. Zhang, E. A. Goodilin, and E. E. Hellstrom, "Composition studies for Ag-sheathed  $\text{Bi}_2\text{Sr}_2\text{CaCu}_2\text{O}_8$  conductors processed in 100%  $\text{O}_2$ ," *Superconductor Science and Technology*, vol. 9, p. 211, 1996.

- [9] X. T. Liu, Q. V. Le, and J. Schwartz, "Influencing factors on the electrical transport properties of split-melt processed  $\text{Bi}_2\text{Sr}_2\text{CaCu}_2\text{O}_x$  round wires," *Superconductor Science and Technology*, vol. 25, p. 075008, 2012.
- [10] X. T. Liu, W. T. Nachtrab, T. Wong, and J. Schwartz, "Effect of Resolidification Conditions on  $\text{Bi}_2\text{Sr}_2\text{CaCu}_2\text{O}_x$  /Ag/AgMg Coil Performance," *Ieee Transactions on Applied Superconductivity*, vol. 19, pp. 2232-2236, 2009.
- [11] G. Naderi and J. Schwartz, "On the roles of  $\text{Bi}_2\text{Sr}_2\text{CuO}_x$  intergrowths in  $\text{Bi}_2\text{Sr}_2\text{CaCu}_2\text{O}_x$ /Ag round wires: c-axis transport and magnetic flux pinning," *Applied Physics Letters*, vol. 104, pp. 152602-152602-5, 2014.
- [12] T. Lang, D. Buhl, and L. J. Gauckler, "Melting of Bi-2212 under controlled oxygen partial pressures with silver," *Physica C: Superconductivity*, vol. 275, pp. 284-292, 1997.
- [13] W. Wu, L. Wang, J. Zhu, X. G. Li, G. Zhou, Y. Qian, Z. Chen, and Y. Zhang, "Oxygen loss effect under both reducing and oxidizing thermal treatments on superconductivity of single-crystal  $\text{Bi}_2\text{Sr}_2\text{CaCu}_2\text{O}_{8+y}$ ," *Journal of Applied Physics*, vol. 76, pp. 595-597, 1994.
- [14] T. Kanai and T. Kamo, "Control of oxygen release from Bi-2212 phase in a partial melt process," *Superconductor Science and Technology*, vol. 6, p. 510, 1993.
- [15] B. Hallstedt, D. Risold, R. Müller, and L. Gauckler, "Modelling of Thermodynamics and Phase Equilibria in Selected Subsystems of the Bi-Sr-Ca-Cu-O System," in *Advances in Superconductivity VII*, K. Yamafuji and T. Morishita, Eds., ed: Springer Japan, 1995, pp. 361-364.
- [16] G. Naderi, X. Liu, W. Nachtrab, and J. Schwartz, "Understanding processing–microstructure–properties relationships in  $\text{Bi}_2\text{Sr}_2\text{CaCu}_2\text{O}_x$  /Ag round wires and enhanced transport through saw-tooth processing," *Superconductor Science and Technology*, vol. 26, p. 105010, 2013.
- [17] E. B. Callaway, G. Naderi, Q. V. Le, and J. Schwartz, "Statistical analysis of the relationship between electrical transport and filament microstructure in

- multifilamentary  $\text{Bi}_2\text{Sr}_2\text{CaCu}_2\text{O}_x/\text{Ag}/\text{Ag-Mg}$  round wires," *Superconductor Science and Technology*, vol. 27, p. 044020, 2014.
- [18] R. Kleiner and P. Müller, "Intrinsic Josephson effects in high- $T_c$  superconductors," *Physical Review B*, vol. 49, pp. 1327-1341, 1994.
- [19] R. A. Klemm, "Bi2212 c-axis twist bicrystal and artificial and natural cross-whisker Josephson junctions: Strong evidence for s-wave superconductivity and incoherent c-axis tunneling," *Journal of Superconductivity*, vol. 18, pp. 697-700, Nov 2005.
- [20] F. Kametani, T. Shen, J. Jiang, C. Scheuerlein, A. Malagoli, M. D. Michiel, Y. Huang, H. Miao, J. A. Parrell, E. E. Hellstrom, and D. C. Larbalestier, "Bubble formation within filaments of melt-processed Bi2212 wires and its strongly negative effect on the critical current density," *Superconductor Science and Technology*, vol. 24, p. 075009, 2011.
- [21] T. Shen, A. Ghosh, L. Cooley, and J. Jiang, "Role of internal gases and creep of Ag in controlling the critical current density of Ag-sheathed  $\text{Bi}_2\text{Sr}_2\text{CaCu}_2\text{O}_x$  wires," *Journal of Applied Physics*, vol. 113, pp. -, 2013.
- [22] J. Jianyi, M. Hanping, H. Yibing, H. Seung, J. A. Parrell, C. Scheuerlein, M. Di Michiel, A. K. Ghosh, U. P. Trociewitz, E. E. Hellstrom, and D. C. Larbalestier, "Reduction of Gas Bubbles and Improved Critical Current Density in Bi-2212 Round Wire by Swaging," *Ieee Transactions on Applied Superconductivity*, vol. 23, pp. 6400206-6400206, 2013.
- [23] M. R. Koblishka, *Magnetic Properties of High-Temperature Superconductors*: Alpha Science International, Limited, 2009.
- [24] J. R. Clem, "Granular and superconducting-glass properties of the high-temperature superconductors," *Physica C: Superconductivity*, vol. 153-155, Part 1, pp. 50-55, 1988.
- [25] R. L. Landingham, "Dense high temperature ceramic oxide superconductors," ed: Google Patents, 1993.

- [26] T. Takagi, Y. M. Chiang, and A. Roshko, "Origin of grain boundary weak links in  $\text{BaPb}_{1-x}\text{Bi}_x\text{O}_3$  superconductor," *Journal of Applied Physics*, vol. 68, pp. 5750-5758, 1990.
- [27] D. J. Miller, T. G. Holesinger, J. D. Hettinger, K. C. Goretta, and K. E. Gray, "Enhanced superconducting properties in  $\text{Bi}_2\text{Sr}_2\text{Ca}_1\text{Cu}_2\text{O}_y$  by thermal and mechanical processing," *IEEE Transactions on Applied Superconductivity*, vol. 3, pp. 1182-1185, 1993.
- [28] H. V. Atkinson and S. Davies, "Fundamental aspects of hot isostatic pressing: An overview," *Metallurgical and Materials Transactions A*, vol. 31, pp. 2981-3000, 2000/12/01 2000.
- [29] S. Kobayashi, K. Yamazaki, T. Kato, K. Ohkura, E. Ueno, K. Fujino, J. Fujikami, N. Ayai, M. Kikuchi, K. Hayashi, K. Sato, and R. Hata, "Controlled over-pressure sintering process of Bi2223 wires," *Physica C: Superconductivity*, vol. 426-431, Part 2, pp. 1132-1137, 2005.
- [30] T. Kato, S. Kobayashi, K. Yamazaki, K. Ohkura, M. Ueyama, N. Ayai, J. Fujikami, E. Ueno, M. Kikuchi, K. Hayashi, and K. Sato, "Development of high performance Ag sheathed Bi2223 wire," *Physica C: Superconductivity*, vol. 412-414, Part 2, pp. 1066-1072, 2004.
- [31] N. Ayai, M. Kikuchi, K. Yamazaki, S. Kobayashi, S. Yamade, E. Ueno, N. J. Fujikami, T. Kato, K. Hayashi, K. Sato, R. Hata, J. Iihara, K. J. Yamaguchi, and J. Shimoyama, "The Bi-2223 Superconducting Wires With 200A-Class Critical Current," *IEEE Transactions on Applied Superconductivity*, vol. 17, pp. 3075-3078, 2007.
- [32] Y. Yuan, J. Jiang, X. Y. Cai, S. Patnaik, A. A. Polyanskii, E. E. Hellstrom, D. C. Larbalestier, R. K. Williams, and Y. Huang, "Microstructure and  $J_c$  improvements in overpressure processed Ag-sheathed Bi-2223 tapes," *IEEE Transactions on Applied Superconductivity*, vol. 13, pp. 2921-2925, 2003.
- [33] M. O. Rikel, R. K. Williams, X. Y. Cai, A. A. Polyanskii, J. Jiang, D. Wesolowski, E. E. Hellstrom, D. C. Larbalestier, K. DeMoranville, and G. N. Riley, Jr., "Overpressure processing Bi2223/Ag tapes," *IEEE Transactions on Applied Superconductivity*, vol. 11, pp. 3026-3029, 2001.

- [34] T. Kanai and N. Inoue, "Development of gas pressure melting (GPM) method for Ag-sheathed Bi-2212 wires," *Journal of Materials Science*, vol. 30, pp. 3200-3206, 1995/06/01 1995.
- [35] P. Lee, Y. Gao, H. S. Sheu, V. Petricek, R. Restori, P. Coppens, A. Darovskikh, J. C. Phillips, A. W. Sleight, and M. A. Subramanian, "Anomalous Scattering Study of the Bi Distribution in the 2212 Superconductor: Implications for Cu Valency," *Science*, vol. 244, pp. 62-63, 1989.
- [36] Y. Le Page, W. R. McKinnon, J. M. Tarascon, and P. Barboux, "Origin of the incommensurate modulation of the 80-K superconductor  $\text{Bi}_2\text{Sr}_2\text{CaCu}_2\text{O}_{8.21}$  derived from isostructural commensurate  $\text{Bi}_{10}\text{Sr}_{15}\text{Fe}_{10}\text{O}_{46}$ ," *Physical Review B*, vol. 40, pp. 6810-6816, 1989.
- [37] S. X. Dou, H. K. Liu, M. H. Apperley, K. H. Song, C. C. Sorrell, K. E. Easterling, J. Niska, and S. J. Guo, "Improvement of critical current density in the Bi-Pb-Sr-Ca-Cu-O system through hot isostatic pressing," *Physica C: Superconductivity*, vol. 167, pp. 525-528, 1990.
- [38] H. K. Liu, J. Horvat, Q. Y. Hu, D. K. Yu, and S. X. Dou, "Effect of hot pressing on the weak-link behaviour of Ag clad Bi based superconducting tapes," *Physica C: Superconductivity*, vol. 259, pp. 187-192, 1996.
- [39] H. Yamasaki and K. Endo, "Nanostructural defects for effective flux pinning in high-quality  $\text{Bi}_2\text{Sr}_2\text{CaCu}_2\text{O}_{8+x}$  epitaxial thin films with high critical current density," *Superconductor Science and Technology*, vol. 24, p. 10, 2014.
- [40] D. Buhl, T. Lang, M. Cantoni, D. Risold, B. Hallstedt, and L. J. Gauckler, "Critical current densities in Bi-2212 thick films," *Physica C: Superconductivity*, vol. 257, pp. 151-159, 1996.
- [41] W. Zhang and E. E. Hellstrom, "The development of an aligned microstructure during melt processing of  $\text{Bi}_2\text{Sr}_2\text{CaCu}_2\text{O}_x$  (BSCCO-2212) doctor-bladed films" *Physica C: Superconductivity*, vol. 218, pp. 141-152, 1993.

- [42] E. E. Hellstrom, R. D. Ray Li, and W. Zhang, "Phase development and microstructure in Bi-based 2212 Ag-clad tapes processed at 880, 890, and 905°C: The Cu-free phase and (Sr,Ca)CuO<sub>2</sub>," *Applied Superconductivity*, vol. 1, pp. 1535-1545, 1993.
- [43] J.-i. Shimoyama, N. Tomita, T. Morimoto, H. Kitaguchi, H. Kumakura, K. Togano, H. Maeda, K. Nomura, and M. Seido, "Improvement of Reproducibility of High Transport J<sub>c</sub> for Bi<sub>2</sub>Sr<sub>2</sub>CaCu<sub>2</sub>O<sub>y</sub>/Ag Tapes by Controlling Bi Content," *Japanese Journal of Applied Physics*, vol. 31, p. L1328, 1992.
- [44] M. Polak, W. Zhang, A. Polyanskii, A. Pashitski, E. E. Hellstrom, and D. C. Larbalestier, "The effect of the maximum processing temperature on the microstructure and electrical properties of melt processed Ag-sheathed Bi<sub>2</sub>Sr<sub>2</sub>CaCu<sub>2</sub>O<sub>2</sub> tape," *IEEE Transactions on Applied Superconductivity*, vol. 7, pp. 1537-1540, 1997.
- [45] A. Matsumoto, H. Kitaguchi, H. Kumakura, J. Nishioka, and T. Hasegawa, "Improvement of the microstructure and critical current densities of Bi-2212 round wires with a precisely controlled heat treatment," *Superconductor Science & Technology*, vol. 17, pp. 989-992, Aug 2004.
- [46] T. Lang, D. Buhl, and L. J. Gauckler, "Influence of the maximum temperature during partial melt-processing of Bi-2212 thick films on microstructure and j<sub>c</sub>," *Physica C: Superconductivity*, vol. 294, pp. 7-16, 1998.
- [47] T. G. Holesinger, M. Hanping, M. Meinesz, H. Yibing, J. Parrell, J. A. Kennison, K. R. Marken, and S. Campbell, "Analysis of High I<sub>c</sub> and J<sub>c</sub> Bi-2212 Conductors With Dilute Second Phase Additions," *IEEE Transactions on Applied Superconductivity*, vol. 21, pp. 2791-2794, 2011.
- [48] W. Zhang and E. E. Hellstrom, "The development of an aligned microstructure during melt processing of Bi<sub>2</sub>Sr<sub>2</sub>CaCu<sub>2</sub>O<sub>x</sub> (BSCCO-2212) doctor-bladed films," *Physica C: Superconductivity*, vol. 218, pp. 141-152, 1993.
- [49] J. L. Routbort and S. J. Rothman, "Oxygen diffusion in cuprate superconductors," *Journal of Applied Physics*, vol. 76, pp. 5615-5628, 1994.

- [50] M. Runde, J. L. Routbort, S. J. Rothman, K. C. Goretta, J. N. Mundy, X. Xu, and J. E. Baker, "Tracer diffusion of oxygen in  $\text{Bi}_2\text{Sr}_2\text{CaCu}_2\text{O}_x$ ," *Physical Review B*, vol. 45, pp. 7375-7382, 1992.
- [51] W. A. Groen and D. M. de Leeuw, "Oxygen content, lattice constants and  $T_c$  of  $\text{Bi}_2\text{Sr}_2\text{CaCu}_2\text{O}_{8+\delta}$ ," *Physica C: Superconductivity*, vol. 159, pp. 417-421, 1989.

## APPENDICES

Appendix A: (SQUID command for  $T_c$  measurement)

Wait For Chamber, Delay 60 secs, No Action

Set Magnetic Field 2000.0Oe at 500.0Oe/sec, Linear, Stable

Wait For Field, Delay 0 secs, No Action

Set Magnetic Field 0.0Oe at 500.0Oe/sec, Oscillate, Stable

Wait For Field, Delay 100 secs, No Action

Set Temperature 120K at 35K/min. Fast Settle

Wait For Temperature, Field, Delay 300 secs, No Action

Set Temperature 5K at 35K/min. No O'Shoot

Wait For Temperature, Delay 300 secs, No Action

Set Magnetic Field 100.0Oe at 10.0Oe/sec, Oscillate, Stable

Wait For Field, Delay 300 secs, No Action

SQUID VSM Moment (VSM) vs Temperature 5K to 70K Sweep Linear Auto-Tracking

SQUID VSM Moment (VSM) vs Temperature 70K to 110K Sweep Linear Auto-Tracking

Set Magnetic Field 0.0Oe at 100.0Oe/sec, Linear, Stable

Set Temperature 300K at 35K/min. Fast Settle

## Chapter 6

### Conclusions and Suggested Future Works

#### Conclusions

This thesis investigates the processing, microstructure and transport relationships of  $\text{Bi}_2\text{Sr}_2\text{CaCu}_2\text{O}_x/\text{Ag}$  (Bi2212/Ag) round wires.

In chapter 2 a new heat treatment method, saw-tooth processing (STP) is introduced based on the hypothesis that additional nucleation sites for Bi2212 are created through additional heat-cool-heat cycles during processing [1]. In the first part of this chapter the microstructural evolution of Bi2212 filaments during processing is discussed and results from STP are compared with those from other processes. In the second part, the effects of STP heat treatment parameters on the microstructure and transport properties are analyzed. In chapter 3, microstructure-properties relationships are discussed by using a statistical approach in which filaments are categorized based on the predominant phases observed by scanning electron microscope (SEM) [2]. In chapter 4 the roles of  $\text{Bi}_2\text{Sr}_2\text{CuO}_x$  intergrowths on c-axis transport and magnetic flux pinning are discussed. In chapter 5 inspired by the achieved breakthrough on transport properties of Bi221/Ag multifilamentary [3], processing, microstructure and transport relationships of Bi2212/Ag wires processed under 100 atm overpressure (OP) are studied.

The main conclusions of this thesis are summarized as following:

- STP includes multiple heating/cooling cycles. Heterogeneous nucleation through controlled, localized melting occurs during heating cycles and slow grain growth occurs during cooling cycles. Improved nucleation and growth form dense, textured Bi2212 grains while minimizing Bi2201 grains and non-superconducting phase formation.
- Variations in the heat treatment parameters affect the grain morphology and the phase assemblage of Bi2212 filaments. The second return temperature ( $T_{r2}$ ) plays the most significant role among all studied parameters. An optimum value for  $T_{r2}$  is found which results in the highest  $J_c$  ( $2760 \text{ A/mm}^2$ ) (self- field, 4.2 K) among all heat treated wires.
- STP increase  $J_c$  by 120% and 70% relative to partial-melt processing at 5 T and self-field respectively, and by 65% and 34% relative to split-melt processing.
- After heat treatment, both low- $J_c$  and high- $J_c$  multifilamentary Bi2212 wires have complex, multiphase microstructures. The new statistical method, which is introduced in this study, categorizes individual filaments in the wire cross-section based on the predominant non-Bi2212 phase(s) present in order to correlate the microstructure to the transport  $J_c$ .
- Image analysis of SEM micrographs shows there are strong relationships between the two types of filaments and the wire  $J_c$ ;  $J_c$  is directly proportional to the percentage of “predominantly-Bi2212” filaments and inversely proportional to the percentage of

“containing-large-Bi2201” filaments. The correlations between  $J_c$  and the other filament types are weak or non-existent. These results indicate the significant enhancements in Bi2212 wire performance requires either avoiding the formation of Bi2201, or ensuring complete conversion of Bi2201 to Bi2212.

- The primary impurity in partial-melt processed multifilamentary Bi2212 wires is Bi2201, which forms as mesoscopic grains and nanoscopic intergrowths. Nanostructural, magnetization and transport studies indicate that Bi2201 intergrowths and c-axis transport play important roles in Bi2212 transport behavior.
- The size of half- and full-cell Bi2201 intergrowths, as compared to the Bi2212 coherence length, and their smooth interface with Bi2212, imply that these narrow intergrowths are not barriers to transport. Instead, Bi2201 intergrowths show Josephson-Junction-like behavior at low field and flux pinning at higher field [4, 5]. Wide Bi2201 intergrowths, however, not only provide flux pinning, but also cause weak-link behavior.
- Our results indicate that future improvements in Bi2212 wires and films require the elimination of Bi2201 grains and large intergrowths, but that the presence of half- and full-cell intergrowths is not problematic. More generally, these results provide insight into the types of defects that should be engineered into the structure and as Bi2212 processing matures, an increased focus on engineering the nanostructure in concert with the microstructure is required.
- Partial melt processing accompanied with OP increases Bi2212 filament density and consequently  $J_c$  of Bi2212/Ag round wires. Yet 100 atm OP affects the phase assemblage of Bi2212 filaments in unknown ways.

- In the pre-annealing step of PMP, OP performs as an intermediate pressure hot iso-static press system. In the peritectic melting section, OP influences on the melting behaviors of Bi2212, in addition to densification. In the sintering step, OP improves the connectivity and oxygen recovery.
- Understanding the exact phase evolution during OP-PMP is necessary to optimize this processing and achieve further improvements; a few °C increases in maximum processing temperature is suggested to improve OP-PMP performance. Choosing the right maximum processing temperature produces enough secondary phases to act as nucleation sites. Further reaction of the secondary phases with Bi2201 produces more layered Bi2212 filaments instead of Bi2201 filaments.

#### **Suggestions for future work**

- Since porosity depress the transport properties of Bi2212/Ag wires using a high pressure (above 200-600 ksi) cold iso-static presses before STP, is suggested to increase the density and to achieve further improvements in  $J_c$ .
- Perform hot stage x-ray diffraction studies at the presence of oxygen to study the phase evolution during partial melt processing.
- Perform phase stability studies between Bi2212 and Bi2201 as a function of oxygen partial pressure and temperature.
- Perform Electron Backscatter Diffraction Analysis to study the local texturing and grain alignment in different filaments.

- Local transport properties measurements on Bi2212 grain colonies in different sections of wires to learn about transport properties as a function of impurity and grain boundary angle.
- Optimizing OP by increasing the maximum temperature, considering the effect of pressure on the melting point. Lowering oxygen partial pressure in the sintering step might also help lesser production of Bi2201. It can be assumed that the major densification of Bi2212 happens prior to the sintering step, therefore splitting the heat treatment and applying the OP only on the melting section (and prior) might be helpful to reduce the formation of Bi2201 grains.
- Using Tri-beam (laser, electron and ion ) tomography to obtain microstructural information along the length of wires

## REFERENCES

- [1] X. T. Liu, Q. V. Le, and J. Schwartz, "Influencing factors on the electrical transport properties of split-melt processed Bi2Sr2CaCu2Ox round wires," *Superconductor Science and Technology*, vol. 25, p. 075008, 2012.
- [2] E. B. Callaway, G. Naderi, Q. V. Le, and J. Schwartz, "Statistical analysis of the relationship between electrical transport and filament microstructure in multifilamentary Bi2Sr 2CaCu2Ox /Ag/Ag-Mg round wires," *Superconductor Science and Technology*, vol. 27, p. 044020, 2014.
- [3] D. C. Larbalestier, J. Jiang, U. P. Trociewitz, F. Kametani, C. Scheuerlein, M. Dalban-Canassy, M. Matras, P. Chen, N. C. Craig, P. J. Lee, and E. E. Hellstrom, "Isotropic round-wire multifilament cuprate superconductor for generation of magnetic fields above 30 T," *Nature Materials*, vol. 13, pp. 375-381, 2014.

- [4] R. Kleiner and P. Müller, "Intrinsic Josephson effects in high-T<sub>c</sub> superconductors," *Physical Review B*, vol. 49, pp. 1327-1341, 1994.
- [5] R. A. Klemm, "Bi2212 c-axis twist bicrystal and artificial and natural cross-whisker Josephson junctions: Strong evidence for s-wave superconductivity and incoherent c-axis tunneling," *Journal of Superconductivity*, vol. 18, pp. 697-700, Nov 2005.